

UNIVERSITÀ DEGLI STUDI DI NAPOLI FEDERICO II



DOTTORATO DI RICERCA IN INGEGNERIA AEROSPAZIALE,
NAVALE, E DELLA QUALITÀ (XXIII CICLO)
DIPARTIMENTO DI INGEGNERIA AEROSPAZIALE

Computational Fluid Dynamics and Computational Aeroacoustics for Turbomachinery Applications

with emphasis on High-Speed Propellers
and Vertical Axis Wind Turbines

Michele De Gennaro

Il Coordinatore:
Ch.mo Prof. Antonio Moccia

Il Tutore:
Ch.mo Prof. Carlo de Nicola

A.A. 2009/2010

*... don't waste time living someone else's life.
Don't be trapped by dogma, which is living with the results of other people's thinking.
Don't let the noise of others' opinions drown out your own inner voice, heart and intuition.
They somehow already know what you truly want to become.
Everything else is secondary...*

This page is intentionally left blank

ABSTRACT

COMPUTATIONAL FLUID DYNAMICS AND
COMPUTATIONAL AEROACOUSTICS FOR
TURBOMACHINERY APPLICATIONS

with emphasis on High-Speed Propellers and
Vertical Axis Wind Turbines

Michele De Gennaro

DIPARTIMENTO DI INGEGNERIA AEROSPAZIALE

Turbomachinery aerodynamic and aeroacoustic modelling is recognized to be one of the main areas of interest in the frame of industrial engineering, due to the large number of applications concerning the rotating fluid machines. Numerical modelling is today widely integrated in the design and development process of industrial components, as well as Computational Fluid Dynamics (CFD) is a tool well integrated into the industrial development and production life-cycles.

This has been made because of two main factors: the increase in the performance of relatively cheap computing systems and the progress made by development of integrated CAE virtual environment even more oriented to design and optimization.

Furthermore well established and validated CFD methodologies able to deal with the high complexity of geometries and multiphysics approaches are available and practicable within the industrial environment.

Nevertheless since for many of applications such as aerodynamics, heat exchange, etc., CFD is largely used, there are still some areas where it represents a challenge, in particular for its industrial applicability. One of these areas is the Computational AeroAcoustics (CAA), whose interest is rapidly growing due to the increasing demand of quick and efficient numerical tools for the design-to-noise approach to airframe components. The major difficulty of CAA is that noise is a secondary effect of other physical phenomena, and noise prediction has to deal with highly complex topics such as turbulence modelling and transition to turbulence prediction. Moreover the sound pressure compared with the hydrodynamic pressure is several orders of magnitude smaller making its numerical prediction very difficult.

The goal of the present work is to perform investigations on two rotating fluid machines: the vertical axis wind turbines (VAWT) and the high speed transonic cruise propellers. The investigations performed were focused on the aerodynamic and aeroacoustic theoretical and numerical modelling in order to achieve the numerical results that actually miss in the literature improving the know-how for two classes of problems which play a central role in the modern industry: the renewable energies and the advanced transportation systems.

VAWT modelling was approached from a theoretical point of view, by the implementation of a modern unsteady aerodynamic model for non-stationary airfoil aerodynamic coefficients prediction (the Beddoes-Leishman model) into a classical theory, the Double Streamtube Paraschivoiu model. The acoustic modelling of WT was approached on a general basis with the modelling of the airfoil self-generated problem. It was chosen as it is one of the most prominent noise sources for wind turbines and it represents a big challenge for CFD. The preliminary literature review pointed out how there are different airfoil self-generated noise typologies, according to the laminar/turbulent characteristics of the flow field, airfoil aerodynamic parameters and far-field flow conditions. Different CFD numerical approaches were used for the different

noise generation mechanisms, including transient RANS/LES simulations with a particular focus for novel turbulence modelling methodologies, involving transitional models and Embedded LES. The acoustic pressure flow computations were performed with the Ffowcs Williams-Hawkings (FW-H) acoustic analogy and pressure time signals post-processed with an in-house built acoustic tool. Deep explorations of acoustic signal noise processing, Fast Fourier Transformation techniques and noise signal corrections have been necessary in order to achieve good agreement between experimental and computational data. The reference test-case was the NACA 0012 airfoil, chosen for the wide amount of experimental data available in literature in a significant range of velocities and angles of attack.

The problem of propeller aerodynamic and aeroacoustic modelling was approached with the CFD and CAA simulation of a subsonic propeller, the NACA 4-(3)(08)-03, chosen for the experimental results available in literature for the 2-bladed and 7-bladed configurations. This test-case allowed us to set up properly the numerical simulation, the CAD model and the computational grid requirements for such kind of geometries.

In a second stage the attention was focused on the NASA SR2 and SR3 geometries, both in the 8-bladed configuration. Experimental data in transonic conditions for wind tunnel and flight test were available for these two geometries, and numerical simulations were performed for 5 different data sets, for asymptotic Mach numbers between 0.6 and 0.9 and rotational speeds between 6000 and 9000 rpm. Results of the simulations are compared with experiments, showing the ability of this approach to predict noise with a discrepancy within a few dB for the different simulated conditions and microphones locations. Particular attention is given to the set of corrections to be applied to acoustic experimental data in order to be consistently compared with free field CFD results. The CFD simulation strategy has been refined to perform complete aerodynamic and aeroacoustic calculations with highly competitive computational cost.

ACKNOWLEDGMENTS

First of all I wish to thank my advisor Prof. Carlo de Nicola for his support in this long (long) path called Ph.D. Then I have to thank to the Industrial Engineering Ph.D. School Coordinator Prof. Antonio Moccia for his comprehension about all the difficulties to conciliate my trips to UK and Austria with the obligations that a Ph.D. imposes.

My best acknowledgment goes to Domenico Caridi, who made physically possible the exceptional months I spent in Leeds and Sheffield, as well to Prof. Mohamed Pourkashanian and Chris Carey for their hospitality in the University of Leeds and in ANSYS UK Ltd. Moreover I cannot forget Helmut Kuehnelt and all the Austrian Institute of Technology, who made possible the best conclusion of my Ph.D. studies.

A great thanks goes also to Benedetto Mele, for the support provided from Naples.

THINKING, THANKING, TALKING ...

Allora, allora... vediamo un pò... volevo inserire un qualcosa in questa tesi che fosse inusuale ed una mattina di novembre mi venne in mente di infilarci dentro queste righe in italiano. Detto-fatto, ed eccoci qui a parlare la più bella lingua del mondo! Beh adesso il pensiero non può che andare ai tre anni appena trascorsi fra Italia, Inghilterra e Austria in perenne viaggio ed alle mille cose che ho imparato in questa avventura chiamata dottorato.

Ho imparato a capire chi mi vuol bene prima di tutto.

La mia famiglia ed Ilaria. Quindi un enorme e gigantesco GRAZIE va a loro. Ho imparato a parlare inglese, un pò di tedesco e a capire che le parole non contano.

Ho imparato a misurare e misurarmi, ho imparato a capire le persone, indipendentemente dal fatto che capisca o meno la loro lingua. Ho imparato a leggerne gli occhi e i gesti. E ho capito chi sono, dove voglio andare e con chi voglio farlo.

Pertanto comunque andranno le cose ... sarà un successo. E di questo ne sono certo.

TABLE OF CONTENTS

1. CFD AND TECHNOLOGY	1
1.1 CFD and Turbomachinery	2
1.2 Wind Power: the Micro Generation	4
1.3 Advanced Aircraft Propulsion: the High Speed Propellers	9
2. CFD AND CAA, THEORETICAL AND NUMERICAL BASIS	16
2.1 Navier-Stokes Equations	17
2.1.1 Mass Conservation Equation	17
2.1.2 Momentum Conservation Equation	17
2.1.3 Energy Conservation Equation	18
2.2 Numerical Models for Navier-Stokes Equations	19
2.2.1 Reynolds Averaged Navier-Stokes Equations (RANS)	19
2.2.2 The Turbulence Closure Problem	22
2.2.3 Turbulence Modelling Fundamentals	25
2.2.4 Transition to Turbulence Modelling	26
2.2.5 Large Eddy Simulation (LES)	31
2.2.6 Innovative Approaches for Navier-Stokes Equations: DES, ELES and SAS	36

2.3	Numerical Models for Turbomachinery Applications	40
2.3.1	Moving Reference Frame Model	40
2.3.2	Sliding Mesh Model	43
2.4	Acoustic Fundamentals	45
2.4.1	Quantification of Sound	49
2.4.2	Propagation of Sound	52
2.4.3	Types of Noise	56
2.5	Aerodynamic Generation of Sound	58
2.5.1	Homogeneous Wave Propagation	58
2.5.2	Non-Homogeneous Wave Propagation	59
2.5.3	Lighthill's Analogy	61
2.5.4	Curle's Equation	62
2.5.5	Ffowcs Williams-Hawkings's Analogy	65
2.5.6	Further Considerations on Aerodynamic Generation of Sound	70
2.6	Numerical Approaches for Aeroacoustics	73
2.6.1	Direct Noise Computation	73
2.6.2	Acoustic Analogy	74
2.6.3	Boundary Element Method and Finite Element Method	74
2.6.4	Broadband Noise Source Models	79
2.7	The solver: ANSYS FLUENT	80
3.	AERODYNAMIC AND AEROACOUSTIC MODELLING OF VERTICAL AXIS WIND TURBINES	82
3.1	Aerodynamics of Vertical Axis Wind Turbines	83
3.1.1	Paraschivoiu Double Streamtube Theory	84
3.1.2	Unsteady Aerodynamics: the Beddoes-Leishman Model	89
3.2	Aerodynamic Simulation of VAWT	97

3.2.1	Integrated DS-BL Approach to VAWT	97
3.2.2	CFD Approach to VAWT	104
3.3	Experimental VAWT Test-Case	107
3.3.1	Geometry and Experimental Data	107
3.3.2	Simulations and Results	109
3.3.3	CFD Optimization for VAWT Applications	114
3.4	Aeroacoustics of Wind Turbines	119
3.4.1	The Airfoil Self-Generated Noise	119
3.4.2	Post-Processing of Noise Pressure Data	121
3.4.3	NACA 0012 Experimental Test-case and Numerical Approach	127
3.4.4	NACA 0012 Self-Generated Noise: Results	132
4. AERODYNAMIC AND AEROACOUSTIC MODELLING OF HIGH SPEED PROPELLERS		141
4.1	Fundamentals of Aerodynamics of Propellers	142
4.1.1	Blade Element Theory	142
4.2	Subsonic Propeller Test-Case: NACA 4-(3)(08)-03	149
4.2.1	Geometry and Experimental Data	149
4.2.2	Simulations and Results	155
4.3	Transonic Cruise Propellers: NASA SR2 and SR3	160
4.3.1	Geometry and Experimental Data	161
4.3.2	NASA SR2 and SR3 Aerodynamic and Aeroacoustic Modelling	165
4.3.3	NASA SR2 Results: Data Sets 1-2-3	172
4.3.4	NASA SR3 Results: Data Sets 4-5	181
5. CONCLUSIONS		186
REFERENCES		190

NOMENCLATURE

<i>tilde</i> ($\tilde{}$)	instantaneous quantity
<i>capital case</i> (U_i)	time-averaged quantity
<i>lower case</i> (u_i)	fluctuating quantity
<i>prime</i> (\prime)	sub-grid quantity (LES)
u_i	<i>i</i> -the component of the fluid velocity (instantaneous)
$T_{ij}^{(v)}$	viscous stresses tensor
ρ	density
μ	viscosity
s_{ij}	instantaneous strain rate tensor
κ	wave number
c	speed of sound
G	green function
k	turbulence kinetic energy
M	Mach number
n	surface normal vector
p	pressure
\mathbf{g}	gravitational acceleration
x_i	generic direction
p_{ref}	reference pressure

Re	Reynolds number
T_{ij}	Lighthill stress tensor components
γ	intermittency
$Re_{\theta t}$	momentum thickness Reynolds number
δ_{ij}	Kronecker delta tensor
ε	turbulence dissipation rate
ω	specific dissipation rate
μ_t	dynamic turbulence viscosity
ν	kinematic viscosity
τ_{ij}	stress tensor components
S	generic source term
F	generic force
\underline{v}	velocity vector
\underline{v}_r	relative velocity vector
$\underline{\omega}$	rotational velocity vector
Z	impedance
$H(f)$	Heaviside function
Q	directivity factor
$L_{p,wli}$	acoustic pressure, power and intensity level
W	sound power
I	sound intensity
E	energy
l_o	integral scale
λ	Taylor scale
η	Kolmogorov scale
u, u'	Paraschivoiu velocity interference factors
$f_{up,down}$	upstream, downstream wind function
$w_{3/4}$	$3/4$ chord downwash
α	generic AoA
$C_{l,d,m}$	lift,drag and pitch aerodynamic coefficients
f^t	separation point location normalized to chord

Γ	circulation
$C_{N,T,P}$	normal and tangential force coefficients, power coefficient
$w_{a,t}$	axial and tangential induced velocities
λ, J	advance ratio
$V_{R,T}$	velocity components
N	number of blades
σ	propeller solidity
F	Prandtl's factor
y^+	normalized wall coordinate
β	blade angle at 75 % of blade radius
θ	azimuthal/longitudinal visual angle

ACRONYMS

2D	Two Dimensions
3D	Three Dimensions
CAE	Computer Aided Engineering
CFD	Computational Fluid Dynamics
CAA	Computational Aero Acoustics
WT	Wind Turbine
HAWT	Horizontal Axis Wind Turbine
VAWT	Vertical Axis Wind Turbine
LCA	Life Cycle Assessment
GHG	GreenHouse Gases
N-S	Navier-Stokes equations
RANS	Reynolds Averaged Navier-Stokes
URANS	Unsteady RANS
LES	Large Eddy Simulation
DES	Detached Eddy Simulation
ELES	Embedded LES
SAS	Scale Adaptive Simulation
DNS	Direct Numerical Simulation
FFT	Fast Fourier Transform

FW-H	Ffowcs Williams and Hawkings
MRF	Multiple Reference Frame
SLM	Sliding Mesh
SPL	Sound Pressure Level
OPSL	Overall Sound Pressure Level
WF	Wall Function
T-S	Tollmien-Schlichting
DFT	Discrete Fourier Transform
FFT	Fast Fourier Transform
BEM	Boundary Element Method
FEM	Finite Element Method
BIE	Boundary Integral Equation
HBIE	Hypersingular Boundary Integral Equation
BET	Blade Element Theory
AoA	Angle of Attack
FMG	Full MultiGrid
WTL	Wind Tunnel
FT	Flight Test
RPM	Root Per Minute
RPS	Root Per Second
TVR	Turbulent Viscosity Ratio
BPF	Blade Passing Frequency
DS	Paraschivoiu Double Streamtube Theory
BL	Beddoes-Leishman
ODE	Ordinary Differential Equations
TE	Trailing Edge
WTSP	Wind Turbine Simulator Package
TSR	Tip Speed Ratio
PT	Pressure-Takes
SG	Strain-Gages

Chapter 1

CFD and Technology

The global market is lead today by the most economically influent countries. Some centuries ago economic power was mainly related to the war-power of a country while today a central role is played by Technology.

Technology means the ability of men to modify the world to achieve benefits and ideally increase the overall quality of living. In the last century human life changed radically, and the role of technology into society became even more important. Today the technologic level of a country strongly depends by the efforts made in the fields of mathematics, physics and biology, being able to bring the economy to a competitive level on a global scale.

Moving the first step by these considerations this Thesis is focused on applied Mathematics for Computational Fluid Dynamics, today widely applied into different scientific fields, such as Energy, Chemistry, Biology and Medicine and in general wherever a fluid flow field (air, water, blood etc.) is important for the comprehension and modelling of involved phenomena. In this first chapter the attention is focused on the explanation of the whole job presented in this manuscript, focusing on its topics and on commercial impact of the performed applications.

1.1 CFD and Turbomachinery

In mechanical engineering the word Turbomachinery describes machines that transfer energy between a rotor and a fluid, including both turbines and compressors and, in general, all situations where rotating bodies are involved in.

For the huge number of applications it is not hard to understand why turbomachinery has been one of the most developed research areas for the applied fluid dynamics.

Turbomachinery dedicated departments and business fields exist in every company which operates in the frame of CFD applied to aerospace, aeronautics and energy and it implies a constant research and development of all most important CFD branches: CAD and mesh tools, moving grid techniques, turbulence and CPU-efficient numerical schemes. Turbomachinery applications have been the main subject of this thesis and the attention has been focused on two applications: wind turbines and propellers.

Today green technologies play an even more important role concerning to the increasing energy demand of the developed countries. In 1997 with the Kyoto Protocol to the United Nations Framework Convention on Climate Change (UNFCCC or FCCC), aimed at fighting global warming. It is an international environmental treaty with the goal of achieving "stabilization of greenhouse gas concentrations in the atmosphere at a level that would prevent dangerous anthropogenic interference with the climate system" [2].

The Protocol was initially adopted on 11 December 1997 in Kyoto, Japan and entered into force on 16 February 2005. As of November 2009, 187 states have signed and ratified the protocol.

Under the Protocol, 39 industrialized countries and the European Union commit themselves to a reduction of production of four greenhouse gases (GHG) (carbon dioxide, methane, nitrous oxide, sulphur hexafluoride) and two groups of gases (hydrofluorocarbons and perfluorocarbons). Moreover all countries agreed to reduce their collective greenhouse gas emissions by 5.2% from the 1990 level [3].

It is clear that the reduction of emissions implies the research for alternative energy sources, renewable and environmentally respectful, able to satisfy the increasing energy demand related to the growth of the economy. Wind energy is one of the candidates able to satisfy part of this demand, so in the last 10 years wind power industry and wind power research was strongly promoted.

According to the World Wind Energy Association the wind energy trends of last 10 years is growing with a rate equal to 25-30% per year, as reported by the World Wind Energy Report in 2009 [4]. This trend is distributed on the micro, medium and large size wind power generation, showing how in last 2/3 years the micro generation grew up very quickly under the push of small private investments for the in-house power generator systems.

From a technological point of view there is a big difference between the micro and macro generation. It is mainly related to the aerodynamic constraints of the problem and in general the Horizontal Axis Wind Turbine (HAWT) is used for macro-generation and the Vertical Axis Wind Turbine (VAWT) is used for micro-generation.

In this thesis the attention is focused on the VAWT, and in particular on the aerodynamic modelling and tools implementation for VAWT applications. The problem is approached from a theoretical and a numerical point of view, building up a simplified model for VAWT aerodynamic simulation being able to provide fundamental information on the aerodynamic behavior of the turbine for the design phase.

The second part of this thesis is focused on the propellers and in particular on high-speed geometries for turboprop applications. Moreover most of the work is based on a wide NASA R&D research program carried out in partnership with Lockheed from 1970 to 1990 [1]. This huge program was focused on the optimization and design of turboprop propulsion systems for civil aviation and it included experimental and numerical research for the design and simulation of low noise, transonic cruise, energy efficient propeller geometries. The excellent work carried out by NASA in 20 years and the huge amount of data available make this program a milestone of the applied R&D for civil aviation and maybe one of the first attempts to move the objective of the development from the searching for performances to the fuel-saving and environmentally green technologies.

Based on data published by NASA from the late 1970s to the early 1990s different propeller geometries have been tested and simulated with the CFD commercial software ANSYS-FLUENT[®], focusing on both aerodynamic and aeroacoustic simulation for turboprop applications.

1.2 Wind Power: the Micro Generation

Wind power is the conversion of wind energy into a useful form of energy (such as electricity) using wind turbines. Wind energy, together with hydrodynamic and solar energy, is the cleaner renewable energy source, as it does not imply any kind of waste during the energy generation process.

As stated in the paragraph above, it is widely accepted that an exponential increasing demand of energy is an issue for all developed economies. The quick growth of emerging countries, like China and India, caused an exponential increase of energy demand that has to be satisfied with fossil fuels (coal and petroleum), causing a continuous increase of their prices together with the CO₂ emissions, contributing to the acceleration of global warming process.

According to the sustainability principles stated by Kyoto protocol, fossil fuels have to be systematically substituted by alternative energy sources as much cheap as possible, but also environmentally clean and renewable.

Many alternative energy sources are today available, with the consequent confusion about their real costs, impact on environment and on human health. A good evaluation of impact of energy sources can be done applying the Life Cycle Assessment (LCA) approach, a statistical approach where all costs, from production to destruction, for a generic product are taken in account to have a global overview of its real economical impact.

In 2001 the University of Stuttgart published an interesting report [7] where a detailed evaluation of the real impact of different energy sources was performed, achieving the results showed in Figure 1.1 and 1.2.

In Figure 1.1 the evaluation of human health risk measured as years of life lost per TWh of energy produced is provided without taking in account extraordinary events (e.g. nuclear accidents), while in Figure 1.2 the real costs breakdown for energy production in Euro-Cent/KWh is given.

It is important to point out that this analysis is particularly interesting because it takes into account the real cost for the society of the energy production, including health damage and global warming.

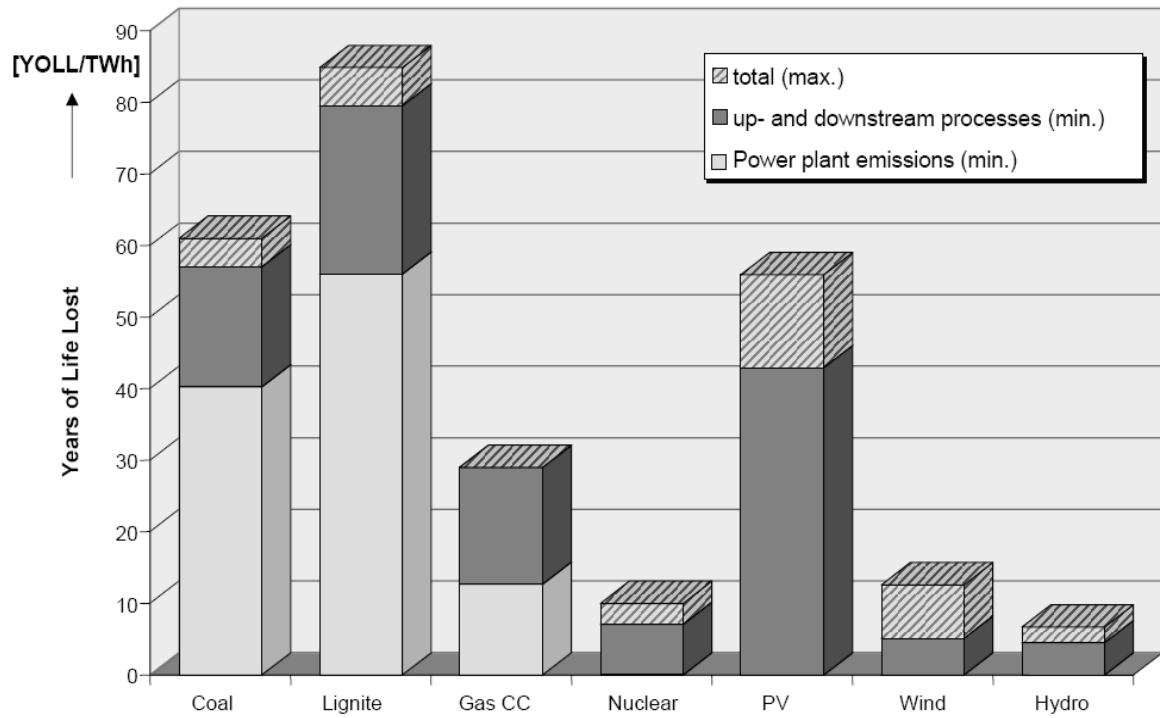


Figure 1.1: human health risk evaluation for different energy sources

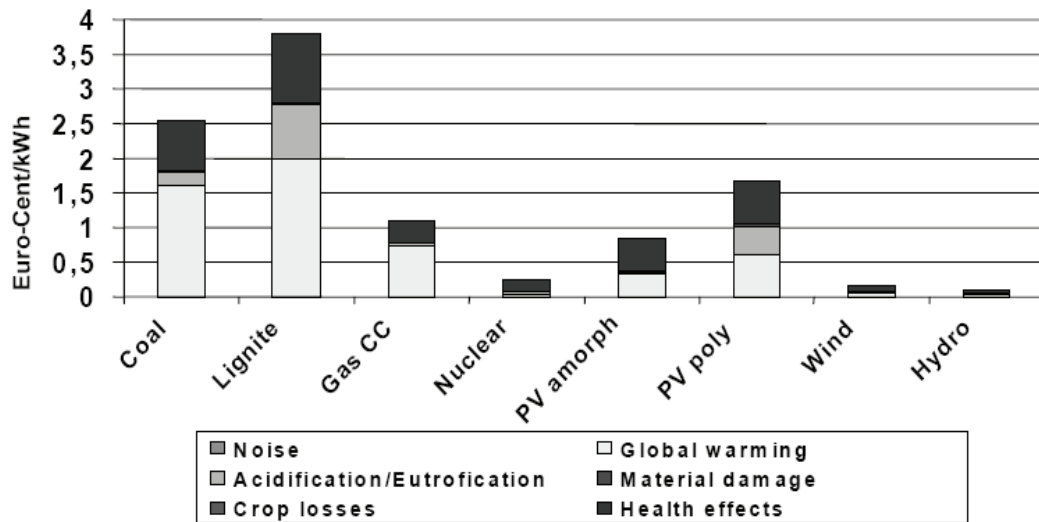


Figure 1.2: direct/indirect costs evaluation for different energy sources

Looking at these data it is easy to conclude that the Wind and Hydro energy are the best candidates for a massive environmentally friendly energy production, and this is also confirmed by the increasing interest towards them.

Wind turbines can be roughly classified according to the design energy production in three groups:

- Small size WT: energy production $< 5\text{kW}$ in design condition, suitable for in-house applications.
- Medium size WT: $5\text{kW} < \text{energy production} < 100\text{kW}$ in design condition, suitable for buildings and small industries.
- Large size WT: energy production $> 100\text{kW}$ in design conditions, suitable for industries and large living environments power supply systems.

The costs related to the installation and management of wind power implants are strongly related to the size of the WT and, even if the realization of large wind farms is something only feasible with big investments, the market of private micro-generation is growing up very quickly and promises a good prospective for the future.

The idea behind small-scale production of wind-energy consists in the possibility to install small wind turbines in urban environment to face the energy demand of buildings and families. A small domestic production of wind energy, in some aspects comparable with the photovoltaic, could play a key role in next years to promote the large and massive production of renewable energy. On the other hand small size domestic wind turbines imply low cost of production and maintenance, affordable by a family budget, long production life and low noise emission. For that reason attention is focused on VAWT, the only kind of wind turbine suitable for such applications.

There are many ways to obtain energy from wind as well a lot of different shapes of wind turbines are available. All of them give torque to a transmission axis connected to a turbine, and the generated power is given by the product of this torque and rotational speed multiplied by the efficiency scaling factors. The most general classification of wind turbines can be done according to the nature of the aerodynamic force devoted to energy production: the lift or the drag.



Figure 1.3: drag-based WT (left), lift-based WT (right)

In Figure 1.3 pictures of drag-based (left) and lift-based (right) wind turbine are provided. The efficiency of a WT is defined as ratio of produced power with the theoretical power of wind given by dynamic air-pressure multiplied by the wind velocity. The most efficient configuration is the lift-based WT, moreover some kinds of drag-based wind turbine are still in development for rough applications, due to their simple and basic behavior and construction.

As already mentioned in paragraph 1.1 the lift-based WT can be again classified in HAWT (Horizontal Axis Wind Turbine) where the axis of rotation is parallel to wind direction and VAWT (Vertical Axis Wind Turbine) where the axis of rotation is perpendicular to wind direction. Moreover VAWT are classified in straight blade and curved blade VAWT, often called Darrieus WT, Figure 1.4.

The difference of the shape of the blade for these two types of WT is due by structural motivations, related to centrifugal stresses of the blade tip. Basically the straight blade is more efficient than the curved blade, so this solution is used when stresses are low, which means for small and medium size wind turbines. The aerodynamics of the HAWT and VAWT is very different, and traditionally a wide and complete theoretical background is available in literature for HAWT only, while only few data, mainly related to a research project carried out from 1980 to 1995 in Sandia National Laboratory (New Mexico, USA), are available for the VAWT.



Figure 1.4: curved blade Darrieus VAWT (left), straight blade VAWT (right)

This difference is mainly caused by the deep difference between the two kinds of turbines. In particular a HAWT has an aerodynamic behavior similar to a propeller, with a quasi-steady load in the blade for all its nominal conditions, while the VAWT aerodynamics is totally unsteady and affected by different kinds of unsteadiness. In the chapter 3, totally focused on the straight-blade VAWT modelling, a detailed literature review of classical approaches to unsteady aerodynamic simulation will be provided in order to propose a new combined methodology designed for VAWT aerodynamic simulation.

Therefore CFD analysis of relevant test-cases will be performed, comparing computational results and experimental data.

1.3 Advanced Aircraft Propulsion: the High Speed Propellers

In the last 20 years, the flight services market has significantly increased its business volume led by the increase of demand for fast and cheap connections among European countries.

The proliferation of regional jet aircraft (e.g. A319/320/321, or B737) is a product of this trend; they are designed and optimized according to market requirements, with a passenger capacity approximately between 150 and 210 seats, and ranges between 800 and 1500 km, able to cover the most of the flight market in Europe.

Looking at the last 10 years in particular, this demand moved also towards shorter routes affected by geographical barriers (i.e. sea or mountain chains) where other solutions (i.e. trains, ferries) are not able to provide the quick and cheap service demanded.

Design trends are motivated also by the general interest from all aerospace manufacturer companies in the reduction of fuel-related costs and the environmental footprint of aircraft.

These two phenomena underlie a recent re-emergence of interest in the regional turboprop aircraft, smaller than the regional jet and able to be competitive for shorter ranges, less fuel-demanding and more environmentally respectful. A key point in the modern turboprop industry is the comfort perceived by passenger (especially in terms of vibrations and noise), together with the increase of cruise speed of aircraft.

Looking at the recent success of the Bombardier Dash Q400, a new concept turboprop aircraft which is currently used by a number of companies in Europe, it is clear that it covers a key market window, providing a cruise speed of 670 km/h, high level of comfort experienced by passenger, together with a reduction of about 30% in fuel demand and CO₂ emissions relative to an equivalent small size turbofan aircraft [5]. Therefore we can anticipate a growing interest among all aircraft manufacturer towards the advanced turboprop concept in the coming decades, in order to increase the cruise speed up to actual turbofan standard, and improve comfort issues.

In order to have a better overview of the problem it could be useful refer to the paper of *Smirti et Al.* [6], where the impact of fuel cost on civil aviation is investigated.

This paper shows that the determination of minimum cost aircraft operations over distances of 1000 miles or less is highly sensitive to fuel price and passenger costs. Today the Regional Jet is in general preferred to the Turboprop aircraft for the higher speed and the lower costs, but the balance between operating and passenger costs makes the regional jet a lower cost aircraft for many stage lengths up to a fuel price of about 3.50\$/gallon.

At fuel prices seen up to 2007, the most of the routes had a lower cost per passenger with the regional jet solution. During the global economic crisis in 2008 and 2009 the fuel price grew up to 2.50\$/gallon, making the turboprop more attractive for a certain number of routes. The analysts predictions for the U.S. market state that a price over 3.5\$/gallon should be expected for 2012 (figure 1.5), with a huge impact on the costs of civil transportation.

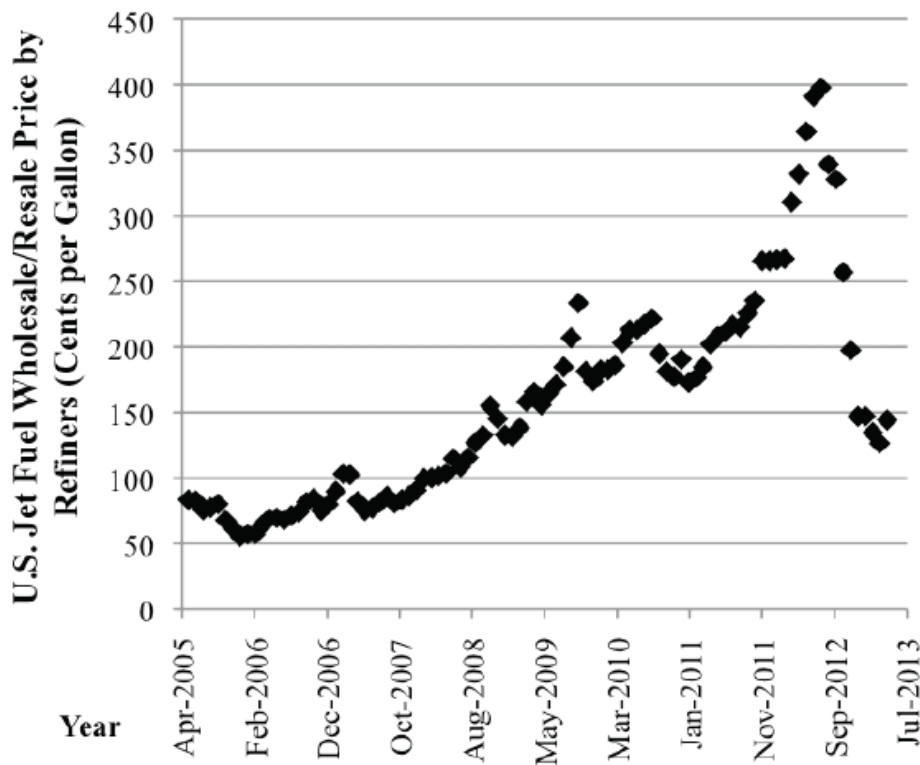


Figure 1.5: U.S. Jet Fuel Wholesale/Resale Price by Refiners Prediction in Cents/gallon.

This impact is quantified by the turboprop penetration market coefficient as function of fuel price (figure 1.6), bringing the percentage of turboprop civil aviation approximately to 10% for a fuel price equal to 4.00\$/gallon.

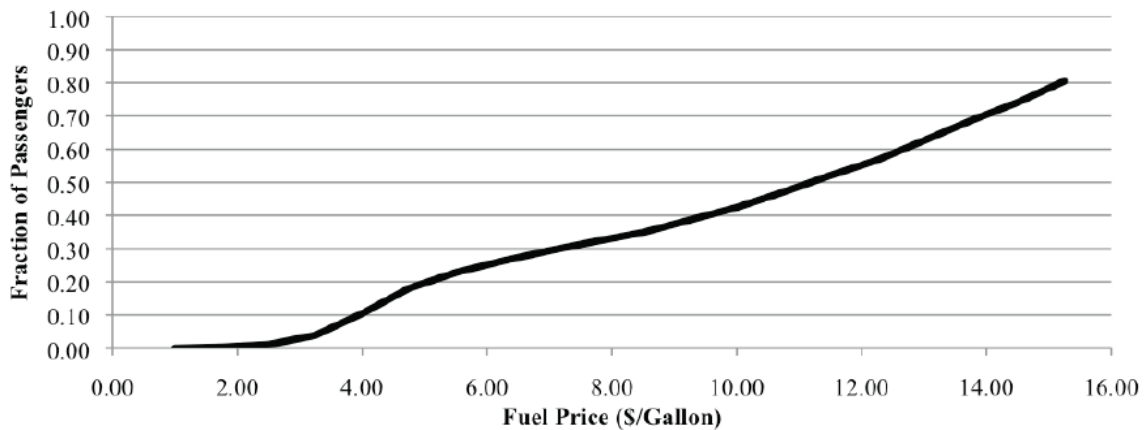


Figure 1.6: market penetration coefficient as function of fuel price

In addition to fuel price fluctuations, cost uncertainties arise due to the emission of GreenHouse Gases (GHG) the gases that cause the climate change.

Transportation plays a major role in GHG emission, being alone responsible of about 25% of total emission, making it the second largest sector after electric power generation.

Civil aviation accounts for 10% of transportation emissions which means about the 3% of the total emissions. Taking into consideration this huge impact on pollution caused by aviation it is easy to predict that it will play an additional role into turboprop development in next years.

Focusing the attention on the European market, in figure 1.7 the mobility demand over Europe territories is provided according to the European map for mobility needs [8]. As shown it seems to be clear that most of the mobility demand is concentrated on short routes, below 500 km. Obviously the mobility demand is satisfied by all transportations systems (motorways, railways aviation and ferries) but it is important to consider that for fast connections, business demand and geographical barriers the civil aviation has a market also for the short range.

For a better understanding it is possible give an example to focus the attention on a real market case. Our test-case is based on comparison of two different low-cost companies operating in Europe, in a good economic condition.

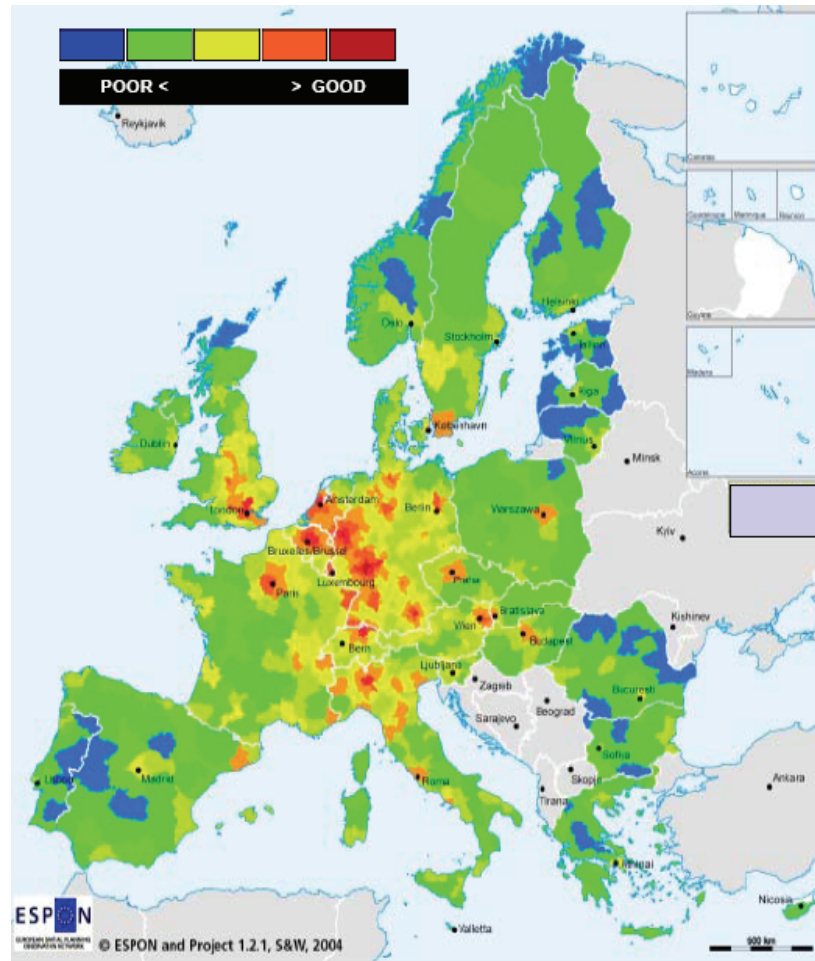


Figure 1.7: mobility and accessibility market demand,
European map for mobility needs 2004 [8].

The first one is the Easyjet [9], born in UK in 1995, which serves 104 destinations with 186 aircrafts (January 2009). The second company is the Flybaboo [10], a company born in Switzerland in 2003 which serves 15 destinations with 5 aircrafts (October 2009).

The size as well the business volume of these two companies is very different, but it is interesting a deeper analysis to understand their market strategies and the keys of their success.

The European low-cost flight companies market can be represented as an oligopolistic market where 2 actors play the role of leaders: Easyjet and Ryanair.

They control the market and all other companies cover business segments of partial interest, often related to a small portfolio of customers and destinations. Easyjet and Ryanair have this predominant position in Europe because they have been the first low-cost companies

in Europe, being able to accumulate a chronological advantage on competitors concentrating their business on a big-scale based market strategy.

Both of them offer a great number of destinations, but the offer is not differentiated in term of range. All destinations are in a range between 500 and 1500 km, that we call medium range. This is mostly related to the efficient range and required passenger fluxes for aircraft used by Easyjet and Ryanair, therefore it is not convenient fly if these two hypotheses are not fitted by market. This is the market strategy of the first actor we consider, the Easyjet.

A different and complementary business solution in this scenario is the strategy applied by new and small companies born from 2001 and 2003, as our second actor Flybaboo.

Flybaboo flies with a different type of aircraft, on different routes with smaller passenger flux, covering a different market segment.

According to this statement let us consider the comparison between Easyjet and Flybaboo flight map respectively from the hub of Milano Malpensa and Geneva (Figure 1.8).

Looking at the Easyjet map is possible to see that the closer destination to Milano Malpensa is Roma Fiumicino, approximately 500 Km, that is the lower limit of medium range. All other destinations are located over 500 km of range, and this is true for all European hubs served by this company (London, Paris and Madrid).

Looking at the Flybaboo flight map is clear that flight distance from Geneva to Lugano is only 150 Km, and that 8 destinations (50% of operating routes) from Geneva are located in a distance of less than 500 Km. Looking at the timetables of this company the 50% of operating routes become the 75% (approximately) of its total flight offer.

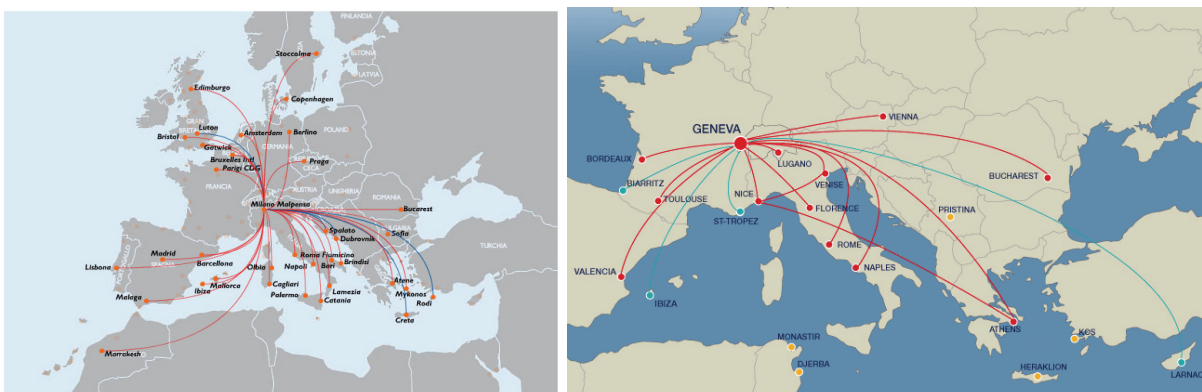


Figure 1.8 Easyjet (left) and Flybaboo (right) flight map (2009)

This difference is reflected by the fleets of these two companies, provided in Table 1.1. It appears immediately clear that Easyjet does not differentiate its fleet, while Flybaboo operates with smaller aircraft, with different propulsion systems. This is strictly related to the typical range of efficiency of turbofan and turboprop engine. The increasing request in the market of flight services of short distance makes today the Turboprop solution the best candidate for the short-range civil aviation for next years.

Easyjet Fleet		
Aircraft	In fleet	Passengers (economy)
Airbus A319-111	148	156
Airbus A320-232	9	174/180
Airbus A321-231	4	210
Boeing 737-700	25	149

Flybaboo Fleet		
Aircraft	In fleet	Passengers (economy)
Bombardier DashQ-400	2	74
Embraer 190LR	3	100

Table 1.1: Easyjet and Flybaboo fleet details (2009)

The importance of this new business is also proved by the research carried out by aircraft industries in the Turboprop propulsion to improve its performance and its level of comfort.

For this increasing interest for short-range flights market, for the importance of low operating costs as well of low CO₂ emissions, the research in the high-speed propeller design, simulation and optimization plays a key-role in the modern aircraft industry market.

In this thesis CFD has been used for simulation of Aerodynamic and Aeroacoustic performance of Transonic Cruise propellers SR2 and SR3, outcome of a research work carried out by NASA from 1970 to 1990. Very good agreement between experimental data and CFD results have been achieved with different geometries in transonic conditions, with the

definition of guidelines for CFD and CAA simulation of high speed propellers. A theoretical overview of numerical methodologies for aerodynamic and aeroacoustic simulation will be object of description in the chapter 2, while results on different test-cases and conditions will be provided in the chapter 4.

Chapter 2

CFD and CAA, Theoretical and Numerical Basis

In this chapter the attention is focused on theoretical and numerical aspects of CFD. In particular, after a fast review of constitutive equations of fluids, large space is dedicated to numerical approaches for N-S equations with a detailed overview of RANS and turbulence models, LES, DES, ELES and SAS, with a particular focus on turbomachinery numerical aspects. The second part of this chapter focuses on CAA and theoretical basis to numerical models are given in order to provide the complete scenario of the State of the Art of numerical approaches for acoustics, with the aim to explain similarities and differences between the models and provide the basis to choose the proper aeroacoustic approach for each problem.

All the topics discussed are oriented to the industrial implementation and use of commercial softwares in order to be able to answer to the market demands of industrial CFD and CAA with a particular and constant attention towards industrial applications.

2.1 Navier-Stokes Equations

The mechanics of incompressible fluids is regulated by the N-S equations, which consist of the conservation equations for the mass and the momentum. For fluids which involve heat transfer or compressibility, an additional equation for energy conservation has to be solved to compute the relation between pressure, temperature and density.

Finally, 2 scalars (mass and energy) and 1 vectorial (momentum) equations have to be solved for a 3D flow-field simulation. This system of 5 scalar equations is known as Navier-Stokes equations model.

For flows involving species mixing or reactions, turbulence and different phases additional equations need to be solved. In next paragraphs a short discussion about the conservation equations for laminar flow in an inertial (non-accelerating) reference frame are provided.

2.1.1 Mass Conservation Equation

The conservation of mass, or continuity equation, can be written as follows :

$$\frac{\partial \rho}{\partial t} + \underline{\nabla} \cdot (\rho \underline{v}) = S_m \quad (2.1)$$

Equation (2.1) is the general form of the mass conservation equation and is valid for incompressible as well as compressible flows. The first term is the time derivative of density, the second term is the convective one, related to mass transport, while the last term is the source, responsible of production or destruction of mass (e.g., due to vaporization) or related to any other arbitrary source.

2.1.2 Momentum Conservation Equation

Conservation of momentum for compressible flow in an inertial reference frame is given by equation (2.2).

$$\frac{\partial(\rho \underline{v})}{\partial t} + \underline{\nabla} \cdot (\rho \underline{v} \underline{v}) = -\underline{\nabla} p + \underline{\nabla} \cdot \left(\mu (\underline{\nabla} \underline{v} + \underline{\nabla} \underline{v}^T) - \frac{2}{3} \underline{\nabla} \cdot \underline{v} \underline{I} \right) + \rho \underline{g} + \underline{F} \quad (2.2)$$

Starting with the left side, the first term is the unsteady term, related to time-variation of momentum while the second one is the convective term, related to momentum transport with velocity. In the right side of equation the first term is the pressure gradient, the second one is the divergence of stress tensor, related to viscous effects, the third term is the gravity effect while the fourth term is the production, related to external forces which act on the fluid domain.

Equation (2.2) is a vectorial equation that can be rewritten in three scalar components for \underline{v} (u, v, w). A central role in this equation is played by the computation of the stress tensor. In particular the oldest and most famous numerical approach (RANS) for N-S resolves an ensemble version of governing equations introducing apparent stresses, known as Reynolds stresses.

The Reynolds stress tensor is made by a set of unknowns for which various models can provide different levels of closure (the turbulence models). This approach will be object of further and more detailed descriptions in next paragraphs.

2.1.3 Energy Conservation Equation

Conservation equation of energy is provided in (2.3).

$$\frac{\partial \rho E}{\partial t} + \underline{\nabla} \cdot (\underline{v}(\rho E + p)) = -\underline{\nabla} \cdot \left(\sum_j h_j \underline{J}_j \right) + S_h \quad (2.3)$$

The first term on the left side is the unsteady term; the second one is the convective term, while on the right side the first term is a generic diffusion term while the last one is a source term. Equation (2.3) needs to be coupled with (2.1) and (2.2) for the computation of a compressible flow field.

2.2 Numerical Models for Navier-Stokes Equations

Navier-Stokes equations, as mentioned above, are a system of 5 scalar partial differential equations, and should be closed with space and time boundary conditions. Only for a few cases an analytical solution exists, so they should usually be solved numerically.

There are several methodologies to approach this problem by a numerical point of view, and several orders of solution are available with different computational requirements. In this paragraph an overview of N-S approaches is given, starting from Reynolds Averaged Navier-Stokes approach (RANS) to Direct Navier-Stoker (DNS) simulation, to define the field of applicability and the mostly common problems related to each of them.

2.2.1 Reynolds Averaged Navier-Stokes Equations (RANS)

The RANS (Reynolds Averaged Navier-Stokes) methodology is the most used approach for engineering applications. It involves N-S equations resolution as well turbulence modeling, with the CPU-requirements relatively small.

The basic idea consists into the averaging of the conservation equations over a sufficiently long time period in order to lose every turbulent fluctuation but keeping the time dependence of the averaged quantities. The time averaged component over a period T and the fluctuating component of a generic quantity are defined by (2.4) and (2.5) respectively.

$$\Phi(\underline{r}, t) = \frac{1}{T} \int_t^{t+T} \varphi(\underline{r}, \tau) d\tau \quad (2.4)$$

$$\varphi_i(\underline{r}, t) = \tilde{\varphi}(\underline{r}, t) - \Phi(\underline{r}, t) \quad (2.5)$$

The conservation equations, in their incompressible formulation, for the instantaneous quantities can be calculated by equations (2.1) and (2.2) and rewritten with the Cartesian tensor and Einstein summation notation in set of equations (2.6), where u_i represents the i -th component of the fluid velocity at a point x_i in space and time t . Also p represents the static pressure, $T_{ij}^{(v)}$, the viscous (or deviatoric) stresses, and ρ the fluid density.

$$\begin{aligned} \frac{\partial \tilde{u}_i}{\partial x_i} &= 0 \\ \rho \left[\frac{\partial \tilde{u}_i}{\partial t} + \tilde{u}_j \frac{\partial \tilde{u}_i}{\partial x_j} \right] &= -\frac{\partial \tilde{p}}{\partial x_i} + \frac{\partial T_{ij}^{(v)}}{\partial x_j} \end{aligned} \quad (2.6)$$

The tilde in (2.6) equations is representative of instantaneous quantities. The viscous stresses (the stress minus the mean normal stress) are represented by the tensor $T_{ij}^{(v)}$. In many flows of interest, stress can be related to the fluid motion by a constitutive relation in the form (2.7).

$$T_{ij}^{(v)} = 2\mu \left[s_{ij} - \frac{1}{3} s_{kk} \delta_{ij} \right] \quad (2.7)$$

The viscosity, μ , is a property of the while s_{ij} is the instantaneous strain rate tensor defined by (2.8).

$$s_{ij} = \frac{1}{2} \left[\frac{\partial \tilde{u}_i}{\partial x_j} + \frac{\partial \tilde{u}_j}{\partial x_i} \right] \quad (2.8)$$

Although laminar solutions to the equations often exist and they are consistent with the boundary conditions, while perturbations to these solutions (sometimes even infinitesimal) can cause them to become turbulent. To see how this can happen, it is convenient to analyze the flow in two parts, a mean (or average) component and a fluctuating component. Thus the instantaneous velocity and stresses can be written as:

$$\begin{aligned} \tilde{u}_i &= U_i + u_i \\ \tilde{p} &= P + p_i \\ \tilde{T}_{ij}^{(v)} &= T_{ij}^{(v)} + \tau_{ij}^{(v)} \end{aligned} \quad (2.9)$$

Where U_i , P and $T_{ij}^{(v)}$ represent the mean motion, and u_i , p and $\tau_{ij}^{(v)}$ the fluctuating motions. This technique for decomposition of the instantaneous motion is referred to as the Reynolds decomposition. It's important to note that if the averaged quantities are defined as

ensemble this means that they are in general time-dependent. For the rest of this paragraph, unless otherwise stated, the density will be assumed constant so its fluctuation is zero. Substitution of equations (2.9) into equations (2.6) yields to the (2.10)

$$\frac{\partial(U_j + u_j)}{\partial x_j} = 0$$

$$\rho \left[\frac{\partial(U_i + u_i)}{\partial t} + (U_j + u_j) \frac{\partial(U_i + u_i)}{\partial x_j} \right] = -\frac{\partial(P + p)}{\partial x_i} + \frac{\partial(T_{ij}^{(v)} + \tau_{ij}^{(v)})}{\partial x_j} \quad (2.10)$$

These equations can now be averaged to yield to an equation expressing mass and momentum conservation for the averaged motion. Thus the equations for the averaged motion reduce to equations (2.11).

$$\frac{\partial U_j}{\partial x_j} = 0$$

$$\rho \left[\frac{\partial U_i}{\partial t} + U_j \frac{\partial U_i}{\partial x_j} \right] = -\frac{\partial P}{\partial x_i} + \frac{\partial T_{ij}^{(v)}}{\partial x_j} - \rho \left\langle u_j \frac{\partial u_i}{\partial x_j} \right\rangle \quad (2.11)$$

It's important to see how for the averaged quantities the form of continuity equation is preserved, so the linearity of the conservation of the mass. This is not true for momentum, where the term of non-linearity derived from convection has been brought to the right side of the equation. Multiplying the mass conservation for fluctuating quantity by u_i and averaging we can rewrite the second equation of (2.11) to obtain the final formulation of momentum equation (2.12).

$$\rho \left[\frac{\partial U_i}{\partial t} + U_j \frac{\partial U_i}{\partial x_j} \right] = -\frac{\partial P}{\partial x_i} + \frac{\partial}{\partial x_j} \left[T_{ij}^{(v)} - \rho \langle u_i u_j \rangle \right] \quad (2.12)$$

Now the terms in square brackets on the right have the dimensions of stress. The first term is, in fact, the viscous stress. The second term, on the other hand, is not a stress at all, but simply a re-worked version of the fluctuating contribution to the non-linear acceleration terms. This equation written this way, however, indicates that at least as far as the motion is concerned, the momentum acts as a stress, hence its name, the Reynolds stress.

2.2.2 The Turbulence Closure Problem

It is the appearance of the Reynolds stress which makes the turbulence problem so difficult, at least from the engineering perspective. Even though we can pretend it is a stress, the physics which give rise to it are very different from the viscous stress. The viscous stress can be related directly to the other flow properties by constitutive equations, which in turn depends only on the properties of the fluid.

The reason this works is that when we make such closure approximations for a fluid, we are averaging over characteristic length and time scales much smaller than those of the flows we are interested in. Yet at the same time, these scales are much larger than the molecular length and time scales which characterize the molecular interactions that are actually causing the momentum transfer (this is what the continuum approximation is all about). On the other hand this is not true for the Reynolds stress, because the scales of the fluctuating motion which give rise to it are the scales we are interested in, and this implies that the closure idea which worked so well for the viscous stress should not be expected to work well for the Reynolds stress too.

From the point of view of the averaged motion, at least, the problem with the non-linearity of the instantaneous equations is that they introduce new unknowns, the Reynolds stresses into the averaged equations. There are six individual stresses components we must deal with to be exact: $\langle u_1^2 \rangle$, $\langle u_2^2 \rangle$, $\langle u_3^2 \rangle$, $\langle u_1 u_2 \rangle$, $\langle u_1 u_3 \rangle$ and $\langle u_2 u_3 \rangle$. These quantities have to be related to the mean motion itself before the equations can be solved, since the number of unknowns and number of equations must be equal. The absence of these additional equations is often referred to as the Turbulence Closure Problem. To overcome this problem the idea is to introduce a model to calculate Reynolds stress tensor. The first model that we can introduce consists of an additional equation, where Reynolds stress term is related to velocity mean variable by a linear relation which gradient is μ_t , the so-called turbulent or eddy viscosity. Is clear that this simple idea might not be the best way to approach the problem of relating the Reynolds stress to the mean motion, by the way it is the simplest approach to the closure problem.

An alternative approach consists of deriving dynamical equations for the Reynolds stresses from the equations governing the fluctuations themselves. This approach recognizes that the Reynolds stress is really a functional of the velocity which means that stress in a point depends on velocity everywhere and for all past times, not just in a particular point and in a

particular instant in time. The analysis begins with the equation for the instantaneous fluctuating velocity, (2.13).

$$\rho \left[\frac{\partial u_i}{\partial t} + U_j \frac{\partial u_i}{\partial x_j} \right] = -\frac{\partial p}{\partial x_i} + \frac{\partial \tau_{ij}^{(v)}}{\partial x_j} - \rho \left[u_j \frac{\partial U_i}{\partial x_j} \right] - \left\{ u_j \frac{\partial u_i}{\partial x_j} - \rho \left\langle u_j \frac{\partial u_i}{\partial x_j} \right\rangle \right\} \quad (2.13)$$

Multiplying equation (2.13) by u_k and averaging it yields to (2.14).

$$\rho \left[\left\langle u_k \frac{\partial u_i}{\partial t} \right\rangle + U_j \left\langle u_k \frac{\partial u_i}{\partial x_j} \right\rangle \right] = -\left\langle u_k \frac{\partial p}{\partial x_i} \right\rangle + \left\langle u_k \frac{\partial \tau_{ij}^{(v)}}{\partial x_j} \right\rangle - \rho \left[\left\langle u_k u_j \right\rangle \frac{\partial U_i}{\partial x_j} \right] - \left\{ \rho \left\langle u_k u_j \frac{\partial u_i}{\partial x_j} \right\rangle \right\} \quad (2.14)$$

Now since both i and k are free indices they can be interchanged to yield a second equation given by (2.15), (alternatively equation (2.13) can be rewritten with free index k , then multiplied by u_i and averaged):

$$\rho \left[\left\langle u_i \frac{\partial u_k}{\partial t} \right\rangle + U_j \left\langle u_i \frac{\partial u_k}{\partial x_j} \right\rangle \right] = -\left\langle u_i \frac{\partial p}{\partial x_k} \right\rangle + \left\langle u_i \frac{\partial \tau_{kj}^{(v)}}{\partial x_j} \right\rangle - \rho \left[\left\langle u_i u_j \right\rangle \frac{\partial U_k}{\partial x_j} \right] - \left\{ \rho \left\langle u_i u_j \frac{\partial u_k}{\partial x_j} \right\rangle \right\} \quad (2.15)$$

Equations (2.14) and (2.15) can be added together to yield an equation for the Reynolds stress. Adding homologous terms of this two equations we obtain for the Reynolds stress equation right side term four components. Rearranging these terms using Newtonian constitutive equation and mass conservation equation for fluctuating quantities multiplied by u_k we can rewrite the Reynolds stress equation in the final formulation given in (2.16).

$$\begin{aligned} & \frac{\partial}{\partial t} \langle u_i u_k \rangle + U_j \frac{\partial}{\partial x_j} \langle u_i u_k \rangle = \\ & - \left\langle \frac{p}{\rho} \left[\frac{\partial u_i}{\partial x_k} + \frac{\partial u_k}{\partial x_i} \right] \right\rangle + \frac{\partial}{\partial x_j} \left\{ - \left[\langle p u_k \rangle \delta_{ij} + \langle p u_i \rangle \delta_{kj} \right] - \langle u_i u_k u_j \rangle + 2\nu \left[\langle s_{ij} u_k \rangle + \langle s_{ij} u_k \rangle \right] \right\} \\ & - \left[\left\langle u_i u_j \right\rangle \frac{\partial U_k}{\partial x_j} + \left\langle u_k u_j \right\rangle \frac{\partial U_i}{\partial x_j} \right] - 2\nu \left[\left\langle s_{ij} \frac{\partial u_k}{\partial x_j} \right\rangle + \left\langle s_{kj} \frac{\partial u_i}{\partial x_j} \right\rangle \right] \end{aligned} \quad (2.16)$$

This is the so-called Reynolds stress equation which has been the primary vehicle for much of the turbulence modeling efforts of the past few decades. The left hand side of the Reynolds stress equation can easily be recognized as the rate of change of the Reynolds stress following the mean motion. The problems are all on the right-hand side. These terms are referred to respectively as:

- the pressure-strain rate term
- the turbulence transport (or divergence) term
- the "production" term
- the "dissipation" term.

Obviously these terms do not involve only U_i and $\langle u_i u_j \rangle$, but depend on many more new unknowns. It is clear that, contrary to our hopes, we have not derived a single equation relating the Reynolds stress to the mean motion. Instead, our Reynolds stress transport equation is exceedingly complex. Whereas the process of averaging the equation for the mean motion introduced only six new, independent unknowns, the Reynolds stress $\langle u_i u_j \rangle$, the search for a transport equation which will relate these to the mean motion has produced new 75 unknowns. Nevertheless not all of these are independent, since some can be derived from others, the goal of reducing the number of unknowns has clearly not been met. Equations governing each of these new quantities can be derived from the original dynamical equations, just as we did for the Reynolds stress. Unfortunately new quantities continue to be introduced with each new equation, and at a faster rate than the increase in the number of equations. Now the full implications of the closure problem introduced by the Reynolds decomposition and averaging have become apparent. No matter how many new equations are derived, the number of new unknown quantities introduced will always increase more rapidly. It should be obvious by now that the turbulence closure problem will not be solved by the straight-forward derivation of new equations, nor by direct analogy with viscous stresses. Rather, closure attempts will have to depend on an intimate knowledge of the dynamics of the turbulence itself. Only by understanding how the turbulence behaves can one hope to guess an appropriate set of constitutive equations and understand the limits of them. This is, of course, another consequence of the fact that the turbulence is a property of the flow itself, and not of the fluid.

2.2.3 Turbulence Modelling Fundamentals

The Reynolds-averaged approach to turbulence modeling requires that the Reynolds stresses in Equation (2.16) has to be appropriately modelled. A common method employs the Boussinesq hypothesis to relate the Reynolds stresses to the mean velocity gradients (2.17).

$$\rho u_i u_j = \mu_t \left(\frac{\partial u_i}{\partial x_j} + \frac{\partial u_j}{\partial x_i} \right) - \frac{2}{3} \left(\rho k + \mu_t \frac{\partial u_k}{\partial x_k} \right) \delta_{ij} \quad (2.17)$$

The Boussinesq hypothesis is commonly used in most approaches for turbulence modelling. The advantage of this approach is the relatively low computational cost associated with the computation of the turbulent viscosity, μ_t . In the case of the Spalart-Allmaras model (one-equation model), only one additional transport equation (representing turbulent viscosity) is solved. In the case of the k - ε and k - ω models, two additional transport equations (for the turbulence kinetic energy, k , and either the turbulence dissipation rate ε , or the species dissipation rate, ω) are solved, and μ_t is computed as a function of these two variables. The main disadvantage of the Boussinesq hypothesis as presented is that it assumes μ_t is an isotropic scalar quantity, which is not strictly true.

The choice of a turbulence model is always a tricky problem, where an important role is played by the computational effort budget considerations. So a list of most commonly used turbulence models, ordered by categories according to computational effort, is provided.

I. 0-Equations Models (Algebraic Models)

- Cebeci-Smith Model
- Baldwin-Lomax Model
- Johnson-King Model
- Roughness dependant Models

II. 1-Equation Model

- Prandtl's Models
- Baldwin-Barth Model
- Spalart-Allmaras Model

III. 2-Equations Models

- Standard k- ε Model

- Realizable k- ϵ Model
- RNG k- ϵ Model
- Wilcox k- ω Model
- Menter SST k- ω Model

IV. Other Models (more than two equations)

- v^2 - f Model
- ζ - f Model
- RSM Model

All these models provide different closures to turbulence problem, and some of them are coupled with near-wall treatments. Near-wall treatment consists of the possibility to couple RANS simulation and turbulence models with a predetermined resolution of the boundary layer, made by the so called wall functions. A WF is a function for a generic thermodynamic variable close to a wall boundary. In fact it is well known that, close to wall boundaries, strong variation of temperature and velocity are present and they need high (sometimes prohibitive) mesh accuracy to be appropriately resolved, with strong increase of computational effort. To overcome this problem a standard shape for temperature and velocity can be given as function of distance to wall (linear in the laminar sub-layer and logarithmic in the turbulent boundary layer). In this way it is possible to resolve the boundary layer with a low number of cells and reconstruct “artificially” the wall stresses according to WF.

Further details on turbulence models and wall treatments are available in the literature.

2.2.4 Transition to Turbulence Modelling

Transition to turbulence is the series of processes by which a flow passes from regular or laminar to irregular or turbulent conditions as the control parameter, usually the Reynolds number is increased.

In general turbulence is characterized by highly enhanced transfers of momentum, heat and chemical species, when compared to molecular transfers in laminar flow. Understanding the transition in view of its control is an important issue. Though qualitative descriptions might be found earlier, the history of the problem at a quantitative level begins with pipe flow experiments by Reynolds in 1883 [11].

The concept of transition scenario was implicitly introduced by *Landau et Al.* in 1944 [12] and later revised by Ruelle and Takens in 1971 [13]. According to Landau, turbulence is reached at the end of an indefinite superposition of successive oscillatory bifurcations, each bringing its unknown phase into the dynamics of the system. In contrast, Ruelle and Takens mathematically showed that quasi-periodicity is not generic when nonlinearities are acting. They identified turbulence with the stochastic regime of deterministic chaos [14] characterized by long term unpredictability due to sensitivity to initial conditions and reached only after a finite and small number of bifurcations.

From a physical point of view, instabilities and the transition to turbulence occur in systems driven far from equilibrium. At equilibrium, a macroscopic system stays in a time-independent, spatially uniform state. Departures from that state regress spontaneously as an effect of microscopic fluctuations, resulting in dissipation. When driven out of equilibrium, the system may respond in some unexpected way, as a result of the competition between driving and restoring forces.

In fluid mechanics, the distance to equilibrium is measured by the Reynolds number which compares the effects of applied shear disturbing the fluid to those of viscous dissipation ironing out velocity non-homogeneities. The state directly stemming from equilibrium is referred to as the base flow. Let L be the length scale over which velocity variations of magnitude U are imposed, and let ν be the kinematic viscosity. Viscous dissipation operates on a time scale $\tau_v = L^2/\nu$ while the shear introduces its own time scale $\tau_s = L/U$. When the Reynolds number $Re = \tau_v/\tau_s = LU/\nu$ is small, e.g. τ_v much shorter than τ_s , viscous dissipation rapidly irons out velocity disturbances and the flow responds smoothly to the perturbation, laminar flow prevails. On the contrary, when Re is large, viscosity has no longer a sufficient time to damp fluctuations that may be amplified by the shear. The fluid becomes unstable and ultimately turbulent when driven sufficiently far from equilibrium. The structure of the Reynolds number, measuring the relative intensities time-scales/length-scales of different processes, is typical of a control parameter.

Focusing on the aerodynamic aspects of the transition to turbulence all the relevant issues are provided by H. Schlichting in [15]. In a very simplified way transition can be ascribed to the growth in amplitude of disturbance waves (Tollmien-Schlichting waves) that exist in the boundary layer over an aerodynamic surface. These waves are convected by the flow and

cause some isolated spot of turbulence into the laminar boundary layer that lead to a fully developed turbulent flow. The growth of flow T-S waves is influenced by:

- Pressure gradient and centrifugal force (e.g. adverse pressure gradient induces the transition)
- Wall roughness
- Heat transfer and compressibility
- Free-stream turbulence and non-homogeneous inlet conditions (e.g. oscillating asymptotic flow)
- Body shape (effect of body convexity on pressure gradient and 3D transition phenomena)

According to this approach a unique transition point cannot be identified, but it is possible to argue about a transition region that starts when turbulent spots appear and finishes when a fully developed turbulent flow is established. However this region is generally small and its lower limit is generally identified as the transition point.

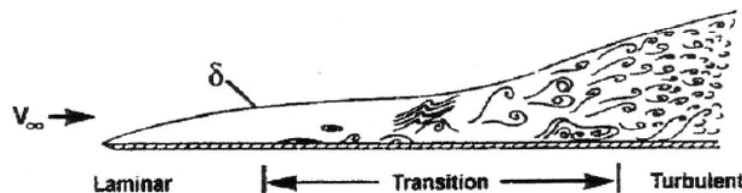


Figure 2.1: The natural transition process (Schlichting [15])

Moreover transition to turbulence affects also the separation and these two phenomena are strictly connected. In some cases the flow separation can induce transition and consequent reattachment, causing the presence of laminar/turbulent bubbles over surfaces.

Transition to turbulence can be predicted with several computational methods modeling the growth mechanism of the instabilities of the T-S waves. The most widely used approach is the Smith & Gamberoni e^n method [16], [17], presented in 1956 based on the linear instability theory and implemented in the popular panel solver XFOIL [18]. A detailed explanation and historical review of this method is provided in [19].

Transition prediction via CFD and in particular via RANS modelling for industrial applications has always been one of the most important issues to manage in order to achieve good simulation results.

In fact forces resultants on aerodynamic surfaces depend by friction coefficient that depends by laminar/turbulent flow characteristics. For this reason a good prediction of overall performance of an aerodynamic body (e.g. airfoil drag) implies a good prediction of transition point.

Recently new models, dedicated to transitional flows modelling, have been developed and implemented into commercial CFD packages. The most important models have been implemented into ANSYS-FLUENT[®] and they are:

- Transitional k - ω SST turbulence model
- k - kl - ω turbulence model

Both of them are coupled with RANS approach via turbulence modelling, introducing additional equations focused on transition prediction.

The first of them is the Transitional k - ω SST, a 4-equations model based on the coupling of the Menter 2-equations SST model with two additional equations: one for the intermittency and one for the transition onset criteria, in terms of momentum-thickness Reynolds number. The k - ω SST model consists of equations (2.18) for balance of turbulent kinetic energy k and specific dissipation rate ω [20].

$$\begin{aligned} \frac{\partial(\rho k)}{\partial t} + \frac{\partial(\rho U_j k)}{\partial x_j} &= \frac{\partial}{\partial x_j} \left[\Gamma_k \frac{\partial k}{\partial x_j} \right] + G_k - Y_k + S_k \\ \frac{\partial(\rho \omega)}{\partial t} + \frac{\partial(\rho U_j \omega)}{\partial x_j} &= \frac{\partial}{\partial x_j} \left[\Gamma_\omega \frac{\partial \omega}{\partial x_j} \right] + G_\omega - Y_\omega + D_\omega + S_\omega \end{aligned} \quad (2.18)$$

In equation (2.18) Γ represents the effective diffusivity, G the production of k and ω due to mean velocity gradients, Y represents their dissipation due to turbulence, while D_ω represents the cross-diffusion of ω due to the transformation of the dissipation rate ε into the specific dissipation rate ω .

Transition is introduced in this model by Langstry and Menter [21] in the form of empirical correlations to cover standard bypass transition as well as flows in low free-stream turbulence environments.

The system (2.18) is coupled with balance equation for intermittency γ and for transition momentum thickness Reynolds number $Re_{\theta t}$ leading to the two additional equations provided in (2.19).

$$\begin{aligned} \frac{\partial(\rho\gamma)}{\partial t} + \frac{\partial(\rho U_j \gamma)}{\partial x_j} &= P_{\gamma 1} - E_{\gamma 1} + P_{\gamma 2} - E_{\gamma 2} + \frac{\partial}{\partial x_j} \left[\left(\mu + \frac{\mu_t}{\sigma_\gamma} \right) \frac{\partial \gamma}{\partial x_j} \right] \\ \frac{\partial(\rho Re_{\theta t})}{\partial t} + \frac{\partial(\rho U_j Re_{\theta t})}{\partial x_j} &= P_{\theta t} + \frac{\partial}{\partial x_j} \left[\sigma_{\theta t} (\mu + \mu_t) \frac{\partial Re_{\theta t}}{\partial x_j} \right] \end{aligned} \quad (2.19)$$

Here the P and E sources terms of equation (2.19) can be classified in transition sources (subscript $\gamma 1$) and destruction/relaminarization sources (subscript $\gamma 2$). The onset transition is controlled by these sources in the form of empirical functions.

Intermittency is coupled with momentum thickness Reynolds number by the $P_{\theta t}$ term, so it affects the production of this quantity via empirical correlations. These are ANSYS proprietary material and they cannot be provided.

On the other hand $k\text{-}k\text{-}\omega$ turbulence model is a three-equation eddy-viscosity type model, which introduces transport equations for turbulent kinetic energy k_T , laminar kinetic energy k_L and the inverse turbulent scale ω . In (2.20) balance equations for these quantities are provided.

$$\begin{aligned} \frac{Dk_T}{Dt} &= \frac{\partial}{\partial x_j} \left[\left(\nu + \frac{\alpha_T}{\alpha_k} \right) \frac{\partial k_T}{\partial x_j} \right] + P_{k_T} + R + R_{NAT} - \omega k_T - D_T \\ \frac{Dk_L}{Dt} &= \frac{\partial}{\partial x_j} \left[\nu \frac{\partial k_T}{\partial x_j} \right] + P_{k_L} - R - R_{NAT} - D_L \\ \frac{D\omega}{Dt} &= \frac{\partial}{\partial x_j} \left[\left(\nu + \frac{\alpha_T}{\alpha_\omega} \right) \frac{\partial \omega}{\partial x_j} \right] + C_{\omega 1} \frac{\omega}{k_T} P_{k_T} + \left(\frac{C_{\omega R}}{f_W} - 1 \right) \frac{\omega}{k_T} (R + R_{NAT}) - C_{\omega 2} \omega^2 + C_{\omega 3} f_\omega \alpha_T f_W^2 \frac{\sqrt{k_T}}{d^3} \end{aligned} \quad (2.20)$$

Here the P terms are productions, R is the averaged effect of the breakdown of streamwise fluctuations into turbulence during bypass transition, R_{NAT} is a natural transition production term, while D is the dissipation term. More details about model's coefficients are provided in the references [22] and [23].

These models, both recently developed, provide very interesting characteristics able to be applied in all the problems where the transition to turbulence plays a fundamental role for the final results, without increasing too much the computational cost of the simulation, with an approach embedded into a commercial tool, avoiding the need of external tools (e.g. external boundary layer solver). In particular the solutions provided in next chapter with the transitional models seem to be more sensitive to flow instabilities than a solution achieved with the standard turbulence models, reducing the effect of RANS model to damp solution details and instabilities.

2.2.5 Large Eddy Simulation (LES)

Turbulent flows are characterized by eddies with a wide range of length and time scales. The largest eddies are typically comparable in size to the characteristic length of the mean flow while the smallest scales are responsible for the dissipation of turbulent kinetic energy. It is theoretically possible the resolution of whole spectrum of turbulent scales using the Direct Numerical Simulation (DNS) approach. No modelling is required in DNS, nevertheless its computational effort is so high that it is senseless for engineering problems. Moreover the computational cost of DNS is proportional to third power of Reynolds number, so it is practically feasible only for (very) low Mach numbers.

A possible solution to overcome RANS limitations without DNS is the Large Eddy Simulation (LES), a hybrid technique that allows to explicitly solve for the large eddies in a calculation and implicitly account for the small eddies by using a subgrid-scale model.

Mathematically LES needs of separating the velocity field into a resolved part and a sub-grid part. The resolved part of the field represent the "large" eddies, while the subgrid part of the velocity represent the "small scales" whose effect on the resolved field is included through the subgrid model. Formally this happens with a filtering technique.

Let us consider equation (2.9) for the instantaneous flow velocity u_i and let us consider U_i the resolved scales while u_i the modeled scales. Applying the convolution of $u(\underline{x})$ with a filtering function G (2.21)

$$\bar{u}(\underline{x}) = \int G(\underline{x} - \underline{\xi}) u(\underline{\xi}) d\underline{\xi} \quad (2.21)$$

is possible to isolate the resolved by the modeled part. In the most part of commercial implementation of LES the filter is space-dependant and they use the grid itself for filtering (Figure 2.2). This implies that the grid for LES plays the role of a “direct measure” of how many scales are directly resolved.

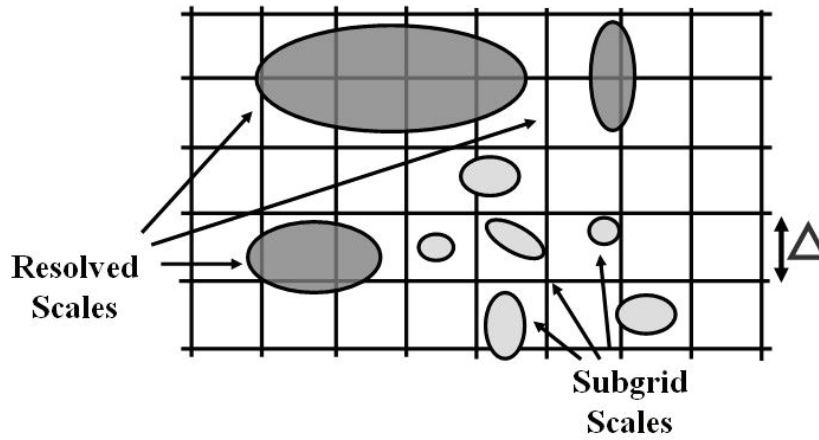


Figure 2.2: LES Grid-Based Filtering Technique

Without going into details of filtering theory, let us develop a simplified LES approach for incompressible N-S equations. Let us consider the momentum equation (2.6) and apply the filtering to velocity and pressure. The equation obtained is the (2.22).

$$\frac{\partial \bar{u}_i}{\partial t} + \bar{u}_i \frac{\partial \bar{u}_i}{\partial x_j} = -\frac{1}{\rho} \frac{\partial \bar{p}}{\partial x_i} + \frac{\partial}{\partial x_j} \left(\nu \frac{\partial \bar{u}_i}{\partial x_j} \right) + \frac{1}{\rho} \frac{\partial \bar{\tau}_{ij}}{\partial x_j} \quad (2.22)$$

We have assumed that the filtering operation and the differentiation operation commute, which is not generally the case but it is thought that the errors associated with this assumption are usually small. The extra term $\partial \bar{\tau}_{ij} / \partial x_j$ arises from the non-linear advection terms, due to the fact that (2.23)

$$\overline{u_j \frac{\partial u_i}{\partial x_j}} \neq \bar{u}_j \frac{\partial \bar{u}_i}{\partial x_j} \quad (2.23)$$

and hence (2.24).

$$\tau_{ij} = \overline{\overline{u_i u_j}} - \overline{u_i u_j} \quad (2.24)$$

This means that Reynolds stress for resolved part of eddies can be approached directly. Similar equations can be derived for the subgrid-scale field (e.g. the residual field) and subgrid-scale turbulence models usually employ the Boussinesq hypothesis, and seek to calculate the deviatoric part of Reynolds stress tensor, in a similar way respect to turbulence models.

As mentioned above the grid has an additional and particular role in LES applications as measure of solved scales. This implies that the grid for LES calculations has to be built in order to give a precise “level of accuracy” that means a certain percentage of eddies resolved. To clarify this point is useful to remind the Kolmogorov spectrum of energy [26], [27], [28].

According to Kolmogorov, the bulk of the energy is contained in the larger eddies in the size range $l = l_0/6 < l < 6l_0$ (where l_0 is the characteristic length of the problem) which is therefore called the energy-containing range.

For lower scales in the energy spectrum there is the inertial sub range, where the energy decay is given by the dissipation rate ε , and for smaller eddies the final dissipation range.

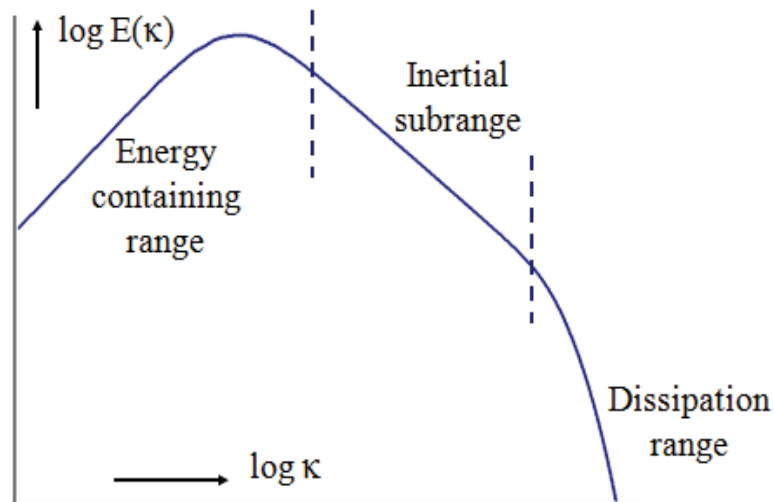


Figure 2.3: The Kolmogorov energy spectrum

The different ranges can be shown as a function of wave number. If we consider $E(\kappa)$ as the energy contained in eddies of size l and wave number κ , ($\kappa = 2\pi/l$) the energy spectrum appears like in Figure 2.3.

By definition k is the integral of $E(\kappa)$ over all wave numbers (2.25)

$$k = \int_0^{\infty} E(\kappa) d\kappa \quad (2.25)$$

while the energy contained in eddies with wave numbers between κ_A and κ_B is then:

$$k_{(\kappa_A, \kappa_B)} = \int_{\kappa_A}^{\kappa_B} E(\kappa) d\kappa \quad (2.26)$$

According to the second similarity hypothesis $E(\kappa)$ will solely depend on κ and ε . We can then perform the following dimensional analysis:

$$\begin{aligned} [k] &= \text{m}^2 \text{sec}^{-2} \quad - \quad [\varepsilon] = \text{m}^2 \text{sec}^{-3} \quad - \quad [\kappa] = \text{m}^{-1} \\ [E(\kappa)] &= [k] / [\kappa] = \text{m}^3 \text{sec}^{-2} \rightarrow E(\kappa) = C \varepsilon^{2/3} \kappa^{-5/3} \end{aligned}$$

The last equation describes the famous Kolmogorov $-5/3$ spectrum. C is the universal Kolmogorov constant, which experimentally was determined to be equal to 1.5.

Model equations for $E(\kappa)$ in the production range and dissipation range have been developed. The full spectrum is given by (2.27).

$$E(\kappa) = C \varepsilon^{2/3} \kappa^{-5/3} f_L f_\eta \quad (2.27)$$

The production range is governed by f_L (which goes to unity for large κl_0)

$$f_L = \left(\frac{\kappa l_0}{\left[(\kappa l_0)^2 + c_L \right]^{1/2}} \right)^{p_0 + 5/3} \quad (2.25)$$

while the dissipation range is governed by f_η (which goes to unity for small $\kappa\eta$)

$$f_\eta = e^{-\left\{-\beta\left[\left(\kappa\eta\right)^4 + c_\eta^4\right]^{1/4} - c_\eta\right\}} \quad (2.26)$$

The model constants were determined experimentally and based on the constraint that $E(\kappa)$ integrate to k . Their values are:

$$c_L \approx 6.78; \quad c_\eta \approx 0.40; \quad C = 1.5; \quad p_0 = 2; \quad \beta = 5.2.$$

Summarizing:

- The integral length scale is a measure of the large scale eddies in the production range:

$$l_0 \propto k^{3/2} / \varepsilon \quad (2.27)$$

The proportionality constant is of the order one.

- The Taylor micro scale is a measure of the size of the eddies in the inertial sub range:

$$\lambda \approx \sqrt{\frac{10\nu k}{\varepsilon}} \quad (2.28)$$

- The Kolmogorov micro scale is the size of the smallest eddies present in the flow:

$$\eta = \left(\nu^3 / \varepsilon\right)^{1/4} \quad (2.29)$$

The length scales can be related as follows:

$$\begin{aligned} \lambda / l_0 &= \sqrt{10} \text{Re}_L^{-1/2} \\ \eta / l_0 &= \text{Re}_L^{-3/4} \\ \lambda / \eta &= \sqrt{10} \text{Re}_L^{1/4} \\ \lambda &= \sqrt{10} \eta^{2/3} l_0^{1/3} \end{aligned} \quad (2.30)$$

Kolmogorov theory is an asymptotic theory; it has been shown to work well in the limit of very high Reynolds numbers.

The exact shape of the normalized spectra may deviate from Kolmogorov model spectra for intermediate Reynolds numbers. For example for many laboratory scale flows which have Reynolds numbers in the order of 10K, the exponent of $E(\kappa) \approx \kappa^{-p}$ in the inertial sub range is often measured to be $p \approx 1.5$ instead of $5/3$ (≈ 1.67).

Kolmogorov theory assumes that the energy cascade is one way: from large eddies to small eddies. Experimental studies have shown that energy is also transferred from smaller scales to larger scales (a process called backscatter), albeit at a much lower rate and the dominant energy transfer is indeed from large to small. Moreover the theory assumes that turbulence at high Reynolds numbers is completely random, meaning that large scale coherent structures may also form.

Implications of Kolmogorov theory on LES are huge. Apart for the deeper comprehension of turbulence, Kolmogorov integral length scale says us how to generate a LES grid to directly estimate a certain value of turbulent kinetic energy. In fact it is possible to determine the eddies size according to (2.27) starting from a RANS solution where k and ε have been calculated. According to this guideline and according to how many percentage of turbulent kinetic energy should be solved a preliminary estimation of grid size can be computed by RANS post-processing to build up an appropriate grid for LES simulation. This is probably the most important practical implication of this theory.

2.2.6 Innovative Approaches for Navier-Stokes Equations: DES, ELES and SAS

Basically the main problem related to the CFD is the computational cost imposed by the simulation of time and space scales involved, that range from the size of the body that is going to be simulated (e.g. 10^0 m) to the size of the turbulent eddies (e.g. $10^{-6/7}$ m) in the dissipation range.

RANS and LES approaches have been for many years the only alternatives to the Direct simulation of Navier-Stokes (DNS) equations.

These approaches deal with the accuracy of the solution and the computational cost, accepting to simulate some scales and drop-off some other scales in order to capture the relevant phenomena in which the user is interested in.

In particular RANS is the most widely used CFD approach and the real work-horse for fluid dynamic simulation. It is able to capture large scales vortices (whose size is comparable with body size), and to predict pressure load and aerodynamic forces over surfaces. However it loses all small details of the solution (e.g. small turbulent eddies production and convection mechanisms) that in some cases can play a fundamental role in some phenomena like aerodynamic noise production.

On the other hand LES can be considered much more accurate as it is able to capture all solution details up to the grid size, but this implies a long grid generation process together with a high computational cost. In practice LES results to be unfeasible for the most of practical problems that have to be modeled via RANS.

In the last 15 years new approaches emerged combining low computational cost and reasonable solution accuracy. In fact as soon as it was clear that LES approach will be still too computational demanding for almost all practical design problems for many decades, the market strongly demanded new approaches able to overcome the limits imposed by RANS without increasing too much the computational impact of the simulations.

In 1997 Detached Eddy Simulation (DES) was proposed. DES is mostly based on the coupling of LES filtering technique with a novel switch criterion. The idea behind is to adjust the filtering size on two properties: the grid size (as already done by LES), and the flow properties (the new idea introduced by DES), via an algebraic switch [30], [31]. This allows a better control for the user of RANS and LES models application in different regions of flow field, saving CPU-time in the zones located far from the body that could not affect the analysis results.

However some problems of instabilities caused by RANS-LES coupling can appear close to the boundaries and consequently some corrections have to be applied (e.g. Delayed DES).

In the frame of hybrid approaches it is also important to mention the Embedded LES (ELES), a numerical approach able to couple into the simulation RANS-handled and LES-handled regions. As DES it consists in a deal between RANS and LES approaches, but the switch criteria between the two methodologies is not based on the flow properties but on

geometric constraints. In practice a sub-region of the domain (e.g. a box) is identified and the flow resolved by RANS equations outside and LES equations inside.

This approach deals with the necessity of a local high resolution of the simulation provided by LES, together with the reasonable computational cost of the simulation typical of RANS approach.

ELES approach is essentially based on a zonal approach where the user pre-specifies the desired modelling concepts for the given zones ahead of the simulations. This implies that the code has to be able to handle a pre-defined RANS/LES interface that is clearly the critical element for ELES. Moreover it has to be able to connect a RANS solution to a LES solution, passing the information between the zones through the interface.

The information passage is made with a methodology essentially based on the vortex method based on the work of *Mathey et Al.* [32]. It generates turbulent structures based on the information provided by RANS model (Reynolds stresses and length scale) and it uses them as upstream condition for LES region at the interface. This approach is affected by the problem of “double accounting” of turbulence, as turbulence structures are transported across the interface. In fact this approach produces excessive amounts of turbulent kinetic energy, and this is mainly due to the high production rates of the RANS model inside the LES zone that are convected through the interface.

This problem can be avoided via two different approaches: the RANS frozen field approach and the SAS-LES approach. The first one is essentially based on a freezing of RANS turbulence quantities into the LES region during the ELES run, in order to avoid an excessive growth of turbulent kinetic energy. The second approach, is based on a Scale Adaptive Simulation (SAS) based treatment at the interface RANS region to resolve scales and a LES-like solution in strongly unstable flows. This produces a reduction of turbulence production into LES region, providing a smooth variation of turbulent quantities through the interface.

However ELES approach is a rather novel technique, and it can be useful as alternative to DES for all that problems where the vorticity and turbulence production and transport mechanisms are well-confined into a specific region of the domain.

Moreover in 2004 Scale Adaptive Simulation (SAS) was proposed. This approach, proposed by *Menter et Al.* [34], [35], [36], is maybe one of the most innovative approaches of the last decades. It consists in an Unsteady RANS approach coupled with a $k-\omega$ SST for

turbulence modelling. The balance equation of ω (specific vorticity) is corrected with an additional source term regulated by the Von Karman length scale. It is able to detect the vorticity sources into the flow field and introduces an artificial vorticity in order to substitute the part that is dropped off by the averaging of equations.

Approach	Computational Effort	Remarks
RANS	Low/Medium	Good Prediction of Aerodynamic Loads, suitable for the most of Industrial Problems
LES	High	Good Accuracy of Flow Solution Unfeasible for the most of industrial problems
DNS	Prohibitive	Unfeasible for any industrial problem
DES	Medium/High	Good Accuracy of Flow Solution Suitable for some Industrial Problems
ELES	Medium/High	Good Accuracy of Flow Solution Suitable for some Industrial Problems
SAS	Low/Medium	High Accuracy of Flow Solution, Unsteadiness required Not many applications yet

Table 2.1: Summary of the computational effort of the CFD numerical approaches

The remarkable property of this approach is that it is able to provide a detail of the solution comparable with a LES simulation with the cost of a URANS simulation, especially when the flow field is characterized by large regions of convective transport of vorticity. However, from a practical point of view, the artificial introduction of vorticity needs to be switched on, and this is done by mathematical sensors based on the detection of flow unsteadiness. This means that the model works properly only when the flow is characterized by a clear vortex shedding mechanism (e.g. blunt bodies), while it could fail in the case of a mostly steady solution. In table 2.1 a summary of the above mentioned approaches for CFD is provided, with indications about their CPU-cost and their remarkable properties.

2.3 Numerical Models for Turbomachinery Applications

The paragraph 2.3 is dedicated to CFD numerical models for turbomachinery applications. The aim of this paragraph consists in providing the numerical basis to perform CFD simulation of rotating bodies, showing capabilities and limitations of the approaches implemented into several commercial packages.

As stated above the main issue in turbomachinery applications is the introduction of a rotating body to apply forces on the fluid (e.g. compression or expansion).

From an analytical point of view the rotation should be introduced into constitutive equations of motion, and there are mainly two approaches: the Moving Reference Frame (MRF) and the Sliding Mesh (SLM). The first one consists in rewriting N-S equations in a rotating frame, while the second one introduces rotation assigning a rotational component of velocity to all nodes of the domain (physical grid rotation). It is immediately understandable that SLM approach is more realistic than MRF, but also more CPU-demanding.

Just for example rotation of grid intrinsically depends on time-evolution of simulation, so this approach is not suitable for steady simulations while it is possible a steady calculation performed with MRF, according to the evidence that in most of the turbomachinery problems the solution (e.g. pressure loads, forces) is not time-dependant.

A detailed description of numerical modeling of MRF and SLM approaches will be given in next paragraphs.

2.3.1 Moving Reference Frame Model

Moving Reference Frame (MRF) model consists in the solution of equations of motion in steady formulation in a moving frame in place of the solution of the same equations in an unsteady formulation in a stationary (inertial) reference frame.

In fact for a steadily rotating frame (e.g., the rotational speed is constant), it is possible to transform the equations of motion to the rotating frame such that steady-state solutions are possible. This approach is based on the assumption that in most of practical interest cases steady solutions are required for rotating bodies, without taking in account of unsteadiness details of flow field (e.g. vortex shedding). On the other hand an unsteady solution with the MRF model can be computed to simulate also these details.

Let us consider a coordinate system which is rotating steadily with angular velocity $\underline{\omega}$ relative to a stationary (inertial) reference frame, as illustrated in Figure 2.4. The origin of the rotating system is located by a position vector \underline{r}_o .

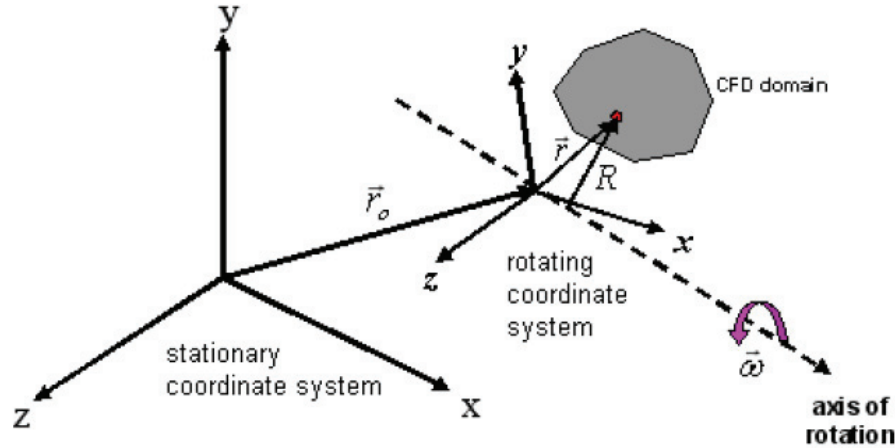


Figure 2.4: rotating body into inertial reference frame

The computational domain for the CFD problem is defined with respect to the rotating frame such that an arbitrary point in the CFD domain is located by a position vector \underline{r} from the origin of the rotating frame.

The fluid velocities can be transformed from the stationary frame to the rotating frame using the relation (2.31)

$$\underline{v}_r = \underline{v} - (\underline{\omega} \times \underline{r}) \quad (2.31)$$

In the above, \underline{v}_r is the relative velocity (the velocity viewed from the rotating frame) while \underline{v} is the absolute velocity (the velocity viewed from the stationary frame).

When the equations of motion are solved in the rotating reference frame, the acceleration of the fluid is augmented by additional terms that appear in the momentum equations [23], [24]. Moreover, the equations can be formulated expressing absolute or relative velocity as dependant variable of momentum equation. These two formulations are equivalent and the only difference is in the practical meaning of the two velocities.

Constitutive N-S equations are given below according to the relative velocity formulation for continuity, momentum and energy respectively (2.32).

$$\begin{aligned}
 \frac{\partial \rho}{\partial t} + \underline{\nabla} \cdot \rho \underline{v}_r &= 0 \\
 \frac{\partial}{\partial t} (\rho \underline{v}_r) + \underline{\nabla} \cdot (\rho \underline{v}_r \underline{v}_r) + \rho (2\underline{\omega} \times \underline{v}_r + \underline{\omega} \times \underline{\omega} \times \underline{v}_r) &= -\underline{\nabla} p + \underline{\nabla} \cdot \underline{\underline{\tau}} + \underline{F} \\
 \frac{\partial}{\partial t} (\rho E_r) + \underline{\nabla} \cdot (\rho \underline{v}_r H_r) &= \underline{\nabla} \cdot (k \underline{\nabla} T + \underline{\underline{\tau}} \cdot \underline{v}_r) + S_H
 \end{aligned} \tag{2.32}$$

The momentum equation contains two additional acceleration terms, the Coriolis acceleration and the centripetal acceleration. In addition viscous stress tensor does not change respect equation (2.2) except for the introduction of the relative velocity. Energy equation is written in the form of internal energy E_r , introducing the total enthalpy H_r .

$$E_r = h - \frac{p}{\rho} + \frac{1}{2} (v_r^2 - (\omega r)^2) \quad H_r = E_r - \frac{p}{\rho} \tag{2.33}$$

MRF model can be applied defining different zones in the domain (rotating and non-rotating) solving RANS formulation of equations (2.32).

Moreover rotational periodic boundaries can be applied where periodical surfaces are present in the domain (Figure 2.5).

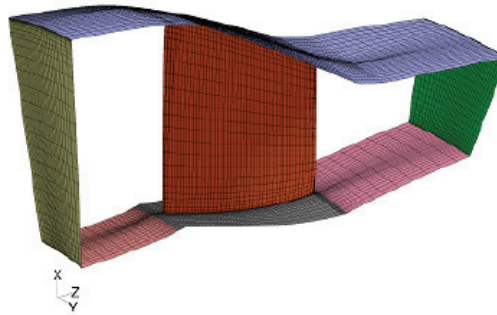


Figure 2.5: rotating blade into 3 sections domain

For these reasons MRF model is widely used for industrial applications, being one of the most versatile and low CPU-demanding approaches for turbomachinery simulation.

2.3.2 Sliding Mesh Model

When accurate time-dependant simulations in turbomachinery need to be performed Sliding Mesh (SLM) technique is the most suitable approach. As stated before MRF approach is a model applied to steady-state cases, thus neglecting unsteady interactions between moving bodies. The SLM model cannot neglect unsteady interactions and is based on the relative motion (translational or rotational) of two grid domains or cell zones. Each cell zone is bounded by at least one “interface zone” where it meets the opposing cell zone and this interface zone is a surface where fluid variables can be transported from one zone to the other and vice versa with an interpolation process.

For a better understanding of the SLM approach let us consider the Figure 2.6, where two adjacent zones are represented. At each time step unsteady RANS equations are solved in each cell zone, and fluxes are computed across adjacent faces over the grid interface. When time step increase a rigid translation is given to one cell zone, and after this translation the grid faces cannot be aligned on the grid interface.

The fluxes previously calculated needs to be recomputed as the interface position changed for the domain translation, and this happens every time step being the main reason for the high computational demanding of SLM technique.

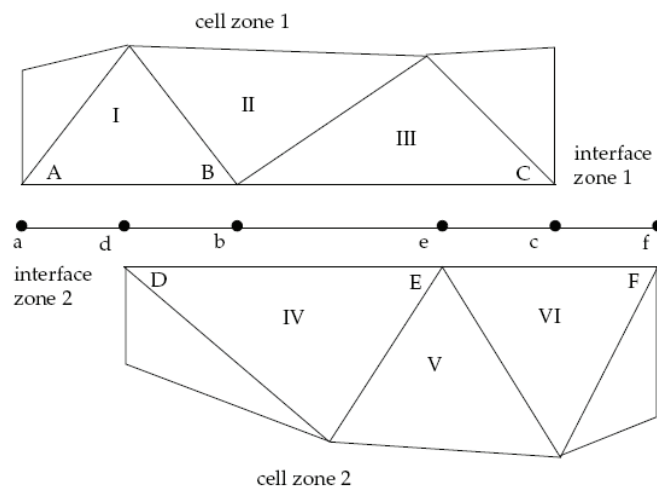


Figure 2.6: sliding domains

In the example shown in Figure 2.6, the interface zones are composed of faces A-B and B-C, and faces D-E and E-F. The intersection of these zones produces the faces a-d, d-b, b-e, C, and faces D-E and E-F.

etc. Faces produced in the region where the two cell zones overlap (d-b, b-e, and e-c) are grouped to form an interior zone, while the remaining faces (a-d and c-f) are paired up to form a periodic zone. To compute the flux across the interface into cell IV, for example, face D-E is ignored and faces d-b and b-e are used instead, bringing information into cell IV from cells I and III, respectively.

SLM approach is widely used in turbomachinery simulation wherever there is an explicit interest for unsteadiness of flow field in rotating machines, or when there is a non axis-symmetry of the domain.

2.4 Acoustics Fundamentals

To provide the necessary background for the understanding of the topics covered in next chapters, basic definitions and other aspects related to the physics of sound and noise are provided. This and the next paragraph are mostly based on the work of Caridi [57].

Most definitions have been internationally standardized and are listed in standards publications such as IEC 60050-801(1994).

Noise can be defined as "disagreeable or undesired sound" or other disturbance. From the acoustics point of view, sound and noise constitute the same phenomenon of atmospheric pressure fluctuations about the mean atmospheric pressure; the differentiation is greatly subjective. What is sound to one person can be noise to somebody else.

Sound (or noise) is the result of pressure variations, or oscillations, in an elastic medium (e.g., air, water, solids), generated by a vibrating surface, or turbulent fluid flow. Sound propagates in the form of longitudinal (as opposed to transverse) waves, involving a succession of compressions and rarefactions in the elastic medium. When a sound wave propagates in air the oscillations in pressure are above and below the ambient atmospheric pressure.

The speed of sound propagation, c , the frequency, f , and the wavelength, λ , are related by the equation (2.34).

$$c = f \cdot \lambda \quad (2.34)$$

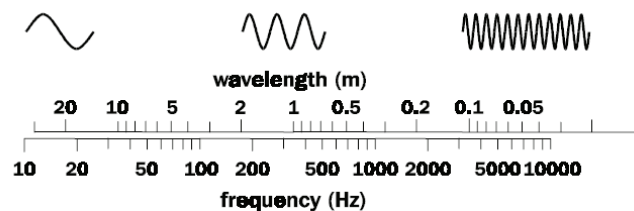


Figure 2.7: wavelength versus frequency (air medium)

The speed of propagation, c , of sound in air is 343 m/s, at 20 °C and 1 atmosphere pressure. At other temperatures (not too different from 20 °C), it may be calculated using the (2.35)

$$c = 332 + 0.6T \quad (2.35)$$

where T is the temperature in °C. Alternatively, making use of the equation of state for gases, the speed of sound may be written as:

$$c = \sqrt{\gamma R T_k / M} \quad (2.36)$$

where T_k is the temperature in K, R is the universal gas constant which has the value 8.314 J per mole K, and M is the molecular weight, which for air is 0.029 kg/mole. For air, the ratio of specific heats, γ , is 1.402.

All of the properties just discussed (except the speed of sound) apply only to a pure tone (single frequency). However, sounds usually encountered are not pure tones. In general, sounds are complex mixtures of pressure variations that vary with respect to phase, frequency, and amplitude. For such complex sounds, there is no simple mathematical relation between the different characteristics. However, any signal may be considered as a combination of a certain number (possibly infinite) of sinusoidal waves, each of which may be described as outlined above. These sinusoidal components of sound constitute the frequency spectrum of the signal. It is customary to refer to spectral density level when the measurement band is one Hz wide, to one third octave or octave band level when the measurement band is one third octave or one octave wide and to spectrum level for measurement bands of other widths. Two special kinds of spectra are commonly referred to as white random noise and pink random noise. White random noise contains equal energy per hertz and thus has a constant spectral density level. Pink random noise contains equal energy per measurement band and thus has an octave or one-third octave band level which is constant with frequency.

At this point is important provide some sound field definitions. For more detail see *ISO 12001*. Sound can be classified in general in

- Free Field
- Near Field
- Far Field
- Direct Field
- Reverberant Field

The free field is a region in space where sound may propagate free from any form of obstruction.

The near field of a source is the region close to a source where the sound pressure and acoustic particle velocity are not in phase. In this region the sound field does not decrease by 6 dB each time the distance from the source is doubled. The near field is limited to a distance from the source equal to about a wavelength of sound or equal to three times the largest dimension of the sound source (whichever is the larger).

The far field of a source begins where the near field ends and extends to infinity. Note that the transition from near to far field is gradual in the transition region. In the far field, the direct field radiated by most machinery sources will decay at the rate of 6 dB each time the distance from the source is doubled. For line sources such as traffic noise, the decay rate varies between 3 and 4 dB.

The direct field of a sound source is defined as that part of the sound field which has not suffered any reflection from any room surfaces or obstacles.

The reverberant field of a source is defined as that part of the sound field radiated by a source which has experienced at least one reflection from a boundary of the room or enclosure containing the source.

Frequency analysis may be thought of as a process by which a time varying signal in the time domain is transformed to its frequency components in the frequency domain. It can be used for quantification of a noise problem, as both criteria and proposed controls are frequency dependent. In particular, tonal components which are identified by the analysis may be treated somewhat differently than broadband noise. Sometimes frequency analysis is used for noise source identification and in all cases frequency analysis will allow determination of the effectiveness of controls.

There are a number of instruments available for carrying out a frequency analysis of arbitrarily time-varying signals. To facilitate comparison of measurements between instruments, frequency analysis bands have been standardized. Thus the International Standards Organization has agreed upon "preferred" frequency bands for sound measurement and analysis.

The widest band used for frequency analysis is the octave band; that is, the upper frequency limit of the band is approximately twice the lower limit. Each octave band is described by its "centre frequency", which is the geometric mean of the upper and lower

frequency limits. The preferred octave bands are shown in Figure 2.8, in terms of their centre frequencies. Occasionally, a little more information about the detailed structure of the noise may be required than the octave band will provide. This can be obtained by selecting narrower bands; for example, one-third octave bands. As the name suggests, these are bands of frequency approximately one-third of the width of an octave band. Preferred one-third octave bands of frequency have been agreed upon and are also shown in Figure 2.8.

Band number	Octave band center frequency	One-third octave band center frequency	Band limits	
			Lower	Upper
14 } 15 } 16 }	31.5	25	22	28
		31.5	28	35
		40	35	44
17 } 18 } 19 }	63	50	44	57
		63	57	71
		80	71	88
20 } 21 } 22 }	125	100	88	113
		125	113	141
		160	141	176
23 } 24 } 25 }	250	200	176	225
		250	225	283
		315	283	353
26 } 27 } 28 }	500	400	353	440
		500	440	565
		630	565	707
29 } 30 } 31 }	1000	800	707	880
		1000	880	1130
		1250	1130	1414
32 } 33 } 34 }	2000	1600	1414	1760
		2000	1760	2250
		2500	2250	2825
35 } 36 } 37 }	4000	3150	2825	3530
		4000	3530	4400
		5000	4400	5650
38 } 39 } 40 }	8000	6300	5650	7070
		8000	7070	8800
		10000	8800	11300
41 } 42 } 43 }	16000	12500	11300	14140
		16000	14140	17600
		20000	17600	22500

NOTE: Requirements for filters see IEC 61260; there index numbers are used instead of band numbers. The index numbers are not identical, starting with No. "0" at 1 kHz.

Figure 2.8: frequency band table

Instruments are available for other forms of band analysis. However, they do not enjoy the advantage of standardization so that the inter-comparison of readings taken on such instruments may be difficult. One way to ameliorate the problem is to present such readings as mean levels per unit frequency. Data presented in this way are referred to as Spectral Density Levels (SPL) as opposed to band levels. In this case the measured level is reduced by ten times the logarithm to the base ten of the bandwidth. For example, referring to Figure 2.8, if the 500 Hz octave band which has a bandwidth of 354 Hz were presented in this way, the measured octave band level would be reduced by $10\log_{10}(354) = 25.5$ dB to give an estimate of the spectral density level at 500 Hz.

The problem is not entirely alleviated, as the effective bandwidth will depend upon the sharpness of the filter cut-off, which is also not standardized. Generally, the bandwidth is taken as lying between the frequencies, on either side of the pass band, at which the signal is down 3 dB from the signal at the centre of the band.

There are two ways of transforming a signal from the time domain to the frequency domain. The first involves the use of band limited digital or analog filters. The second involves the use of Fourier analysis where the time domain signal is transformed using a Fourier series. This is implemented in practice digitally (referred to as the DFT - Discrete Fourier Transform) using a very efficient algorithm known as the FFT (Fast Fourier Transform).

2.4.1 Quantification of Sound

The Sound intensity is a vector quantity determined as the product of sound pressure and the component of particle velocity in the direction of the intensity vector. It is a measure of the rate at which work is done on a conducting medium by an advancing sound wave and thus the rate of power transmission through a surface normal to the intensity vector. It is expressed as watts per square meter (W/m^2). In a free-field environment, i.e., no reflected sound waves and well away from any sound sources, the sound intensity is related to the root mean square acoustic pressure as follows

$$I = \frac{p_{rms}^2}{\rho c} \quad (2.37)$$

where ρ is the density of air (kg/m^3), and c is the speed of sound (m/sec). The quantity, ρc is called the "acoustic impedance" and is equal to 414 Ns/m^3 at 20° C and one atmosphere.

The total sound energy emitted by a source per unit time is the sound power, W , which is measured in watts. It is defined as the total sound energy radiated by the source in the specified frequency band over a certain time interval divided by the interval. It is obtained by integrating the sound intensity over an imaginary surface surrounding a source. Thus, in general the power, W , radiated by any acoustic source is

$$W = \int_A \underline{I} \cdot \underline{n} dA \quad (2.38)$$

where the dot multiplication of \underline{I} with the unit vector, \underline{n} , indicates that it is the intensity component normal to the enclosing surface which is used. Most often, a convenient surface is an encompassing sphere or spherical section, but sometimes other surfaces are chosen, as dictated by the circumstances of the particular case considered.

For a sound source producing uniformly spherical waves (or radiating equally in all directions), a spherical surface is most convenient, and in this case the above equation leads to the following expression:

$$W = 4\pi r^2 I \quad (2.39)$$

where the magnitude of the acoustic intensity, I , is measured at a distance r from the source. In this case the source has been treated as though it radiates uniformly in all directions.

The range of sound pressures that can be heard by the human ear is very large. The minimum acoustic pressure audible to the young human ear judged to be in good health, and unsullied by too much exposure to excessively loud music, is approximately $20 \times 10^{-6} \text{ Pa}$, or 2×10^{-10} atmospheres (since 1 atmosphere equals $101.3 \times 10^3 \text{ Pa}$). The minimum audible level occurs at about 4,000 Hz and is a physical limit imposed by molecular motion. Lower sound pressure levels would be swamped by thermal noise due to molecular motion in air.

For the normal human ear, pain is experienced at sound pressures of the order of 60 Pa or 6×10^{-4} atmospheres. Evidently, acoustic pressures ordinarily are quite small fluctuations about

the mean. A linear scale based on the square of the sound pressure would require 1013 unit divisions to cover the range of human experience; however, the human brain is not organized to encompass such a range. The remarkable dynamic range of the ear suggests that some kind of compressed scale should be used. A scale suitable for expressing the square of the sound pressure in units best matched to subjective response is logarithmic rather than linear. Thus a unit named the Bel was introduced which is the logarithm of the ratio of two quantities, one of which is a reference quantity. To avoid a scale which is too compressed over the sensitivity range of the ear, a factor of 10 is introduced, giving rise to the decibel. The level of sound pressure p is then said to be L_p decibels (dB) greater or less than a reference sound pressure p_{ref} according to the following equation.

$$L_p = 10 \log_{10} \frac{p_{rms}^2}{p_{ref}^2} = 20 \log_{10} \frac{p_{rms}}{p_{ref}} = 20 \log_{10} p_{rms} - 20 \log_{10} p_{ref} \quad (\text{dB}) \quad (2.40)$$

For the purpose of absolute level determination, the sound pressure is expressed in terms of a datum pressure corresponding to the lowest sound pressure which the young normal ear can detect. The result is called the sound pressure level, L_p (or SPL), which has the units of decibels (dB). This is the quantity which is measured with a sound level meter.

The sound pressure is a measured root mean square (r.m.s.) value and the internationally agreed reference pressure $p_{ref} = 2 \times 10^{-5} \text{ N m}^{-2}$ or 20 μPa . The sound intensity level, L_I , may be defined as follows.

$$L_I = 10 \log_{10} \frac{(\text{sound intensity})}{(\text{ref. sound intensity})} = 10 \log_{10} \frac{I}{I_{ref}} \quad (\text{dB}) \quad (2.41)$$

An internationally agreed reference intensity, I_{ref} , is 10^{-12} Wm^{-2} . Use of the relationship between acoustic intensity and pressure in the far field of a source gives the following useful result:

$$L_I = L_p + 10 \log_{10} \frac{400}{\rho c} \quad (2.42)$$

$$L_I = L_p + 26 - 10 \log_{10}(\rho c) \quad (\text{dB}) \quad (2.43)$$

At sea level and 20°C the characteristic impedance, ρc , is 414 kg m⁻² s⁻¹, so that for both plane and spherical waves.

$$L_I = L_p - 0.2 \quad (\text{dB}) \quad (2.44)$$

The sound power level, L_w (or PWL), may be defined as follows.

$$L_w = 10 \log_{10} \frac{(\text{sound power})}{(\text{ref. sound power})} = 10 \log_{10} \frac{W}{W_{ref}} \quad (\text{dB}) \quad (2.45)$$

The internationally agreed reference power is 10⁻¹² W.

2.4.2 Propagation of Sound

A free field is a homogeneous medium, free from boundaries or reflecting surfaces. Considering the simplest form of a sound source, which would radiate sound equally in all directions from an apparent point, the energy emitted at a given time will diffuse in all directions and, one second later, will be distributed over the surface of a sphere of 340 m radius. This type of propagation is said to be spherical and is illustrated in Figure 2.9.

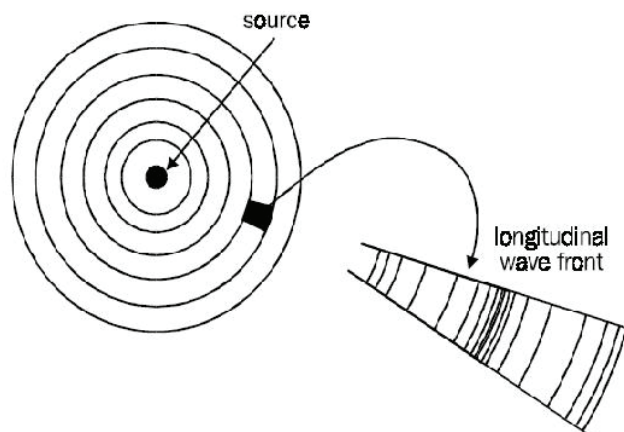


Figure 2.9: radiation of spherical source in a free field

In a free field, the intensity and sound pressure at a given point, at a distance r (in meters) from the source, is expressed by the following equation:

$$p^2 = \rho c I = \frac{\rho c W}{4\pi r^2} \quad (2.46)$$

where ρ and c are the air density and speed of sound respectively. In terms of sound pressure the preceding equation can be written as

$$L_p = L_w + 10 \log_{10} \left(\frac{\rho c}{400} \right) - 10 \log_{10} (4\pi r^2) \quad (2.47)$$

which is often approximated as

$$L_p = L_w - 10 \log_{10} (4\pi r^2) \quad (2.48)$$

Measurements of source sound power, L_w , can be complicated in practice [37]. However, if the sound pressure level, L_m , is measured at some reference distance, r_m , from the noise source (usually greater than 1 meter to avoid source near field effects which complicate the sound field close to a source), then the sound pressure level at some other distance, r , may be estimated using:

$$L_p = L_m - 20 \log_{10} \left(\frac{r}{r_m} \right) \quad (2.49)$$

From the preceding expression it can be seen that in free field conditions, the noise level decreases by 6 dB each time the distance between the source and the observer doubles. However, true free-field conditions are rarely encountered in practice, so in general the equation relating sound pressure level and sound power level must be modified to account for the presence of reflecting surfaces. This is done by introducing a directivity factor, Q , defined in terms of the intensity I_θ , function of angular coordinates (θ, ψ) and the mean intensity.

$$Q_{\theta} = \frac{I_{\theta}}{I_{av}} \quad (2.50)$$

The directivity index is defined as (2.51) [37].

$$DI = 10 \log_{10} Q_{\theta} \quad (2.51)$$

The presence of a reflecting surface near to a source will affect the sound radiated and the apparent directional properties of the source. Similarly, the presence of a reflecting surface near to a receiver will affect the sound received by the receiver. In general, a reflecting surface will affect not only the directional properties of a source but also the total power radiated by the source. As the problem can be quite complicated the simplifying assumption is often made and will be made here, that the source is of constant power output which means that its output sound power is not affected by reflecting surfaces [37]. For a simple source near to a reflecting surface outdoors

$$W = I \frac{4\pi r^2}{Q} = p^2_{rms} \frac{4\pi r^2}{\rho c Q} \quad (2.52)$$

which may be written in terms of levels as

$$L_p = L_w + 10 \log_{10} \left(\frac{Q}{4\pi r^2} \right) = L_w + 10 \log_{10} \left(\frac{1}{4\pi r^2} \right) + DI \quad (2.53)$$

Whenever sound waves encounter an obstacle, such as when a noise source is placed within boundaries, part of the acoustic energy is reflected, part is absorbed and part is transmitted. The relative amounts of acoustic energy reflected, absorbed and transmitted greatly depend on the nature of the obstacle. Different surfaces have different ways of reflecting, absorbing and transmitting an incident sound wave. A hard, compact, smooth surface will reflect much more, and absorb much less, acoustic energy than a porous, soft surface. If the boundary surfaces of a room consist of a material which reflects the incident sound, the sound produced by a source inside the room (the direct sound) rebounds from one

boundary to another, giving origin to the reflected sound. The higher the proportion of the incident sound reflected, the higher the contribution of the reflected sound to the total sound in the closed space. This "built-up" noise will continue even after the noise source has been turned off. This phenomenon is called reverberation and the space where it happens is called a reverberant sound field, where the noise level is dependent not only on the acoustic power radiated, but also on the size of the room and the acoustic absorption properties of the boundaries. As the surfaces become less reflective, and more absorbing of noise, the reflected noise becomes less and the situation tends to a "free field" condition where the only significant sound is the direct sound. By covering the boundaries of a limited space with materials which have a very high absorption coefficient, it is possible to arrive at characteristics of sound propagation similar to free field conditions. Such a space is called an anechoic chamber, and such chambers are used for acoustical research and sound power measurements. In practice, there is always some absorption at each reflection and therefore most work spaces may be considered as semi-reverberant. The phenomenon of reverberation has little effect in the area very close to the source, where the direct sound dominates. However, far from the source, and unless the walls are very absorbing, the noise level will be greatly influenced by the reflected, or indirect, sound. The sound pressure level in a room may be considered as a combination of the direct field (sound radiated directly from the source before undergoing a reflection) and the reverberant field (sound which has been reflected from a surface at least once) and for a room for which one dimension is not more than about five times the other two, the sound pressure level generated at distance r from a source producing a sound power level of L_W may be calculated using

$$L_p = L_W + 10 \log_{10} \left(\frac{Q}{4\pi r^2} + \frac{4(1-\bar{\alpha})}{S\bar{\alpha}} \right) \quad (2.54)$$

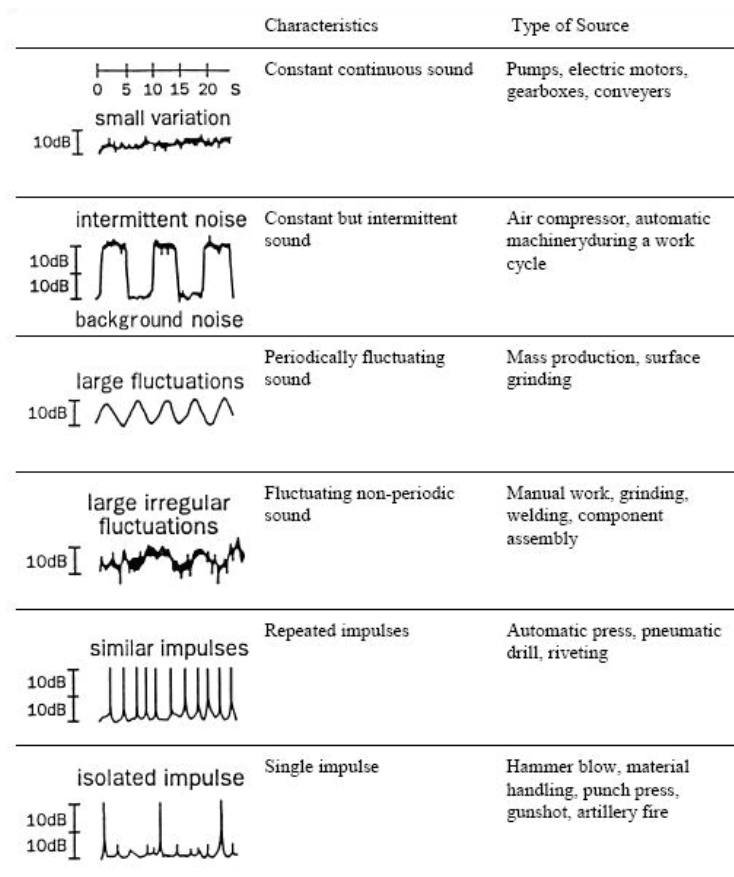
where $\bar{\alpha}$ is the average absorption coefficient of all surfaces in the room [37].

2.4.3 Types of Noise

Noise may be classified as steady, non-steady or impulsive, depending upon the temporal variations in sound pressure level (see ISO 12001). Different types of noise could be:

- Steady Noise
- Fluctuating Noise
- Tonal Noise
- Intermittent Noise
- Impulsive Noise

Steady noise is a noise with negligibly small fluctuations of sound pressure level within the period of observation.



Noise characteristics classified according to the way they vary with time. Constant noise remains within 5 dB for a long time. Constant noise which starts and stops is called intermittent. Fluctuating noise varies significantly but has a constant long term average ($L_{Aeq,T}$). Impulse noise lasts for less than one second.

Figure 2.10: Classification of Noise

If a slightly more precise single-number description is needed, assessment by NR (Noise Rating) curves may be used. A noise is called non-steady when its sound pressure levels shift significantly during the period of observation. This type of noise can be divided into intermittent noise and fluctuating noise. Fluctuating noise is a noise for which the level changes continuously and to a great extent during the period of observation. Tonal noise may be either continuous or fluctuating and is characterized by one or two single frequencies. This type of noise is much more annoying than broadband noise characterized by energy at many different frequencies and of the same sound pressure level as the tonal noise. Intermittent noise is noise for which the level drops to the level of the background noise several times during the period of observation. The time during which the level remains at a constant value different from that of the ambient background noise must be one second or more. Impulsive noise consists of one or more bursts of sound energy, each of a duration less than about 1s. Impulses are usually classified as type A and type B as described in Figure 2.11, according to the time history of instantaneous sound pressure (ISO 10843). Type A characterizes typically gun shot types of impulses, while type B is the one most often found in industry (e.g., punch press impulses). The characteristics of these impulses are the peak pressure value, the rise time and the duration of the peak.

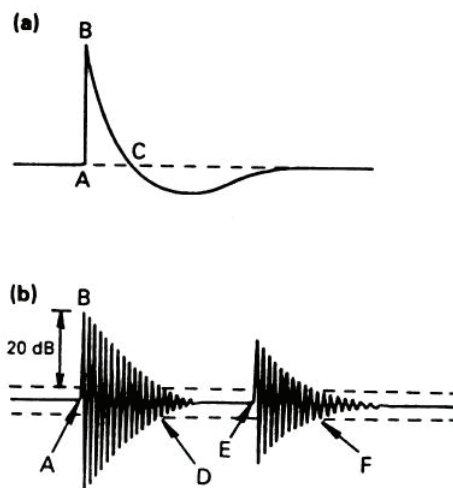


Figure 2.11: idealized waveforms of impulse noises. Peak level = pressure difference AB; rise time = time difference AB; A duration = time difference AC; B duration = time difference AD (+ EF when a reflection is present). (a) Explosive generated noise. (b) Impact generated noise.

2.5 Aerodynamic Generation of Sound

In contrast to computational aerodynamics, which has advanced to a fairly mature state, Computational AeroAcoustics (CAA) has only recently emerged as a separate area in the wide world of CFD. Due to the nonlinearity of the governing equations it is very difficult to predict the sound production of fluid flows. This sound production occurs typically at high speed flows, for which nonlinear inertial terms in the equation of motion are much larger than the viscous terms. As sound production represents only a very minute fraction of the energy in the flow the direct prediction of sound generation is very difficult. This is particularly dramatic in free space and at low subsonic speeds. The fact that the sound field is in some sense a small perturbation of the flow, can, however, be used to obtain approximate solutions. Aeroacoustics provides such approximations and at the same time a definition of the acoustical field as an extrapolation of an ideal reference flows. The difference between the actual flow and the reference flow is identified as a source of sound. This idea was introduced by Lighthill who called this an analogy. While in acoustics of quiescent media it is rather indifferent whether we consider a wave equation for the pressure or the density, in aeroacoustics the choice of a different variable corresponds to a different choice of the reference flow and hence to another analogy [38].

2.5.1 Homogeneous Wave Propagation

In order to make a simplification, let us consider a zero averaged flow field and the viscosity effects negligible. Since to an acoustic wave are related fluctuations of all the motion variables, each quantity can be considered the sum of an averaged component and a fluctuating component, usually called the acoustic component:

$$\begin{aligned}
 p(\underline{x}, t) &= \bar{p} + p'(\underline{x}, t) \\
 \rho(\underline{x}, t) &= \bar{\rho} + \rho'(\underline{x}, t) \\
 u_i(\underline{x}, t) &= \bar{u}_i + u_i'(\underline{x}, t)
 \end{aligned}
 \tag{2.55}$$

Because of the hypothesis on the averaged flow field, $\bar{u}_i=0$, the quantities \bar{p} and $\bar{\rho}$ have to be considered constants. Thanks to these assumptions and neglecting the higher order terms, the Navier Stokes equations can be linearized.

Assuming the air to be a perfect gas ($p = \rho RT$)

$$p' = c_o^2 \rho' \quad (2.56)$$

and taking the time derivative of the continuity linearized equation and subtracting divergence of linearized momentum equation, yields

$$\frac{\partial^2 \rho'}{\partial t^2} - \frac{\partial^2 p'}{\partial x_i^2} = 0 \quad (2.57)$$

Applying the relation (2.56) to the equation (2.57) it is possible to obtain the homogeneous equation for the pressure fluctuation (2.58)

$$\frac{1}{c_o^2} \frac{\partial^2 p'}{\partial t^2} - \frac{\partial^2 p'}{\partial x_i^2} = 0 \quad (2.58)$$

that is the homogeneous wave propagation equation. In a mono-dimensional case a solution of this equation is given by (2.59)

$$p(x,t) = f_1(c_o t - x) + f_2(c_o t + x) \quad (2.59)$$

where f_1 and f_2 are two arbitrarily functions.

2.5.2 Non-Homogeneous Wave Propagation

The theories that describe the aerodynamic sound often lead to a non-homogeneous wave equation. For a better understanding of these theories, the purpose of this section is to give a

brief introduction to the way of solving a non-homogenous wave equation. In general a wave equation assumes the following form

$$\left(\frac{1}{c_o^2} \frac{\partial^2}{\partial t^2} - \nabla^2 \right) p = f(\underline{x}, t) \quad (2.60)$$

where c_o is the wave speed propagation and $f(\underline{x}, t)$ is a generic distribution of sources. In order to solve this equation there is the need to use the Green function, which is defined as the solution of the wave equation related to a punctual and impulsive source, localized in the point $\underline{x} = \underline{y}$, that exists only at time $t = \tau$. The Green function is the solution for pressure of the differential equation where source terms are the Dirac pulses in space and time (2.61)

$$\left(\frac{1}{c_o^2} \frac{\partial^2}{\partial t^2} - \nabla^2 \right) G = \delta(\underline{x} - \underline{y}) \delta(t - \tau) \quad (2.61)$$

which lead to the result (2.62).

$$G(\underline{x}, \underline{y}, t - \tau) = \frac{1}{4\pi |\underline{x} - \underline{y}|} \delta \left(t - \tau - \frac{|\underline{x} - \underline{y}|}{c_o} \right) \quad (2.62)$$

The analysis of the Green function shows that it represents a spherical impulsive wave which expands at the speed c_o starting from the point \underline{y} . The wave amplitude has an inverse proportionality with a distance $|\underline{x} - \underline{y}|$ from the point \underline{y} . If we consider $f(\underline{x}, t)$ a generically distribution of infinitesimal impulsive sources, we have:

$$f(\underline{x}, t) = \iint f(\underline{y}, \tau) \delta(\underline{x} - \underline{y}) \delta(t - \tau) dV(\underline{y}) d\tau \quad (2.63)$$

The solution of the wave equation of the type

$$f(\underline{y}, \tau) \delta(\underline{x} - \underline{y}) \delta(t - \tau) dV(\underline{y}) d\tau \quad (2.64)$$

is given by the wave

$$f(\underline{y}, \tau) G(\underline{x}, \underline{y}, t - \tau) dV(\underline{y}) d\tau \quad (2.65)$$

Summing all the contributions, it's possible to obtain a solution for the non-homogeneous wave equation:

$$\begin{aligned} p(\underline{x}, t) &= \iint_{\infty} f(\underline{y}, \tau) G(\underline{x}, \underline{y}, t - \tau) dV(\underline{y}) d\tau = \frac{1}{4\pi} \iint_{\infty} \frac{f(\underline{y}, \tau)}{|\underline{x} - \underline{y}|} \delta\left(t - \tau - \frac{|\underline{x} - \underline{y}|}{c_o}\right) dV(\underline{y}) d\tau = \\ &= \frac{1}{4\pi} \iint_{\infty} \frac{f\left(\underline{y}, t - \frac{|\underline{x} - \underline{y}|}{c_o}\right)}{|\underline{x} - \underline{y}|} dV(\underline{y}) d\tau \end{aligned} \quad (2.66)$$

2.5.3 Lighthill's Analogy

For a long period since Lighthill's papers appearance [39], [40], aeroacoustic computation has focused on solution of his acoustic analogy. In brief, Lighthill devised an arrangement of the continuity and momentum equations of fluid mechanics where all terms not appearing in the linear-wave operator are grouped into a double divergence of a source-like term now known as the Lighthill stress tensor. The result of these manipulations is an equation featuring the wave operator (operating on the density perturbation) on the left-hand side and with all nonlinear effects accounted for by the Lighthill stress tensor

$$\frac{\partial^2 \rho}{\partial t^2} - c_o^2 \frac{\partial^2 \rho}{\partial x_i^2} = \frac{\partial^2 T_{ij}}{\partial x_i \partial x_j} \quad (2.67)$$

where

$$T_{ij} = \rho u_i u_j - \tau_{ij} + (p - c_o^2 \rho) \delta_{ij} \quad (2.68)$$

This equation is obtained by subtracting to the time derivative of the continuity equation the divergence of the momentum equation and the term $c_o^2 \frac{\partial^2 \rho}{\partial x_i^2}$.

Assuming the right hand side of equation (2.67) is known and independent from the left hand side of the previous equation, it's possible to apply the methodology shown in the previous section, which leads to

$$\rho(\vec{x}, t) - \rho_o = \frac{1}{4\pi c_o^2} \int \frac{1}{r} \frac{\partial^2 T_{ij}}{\partial y_i \partial y_j} dV(\vec{y}) = \frac{1}{4\pi c_o^2} \frac{\partial^2}{\partial y_i \partial y_j} \int \frac{T_{ij}}{r} dV(\vec{y}) \quad (2.69)$$

The square brackets indicate evaluation of the integrand at the retarded time, $\tau = t - \frac{r}{c_o}$ and r is the distance between the source and the observer. It represents the time at which the source emits the sound wave that will arrive to the observer location at time t . This equation shows that the sound generated by turbulence is equivalent to the sound generated in a steady fluid with a tensions distribution described by the Lighthill's tensor.

2.5.4 Curle's Equation

The Lighthill's theory sometimes can't be immediately applied since it doesn't consider the presence of solid boundaries in the fluid domain. Curle extended the Lighthill's theory in order to consider these effects, [41]. The general integral of the non homogeneous wave equation in a limited domain is

$$\rho(\underline{x}, t) - \rho_o = \frac{1}{4\pi c_o^2} \int \frac{1}{r} \frac{\partial^2 T_{ij}}{\partial y_i \partial y_j} dV(\underline{y}) - \frac{1}{4\pi} \int_S \left(\frac{1}{r} \frac{\partial \rho}{\partial n} + \frac{1}{r^2} \frac{\partial r}{\partial n} \rho + \frac{1}{rc_o} \frac{\partial r}{\partial n} \frac{\partial \rho}{\partial \tau} \right) dS(\underline{y}) \quad (2.70)$$

where n is the unit versor orthogonal to the surface, pointing to the fluid domain. Starting from this solution, Curle obtains a formulation analogous to Lighthill's, with the addition of an integration on an integration on the surface immersed in the fluid domain. To obtain this formulation the integrals of the previous equation have been rearranged. For the volume integration we have the (2.71).

$$\frac{1}{4\pi c_o^2} \int_{\infty} \frac{1}{r} \frac{\partial^2 T_{ij}}{\partial y_i \partial y_j} dV(\underline{y}) = \int_{\infty} \int_V \frac{\partial^2 T_{ij}}{\partial y_i \partial y_j}(\underline{y}, \tau) G(\underline{x} - \underline{y}, t - \tau) dV(\underline{y}) d\tau \quad (2.71)$$

Since the argument of the Green function is $\underline{x} - \underline{y}$ it is possible to say that $\frac{\partial G}{\partial y_i} = -\frac{\partial G}{\partial x_i}$.

Using the divergence theorem we have

$$\begin{aligned} \frac{1}{4\pi c_o^2} \int_{\infty} \frac{1}{r} \frac{\partial^2 T_{ij}}{\partial y_i \partial y_j} dV(\underline{y}) &= \int_{\infty} \int_V \frac{\partial}{\partial y_i} \left(\frac{\partial T_{ij}}{\partial y_i}(\underline{y}, \tau) G(\underline{x} - \underline{y}, t - \tau) \right) dV(\underline{y}) d\tau + \\ &- \int_{\infty} \int_V \frac{\partial T_{ij}}{\partial y_i}(\underline{y}, \tau) \frac{\partial}{\partial y_i} G(\underline{x} - \underline{y}, t - \tau) dV(\underline{y}) d\tau = - \int_{\infty} \int_S n_i \frac{\partial T_{ij}}{\partial y_i}(\underline{y}, \tau) G(\underline{x} - \underline{y}, t - \tau) dS(\underline{y}) d\tau + \\ &+ \int_{\infty} \int_V \frac{\partial T_{ij}}{\partial y_i}(\underline{y}, \tau) \frac{\partial}{\partial x_i} G(\underline{x} - \underline{y}, t - \tau) dV(\underline{y}) d\tau \end{aligned} \quad (2.72)$$

Since the dependent variables are τ and \underline{y} , $\frac{\partial}{\partial x_i}$ can be carried out from the integral. The

same work for the y_i leads to

$$\begin{aligned} \frac{1}{4\pi c_o^2} \int_{\infty} \frac{1}{r} \frac{\partial^2 T_{ij}}{\partial y_i \partial y_j} dV(\underline{y}) &= - \int_{\infty} \int_S n_i \frac{\partial T_{ij}}{\partial y_i}(\underline{y}, \tau) G(\underline{x} - \underline{y}, t - \tau) dS(\underline{y}) d\tau + \\ &+ \frac{\partial}{\partial x_i} \int_{\infty} \int_V \frac{\partial}{\partial y_i} \left(T_{ij}(\underline{y}, \tau) G(\underline{x} - \underline{y}, t - \tau) \right) dV(\underline{y}) d\tau - \frac{\partial}{\partial x_i} \int_{\infty} \int_V T_{ij}(\underline{y}, \tau) \frac{\partial}{\partial y_i} G(\underline{x} - \underline{y}, t - \tau) dV(\underline{y}) d\tau = \\ &= - \int_{\infty} \int_S n_i \frac{\partial T_{ij}}{\partial y_i}(\underline{y}, \tau) G(\underline{x} - \underline{y}, t - \tau) dS(\underline{y}) d\tau + \frac{\partial}{\partial x_i} \int_{\infty} \int_S n_j T_{ij}(\underline{y}, \tau) G(\underline{x} - \underline{y}, t - \tau) dS(\underline{y}) d\tau + \\ &- \frac{\partial^2}{\partial x_i \partial x_j} \int_{\infty} \int_V T_{ij}(\underline{y}, \tau) G(\underline{x} - \underline{y}, t - \tau) dV(\underline{y}) d\tau \end{aligned} \quad (2.73)$$

making an integration over the delta Dirac functions, it leads to

$$\begin{aligned} \frac{1}{4\pi c_o^2} \int \frac{1}{r} \frac{\partial^2 T_{ij}}{\partial y_i \partial y_j} dV(\underline{y}) &= \frac{1}{4\pi c_o^2} \frac{\partial^2}{\partial x_i \partial x_j} \int \frac{T_{ij}(\underline{y}, \tau)}{r} dV(\underline{y}) - \frac{1}{4\pi c_o^2} \frac{\partial}{\partial x_i} \int n_j \frac{T_{ij}(\underline{y}, \tau)}{r} dS(\underline{y}) + \\ &- \frac{1}{4\pi c_o^2} \int \frac{n_i}{r} \frac{\partial T_{ij}(\underline{y}, \tau)}{\partial y_i} dS(\underline{y}) \end{aligned} \quad (2.74)$$

where τ represents the retarded time. The last steps of Curle's formulation are the rearrangements of the surface integrals making use of the following relationships.

$$\frac{\partial}{\partial n} = n_i \frac{\partial}{\partial y_i} \quad \frac{\partial}{\partial x_i} \left[\frac{f(\tau)}{r} \right] = - \left[\frac{f}{r^2} + \frac{1}{c_o r} \frac{\partial}{\partial \tau} \right] \frac{\partial r}{\partial x_i} \quad (2.75)$$

Hence the surface integral becomes

$$\begin{aligned} \int_s \left(\frac{1}{r} \frac{\partial \rho}{\partial n} + \frac{1}{r^2} \frac{\partial r}{\partial n} \rho + \frac{1}{rc_o} \frac{\partial r}{\partial n} \frac{\partial \rho}{\partial \tau} \right) dS(\underline{y}) &= \int_s n_i \left(\frac{1}{r} \frac{\partial \rho}{\partial y_i} + \frac{1}{r^2} \frac{\partial r}{\partial y_i} \rho + \frac{1}{rc_o} \frac{\partial r}{\partial y_i} \frac{\partial \rho}{\partial \tau} \right) dS(\underline{y}) = \\ &= \int_s n_i \left(\frac{1}{r} \frac{\partial (\rho \delta_{ij})}{\partial y_i} - \frac{1}{r^2} \frac{\partial r}{\partial y_i} \rho + \frac{1}{rc_o} \frac{\partial r}{\partial y_i} \frac{\partial \rho}{\partial \tau} \right) dS(\underline{y}) = \int_s \frac{n_i}{r} \frac{\partial (\rho \delta_{ij})}{\partial y_i} dS(\underline{y}) + \frac{\partial}{\partial x_i} \int_s \frac{n_i}{r} \rho \delta_{ij} dS(\underline{y}) \end{aligned} \quad (2.76)$$

which leads to

$$\begin{aligned} \rho(\underline{x}, t) - \rho_o &= \frac{1}{4\pi c_o^2} \frac{\partial^2}{\partial x_i \partial x_j} \int \frac{T_{ij}}{r} dV(\underline{y}) - \frac{1}{4\pi c_o^2} \frac{\partial}{\partial x_i} \int \frac{n_j}{r} (T_{ij} + c_o^2 \rho \delta_{ij}) dS(\underline{y}) + \\ &- \frac{1}{4\pi c_o^2} \int \frac{n_i}{r} \frac{\partial}{\partial y_i} (T_{ij} + c_o^2 \rho \delta_{ij}) dS(\underline{y}) \end{aligned} \quad (2.77)$$

From the definition of the Lighthill tensor and from the momentum equation it is possible to obtain

$$\frac{n_i}{r} \frac{\partial}{\partial y_i} (T_{ij} + c_o^2 \rho \delta_{ij}) = - \frac{n_i}{r} \frac{\partial \rho u_i}{\partial t} \quad (2.78)$$

leading to

$$\begin{aligned} \rho(\underline{x}, t) - \rho_o &= \frac{1}{4\pi c_o^2} \frac{\partial^2}{\partial x_i \partial x_j} \int_{\infty} \frac{T_{ij}}{r} dV(\underline{y}) - \frac{1}{4\pi c_o^2} \frac{\partial}{\partial x_i} \int_S \frac{n_j}{r} (\rho u_i u_j + p \delta_{ij} - \tau_{ij}) dS(\underline{y}) + \\ &+ \frac{1}{4\pi c_o^2} \int_S \frac{\rho u_i n_i}{r} dS(\underline{y}) \end{aligned} \quad (2.79)$$

For solid surfaces the velocity on the surface vanishes, hence the final result of Curle's equation is the (2.80)

$$\rho(\underline{x}, t) - \rho_o = \frac{1}{4\pi c_o^2} \frac{\partial^2}{\partial x_i \partial x_j} \int_{\infty} \frac{T_{ij}}{r} dV(\underline{y}) - \frac{1}{4\pi c_o^2} \frac{\partial}{\partial x_i} \int_S \frac{n_j}{r} (p \delta_{ij} - \tau_{ij}) dS(\underline{y}) \quad (2.80)$$

2.5.5 Ffowcs Williams & Hawkings's Analogy

A generalization of Lighthill's theory to include aerodynamic surfaces in motion, proposed by Ffowcs Williams & Hawkings [44] has provided the basis for a significant amount of analysis of the noise produced by rotating blades, including helicopter rotors, propeller blades, and fans. The Ffowcs Williams & Hawkings (FW-H) theory includes surface source terms in addition to the quadrupole-like source introduced by Lighthill. The surface sources are generally referred to as thickness (or monopole) sources and loading (or dipole) sources.

They are also often termed linear in that no explicitly nonlinear terms appear in them and the propagation from the surfaces has no nonlinear component. It should be noted, however, that the loading sources, which consist of surface pressures, may be computed using nonlinear aerodynamic methods. The following work is the same reported by Crighton [42].

Let us consider a surface S immersed in a fluid, which moves at a speed equal to v_i and defined by the function $f(\underline{x}, t)$:

$$\begin{cases} f(\underline{x}, t) < 0, & \text{inside } S \\ f(\underline{x}, t) = 0 & \text{on } S \\ f(\underline{x}, t) > 0 & \text{outside } S \end{cases} \quad (2.81)$$

Typically S is the surface of the body. However it is not strictly necessary since the theory developed in this section is not only true for surfaces that limit the body but also for surfaces that simply contain the body. The $f(\underline{x}, t)$ function satisfies the following relation

$$\frac{\partial f}{\partial t} + v_i \frac{\partial f}{\partial x_i} = 0 \quad (2.82)$$

since the density at an infinite distance from the body is constant, it's possible to obtain

$$\frac{\partial(\rho - \rho_o)}{\partial t} + \frac{\partial \rho u_i}{\partial x_i} = 0 \quad (2.83)$$

Multiplying the continuity equation by the Heaviside function

$$\frac{\partial(\rho - \rho_o)}{\partial t} H(f) + \frac{\partial \rho u_i}{\partial x_i} H(f) = 0 \quad (2.84)$$

or equivalently

$$\frac{\partial(\rho - \rho_o)H(f)}{\partial t} + \frac{\partial \rho u_i H(f)}{\partial x_i} = \frac{\partial H(f)}{\partial t} (\rho - \rho_o) + \frac{\partial H(f)}{\partial x_i} \rho u_i \quad (2.85)$$

Remembering the properties of the Heaviside function

$$\begin{aligned} \frac{\partial(\rho - \rho_o)H(f)}{\partial t} + \frac{\partial \rho u_i H(f)}{\partial x_i} &= \left[\frac{\partial f}{\partial t} (\rho - \rho_o) + \frac{\partial f}{\partial x_i} \rho u_i \right] \delta(f) = \\ &= [\rho_o v_i + \rho(u_i - v_i)] \frac{\partial f}{\partial x_i} \delta(f) = Q |\nabla f| \delta(f) \end{aligned} \quad (2.86)$$

where it has been considered that $\frac{\partial f}{\partial x_i} = n_i |\nabla f|$, while for Q it has been considered that

$$Q = [\rho_o v_i + \rho(u_i - v_i)]n_i \quad (2.87)$$

and it has to be considered like a source term which exists only on the surface S. It is possible to rearrange the momentum equation in the same way, leading to

$$\begin{aligned} \frac{\partial \rho u_i H(f)}{\partial t} + \frac{\partial \rho u_i u_j H(f)}{\partial x_j} + \frac{\partial p H(f)}{\partial x_i} - \frac{\partial \tau_{ij} H(f)}{\partial x_i} &= \rho u_i \frac{\partial H(f)}{\partial t} + \rho u_i u_j \frac{\partial H(f)}{\partial x_j} + \\ + p \frac{\partial H(f)}{\partial x_i} - \tau_{ij} \frac{\partial H(f)}{\partial x_i} &= \left[\rho u_i \frac{\partial f}{\partial t} + \rho u_i u_j \frac{\partial f}{\partial x_j} + p \delta_{ij} \frac{\partial f}{\partial x_j} - \tau_{ij} \frac{\partial f}{\partial x_j} \right] \delta(f) = \\ = \left[\rho u_i (u_i - v_i) \frac{\partial f}{\partial x_j} + p \delta_{ij} \frac{\partial f}{\partial x_j} - \tau_{ij} \frac{\partial f}{\partial x_j} \right] \delta(f) &= F_i |\nabla f| \delta(f) \end{aligned} \quad (2.88)$$

where

$$F_i = [\rho u_i (u_j - v_j) + p \delta_{ij} - \tau_{ij}] n_i \quad (2.89)$$

$$\left[\frac{\partial^2}{\partial t^2} - c_o^2 \frac{\partial^2}{\partial x_i^2} \right] (\rho - \rho_o) H(f) = \frac{\partial^2 T'_{ij} H(f)}{\partial x_i \partial x_j} - \frac{\partial F_i |\nabla f| \delta(f)}{\partial x_i} + \frac{\partial Q |\nabla f| \delta(f)}{\partial t} \quad (2.90)$$

$$T'_{ij} = \rho u_i u_j - \tau_{ij} + (p - c_o^2 (\rho - \rho_o)) \delta_{ij} \quad (2.91)$$

looks similar to Lighthill's tensor and ρ_o does not affect the sound generation, since it is a constant. The solution of this wave equation is given by

$$\begin{aligned} \rho(\underline{x}, t) - \rho_o &= \frac{\partial^2}{\partial x_i \partial x_j} \iint_{\infty} [T'_{ij} H(f)](\underline{y}, \tau) \frac{\delta(r - c_o(t - \tau))}{4\pi c_o r} dV(\underline{y}) d\tau + \\ - \frac{\partial}{\partial x_i} \iint_{\infty} [F_i |\nabla f| \delta(f)](\underline{y}, \tau) \frac{\delta(r - c_o(t - \tau))}{4\pi c_o r} dV(\underline{y}) d\tau + \\ + \frac{\partial}{\partial t} \iint_{\infty} [Q |\nabla f| \delta(f)](\underline{y}, \tau) \frac{\delta(r - c_o(t - \tau))}{4\pi c_o r} dV(\underline{y}) d\tau \end{aligned} \quad (2.92)$$

In the case of a moving surface, the $f(\underline{x}, t)$ function and the sources terms are better expressed in a surface reference system. If we refer to the new reference system with \underline{y}^* , it follows that

$$\begin{aligned} y_i &= y_i^* + v_i \tau \\ u_i &= u_i^* + v_i \tau \end{aligned} \quad (2.93)$$

The Jacobean of this transformation is equal to unit. Since \underline{y} and r are now both functions of τ , we have to consider the following variable substitution to integrate on τ .

$$\begin{aligned} g(\tau) &= r - c_o(t - \tau)\tau \\ dg &= (\partial r / \partial \tau + c_o)d\tau \end{aligned} \quad (2.94)$$

where

$$\frac{\partial r}{\partial \tau} = \frac{\partial r}{\partial x_i} \frac{\partial y_i}{\partial \tau} = \frac{-2(x_i - y_i)}{2\sqrt{(x_i - y_i)^2}} \frac{\partial y_i}{\partial \tau} = -\frac{x_i - y_i}{r} v_j = -l_j v_j \quad (2.95)$$

Where l_j is the j-component of a unit versor pointing from the source to the observer location. Hence we have

$$dg = (c_o - l_j v_j) d\tau \quad (2.96)$$

Applying the variable substitution to the previous solution it yields

$$\begin{aligned} \rho(\vec{x}, t) - \rho_o &= \frac{\partial^2}{\partial x_i \partial x_j} \iint_{\infty} [T'_{ij} H(f^*)](\vec{y}^*, \tau) \frac{\delta(g)}{4\pi c_o r (c_o - l_j v_j)} dV(\vec{y}^*) d\tau + \\ &- \frac{\partial}{\partial x_i} \iint_{\infty} [F_i^* |\nabla f^*| \delta(f^*)](\vec{y}^*, \tau) \frac{\delta(g)}{4\pi c_o r (c_o - l_j v_j)} dV(\vec{y}^*) d\tau + \\ &+ \frac{\partial}{\partial t} \iint_{\infty} [Q^* |\nabla f^*| \delta(f^*)](\vec{y}^*, \tau) \frac{\delta(g)}{4\pi c_o r (c_o - l_j v_j)} dV(\vec{y}^*) d\tau \end{aligned} \quad (2.97)$$

Where the source terms in the new reference system are

$$Q^* = [\rho_o v_i + \rho u_i^*] n_i \quad (2.98)$$

$$F_i^* = [\rho u_j^* (u_i^* + v_i) + p \delta_{ij} - \tau_{ij}^*] n_i \quad (2.99)$$

$$T_{ij}^* = \rho (u_i^* + v_i)(u_j^* + v_j) - \tau_{ij}^* + (p - c_o^2 (\rho - \rho_o)) \delta_{ij} \quad (2.100)$$

It has to be noticed that $\tau_{ij}^* = \tau_{ij}$. Integrating on dg

$$\begin{aligned} \rho(\underline{x}, t) - \rho_o &= \frac{1}{4\pi c_o^2} \frac{\partial^2}{\partial x_i \partial x_j} \iint_{\infty} \frac{[T_{ij}^* H(f^*)]}{r(1-l_j v_j/c_o)} dV(\underline{y}^*) d\tau + \\ &- \frac{1}{4\pi c_o^2} \frac{\partial}{\partial x_i} \iint_{\infty} \frac{[F_i^* |\nabla f^*| \delta(f^*)]}{r(1-l_j v_j/c_o)} dV(\underline{y}^*) d\tau + \frac{1}{4\pi c_o^2} \frac{\partial}{\partial t} \iint_{\infty} \frac{[Q^* |\nabla f^*| \delta(f^*)]}{r(1-l_j v_j/c_o)} dV(\underline{y}^*) d\tau \end{aligned} \quad (2.101)$$

Where the integrand functions have to be evaluated at $g=0$ or at $\tau = t - r/c_o$.

Integrating on the δ -functions it is possible to obtain the final formulation of the wave equation

$$\begin{aligned} \rho(\underline{x}, t) - \rho_o &= \frac{1}{4\pi c_o^2} \frac{\partial^2}{\partial x_i \partial x_j} \iint_{\infty} \frac{T_{ij}^*}{r(1-l_j v_j/c_o)} dV(\underline{y}^*) d\tau + \\ &- \frac{1}{4\pi c_o^2} \frac{\partial}{\partial x_i} \iint_{\infty} \frac{F_i^*}{r(1-l_j v_j/c_o)} dS(\underline{y}^*) d\tau + \frac{1}{4\pi c_o^2} \frac{\partial}{\partial t} \iint_{\infty} \frac{Q^*}{r(1-l_j v_j/c_o)} dS(\underline{y}^*) d\tau \end{aligned} \quad (2.102)$$

For a solid surface we have, $u_i^* = 0$, thus

$$Q^* = [\rho_o v_i] n_i \quad (2.103)$$

$$F_i^* = [p \delta_{ij} - \tau_{ij}^*] n_i \quad (2.104)$$

The Q^* term is equal to zero in the case of steady surface. In the case of a steady surface and S equal to the body surface the FW-H's equation reduces to the Curle equation.

2.5.6 Further Considerations on Aerodynamic Generation of Sound

A first way to proceed is the direct calculation of the acoustic pressure through a direct simulation of the compressible fluid.

Typically this method is not widely used since it is too computationally expensive, requiring higher order numerical schemes to reduce the dissipation and the dispersion of the acoustic waves, and complicated boundary conditions. For example, non-reflecting boundary conditions (NRBCs) may be required to avoid unphysical reflections contaminating the computational domain. Other methods exist to avoid this phenomenon when NRBCs are not available, including the use of purposefully dissipative grid regions close to domain boundaries.

Alternatively to make an estimation of the aerodynamically generated sound, the acoustic analogy with a turbulence model simulation for computing the sources can be used. This last approach needs sophisticated turbulence models since the good resolution of the flow field is the primary requirement to obtain an accurate prediction of sound sources. Let us investigate the advantages and the weaknesses of the acoustic analogy. In obtaining Lighthill's equation,

from a simple manipulation of the Navier-Stokes Equations, we have supposed that $c_o^2 \frac{\partial^2 \rho}{\partial x_i^2}$

was independent from the left hand side of equation (2.67). This hypothesis is never satisfied since the Lighthill's tensor is dependent on the density itself. In other word the acoustic analogy leads to a good result if the turbulent flow field and the acoustics one are not coupled, that is when we can neglect the effect of acoustics on the flow. The acoustic analogies divide the generation of sound from the propagation, computing the latter by a wave operator.

Let us consider the Lighthill's tensor (2.68), the dominant term, if the flow is turbulent, is the fluctuating Reynolds tensor, hence it's possible to consider (2.105).

$$T_{ij} \cong \rho u_i u_j \quad (2.105)$$

The Reynolds tensor represents a stress related to the particles exchanges in the fluid. Hence this tensor has an effect similar to the viscous stress. In the same way, from a generation of sound point of view, the fluctuating Reynolds tensor has an effect similar to the viscous stresses and is relatively more important than them.

The double divergence of the Reynolds fluctuating tensor, as noticed by Howe [43], can be rearranged for low-Mach number as

$$\frac{\partial^2 \rho_o u_i u_j}{\partial x_i \partial x_j} \cong \text{div}(\rho_o \underline{\omega} \wedge \underline{v}) \quad (2.106)$$

This relationship shows that the vorticity is the main cause of the aerodynamic sound and the main acoustic sources are related to surfaces.

A better evaluation of the wall effect can be made analyzing the order of magnitude of the various terms of the FW-H equation

$$\begin{aligned} \rho(\underline{x}, t) - \rho_o &= \frac{1}{4\pi c_o^2} \frac{\partial^2}{\partial x_i \partial x_j} \iint_{\infty} \frac{T'_{ij}^*}{r(1-l_j v_j/c_o)} dV(\underline{y}^*) d\tau + \\ &- \frac{1}{4\pi c_o^2} \frac{\partial}{\partial x_i} \iint_{\infty} \frac{F_i^*}{r(1-l_j v_j/c_o)} dS(\underline{y}^*) d\tau + \frac{1}{4\pi c_o^2} \frac{\partial}{\partial t} \iint_{\infty} \frac{Q^*}{r(1-l_j v_j/c_o)} dS(\underline{y}^*) d\tau \end{aligned} \quad (2.107)$$

If S corresponds to the body surface, the three terms of the right hand side of previous equation are related to different causes. The first term corresponds to the sound produced by turbulent structures and from dimensional analysis it results

$$p(\underline{x}, t) \cong \frac{\rho D}{4\pi r c^2} U^4 \quad (2.108)$$

and the sound intensity is

$$I(r) \cong \frac{p^2(\underline{x}, t)}{\rho_o c_o} \cong \frac{\rho D^2}{16\pi^2 r^2 c^5} U^8 \quad (2.109)$$

or equivalently

$$I(r) \cong U^3 M^5 \quad (2.110)$$

known as the Lighthill's v^8 -law. The second term represents the component due to the forces that act on the surface, for which the pressure fluctuations can be estimated as

$$p(\underline{x}, t) \cong \frac{\rho D}{4\pi r c} U^3 \quad (2.111)$$

and the sound intensity results in

$$I(r) \cong \frac{p^2(\underline{x}, t)}{\rho_o c_o} \cong \frac{\rho D^2}{16\pi^2 r^2 c^3} U^6 \quad (2.112)$$

or equivalently

$$I(r) \cong U^3 M^3 \quad (2.113)$$

The third term is equal to zero if the surface S is attached to the body and this last one is not affected by vibration. Comparing the first and the second term it is possible to say that the contribution of the surface sources (second term) is dominant. Another approximation in an acoustic analogy is the use of a linear wave operator, in fact this one describes well the wave propagation only for low speed cases ($M < 0.4$).

2.6 Numerical Approaches for Aeroacoustics

As already mentioned into previous sections sound is characterized by pressure fluctuations whose magnitude is much smaller if compared to the aerodynamic or atmospheric pressure. This implies that direct numerical computation of sound related variation of thermodynamic variables is very difficult and CPU-demanding.

Today, in particular for industrial cases, acoustic analogies are widely used for noise computations, but also other approaches are available in order to reduce the complexity of the problem.

The most important methodologies applied in the field of Computational AeroAcoustic (CAA) are given below according to decreasing CPU-requirements.

- Direct Computation of Noise
- Acoustic Analogy
- Boundary Element Method
- Broadband Noise Source Models

Except for acoustic analogy, already widely explained above because of the direct interest for the applications presented in next chapters, other acoustic approaches will be here object of discussion in order to give a wide and complete overview of the state-of-art of CAA.

2.6.1 Direct Noise Computation

Direct noise computation is the most expensive approach in the frame of the CAA. According to this methodology, both generation and propagation of sound waves are directly computed by solving the fluid dynamics equations. Prediction of sound waves always requires time-accurate solutions to the governing equations. Furthermore, in most practical applications of the direct method, one has to employ governing equations that are capable of modeling viscous and turbulence effects.

The direct method is thus computationally too difficult and expensive as it requires highly accurate numerical schemes, very fine computational meshes up to receivers locations and acoustically non-reflecting boundary conditions (NRBC). The computational cost becomes

prohibitive when sound has to be predicted in the far field (e.g. hundreds of chord-lengths in the case of an airfoil).

In many of such situations involving near-field acoustic computations, the sound (or pseudo-sound for that matter) is predominantly due to the local hydrodynamic pressure which can be predicted with a reasonable cost and accuracy.

Since sound propagation is directly resolved in this method, one normally needs to solve the compressible form of the governing equations (e.g., compressible RANS equations, compressible form of filtered equations for LES). Only in situations where the flow is low subsonic and the receivers in the near field locations an incompressible flow formulation can be used.

2.6.2 Acoustic Analogy

As previously discussed, the acoustic analogies for noise computation are a real milestone in the frame of CAA and the most diffused and implemented approaches for industrial noise computations.

For predictions involving mid and far-field noise, the method based on Lighthill's acoustic analogy [39], [40] offers viable alternatives to the direct method and the possibility to be coupled with RANS/DES/LES flow field computations. Different implementations of Acoustic Analogy are available, according to the capability of prediction of sound generated by acoustic sources such as monopoles, dipoles and quadrupoles.

In the frame of commercial CFD packages the acoustic analogy approach is the most used and the FW-H analogy available in ANSYS-FLUENT[®] will be widely applied in next chapters for noise computations of airfoil self-generated noise and high speed propeller noise.

2.6.3 Boundary Element Method and Finite Element Method

The Boundary Element Method (BEM) and the Finite Element Method (FEM) for acoustics are two novel techniques for CAA, even more used for industrial simulations [47], [48], [50] and [51].

These methodologies are based on the resolution of the sound wave equation in the Helmholtz equation formulation into a fluid domain respectively with a boundary element numerical approach based on Green's function or with a finite element approach.

In this way the BEM and the FEM allow to compute the acoustic pressure in some pre-determined points of the computational volume (e.g. microphone locations) with a set of aerodynamic boundary conditions that can be computed with a RANS preliminary calculation.

Even if BEM and FEM solve practically the same equation of the acoustic analogy, their numerical characteristics make them more suitable for a large class of problems, characterized by wall-bounded flows, affected by sound waves reflection and refraction, near-field calculations and low Mach number problems [45].

Consider the acoustic field in a fluid domain E with boundary S . Domain E can be either an interior domain inside S or an exterior domain outside S , Figure 2.12.

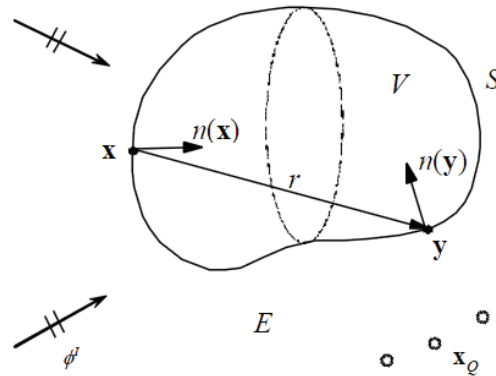


Figure 2.12: acoustic domain E outside a structure S

Then consider the wave propagation equation provided in (2.58) where the acoustic pressure is assumed to be ϕ and the source right-hand side term is assumed to be equal to the monopole source $Q\delta(\underline{x}, \underline{x}_Q)$.

Finally to the propagation equation (2.114) can be achieved

$$\nabla^2 \phi + k^2 \phi + Q\delta(\underline{x}, \underline{x}_Q) = 0 \quad (2.114)$$

defined into the volume domain E . It is called Helmholtz equation and $k = \omega/c$ is the wavenumber and $\delta(\underline{x}, \underline{x}_Q)$ the unitary space impulse located at \underline{x}_Q inside the fluid domain E .

The acoustic boundary conditions to Helmholtz equation can be of three types:

$$\text{Pressure B.C. } \phi = \bar{\phi} \quad \text{on } S \quad (2.115)$$

$$\text{Velocity B.C. } v_n = \frac{1}{i\omega\rho} \frac{\partial \bar{\phi}}{\partial n} \quad \text{on } S \quad (2.116)$$

$$\text{Specific Impedance } \bar{Z} = \frac{\phi}{(-v_n)} \quad \text{on } S \quad (2.117)$$

where ρ is the mass density, v_n the normal boundary velocity (n is the outward normal), ω the circular frequency and i the imaginary unit.

In a boundary problem equation (2.114) needs to be solved in the frequency domain. Once a frequency solution $\phi(\underline{x}, \omega)$ is obtained the time domain solution can be calculated as $\phi(\underline{x}, \omega)e^{-i\omega t}$.

There are two common types of acoustic wave problems. One is called the *radiation problem* in which a structure is in vibration and causes disturbances in acoustic field, the other one is the *scattering problem*, where a structure is assumed to be motionless and an incoming disturbance interacts with it and waves are scattered by structure itself. In addition to previously given B.C. for exterior (free-field) domain the field at infinity must satisfy the Sommerfeld radiation condition (2.118)

$$\lim_{R \rightarrow \infty} \left[R \left| \frac{\partial \phi}{\partial R} - ik\phi \right| \right] = 0 \quad (2.118)$$

where R is the radius of a large sphere covering the surface S . Basically the Sommerfeld condition says that any acoustic disturbances caused by surface S should be killed out at infinity based on energy considerations.

Helmholtz equation can be transformed into a Boundary Integral Equation (BIEs) and solved using BEM. The conventional BIEs is given by (2.119)

$$c(\underline{x})\phi(\underline{x}) = \int_S \left[G(\underline{x}, \underline{y}, \omega)q(\underline{y}) - F(\underline{x}, \underline{y}, \omega)\phi(\underline{y}) \right] dS(\underline{y}) + \phi'(\underline{x}) + QG(\underline{x}, \underline{x}_Q, \omega) \quad (2.119)$$

where $c(x)=1/2$ (constant), $q = \partial\phi/\partial n$, ϕ' is a plane incident wave, and the kernels (Green's functions) are given by (2.120) and (2.121)

$$G(\underline{x}, \underline{y}, \omega) = \frac{1}{4\pi r} e^{ikr} \quad (2.120)$$

$$F(\underline{x}, \underline{y}, \omega) = \frac{\partial G(\underline{x}, \underline{y}, \omega)}{\partial n(\underline{y})} \quad (2.121)$$

where r is the distance between the source point \underline{x} and the field point \underline{y} .

Equation (2.119) can be used to solve the unknown pressure ϕ on S . The major defect of this approach for exterior domains problems is that it has non-unique solutions at a set of fictitious eigenfrequencies associated with the resonate frequencies of corresponding interior problems. This difficulty is usually referred as fictitious eigenfrequency difficulty and should be solved using the normal derivative (hypersingular) BIE in conjunction with the (2.119).

The Hypersingular Boundary Integral Equation (HBIE) is given by (2.122)

$$\tilde{c}(x)q(x) = \int_S \left[K(\underline{x}, \underline{y}, \omega)q(\underline{y}) - H(\underline{x}, \underline{y}, \omega)\phi(\underline{y}) \right] dS(\underline{y}) + \phi'(\underline{x}) + QK(\underline{x}, \underline{x}_Q, \omega) \quad (2.122)$$

where again $\tilde{c} = 1/2$. New kernels are given in (2.123) and (2.124).

$$K(\underline{x}, \underline{y}, \omega) = \frac{\partial G(\underline{x}, \underline{y}, \omega)}{\partial n(\underline{x})} \quad (2.123)$$

$$H(\underline{x}, \underline{y}, \omega) = \frac{\partial F(\underline{x}, \underline{y}, \omega)}{\partial n(\underline{x})} \quad (2.124)$$

For exterior problems this approach is coupled with (2.119) according the Composite BIE [53]. In practice linear combination of (2.119) and (2.122) is provided in (2.125) where β is the coupling constant.

$$BIE + \beta HBIE = 0 \quad (2.125)$$

This formulation is also known as Burton-Miller BIE formulation [52], and it is able to provide a unique solution at all frequencies if β is a complex number.

Once acoustic pressure ϕ and its normal derivative $\frac{\partial\phi}{\partial n}$ are computed on S using BEM, the acoustic pressure in each point \underline{x} of domain E can be determined applying the following representation integral (2.126).

$$\phi(x) = \int_S [G(\underline{x}, \underline{y}, \omega)q(\underline{y}) - F(\underline{x}, \underline{y}, \omega)\phi(\underline{y})] dS(\underline{y}) + \phi'(\underline{x}) + QG(\underline{x}, \underline{x}_O, \omega) \quad (2.126)$$

This computation can be considered as a kind of post-processing in the BEM solution.

Further and more detailed information on BEM can be found in literature. This methodology is implemented in such commercial packages as SYSNOISE[®] [55] and ACTRAN[®], and in the freeware code FASTBEM[®] [56]. Moreover BEM approach can be also coupled with the fast-multipole technique for speed up numerical convergence, being able to provide very fast calculation results also for complex industrial geometries.

As mentioned above FEM consists in the resolution of the equation (2.114) into the fluid volume E with a finite element approach. The main FEM advantages respect to BEM consist in the possibility to store sparse symmetrical matrices easier to be inverted, in the possibility to adopt different shape functions and handle inhomogeneous acoustic propagations medium.

On the other hand, the resolution method requires an acoustic volume grid designed to provide good accuracy for the range of frequencies of interest for the specific problem, thus the necessity to generate an acoustic grid (in general quite different from the CFD grid) able to provide at least from 10 to 15 points per wavelength.

However this grid usually is rather coarser than CFD grid and the acoustic computations are much less computationally expensive than the fluid dynamic simulation. References and detailed descriptions of FEM approach to acoustics can be found in [45] and [47].

2.6.4 Broadband Noise Source Models

In many practical applications involving turbulent flows, noise does not have any distinct tones, and the sound energy is continuously distributed over a broad range of frequencies.

In those situations involving broadband noise, statistical turbulence quantities readily computable from RANS equations can be used, in conjunction with semi-empirical correlations and Lighthill's acoustic analogy, to shed some light on the source of broadband noise.

Several broadband noise sources models are available in literature, depending on applications. These models are based on the possibility to define a source term that enables the user to quantify the local contribution to the total acoustic power generated by the flow.

Some of them are:

- Proudman's formula
- Jet noise source model
- Boundary layer noise source model
- Source terms in the linearized Euler equations
- Source terms in Lilley's equation

Considering that one would ultimately want to come up with some measures to mitigate the noise generated by the flow, the source models can be employed to extract useful diagnostics on the noise source to determine which portion of the flow is primarily responsible for the noise generation. Furthermore it is remarkable that these source models are not able to predict sound in a pre-definite location in space. Unlike the direct method and the FW-H integral method, the broadband noise source models do not require transient solutions to any governing fluid dynamics equations. All the source models need is what typical RANS models would provide, such as the mean velocity field, turbulent kinetic energy k and the dissipation rate ε . Therefore, the broadband noise source models are the less computationally expensive acoustic models available.

2.7 The solver: ANSYS FLUENT

This last paragraph of the second chapter aims to provide a small introduction to the most developed and diffused CFD solver, ANSYS-FLUENT[®] [23] [24], widely used for the applications presented in next chapters.

ANSYS-FLUENT[®] is a general purpose commercial software for fluid dynamic simulation based in a control volume technique which implements the state-of-the-art of the industrial CFD available today.

The main solver is based on a 3D RANS/URANS approach, coupled with a number of turbulence models from 1-equation to 7-equations. In the most recent version a 3D DES/LES solver is also available, and in the next release (ANSYS 13.0) also the SAS and ELES approaches will be implemented in, in order to provide to customers the possibility to choose among all the computational models today available.

ANSYS-FLUENT[®] is designed to manage structured/unstructured meshes, with tetrahedral, hexahedral and polyhedral elements, and it is basically coupled with two mesh generator, ANSYS-GAMBIT[®] and ANSYS-TGRID[®], respectively devoted to academic and industrial applications. In recent years also ANSYS-ICEM[®] is provided as official mesh generator, developing a new interface and meshing technique based on multiblocks elements and an advanced CAD environment.

Other important features in ANSYS-FLUENT are the Acoustic Models, the Multispecies Models (for reacting/combustion modelling), the Multiphase Models (based on Volume Of Fluid approach).

Acoustic Models implemented in ANSYS-FLUENT[®] are the broadband noise source model and the FW-H Acoustic Analogy.

In the frame of acoustic analogy ANSYS-FLUENT[®] adopts a time-domain integral formulation wherein time histories of sound pressure, or acoustic signals, at prescribed receiver locations are directly computed by evaluating a few surface integrals.

Time-accurate solutions of the flow-field variables, such as pressure, velocity components, and density on source (emission) surfaces, are required to evaluate the surface integrals for the acoustic model taking into account that the flow simulation has to be able to describe with the appropriate accuracy the phenomena which are aimed to be captured (e.g., vortex shedding).

Multiple surfaces can be selected as sources and acoustic data files can be processed using the Fast Fourier Transform (FFT) and associated post processing capabilities to compute and plot such acoustic quantities as the overall Sound Pressure Level (SPL) and power spectra.

One important limitation of ANSYS-FLUENT[®] FW-H model is that it is applicable only for the prediction of the propagation of sound in free space. Thus, while the model can be legitimately used to predict far-field noise due to external aerodynamic flows, such as the flows around ground vehicles and aircrafts, it cannot be used for predicting the noise propagation inside ducts or wall-enclosed elements.

Chapter 3

Aerodynamic and Aeroacoustic Modelling of Vertical Axis Wind Turbines

This chapter is focused on the problem of modelling of Wind Turbines, with a particular attention for the Vertical Axis WT and for the problems connected to this type of fluid machines. Aerodynamics is introduced with a general overview of the problem focusing on the forces generated by a rotating airfoil, decoupling the rotational dynamics, that masters the WT blade asset, to the dynamics of hysteresis, that affects airfoil lift and drag coefficients. Two analytical models are proposed and implemented for the modelling of these mechanisms together with their coupling in a tool for VAWT aerodynamic simulations. This tool has been applied on an experimental test-case [85], and results have been compared with experimental data and CFD computations. Moreover CFD has been used to lead also the optimization of the VAWT test-case geometry, exploring its potentialities for industrial design purposes. The aeroacoustics of WT has been investigated approaching the airfoil self-generated noise. It has been modelled via a CFD-FWH acoustic analogy approach coupled with innovative transitional turbulence models. CFD noise predictions have been compared with experimental results available in [93], [94] .

3.1 Aerodynamics of Vertical Axis Wind Turbines

In this paragraph the aerodynamic modelling of Vertical Axis Wind Turbines will be discussed. In first analysis the problem can be approached and simplified as an airfoil in rotation around an axis. During the rotation the airfoil experiences different velocities and angular assets according to the composition of the free-stream velocity and the rotational velocity. This composition is determined by the position of the airfoil over the revolution, so its aerodynamic conditions can be expressed as function of the azimuthal angular position.

This approach, purely geometric, does not take into account the aerodynamic behavior of the airfoil in terms of induced velocity components (e.g. upwash and downwash) and induced aerodynamic angle. On a general basis the induced components can be split into 2 parts: a first one that affects the upwind zone (first half of the rotation), and a second one that affects the downwind zone (second half of the rotation) as shown in Figure 3.1. The main difference between these two parts consists in the fact that the downwind region is affected by the wake of the upwind region, so it is exposed to a lower free-stream velocity. This approach was introduced by I. Paraschivoiu [58], [59], [61], [63] and allows writing a set of implicit equations to estimate the induced velocity components during the revolution. The detailed description of Paraschivoiu Double Streamtube (DS) approach will be object of discussion of the next paragraph.

However, as it is possible to estimate induced velocity components, it is important to remind that forces on the blade depends also by lift and drag coefficients of the airfoil blade section.

These coefficients can be considered constant when the airfoil is affected by a steady flow, like in the case of axial turbo machines (e.g. propeller and axial fans). In the case of VAWT the unsteadiness of velocity and aerodynamic asset of the blade during the rotation strongly affect the aerodynamic coefficients, changing in a significant way lift and drag and consequently the aerodynamic torque and the generated power of the turbine.

In particular we can state that in nominal conditions the blade is affected by periodic cycles of free stream velocity and angular position, with a period equal to the period of rotation. In these conditions aerodynamic coefficients assume an elliptical shape typical of a hysteretic behavior. The prediction of these aerodynamic characteristics of the airfoil is not easy, and can be approached with several methodologies. A first approach to the unsteady

aerodynamics was proposed by Theodorsen [65] that was able to formulate the problem under the hypotheses of thin airfoil and attached flow. These hypotheses restrict the field of application of Theodorsen theory to “small” perturbations, not suitable in the case of the VAWT.

A first extension of Theodorsen theory can be done taking into account the Beddoes approach [68], [69], [70] for the estimation of separation point as function of lift coefficient of the airfoil and angle of attack, and this can be coupled with the Leishman theory [71], [72] for the estimation of dynamic performances of the airfoil.

These considerations lead to the Beddoes-Leishman aerodynamic model (BL) that reformulates the Theodorsen theory in the form of a system of 4 ODEs (Ordinary Differential Equations) to be solved into a set of state-space variables [71], [73], [74], [75]. This approach will be described into paragraph 3.1.2.

In paragraph 3.2 these two approaches have been developed in order to be coupled and implemented in a tool for VAWT aerodynamic modelling. Attention has been focused on the numerical coupling of the models, and this new integrated approach has been applied for an experimental test-case [85]. CFD computations have been also performed for this test-case and computational results were compared with DS-BL results and experimental data.

Moreover this test-case has also been used as basis to investigate optimization criteria for VAWT aerodynamic oriented design, in term of optimal blade angle set-up and optimal pitch control.

3.1.1 Paraschivoiu Double Streamtube Theory

Calculation of the induced velocities through the rotor is based on the principle of the two actuator disks in tandem, as shown in Figure 3.1. According to this model the wind passes twice through the rotor swept area and the induced velocities differ on the upstream half and the downstream half of the revolution. The flow field velocity comes from the right side (V_∞), reaching a first intermediate value (V_e) after the first half turbine rotation, and a final value (V'') after the complete rotation.

It is important to remind that for the aerodynamic modelling of the WT we are interested in the dynamic simulation of the airfoil rotation that means the knowledge of the aerodynamic conditions of the airfoil (velocity and AoA) in each angular position.

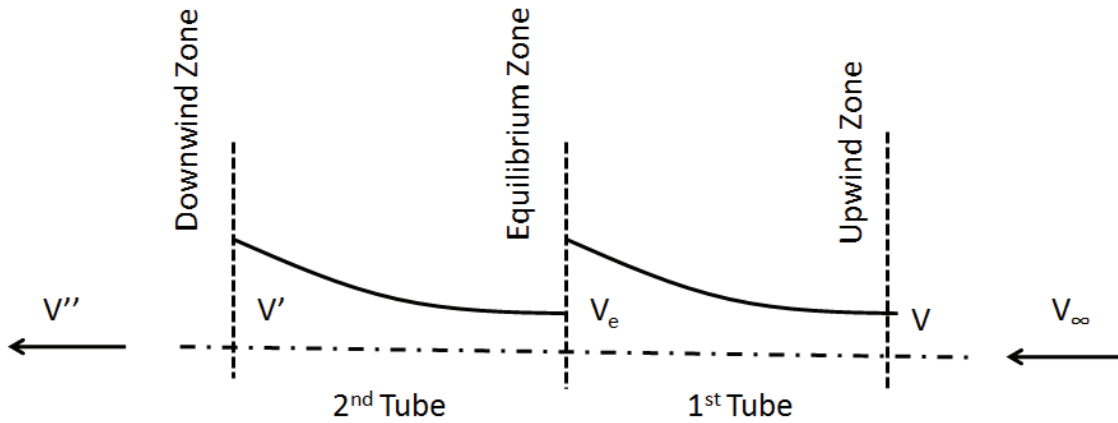


Figure 3.1: Double Streamtube Tandem Model

The analytical method uses the double streamtube model mentioned in order to separate the upwind and downstream components of the flow field, writing different equations for each part of the rotation.

Let us consider V_∞ the asymptotic velocity of the flow field. We can assume that the upwind velocity seen by the turbine is a multiple of the free-field velocity, via a correction coefficient u . This velocity is usually smaller than the free-field one and u is considered as an interference reduction factor [64]. Thus the velocity that approaches the turbine is V is given by the (3.1).

$$V = uV_\infty \quad (3.1)$$

After the first half rotation the velocity is again reduced, according to the theory, reaching the equilibrium velocity condition (3.2)

$$V_e = (2u-1)V_\infty \quad (3.2)$$

and after the second half of the rotation it is reduced by a second coefficient u' , to become the outlet velocity V'' (3.3).

$$V' = u'(2u-1)V_\infty \quad (3.3)$$

A lateral view and a plan view of the turbine are provided in Figure 3.2.

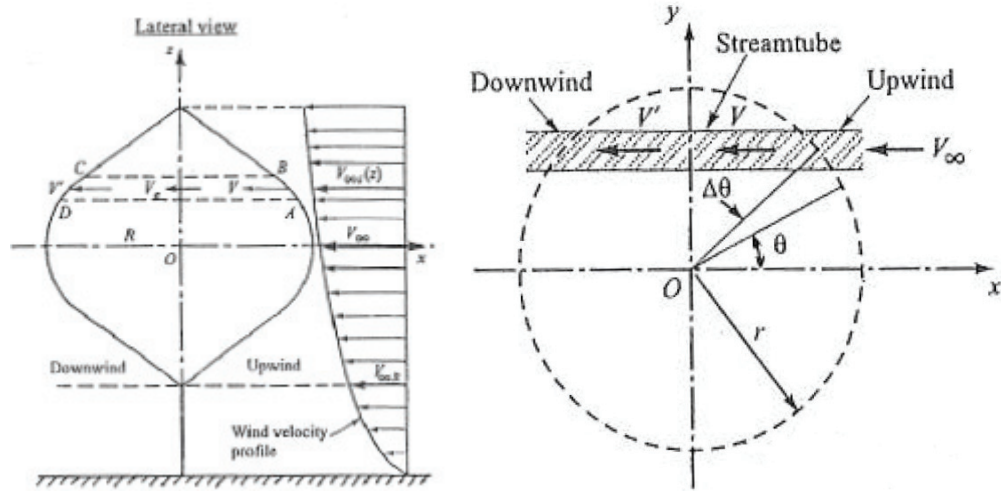


Figure 3.2: lateral view (left) and plan view (right) of the VAWT

The local relative velocity for the upstream half-cycle of the rotor, $-\pi/2 \leq \theta \leq \pi/2$, is calculated from the (3.4)

$$W^2 = V^2 \left[(X - \sin \theta)^2 + \cos^2 \theta \cos^2 \delta \right] \quad (3.4)$$

where $X = r\omega/V$. From geometric considerations the local angle of attack may be derived by the (3.5).

$$\alpha = \sin^{-1} \left[\frac{\cos \theta \cos \delta}{\sqrt{(X - \sin \theta)^2 + \cos^2 \theta \cos^2 \delta}} \right] \quad (3.5)$$

Using the blade element theory and the momentum equation for each streamtube and equating the vertical variation of the induced-drag coefficient of the rotor, one finds the (3.6)

$$f_{up} u = \pi \eta (1 - u) \quad (3.6)$$

where $\eta = r/R$ and the upstream wind function, that characterize the first half-cycle, f_{up} is given by (3.7).

$$f_{up} = \frac{Nc}{8\pi R} \int_{-\pi/2}^{\pi/2} \left(C_N \frac{\cos \theta}{|\cos \theta|} - C_T \frac{\sin \theta}{|\cos \theta| \cos \delta} \right) \left(\frac{W}{V} \right)^2 d\theta \quad (3.7)$$

The blade section normal and tangential force coefficients, C_N and C_T , are calculated from the lift and drag coefficients that are interpolated using a database according to the local Reynolds number and AoA. This first half-cycle aerodynamic condition of the airfoil can be derived solving the equations (3.4) and (3.5). However the estimation of V (3.1) and V_e (3.2) are subordinated to the estimation of the u factor by the implicit solution of the (3.6) and (3.7).

Therefore the local relative velocity for the downstream half-cycle of the rotor, $-3\pi/2 \leq \theta \leq 3\pi/2$, is calculated from the (3.8)

$$W'^2 = V'^2 \left[(X' - \sin \theta)^2 + \cos^2 \theta \cos^2 \delta \right] \quad (3.8)$$

and the local angle of attack may be derived from (3.9).

$$\alpha' = \sin^{-1} \left[\frac{\cos \theta \cos \delta}{\sqrt{(X' - \sin \theta)^2 + \cos^2 \theta \cos^2 \delta}} \right] \quad (3.9)$$

The induced velocity in this part of the rotor V' is a function of both upstream (u) and downstream (u') interference factors and with the condition of continuity the velocity components can be obtained in terms of the other velocity at each level of the rotor.

Following the same logic used for the upwind half of the rotor, consider now the equilibrium induced velocity V_e (3.2) as the input condition of the flow in the downstream region. The iterative process is initialized by $u' = u$ where u is the final value for the upwind

part of the rotor at each level. The implicit equation which contains the interference downstream factor u' becomes

$$f_{down} u' = \pi \eta (1 - u') \quad (3.10)$$

and the induced velocity V' can be written using equations (3.3) and (3.10)

$$V' = \pi \eta (2u - 1) V_{\infty i} / (f_{down} + \pi \eta) \quad (3.11)$$

where the downwind function f_{down} has the expression (3.12).

$$f_{down} = \frac{Nc}{8\pi R} \int_{\pi/2}^{3\pi/2} \left(C_N' \frac{\cos \theta}{|\cos \theta|} - C_T' \frac{\sin \theta}{|\cos \theta| \cos \delta} \right) \left(\frac{W'}{V'} \right)^2 d\theta \quad (3.12)$$

The set of equation (3.11) and (3.12) has to be solved again implicitly to find the u' .

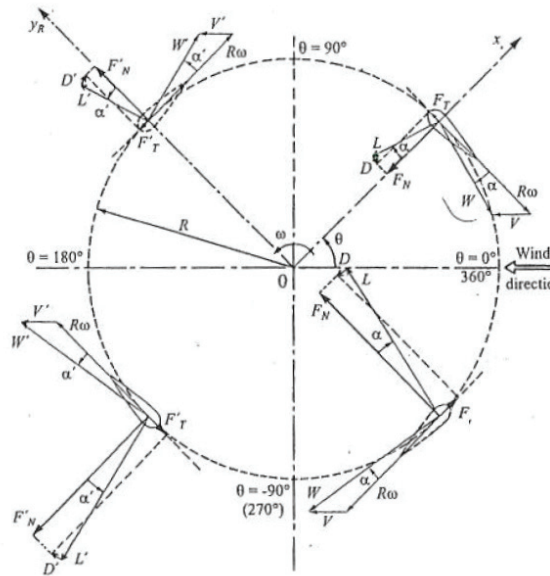


Figure 3.3: velocity and AoA for different angular positions of a rotating airfoil

This aerodynamic model, known as Paraschivoiu Double Streamtube (DS) model, allows us to build up a mathematical model able to give the aerodynamic condition of the wind

turbine airfoil in each angular position during the revolution. Moreover the forces prediction can be considered reliable if there is good knowledge of aerodynamic coefficients, to be implemented into equations (3.7) and (3.12) to estimate the C_N and C_T coefficients. The aerodynamic coefficients of the airfoil can be obtained in many different way (e.g. inviscid approach, experimental database, XFOIL, CFD simulations etc.) but it is important to consider that a large range of AoA is normally experienced by a rotating airfoil (especially in off-design conditions) and that they depend by the oscillatory behavior of the airfoil itself. This last consideration is very important because it means that this approach cannot work stand-alone, but it needs to be coupled with a technique for the evaluation of unsteady aerodynamic coefficients of the airfoil, that will be discussed in the next paragraph.

3.1.2 Unsteady Aerodynamics: the Beddoes-Leishman Model

The unsteady lift on a symmetric airfoil performing harmonic pitch and harmonic variations of asymptotic speed of small amplitude in an attached flow could be approximated by Theodorsen theory [65]. The unsteady effect of vortex shedding due to changes in circulation could be calculated assuming the airfoil infinitely thin and a harmonic wake vorticity which travels with the free-stream velocity. Theodorsen calculated the three-quarter point downwash and Van-der-Wall and Leishman [74] concluded that for moderate frequencies all theories give the same results of Theodorsen. In this case the lift can be calculated by (3.13)

$$L = \pi\rho \frac{c^2}{4} \left(U \dot{\alpha} + \dot{U} \alpha \right) + \pi\rho c U \left(w_{3/4}(0)\phi(s) + \int_0^s \frac{dw_{3/4}}{d\sigma} \phi(s-\sigma) d\sigma \right) \quad (3.13)$$

where $(\dot{\quad})$ is the temporal derivative, c is the chord length, ρ the density of air, α the angle of attack, ϕ an indicial function, $w_{3/4}$ the downwash at three-quarter point of chord and s a non-dimensional time scale (3.14).

$$s = \frac{2}{c} \int_0^t U dt \quad (3.14)$$

The first part of (3.13) is representative of the non-circulatory part of lift, due to the acceleration of mass of air $\pi\rho c^2/4$, while the second part is a circulatory contribution representative of the memory effect of previously shed vorticity into the wake. This effect cannot be modelled analytically but it can be approached with a state-space non-linear set of equations. The memory term can be considered as an effective downwash calculated at three-quarter point (3.15)

$$w_{3/4}^{eff} = w_{3/4}(0)\phi(s) + \int_0^s \frac{dw_{3/4}}{d\sigma} \phi(s-\sigma) d\sigma \quad (3.15)$$

that integrated by part yields to (3.16).

$$w_{3/4}^{eff} = w_{3/4}(s)\phi(0) - \int_0^s w_{3/4}(\sigma) \frac{d\phi(s-\sigma)}{dt'} d\sigma \quad (3.16)$$

Considering the relation (3.14), the (3.16) can be rewritten as (3.17)

$$w_{3/4}^{eff} = w_{3/4}(t)\phi(0) - \int_0^t w_{3/4}(t') \frac{d\phi\left(\frac{2}{c} \int_{t'}^t U(\tau) d\tau\right)}{dt'} dt' \quad (3.17)$$

where t and t' are related respectively to s and σ by (3.14). The function ϕ can be approximated by (3.18)

$$\phi(s) = 1 - A_1 e^{-b_1 s} - A_2 e^{-b_2 s} \quad (3.18)$$

introducing the coefficients $A_{1,2}$ and $b_{1,2}$, that depend on the application. Substituting equation (3.18) with s expressed by (3.14) into (3.17) and differentiating respect t' yields the (3.19)

$$\frac{d\phi\left(\frac{2}{c} \int_{t'}^t U(\tau) d\tau\right)}{dt'} = -\frac{2U(t')}{c} \sum_{i=1}^2 b_i A_i e^{-b_i \frac{2}{c} \int_{t'}^t U(\tau) d\tau} \quad (3.19)$$

that substituted into (3.17) gives the (3.20)

$$w_{3/4}^{eff} = w_{3/4}(t)(1 - A_1 - A_2) + y_1(t) + y_2(t)$$

$$y_i = b_i A_i \frac{2}{c} \int_0^t w_{3/4}(t') U(t') e^{-b_i \frac{2}{c} \int_0^t U(\tau) d\tau} dt' \quad (3.20)$$

where $i=1,2$. By (3.20), differentiating respect t , we obtain that the aerodynamic state is expressed by the differential equation (3.21)

$$\dot{y}_i + b_i \frac{2U}{c} y_i = b_i A_i \frac{2U}{c} w_{3/4} \quad (3.21)$$

where, in place of $w_{3/4}$, is substituted $\alpha_{3/4}$ using the relation $w_{3/4} = U \cdot \alpha_{3/4}$, so introducing the new variable $x_i = y_i / U$, it is possible rewrite the (3.21) as (3.22).

$$\dot{x}_i + \frac{2U}{c} \left(b_i + \frac{c \dot{U}}{2U^2} \right) x_i = b_i A_i \frac{2U}{c} \alpha_{3/4} \quad (3.22)$$

Calculating the two state-variables $x_{1,2}$ is possible compute an effective angle of attack α_E and an unsteady lift coefficient for the attached flow C_l^{att} as follows

$$\alpha_E = \alpha_{3/4}(1 - A_1 - A_2) + x_1(t) + x_2(t) \quad (3.23)$$

$$C_l^{att} = 2\pi(\alpha_E - \alpha_0) + \frac{\pi c \dot{\alpha}}{2U} \quad (3.24)$$

where α_0 is the zero angle of attack due to the cambered airfoil.

The basic assumption of the Beddoes-Leishman model for trailing edge separation is that the static lift coefficient can be expressed by (3.25), which is the lift of a potential Kirchoff flow [75], [76]. In (3.25) $C_{l,\alpha}$ is the linear lift curve slope, and the function f^t is the trailing edge separation point respect to chord, like in Figure 3.4.

$$C_l^{st} = C_{l,\alpha} \left(\frac{1 + \sqrt{f^{st}(\alpha)}}{2} \right)^2 (\alpha - \alpha_0) \quad (3.25)$$

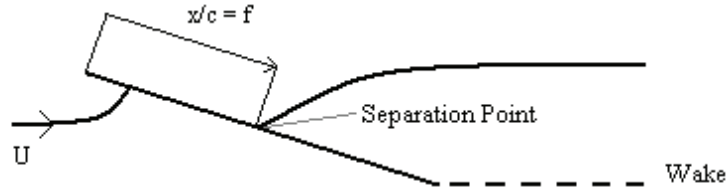


Figure 3.4: position of separation point normalized to the chord

The flow is fully attached for $f = 1$ and fully separated for $f = 0$. By knowledge of static lift curve we can express the normalized position of the separation point f as (3.26)

$$f^{st}(\alpha) = \left(2 \sqrt{\frac{C_l^{st}(\alpha)}{C_{l,\alpha}(\alpha - \alpha_0)}} - 1 \right)^2 \quad (3.26)$$

and the static lift coefficient can be expressed as linear interpolation of fully attached and fully separated coefficients (3.27)

$$C_l^{st} = C_{l,\alpha}(\alpha - \alpha_0)f^{st} + C_l^{fs}(1 - f^{st}) \quad (3.27)$$

where the fully separated coefficient is given by (3.28).

$$C_l^{fs} = \frac{C_l^{st} - C_{l,\alpha}(\alpha - \alpha_0)f^{st}}{1 - f^{st}} \quad (3.28)$$

The $f^{st}(\alpha)$ curve, calculated by (3.26), and $C_l^{fs}(\alpha)$ curve, calculated by (3.28), are provided in Figure 3.5 for a NACA 0018 airfoil, at Reynolds number equal to $2 \cdot 10^6$. The static lift coefficient curve of has been taken by the experimental database of Sheldahl, R. E. and Klimas, P. C., 1981, Sandia National Laboratories, Albuquerque, New Mexico [77].

As we can see the separation point is located at trailing edge ($f = 1$) in linear zone of lift curve, then f progressively decrease to 0, with a smooth shape curve.

The dynamic of trailing edge separation could be described with a two-state variables system of equations, assuming that the time-lag between the pressure and the lift on the airfoil, due to the unsteadiness of flow field, is modelled by (3.29)

$$\dot{x}_3 + \frac{x_3}{T_p} = \frac{C_l^{att}(t)}{T_p} \quad (3.29)$$

where $C_l^{att}(t)$ is the unsteady lift coefficient given by (3.24), and T_p is a time constant. The variable x_3 is the lift coefficient ($C_{l,x3}$) with a time-lag respect to lift coefficient for attached flow.

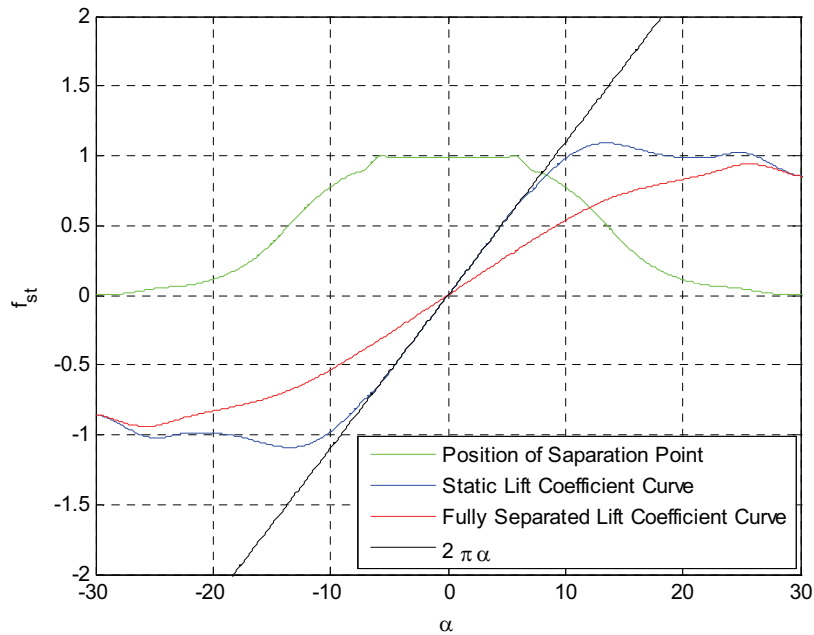


Figure 3.5: position of the separation point calculated by BL model - NACA 0018 - $Re=2 \cdot 10^6$.

By this coefficient we can determine an equivalent AoA, $\alpha_f = C_{l,x3}/C_{l,\alpha} + \alpha_0$, that we can use to calculate a quasi-steady separation point $f(\alpha_f) = f'$ by (3.26).

The second state-variable of TE separation point is due to the dynamics of boundary layer which causes the changes of the position of the separation point, and it is described by equation (3.30)

$$\dot{x}_4 + \frac{x_4}{T_f} = \frac{f'}{T_f} \quad (3.30)$$

where T_f is a time-constant of boundary layer. This fourth state-space equation closes the system of equations of BL model, and its solution allows us to determine the dynamic characteristics of lift, drag and pitch of an airfoil.

The final BL system of equations is composed by (3.22) for $i=1,2$, by (3.29) and (3.30). It appears as (3.31).

$$\left\{ \begin{array}{l} \dot{x}_1 + \frac{2U}{c} \left(b_1 + \frac{c\dot{U}}{2U^2} \right) x_1 = b_1 A_1 \frac{2U}{c} \alpha_{3/4} \\ \dot{x}_2 + \frac{2U}{c} \left(b_2 + \frac{c\dot{U}}{2U^2} \right) x_2 = b_2 A_2 \frac{2U}{c} \alpha_{3/4} \\ \dot{x}_3 + \frac{x_3}{T_p} = \frac{C_l^{att}(t)}{T_p} \\ \dot{x}_4 + \frac{x_4}{T_f} = \frac{f'}{T_f} \end{array} \right. \quad (3.31)$$

The first two equations can be solved explicitly by knowledge of asymptotic field characteristics (U , dU/dt), the model coefficients (A_1 , A_2 , b_1 , b_2), and the instantaneous lift condition. In fact the three-quarter induced angle of incidence ($\alpha_{3/4}$) can be calculated by the positioning of a vortex in the aerodynamic centre of the airfoil, which intensity is equal to total circulation of the field. Using equation (3.32) it is possible to calculate the induced velocity at three-quarter point of chord (the distance x between the aerodynamic centre and the three-quarter point is half of chord), by knowledge of circulation linked to C_l by eq. (3.33) [78].

$$\alpha_{3/4} = \tan^{-1} \left(\frac{\Gamma}{2\pi U x} \right) \quad (3.32)$$

$$\rho U \Gamma = \frac{\rho U^2}{2} c C_l \quad (3.33)$$

In the third equation of system (3.31) the C_l^{att} has to be expressed by (3.24) where α_E is given by (3.23), so it depends on the solution of the previous two equations. In last equation the right term f'' depends by the solution of the third equation by relation (3.34).

$$f'(C_{l,x3}/C_{l,\alpha} + \alpha_0) = \left(2 \sqrt{\frac{C_l^{st}(x_3/C_{l,\alpha} + \alpha_0)}{C_{l,\alpha}(x_3/C_{l,\alpha} + \alpha_0 - \alpha_0)} - 1} \right)^2 \quad (3.34)$$

The final formulation of the system is (3.35)

$$\left\{ \begin{array}{l} \dot{x}_1 + \frac{2U}{c} \left(b_1 + \frac{c\dot{U}}{2U^2} \right) x_1 = b_1 A_1 \frac{2U}{c} \tan^{-1} \left(\frac{C_l}{2\pi} \right) \\ \dot{x}_2 + \frac{2U}{c} \left(b_2 + \frac{c\dot{U}}{2U^2} \right) x_2 = b_2 A_2 \frac{2U}{c} \tan^{-1} \left(\frac{C_l}{2\pi} \right) \\ \dot{x}_3 + \frac{x_3}{T_p} = \frac{C_{l,\alpha} \left(\tan^{-1} \left(\frac{C_l}{2\pi} \right) (1 - A_1 - A_2) + x_1 + x_2 - \alpha_0 \right) + \pi \frac{c}{2U} \dot{\alpha}}{T_p} \\ \dot{x}_4 + \frac{x_4}{T_f} = \frac{\left(2 \sqrt{\frac{C_l^{st}(x_3/C_{l,\alpha} + \alpha_0)}{C_{l,\alpha}(x_3/C_{l,\alpha} + \alpha_0 - \alpha_0)} - 1} \right)^2}{T_f} \end{array} \right. \quad (3.35)$$

that is a closed set of coupled non-linear ordinary differential equations (ODEs).

The unsteady lift coefficient is given by the composition of (3.24) and (3.27) and is expressed by (3.36)

$$C_l^{Dyn} = C_{l,\alpha} (\alpha_E - \alpha_0) x_4 + C_l^{fs} (\alpha_E) (1 - x_4) + \pi \frac{c}{2U} \dot{\alpha} \quad (3.36)$$

and the drag coefficient is given by (3.37)

$$C_d^{Dyn} = C_d^{st}(\alpha_E) + C_l^{Dyn}(\alpha - \alpha_E) + (C_d^{st}(\alpha_E) - C_{d0}) \left(\frac{\sqrt{f^{st}(\alpha_E)} - \sqrt{x_4}}{2} - \frac{f^{st}(\alpha_E) - x_4}{2} \right) \quad (3.37)$$

where C_d^{st} is the static drag coefficient of airfoil. Finally, the pitch coefficient is given by (3.38)

$$C_m^{Dyn} = C_m^{st}(\alpha_E) + C_l^{Dyn} \left(a(x_4) - a(f^{st}(\alpha_E)) \right) - \frac{c\pi}{4U} \dot{\alpha} \quad (3.38)$$

where C_m^{st} is the static pitch coefficient of the airfoil and a is given by (3.39)

$$a = \frac{C_m^{st} - C_{m0}}{C_l^{st}} \quad (3.39)$$

and $C_{m,0}$ is the pitch coefficient at zero AoA.

3.2 Aerodynamic Simulation of VAWT

In this paragraph an overview of simulation techniques adopted for VAWT are provided. Basically simulations have been performed with a CFD approach, based on URANS - Sliding Mesh technique, and with the Paraschivoiu Double Streamtube – Beddoes-Leishman (DS-BL) approach. In particular these two approaches have been coupled and implemented into a numerical tool, the Wind Turbine Simulation Package (WTSP), to be applied to perform simulations tailored on experimental data sets.

A particular attention is focused on the numerical coupling of these methodologies and on the numerical schemes adopted. Moreover comparison between experimental, CFD and WTSP results are provided.

3.2.1 Integrated DS-BL Approach to VAWT

The Wind Turbine Simulator Package (WTSP) has been built in MATLAB[®] in order to implement the coupled DS-BL approach for the simulation of VAWT.

The overall structure of the tool is given in Figure 3.6, while a more detailed block diagram is provided in Figure 3.7.

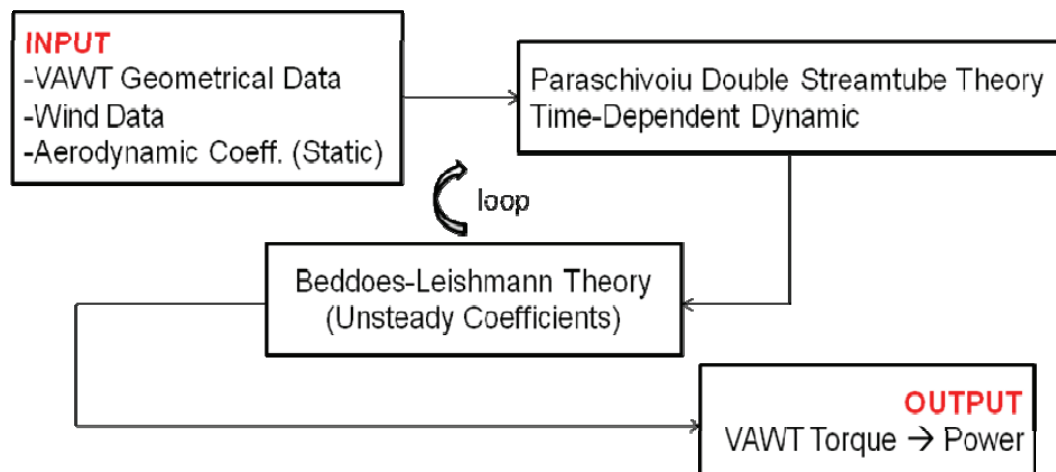


Figure 3.6: overall structure of DS-BL implementation into WTSP tool

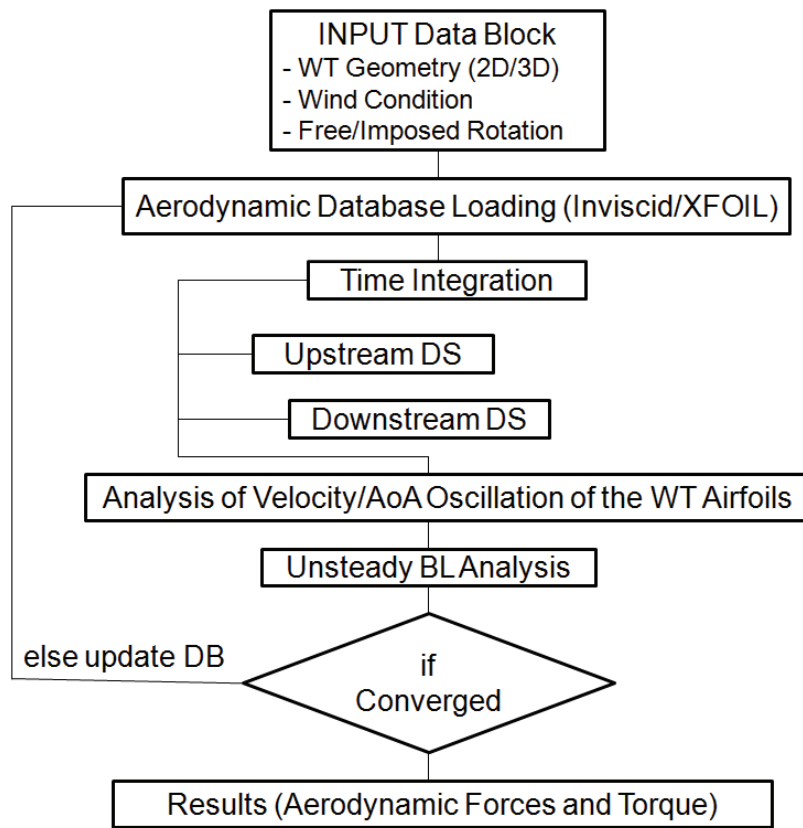


Figure 3.7: WTSP block diagram

The tool consists basically of 4 modules:

- Input data loading module: input of the geometrical data, wind conditions and static aerodynamic coefficients database. It is used a XFOIL database containing lift and drag coefficients from -30 to +30 deg of AoA, from Reynolds number $2 \cdot 10^5$ to 10^7 .
- Time integration module: the tool performs a time-advancement routine for estimation of dynamic behavior of the turbine. It implements the DS methodology and receives the feedback and the aerodynamic coefficients corrections from the BL module. It can work with imposed or free rotational velocities.
- BL module: it imports the velocity and AoA time-histories from the DS module to estimate the corrected non-stationary lift and drag coefficients.
- Output visualization module: it visualizes simulation results, providing time-histories of turbine power, normal and tangential forces on blade, rotational velocity, blade velocity and blade AoA.

Time integration into DS and BL modules can be performed with the three different schemes implemented: the explicit Euler Forward Scheme [79], [80] and two implicit predictor-corrector schemes, the Heun [79], [80] and the Adams-Bashfort-Moulton [81]. The implicit solution of DS equations for upwind-downwind induced velocity components is approached with the false position method [82], [83] providing fast convergence of the solution. In order to show how this scheme works induced velocity components calculated by the DS module and the number of iterations needed to reach convergence of induced components with residuals order of magnitude equal to 10^{-9} are provided in Figure 3.8.

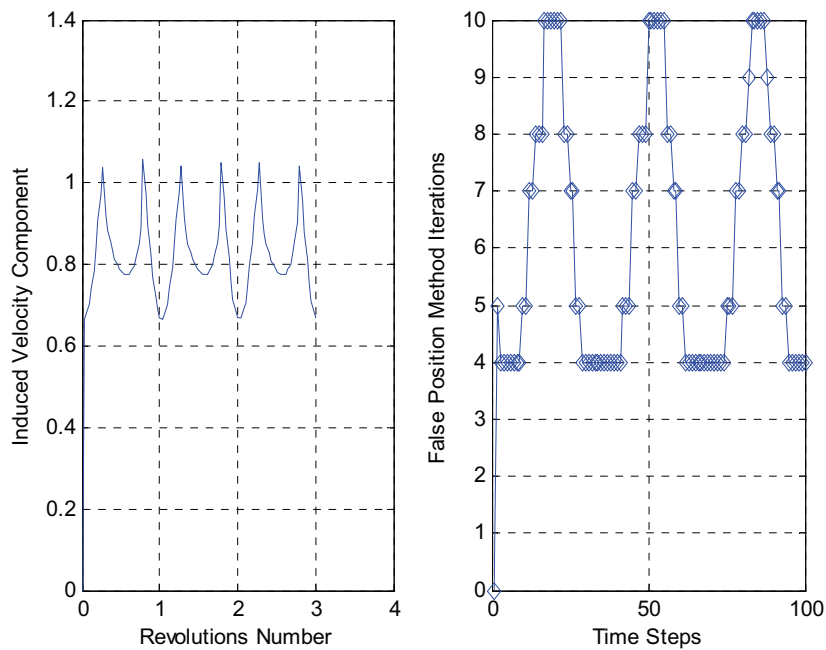


Figure 3.8: DS Induced velocity components convergence.

Final value (left) – False position method iterations number per time-step with residual magnitude in the order of 10^{-9} (right)

BL method convergence is monitored by measuring the residual magnitude of aerodynamic coefficients calculated by equation (3.40). It provides the error estimation measured in the i -th cycle scaled on the first cycle, for the lift coefficient. Convergence is reached when E_i becomes equal or less than 10^{-15} .

$$E_i = \frac{\left| \sum_{\text{Cycle } i+1} C_l^{Dyn} \right| - \left| \sum_{\text{Cycle } i} C_l^{Dyn} \right|}{\left| \sum_{\text{First Cycle}} C_l^{Dyn} \right|} \quad (3.40)$$

The coefficients of the BL method were taken by [73] as function of airfoil thickness, with a linear interpolation between the values provided in Table 3.1 for $A_{1,2}$ and $b_{1,2}$, while the time-constants T_f and T_p were supposed both equal to the period of oscillation of the pitch angle.

	A_1	A_2	b_1	b_2
Flat Plate	0.165	0.335	0.0455	0.3000
24% thickness Airfoil	0.294	0.331	0.0664	0.3266

Table 3.1: Beddoes-Leishman methodology coefficients

To give an idea of the simulation process implemented into the WTSP three snapshots of the output of the software are provided in Figure 3.9. The first one (top) is a plot of the aerodynamic XFOIL database, the second one (mid) is a plot of oscillations of velocity and AoA on the airfoil during the rotation based on the static aerodynamic coefficients, while the last one (bottom) is the correction of lift and drag coefficients calculated by the BL theory for the oscillations mentioned above. It is remarkable that the drag coefficient seems to be affected by a larger correction than the lift coefficient. However, as the lift coefficient is much higher than the drag one, the effect of drag on rotational dynamic is really small. These can be also seen by loading the inviscid database ($C_l = 2\pi\alpha$, $C_d = 0$), whose results on VAWT appear to be quite similar to the XFOIL results. Moreover also a stand-alone simulation of the BL approach has been performed, in order to validate the methodology and compare results with other approaches. The BL approach was used for the simulation of the oscillation of a NACA 0018 airfoil with a symmetrical imposed oscillation around 0 deg with 6 deg of amplitude (from +3 deg to -3 deg) and 0.5 Hz of frequency.

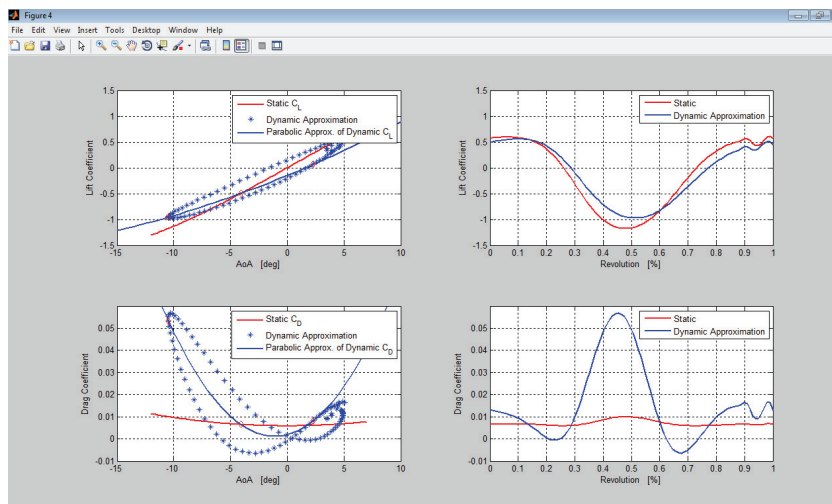
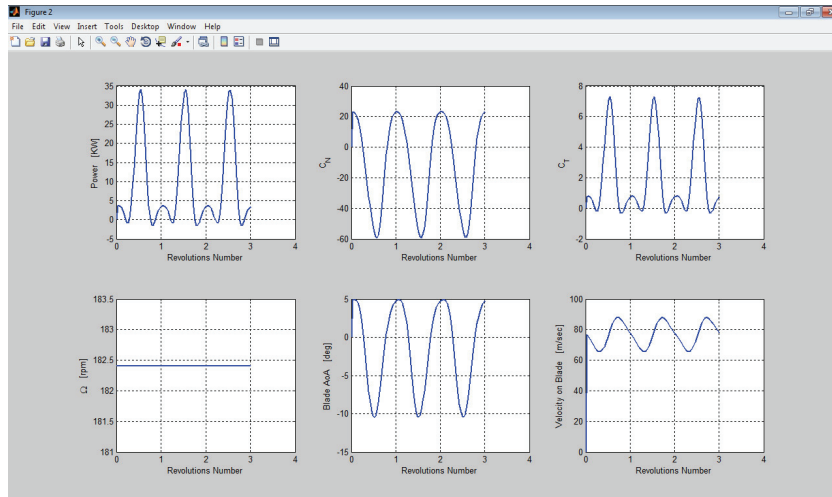
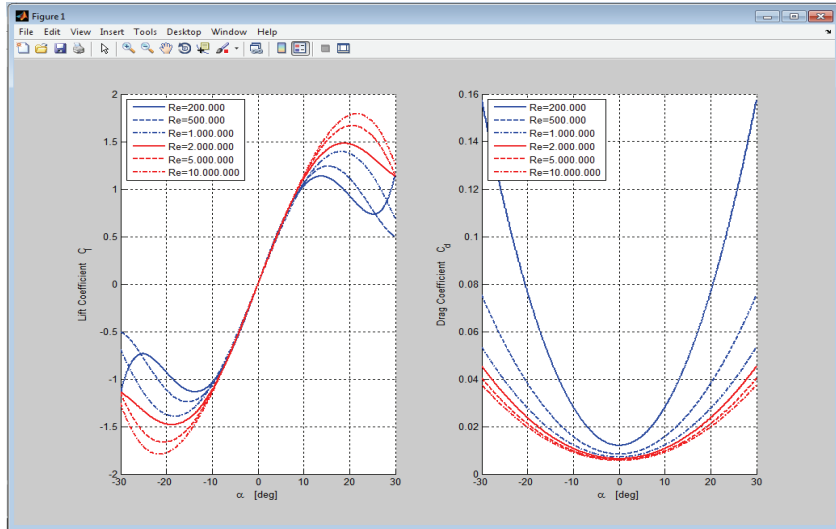


Figure 3.9: WTSP snapshots

XFOIL aerodynamic database (top)
 DS velocity and AoA airfoil oscillations (mid)
 BL unsteady hysteretic aerodynamic coefficients (bottom)

These values have been chosen as they are in the typical range of interest for VAWT applications. Airfoil chord has been taken equal to 0.8 meters and Reynolds number equal to $1.1 \cdot 10^6$.

Results were compared with URANS solution, calculated with ANSYS-FLUENT[®] and an unsteady panel solution calculated with CMARC[®].

The computational grid used for URANS simulation was a grid made by 150 KCells (Figure 3.10) designed to provide $y^+ < 1$ for the tested conditions. The simulation was performed with URANS approach and $k-\omega$ SST turbulence model, coupled with moving mesh approach to impose the oscillation. A comparison of results achieved with the BL, URANS and Unsteady Panels approaches are provided in Figure 3.11, showing a general agreement between these 3 methodologies. In particular the result achieved for the drag coefficient is interesting, as it is largely affected by the hysteresis and seems to be quite well modeled by the BL compared with the URANS solution. However, as stated above, its effect on the overall dynamic behavior of the WT is rather small.

In Figure 3.12 the plot of the residuals for power, normal and tangential forces estimated by WTSP for a typical run are provided. It is important to highlight that the simulation does not reach a real convergence but residual magnitude oscillates around the mean value of 10^{-3} .

This is a consequence of the fact that the velocity and AoA time histories calculated by the DS method generate modified aerodynamic coefficients which generate again modified time histories. So there is not a real final configuration but after 5-6 cycles the solution does not significantly change anymore.

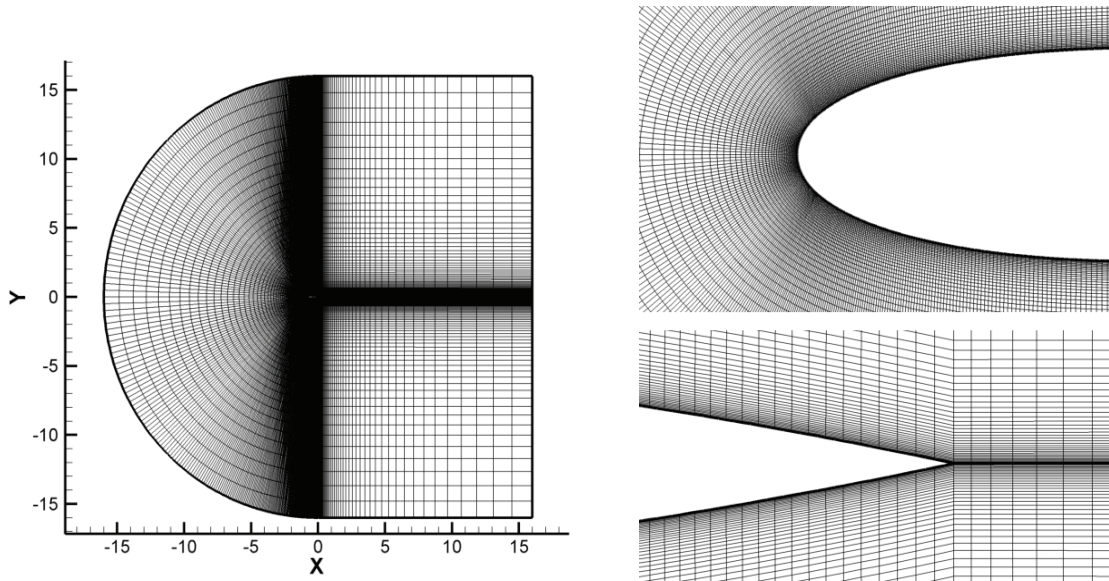


Figure 3.10: NACA 0018 - Computational grid details
Computational domain (left) – Leading edge and trailing edge details (right)

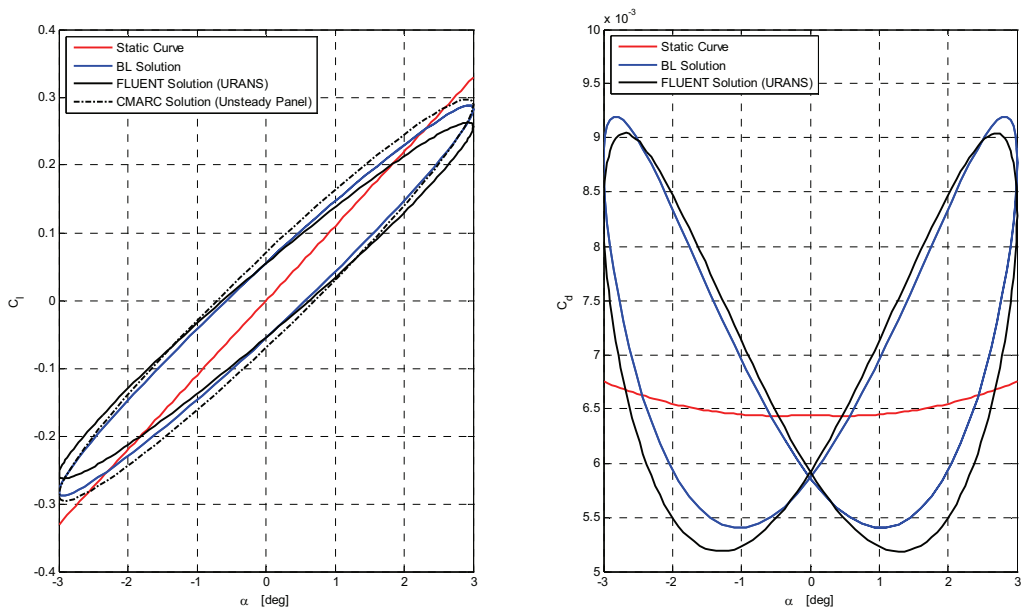


Figure 3.11: BL unsteady lift and drag coefficients vs CMARC vs FLUENT prediction
NACA 0018 airfoil in symmetrical oscillation around 0 deg
oscillation amplitude = 6deg, oscillation frequency = 0.5 Hz, $Re = 1.1 \cdot 10^6$

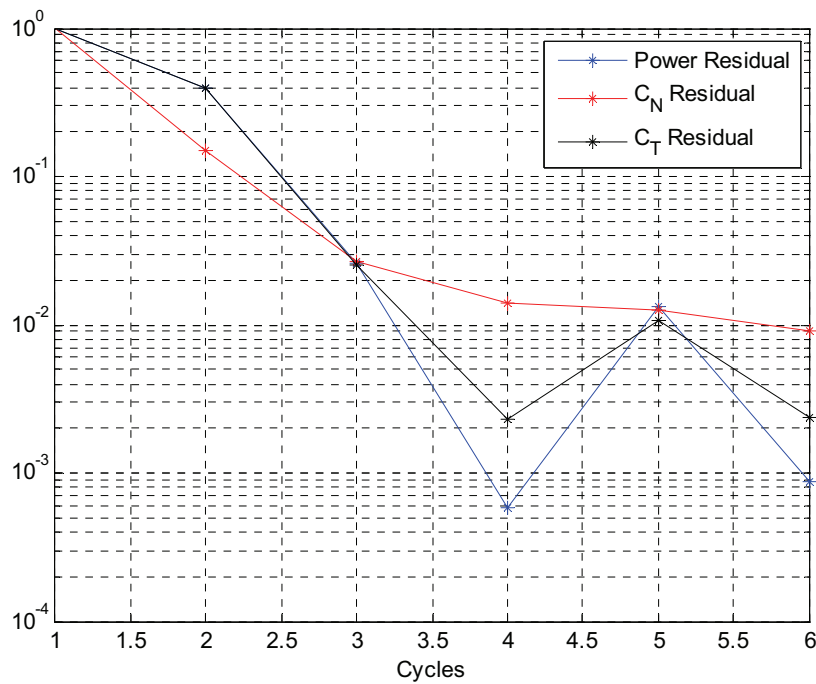


Figure 3.12: WTSP residuals for estimated power, normal and tangential forces

3.2.2 CFD Approach to VAWT

The problem of VAWT simulation was approached also by CFD modelling. The approached geometry is a single blade VAWT [85], consisting of a NACA 0015 airfoil, made for experimental tests. Further details about the experimental set-up will be provided later.

The problem was modeled with a 2D approach based on a circular domain centered in the rotation axis with the far field located at 150 chords of distance. The domain is filled by 67K structured cells organized in 3 sub-domains:

- The external domain (fixed, 19KCells, Figure 3.13 – left)
- The intermediate domain (sliding, 11KCells, Figure 3.13 – right)
- The inner domain (sliding-dynamic, 37KCells, Figure 3.13 – right)

This approach was chosen in order to build a computational grid designed for two objectives: the simulation of the blade rotation and the possibility to change the angular setting of the airfoil for dynamic optimization design purposes.

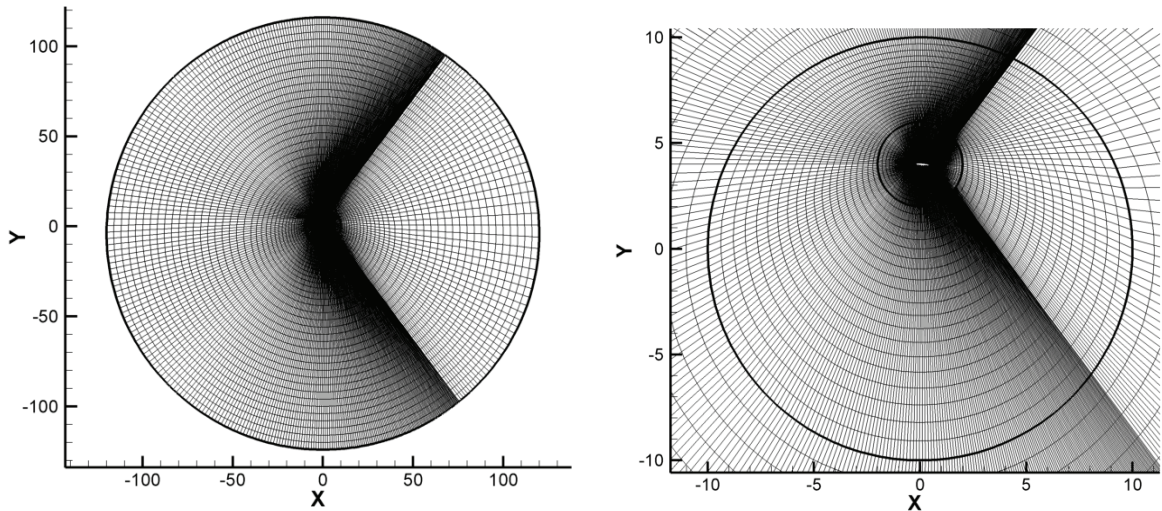


Figure 3.13: single blade VAWT computational grid.
External domain (left) – Intermediate/inner domain (right)

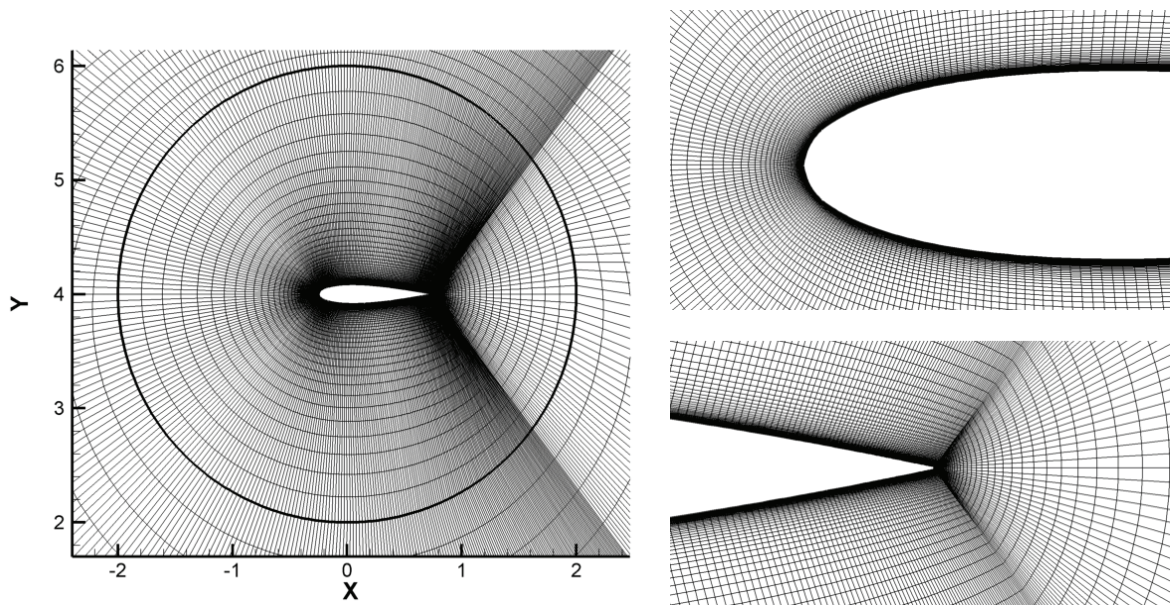


Figure 3.14: single blade VAWT computational grid.
Inner domain (left) – Leading edge/blunt trailing edge airfoil details (right)

Further pictures of the computational grid are provided in Figure 3.14, where details of the inner mesh, the leading edge and the trailing edge are provided.

Moreover the grid is designed to provide a wall $y^+ < 1$ on the airfoil surface for Reynolds number on the range of interest for the simulation performed. The inner domain is centered in the airfoil $\frac{1}{4}$ chord point in order to rotate the blade.

Three UDFs were designed to be coupled with this mesh:

- C_F.c
- g_mot_osc.c, g_mot_osc_1.c

The first one is able to follow the airfoil during the rotation and calculate the instantaneous normal and the tangential force coefficients provided in (3.43) and (3.44), while the second and the third one are able to move the faces and the cells of inner mesh during the rotation in order to simulate an imposed pitching motion of the blade.

This approach has been applied for investigations about optimized control criteria for pitching blade VAWT applications.

3.3 Experimental VAWT Test-Case

The DS-BL and the CFD approaches described in the previous paragraph have been used for the simulation of an experimental VAWT test-case, tailored on the test campaign performed in the frame of a wide research project carried out in the Sandia National Laboratories (Albuquerque, New-Mexico) and the United States Department of Energy in the 1980s [85]. In the paragraphs 3.3.1 the geometry and the experimental data available will be provided while in paragraph 3.3.2 the results achieved with the different computational methodologies will be discussed.

Furthermore in the paragraph 3.3.3 the possibility to optimize the VAWT with a static blade pitching asset or by dynamic pitching control criteria will be investigated and some preliminary results provided. However the topic of VAWT aerodynamic optimization seems to have a great potential also for its applicability on the industrial side but here the problem is just approached and it needs of further and deeper investigations.

3.3.1 Geometry and Experimental Data

The experimental test case adopted for the performed simulations is based on the work of *Strickland et Al.* [85] and it will be described only briefly herein. In general a straight-one-bladed rotor with a NACA 0015 airfoil was built and operated in a water tow tank with a depth of 1.25 meters, a width of 5 meters and a length of 10 meters. The rotor blade was extended to 15 cm to tank bottom. This experimental set-up allowed reproducing with a chord length of 15.24 cm, a diameter of 1.22 meters and a rotor tip speed of 45.7 cm/sec a chord based Reynolds number equal to 67K.

Three towing speed equal to 18.3 cm/sec, 9.1 cm/sec and 6.1 cm/sec were chosen to achieve a tip-to-wind speed ration equal to 2.5, 5.0 and 7.5 respectively. The chord to radius ratio was equal to 0.25.

Pressure measurements were made on both sides of the airfoil at five chord locations (1.7, 4.2, 10, 36 and 81% of chord) and in a span position equal to 30 cm below the water surface. Data repeatability was made performing at least 5 runs for each tested condition. Pressure signal was acquired with a frequency of 1 KHz (with a rotational frequency of 0.12Hz) and

stored on a magnetic tape cartridge. The analog-to-digit conversion was made by the HP6940B digital converter, and signals were analyzed by a desktop PC.

Pressure data were used in order to estimate the pressure coefficient for different angular positions according to (3.41)

$$C_p = \frac{P - P_\infty}{1/2 \rho_\infty U_b^2} \quad (3.41)$$

where it is valid the vectorial sum (3.42).

$$\underline{U}_b = \underline{U}_T + \underline{U}_\infty \quad (3.42)$$

Here the velocities \underline{U}_T and \underline{U}_∞ are the blade tangential and wind velocities, respectively. The pressure P_∞ is the static pressure measured at pressure taps, and the normal and tangential forces coefficients are obtained by integrating the pressure coefficient C_p by a second order polynomial fit according to the (3.43) and (3.44).

$$C_N = \frac{F_N}{1/2 \rho_\infty C U_\infty^2} \quad (3.43)$$

$$C_T = \frac{F_T}{1/2 \rho_\infty C U_\infty^2} \quad (3.44)$$

Measurements of normal and tangential forces were made also using strain gage instrumentation. The two forces were measured using strain gages located on a support mounted at the mid of the chord, and each bridge was arranged to be sensitive only to the desired force. It consisted of 8 350-Ohm strain gages making up two Wheatstone bridge configurations, powered by a 15 vdc Calex supply and amplified by a Calex 176 amplifier and a Krohnite 3343 low pass filter. A 15 vdc signal is applied to the bridge and the unbalanced output voltage was amplified approximately 1000 times to increase the voltage level into the desired range. Therefore it was filtered at a cut-off frequency equal to 0.6 Hz, in order to eliminate the mechanical noise located approximately a 2 Hz. The effect of centrifugal force was dropped off, nevertheless it is small, as well the effects of finite blade (e.g. induced drag

and lift) were canceled according to Graham [100]. A sketch of experimental set-up with pressure takes and strain gages is provided in Figure 3.15.

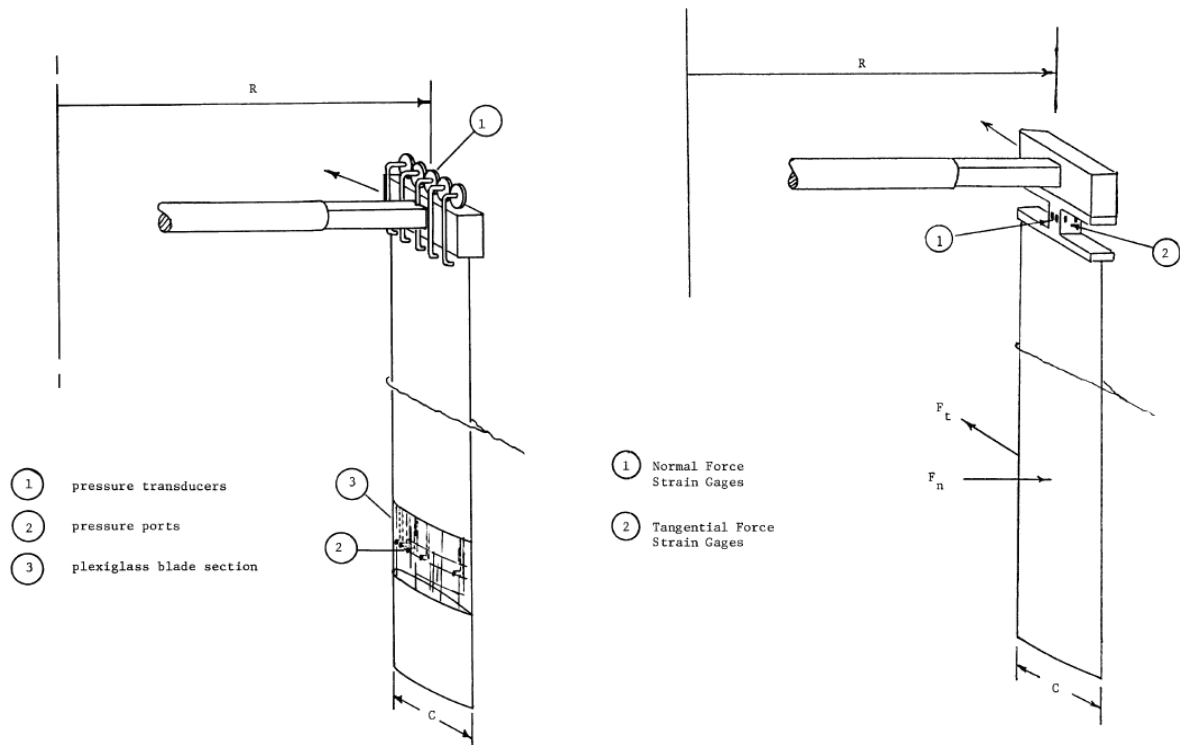


Figure 3.15: single blade VAWT, experimental set-up sketch
Pressure takes instrumented blade (right), strain gages instrumented blade (left)

3.3.2 Simulations and Results

In this paragraph the results of simulations of the single-blade VAWT are provided. Experimental set-up has been described in the previous paragraph and the geometry has been tested for 3 different experimental conditions, changing the Tip Speed Ratio (TSR).

TSR values of experimental reference [85] have been reproduced on a bigger geometry, with a blade chord size equal to 1 meter and a radius equal to 4 meters. The two experimental sets refer respectively to Pressure-Takes (PT) and Strain-Gages (SG). Wind speed has been assumed equal to 10 m/sec, and rotational speed was changed from a minimum of 60 rpm to a maximum of 182.4 rpm to reproduce the same TSR conditions of the experimental reference.

Simulations were performed with the commercial software ANSYS-FLUENT[®] [23] [24], with a URANS model coupled with a moving-mesh approach. Furthermore for the pitching oscillations of the blade for optimization purposes also a dynamic mesh approach was used.

1-Blade VAWT – NACA 0018 Airfoil – Radius = 4 m – Chord = 1 m				
Configuration ID	Wind Speed [m/sec]	Rotational Speed [rpm]	TSR	Reynolds Number (based on Tip Speed)
1	10	60	2.5	$1.7 \cdot 10^6$
2	10	120	5	$3.4 \cdot 10^6$
3	10	182.4	7.6	$5.2 \cdot 10^6$

Table 3.2: VAWT CFD test conditions

In Table 3.3 a summary of CFD solver settings is provided, while in Figure 3.16 the normal and tangential force coefficients time histories predicted by CFD for the TSR = 2.5 case are provided.

P-V Coupling	Density-Based 2 nd order transient implicit (Roe-FDS flux type)
Turbulence Model	$k-\omega$ SST
Flow spatial discretization	2 nd order
$k-\omega$ transport scheme	2 nd order
Blade Rotation	Moving Mesh
Blade Pitch	Dynamic Mesh

Table 3.3: summary of CFD solver setting for VAWT simulation

Convergence was monitored looking at the force coefficients time histories over different revolutions and reached in a few cycles (about 4/5) for all TSR conditions tested. Looking at the Figure 3.16 it is clear how there is rather no difference between the third and the fourth cycle for both normal and tangential forces coefficients.

From Figure 3.17 to 3.19 CFD simulations results are provided for TSR equal to 2.5, 5 and 7.6 respectively.

In general it is remarkable that CFD results match quite well with experimental data in particular for normal force coefficient, while some discrepancies are found for tangential coefficients. However it important to highlight that the C_N is approximately one order of magnitude higher than the C_T , and this influences the results accuracy.

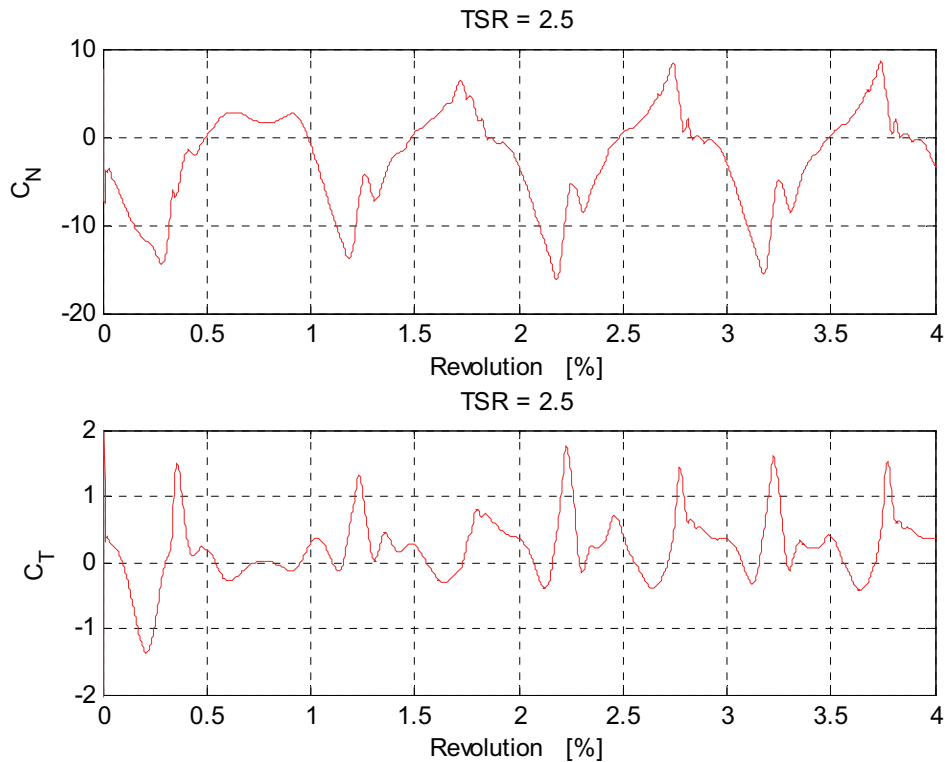


Figure 3.16: single blade VAWT CFD normal and tangential forces predictions for $TSR = 2.5$

Furthermore the C_T depends by drag coefficient, that is usually more sensitive to numerical errors and it is important to take into account that, especially for this coefficient, also discrepancies between the two sets of experimental data are found.

In figure 3.20 the comparison between the experimental data and the WTSP are provided, showing the results of the DS theory stand-alone (black line) and the results of the DS-WT integration (red line) for the $TSR 7.6$ case.

Looking at the DS results it is possible to see how forces are overestimated. This behavior can be ascribed by the fact that in general the airfoil oscillatory motion causes a degradation of the aerodynamic performances of an airfoil. This effect can be seen in Figure 3.9 (bottom) as well in Figure 3.11, where the average gradient of lift hysteretic curve is clearly less than the gradient of the static one.

This degradation, proportional to oscillation frequency, affects the normal and tangential force coefficients reducing their magnitude and this effect is not captured by DS approach stand-alone. The improvement achieved by the BL theory integration is targeted to estimate this degradation, in order to correct the overestimation of the DS theory.

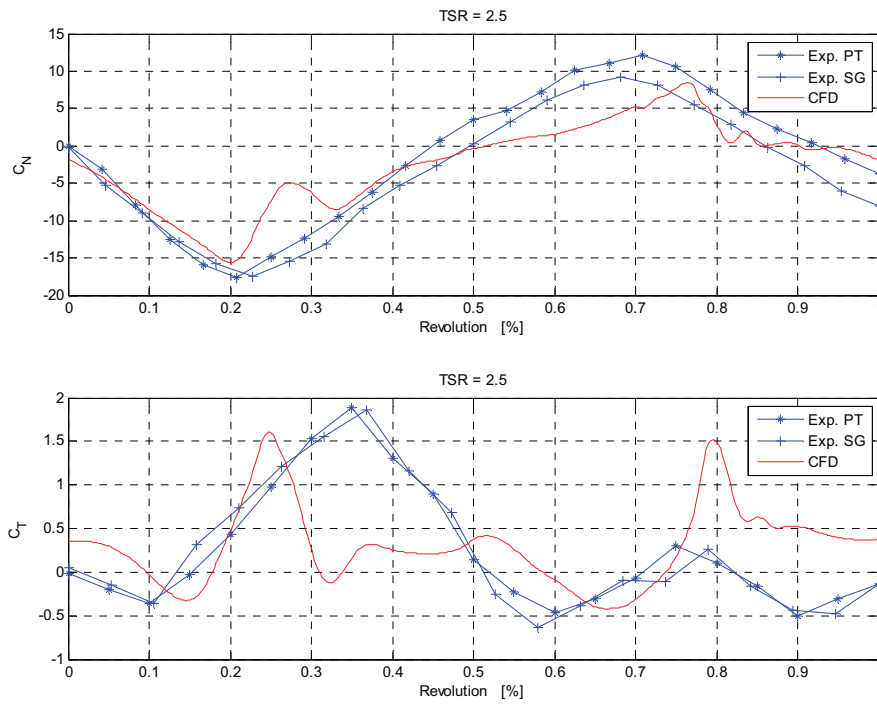


Figure 3.17: single blade VAWT CFD normal and tangential force prediction compared with experimental data for TSR = 2.5

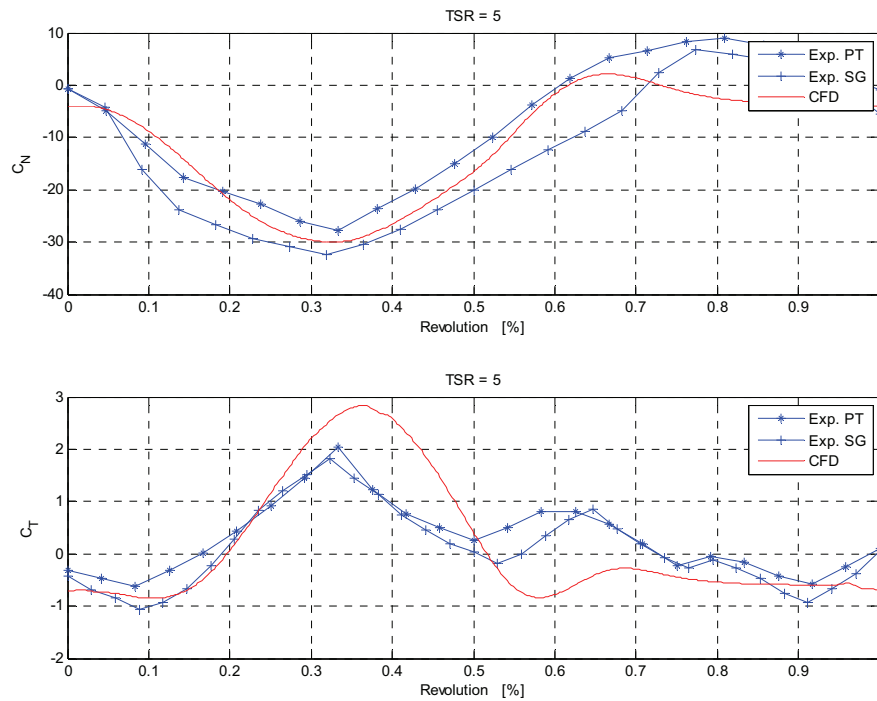


Figure 3.18: single blade VAWT CFD normal and tangential force prediction compared with experimental data for TSR = 5

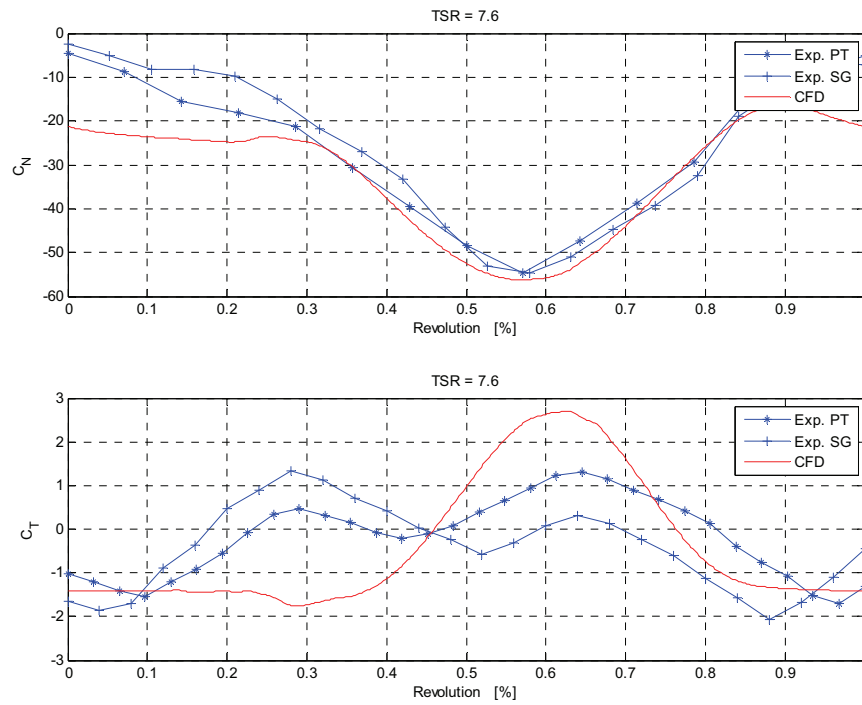


Figure 3.19: single blade VAWT CFD normal and tangential force prediction compared with experimental data for TSR = 7.6

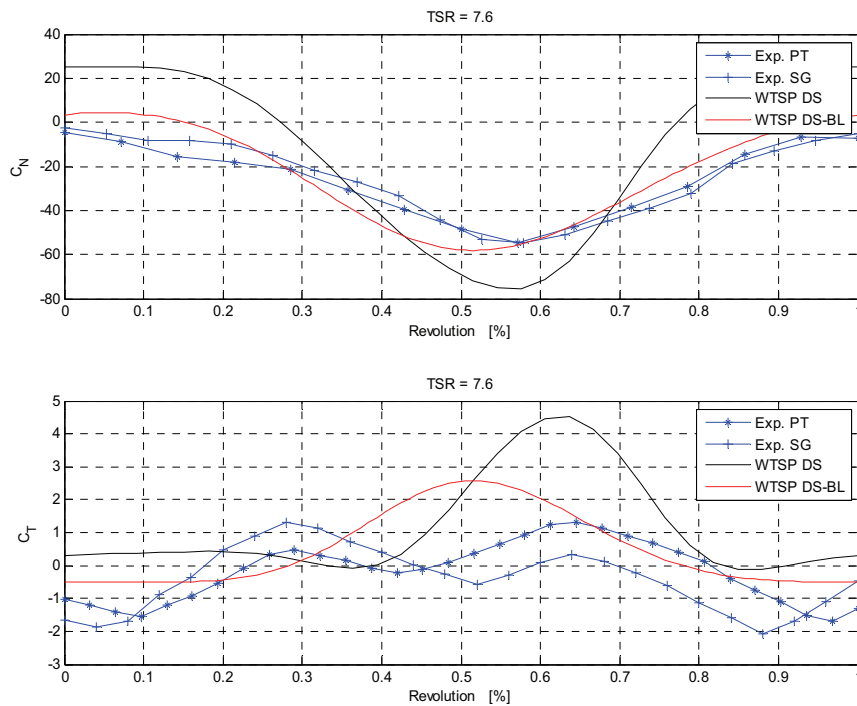


Figure 3.20: single blade VAWT WTSP normal and tangential force prediction compared with experimental data for TSR = 7.6.

The results achieved by the DS-BL approach are provided in Figure 3.20 where the improvement achieved by the integrated approach is pretty obvious, especially for the normal coefficient. However the final results are still affected by an over-estimation of coefficients, which can be ascribed to a lack of accuracy of BL method itself as to a lack of accuracy of the static coefficients database.

Moreover it is remarkable that the big discrepancy found for tangential coefficient can be strongly affected by the overestimation of lift coefficient, as the most of the force on the blade is generated by the lift component projected on the airfoil body axis. This is also confirmed by the deviation between the experimental data and the CFD results.

The integrated DS-BL methodology implemented into the WTSP seems to be an easy and reliable approach to perform the aerodynamic simulation and performance prediction of VAWT at design stage, as it is able to provide some key aerodynamic information on the flow conditions experienced by the airfoil during the revolution (e.g. blade velocity and AoA), that are not easily predictable with other methodologies. Moreover the predictions of the hysteretic performances of the blade lift and drag coefficients provide a good sensitivity of what is going on the blades and useful indications to drive the optimization and design of the turbine.

Moreover it is important to remind that if the CFD approach can be useful to simulate the WT performances it is not easy to understand the instantaneous aerodynamic behavior of the airfoil from the run post-processing. Therefore CFD approach cannot easily provide any practical information about the hysteretic behavior of the airfoils.

3.3.3 CFD Optimization for VAWT Applications

In this paragraph the problem of the CFD optimization of WT will be approached, showing some preliminary results achieved. The base test-case is the same described in the previous paragraph, and the main aim of this study is to show how CFD can be used in order to optimize VAWT power generation.

The optimization problem was approached by the simulation of different blade angular settings, and output power was estimated for each setting by the integration of aerodynamic torque over the entire revolution (3.45). The blade angular setting was defined as the angle between the airfoil chord and the horizontal direction (x-axis) of the computational domain, measured at the upper blade location (Figure 3.13).

$$P = \int_0^{2\pi} M(\theta)\Omega d\theta \quad (3.45)$$

The tested static blade settings range from -12 to +12 deg for the TSR 5 and 7.6, and results are provided respectively in Figure 3.21 and 3.22.

The power, given in the right boxes, is provided just from -6 to +9 deg of blade setting in order to show how for both cases an angular position equal to +3 deg provides a better power output performance than the 0 deg position, bringing this value from -440W to +60W for TSR equal to 5 and from -5.2KW to -4.3KW for TSR equal to 7.6.

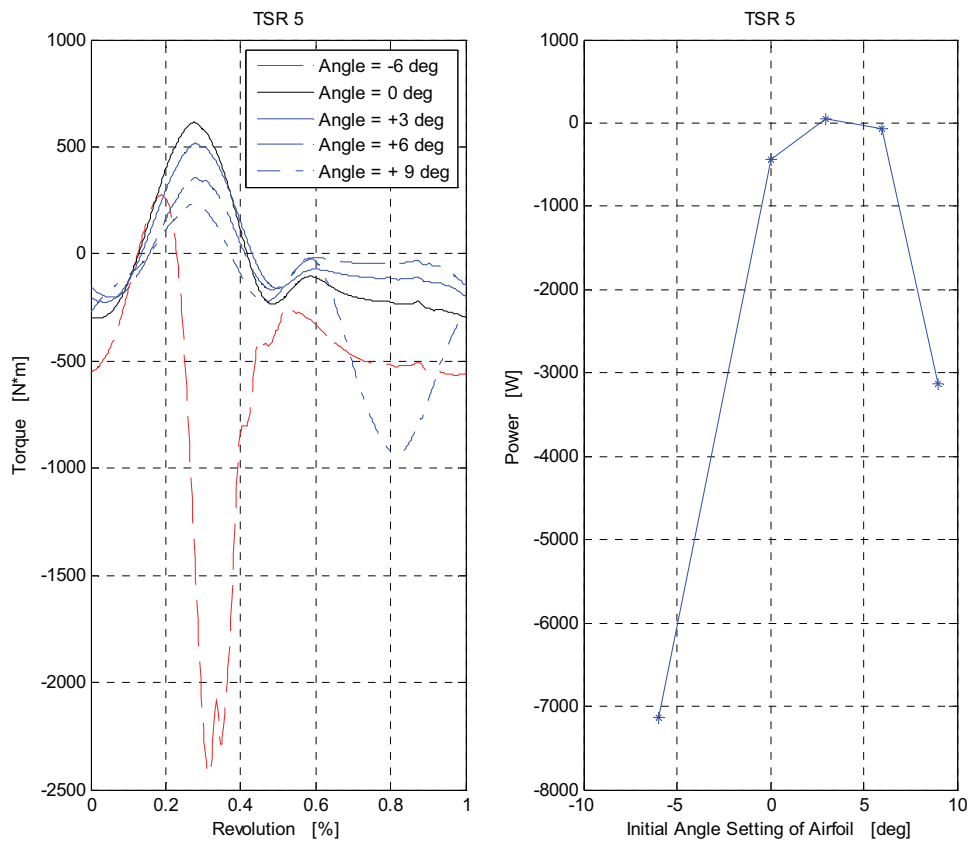


Figure 3.21: single blade VAWT CFD optimization results. Evaluation of produced power for different blade settings angle, TSR = 5

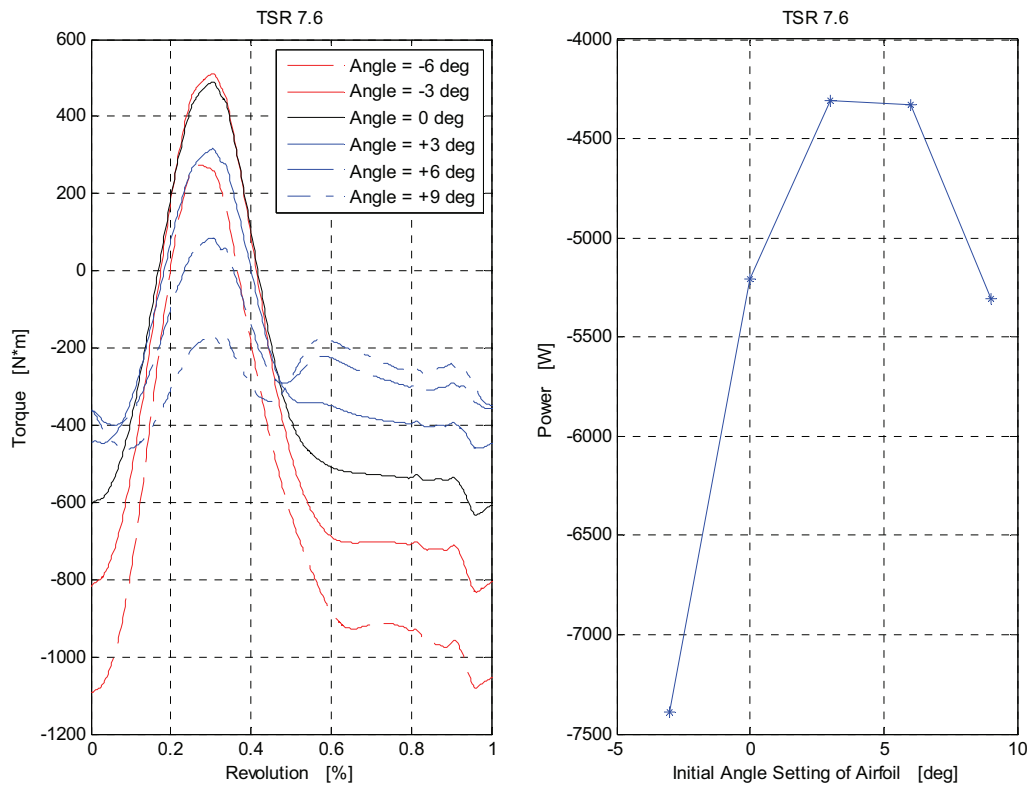


Figure 3.22: single blade VAWT CFD optimization results. Evaluation of produced power for different blade settings angle, TSR = 7.6

It is remarkable that the two configurations tested are not suitable for the energy production as in both cases the power is negative or slightly positive, but they were chosen for the availability of experimental reference data mentioned in the above paragraph.

Moreover in order to achieve a positive amount of output power generated it is mandatory take into consideration the multiple-blade case, as the downwash interference of the blades has a positive effect on the output power generation.

1-Blade VAWT – NACA 0018 Airfoil – Radius = 8 m – Chord = 1 m			
Wind Speed [m/sec]	Rotational Speed [rpm]	TSR	Reynolds Number (based on Tip Speed)
10	25	2.1	$1.5 \cdot 10^6$

Table 3.4: VAWT data for the dynamic optimization

Further investigations were also carried out taking into consideration the possibility to impose to the airfoil an oscillatory motion, in order to maximize the power output.

The oscillatory motion was imposed with a dynamic mesh approach applied to the inner circle domain, Figure 3.14 (left). The angular position of the airfoil was again identified as the angle between the airfoil chord and the horizontal direction and simulations were performed with the WT data provided in table 3.4.

For the oscillatory motion the periodic pitching law imposed is provided in Figure 3.23, while the output power results with and without imposed pitching are provided in Figure 3.24.

Results show how the imposed pitching allows achieving a big increase in WT efficiency, bringing the output power from 786W to 1303W, with a performance increase equal to 65%, proving that the dynamic pitching is able to provide a significant increase of turbine performances.

Moreover it is important to remark that the performed test is just a preliminary study and that more detailed investigations are required in order to better evaluate the strong aerodynamic non-linearity and the effect of different pitching laws.

Of course further optimization of the pitching law itself is possible, together with the implementation of the whole design process into an optimization solver, but no more investigations have been performed about this topic in the frame of this thesis.

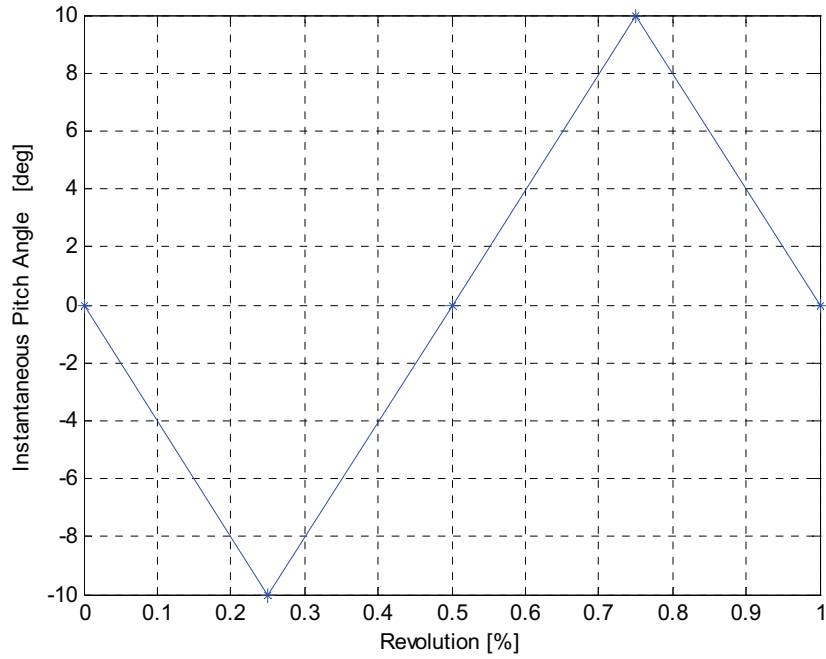


Figure 3.23: periodic pitching law for dynamic optimization of WT

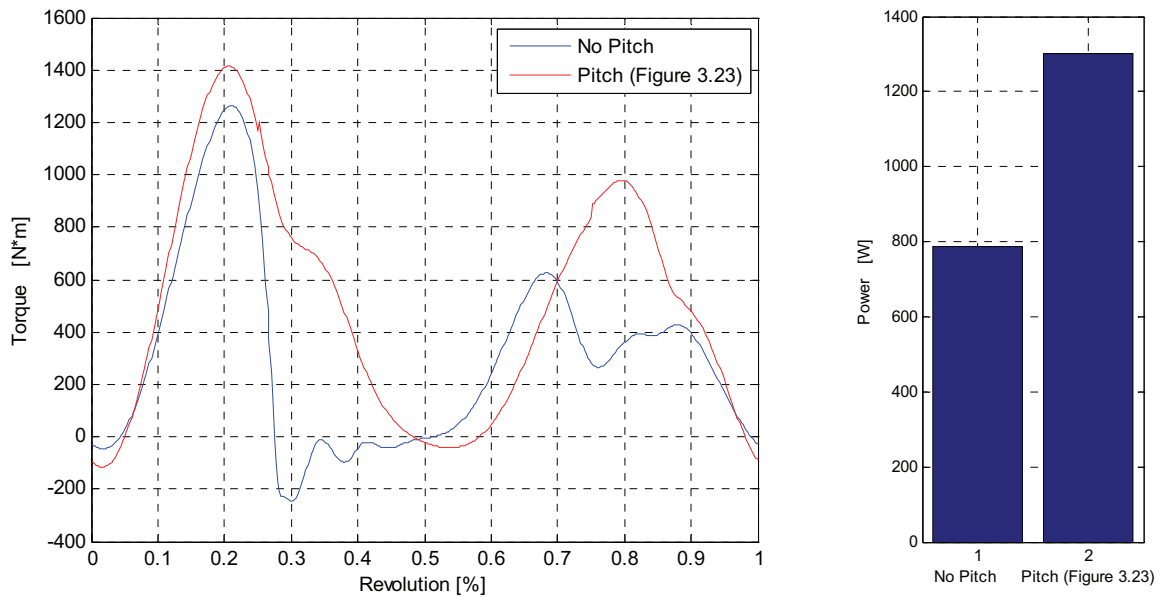


Figure 3.24: dynamic optimization results for VAWT, increase of generated power

3.4 Aeroacoustics of Wind Turbines

This paragraph concerns the aeroacoustic numerical modelling for wind turbines applications approaching the basic physical behavior of the airfoil self-generated noise.

This noise is generated by flow field fluctuations that appear on aerodynamic surfaces, where a laminar, turbulent or separated flow is developed. Each of these aerodynamic regimes can occur on a wind turbine blade and contribute with a specific noise spectrum. In this paragraph a first overview of the airfoil self-generated noise is provided according to [93], then the attention is focused on noise signal post-processing and correction techniques in order to build a tool for noise signals analysis. Moreover the main requirements of this tool are highlighted, providing all the details of the mathematical processing, from the acoustic time pressure history to the noise SPL spectrum in third octave band.

Then the attention is focused on 2 experimental data sets available in literature [93], [94] for the airfoil-self generated noise of the NACA 0012, that were used as basis for the numerical computations performed.

3.4.1 The Airfoil Self-Generated Noise

Advanced aeroacoustic simulation techniques are becoming even more important in design process of airframe components in many industrial fields from the transportation industry to the renewable energy and wind power.

In general analysis there are several mechanisms of noise generation for airframe components, related to laminar-turbulent transition and separation on aerodynamic surfaces. A first classification can be done according if the noise sources are generated by turbulent phenomena (e.g. turbulent noise) or separation phenomena (e.g. vortex shedding behind blunts bodies).

In the first case noise is distributed overall the spectrum, the so-called broadband, while in the second case noise has a tonal spectrum, with peak frequencies correlated to period of the driving phenomenon.

In particular for airfoil self-generated noise both mechanisms can occur, according to aerodynamic characteristic parameters (e.g. Reynolds and Mach numbers, Angle of Attack) or

geometrical parameters (airfoil surface roughness, trailing edge bluntness) and both of them are related themselves, as the laminar-turbulent transition affects the separation and viceversa.

A general classification of airfoil self-generated noise can be done according to [93], where 4 different mechanisms are recognized, Figure 3.25.

- Turbulent Boundary Layer – Trailing Edge noise (TBL-TE)
- Laminar Boundary Layer – Vortex Shedding noise (LBL-VS)
- Separation stall noise
- Trailing-edge bluntness noise

At high Reynolds numbers (based on chord length) and low angle of attack turbulent boundary layer develops over the most of the airfoil. Noise is produced when this turbulent boundary layer passes over the trailing edge (TBL-TE noise generation, Figure 3.25-A).

For lower Reynolds numbers and low angle of attack a large laminar boundary layer develops over airfoil surface, generating laminar instabilities waves before the transition point. These instabilities produce an unsteady pressure load together with a vortex shedding from the trailing edge, which generates a tonal noise (LBL-VS noise generation, Figure 3.25-B).

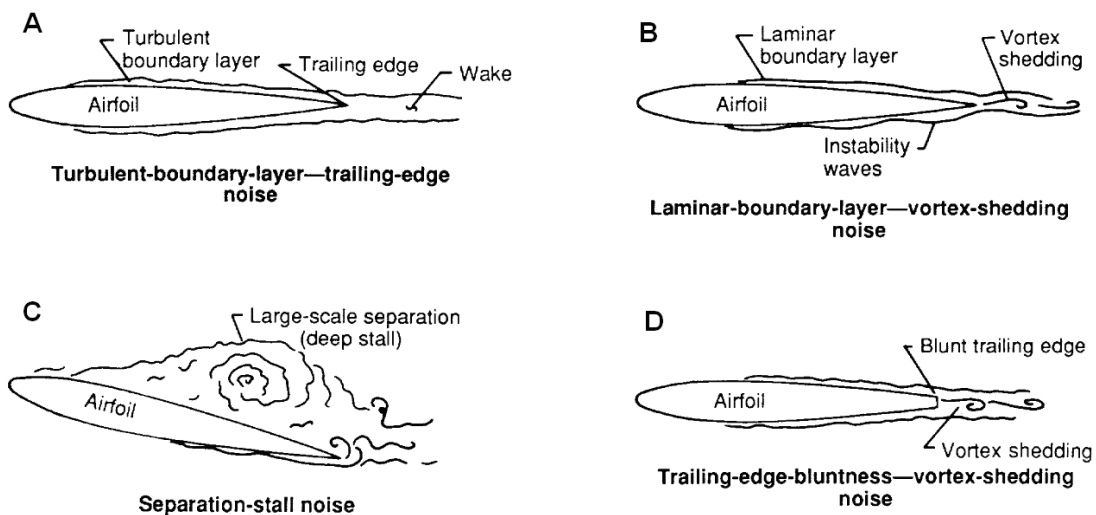


Figure 3.25: Airfoil noise generation mechanisms

For higher angle of attacks, in the pre-stall configuration, the separation point moves towards the leading edge, and the wake region is characterized by a wide separated zone. In this case a large scale vortex shedding characterizes the wake with the generation of a narrowband spectrum noise (separation-stall noise, Figure 3.25-C).

Finally the last noise generation mechanism is related to vortex shedding induced by separation over the blunt trailing edge (trailing-edge bluntness noise, Figure 3.25-D).

3.4.2 Post-Processing of Noise Pressure Data

In order to compute the noise spectrum for the CFD computations performed a MATLAB[®] post-processing tool has been designed to evaluate Sound Pressure Levels (SPL) at microphone locations. This tool is able to import the noise pressure time-history and compute automatically the Discrete Fourier Transform (DFT), the Power Spectral Density (PSD) and its SPL third octave band representation. For explanation purpose let us take a sinusoidal pressure time signal with amplitude equal to 100 Pa and frequency equal to 2000 Hz, sampled with the double of the minimum Nyquist frequency equal to 9 points per period [86], [87]. In figure 3.26 (top-left) the time representation of this signal is provided. The DFT of this signal is computed using the MATLAB[®] FFTW library [88], [89] that decomposes the problem with the Cooley-Turkey algorithm [90] according to signal size.

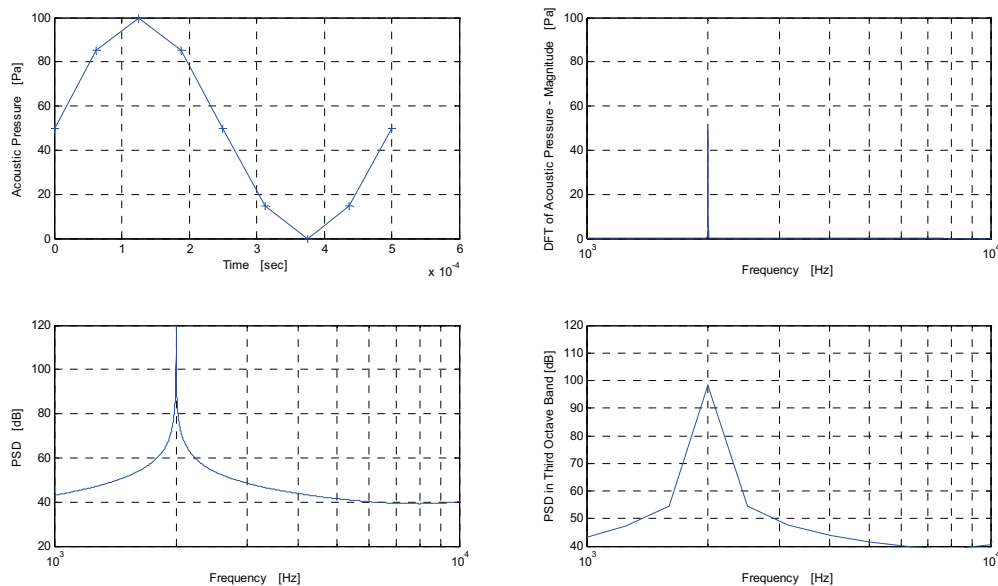


Figure 3.26: acoustic signal post-processing tool output

This approach decomposes a signal of N -point into N_1 and N_2 ($N=N_1 \cdot N_2$) computing N_1 transform of size N_2 and N_2 transform of size N_1 . This decomposition is applied recursively, until the problem can be solved using one of the several machine-generated fixed size “codelets”. The codelets in turn use several algorithms in combination including a variation of Cooley-Turkey [86], a prime factor algorithm [86] and a split radix algorithm [92]. The particular factorization of N is chosen heuristically.

When N is a prime number the FFTW library first decomposes the N -point problem into three $(N-1)$ -point problems using Rader’s algorithm [91], and then uses the Cooley Turkey approach to compute the $(N-1)$ -point DFTs.

In figure 3.26 (top-right) the magnitude of the DFT of the chosen sinusoidal time-signal is provided, checking that the computed DFT satisfies the discrete formulation of the Parseval’s theorem (3.46), where $X=DFT[x]$ and N is the length of the signal.

$$\sum_{n=0}^{N-1} |x[n]|^2 = \frac{1}{N} \sum_{k=0}^{N-1} |X[k]|^2 \quad (3.46)$$

Then the PSD of the signal is calculated using the discrete signal formulation provided in (3.47) in order to compute a PSD with the dimension of $[Pa^2/Hz]$, and it is converted in dB using the (3.48) with a reference pressure value P_{REF} equal to $20 \mu Pa/Hz^{1/2}$.

$$PSD[k] = 2 \left| \frac{X[k]}{N} \right|^2 T \quad [Pa^2 / Hz] \quad (3.47)$$

$$PSD[k] = 10 \log_{10} \left(\frac{PSD[k]}{P_{REF}^2} \right) \quad [dB] \quad (3.48)$$

Then the power spectral content I_{PSD} is calculated by (3.49)

$$I_{PSD} = \sum_{k=1}^{N-1} \left(\frac{PSD[k-1] + PSD[k]}{2} \right) \cdot (f[k] - f[k-1]) \quad [Pa^2] \quad (3.49)$$

while the PSD is plotted in figure 3.26 (bottom-left). The last passage is the conversion of the PSD in third-octave band, according to the border and center values provided in table 3.5. Conversion is made by (3.50)

$$PSD_{1/3}[j] = \frac{\left[\sum_{k=1}^{N-1} \left(\frac{PSD[k-1] + PSD[k]}{2} \right) \cdot (f[k] - f[k-1]) \right]_{k \in [j_{left}, j_{right}]} }{f[j_{right}] - f[j_{left}]} \quad [dB] \quad (3.50)$$

while a plot of the PSD in third octave band is provided in figure 3.26 (bottom-right).

Border – Left [Hz]	Center [Hz]	Border – Right [Hz]
14.1	16	17.8
17.8	20	22.4
22.4	25	28.2
28.2	31.5	35.5
35.5	40	44.7
44.7	50	56.2
56.2	63	70.8
70.8	80	89.1
89.1	100	112
112	125	141
141	160	178
178	200	224
224	250	282
282	315	355
355	400	447
447	500	562
562	630	708
708	800	891
891	1000	1122
1122	1250	1413
1413	1600	1778
1778	2000	2239
2239	2500	2818
2818	3150	3548
3548	4000	4467
4467	5000	5623
5623	6300	7079
7079	8000	8913
8913	10000	11220
11220	12220	14130
14130	16000	17780
17780	20000	22390

Table 3.5: third octave bands, left, centre and right values

This approach for acoustic signal post-processing is formulated to preserve the frequency content and the absolute noise values independently by the sampling and the physical time length of the original signal. These properties have been verified computing the I_{PSD} and the maximum value of the PSD in third octave band ($M_{PSD,1/3}$) for the sinusoidal signal mentioned above sampled with 9, 41 and 161 points per period and for a physical time of 0.1, 1 and 10 seconds. Results are provided in table 3.6, showing the independence mentioned above.

	T = 0.1 sec	T = 1 sec	T = 10 sec
Points per period = 9	$I_{PSD} = 4998.4 \text{ Pa}^2$ $M_{PSD,1/3} = 90.303 \text{ dB}$	$I_{PSD} = 4999.7 \text{ Pa}^2$ $M_{PSD,1/3} = 90.311 \text{ dB}$	$I_{PSD} = 4999.9 \text{ Pa}^2$ $M_{PSD,1/3} = 90.311 \text{ dB}$
Points per period = 41	$I_{PSD} = 4999.8 \text{ Pa}^2$ $M_{PSD,1/3} = 90.311 \text{ dB}$	$I_{PSD} = 5000 \text{ Pa}^2$ $M_{PSD,1/3} = 90.311 \text{ dB}$	$I_{PSD} = 5000 \text{ Pa}^2$ $M_{PSD,1/3} = 90.312 \text{ dB}$
Points per period = 161	$I_{PSD} = 5000 \text{ Pa}^2$ $M_{PSD,1/3} = 90.311 \text{ dB}$	$I_{PSD} = 5000 \text{ Pa}^2$ $M_{PSD,1/3} = 90.311 \text{ dB}$	$I_{PSD} = 5000 \text{ Pa}^2$ $M_{PSD,1/3} = 90.312 \text{ dB}$

Table 3.6: acoustic post-processing results for a sinusoidal signal varying the number of samples per period and the physical time-length of the signal

Moreover acoustic corrections were applied in order to take into account microphone distance to noise sources and span extension of the body.

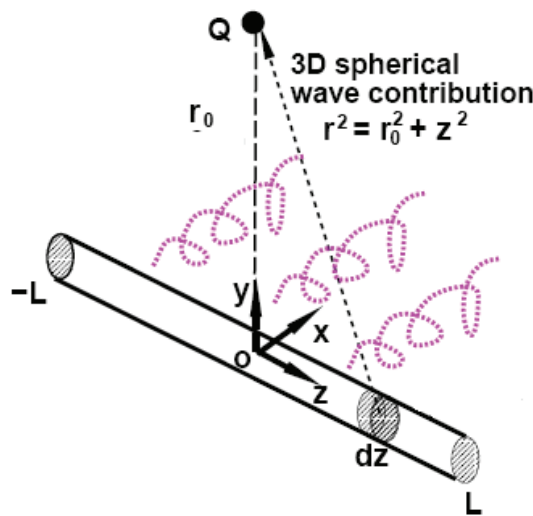


Figure 3.27: sketch for the span extension acoustic correction [97]

A first correction is taken from [97] considering the effect of the spherical propagation of acoustic waves. Let us consider an acoustic source of length $2L_0$ and a microphone located at a distance equal to r_0 like in the sketch in Figure 3.27.

If we take a source of length $2L_1$ the difference between the SPL at microphone location will be given by (3.51).

$$C_{1,Span} = 10 \log_{10} \left(\frac{\left[\text{tg}^{-1} \left(L_0 / r_0 \right) + 0.5 \sin \left(2 \cdot \text{tg}^{-1} \left(L_0 / r_0 \right) \right) \right]}{\left[\text{tg}^{-1} \left(L_1 / r_0 \right) + 0.5 \sin \left(2 \cdot \text{tg}^{-1} \left(L_1 / r_0 \right) \right) \right]} \right) \quad (3.51)$$

This equation does not take into account the possibility to change the distance of microphone respect to the emitting surface, and this effect can be considered by the (3.52) according to [99]

$$C_{1,Dist} = 20 \log_{10} (r_1 / r_0) \quad (3.52)$$

so the complete correction that has to be applied to take into account both effects is given in equation (3.53).

$$C_{1,Span} + C_{1,Dist} = 20 \log_{10} (r_1 / r_0) + 10 \log_{10} \left(\frac{\left[\text{tg}^{-1} \left(L_0 / r_0 \right) + 0.5 \sin \left(2 \cdot \text{tg}^{-1} \left(L_0 / r_0 \right) \right) \right]}{\left[\text{tg}^{-1} \left(L_1 / r_0 \right) + 0.5 \sin \left(2 \cdot \text{tg}^{-1} \left(L_1 / r_0 \right) \right) \right]} \right) \quad (3.53)$$

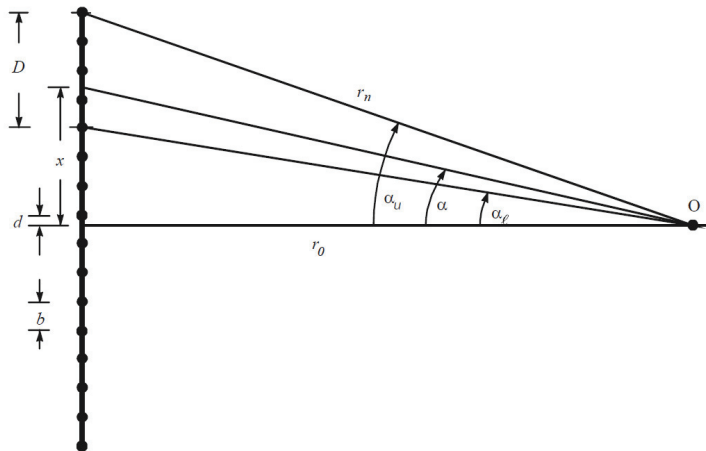


Figure 3.28: sketch for the distance and span extension acoustic correction [98]

Another correction for these effect can be found in [98] according to the sketch provided in Figure 3.28. In this case both span and distance to source are taken into account into angles α_u and α_l and the correction does not need any additional term.

$$C_2 = 10 \log_{10} \left(\frac{\left[\text{tg}^{-1}(\alpha_{u0} - \alpha_{l0}) / r_0 \right]}{\left[\text{tg}^{-1}(\alpha_{u1} - \alpha_{l1}) / r_1 \right]} \right) \quad (3.54)$$

In figure 3.29 a comparison between the corrections provided in (3.53) and (3.54) is given. In this case r_0 and r_1 have been assumed equal to 1 and 0.50 meters respectively, L_1 has been taken equal to 2 meters while L_0 varies from 0.1 to 1 meter. The correction is estimated between -7 and -17 dB and the diagram shows how the two relations give approximately the same result.

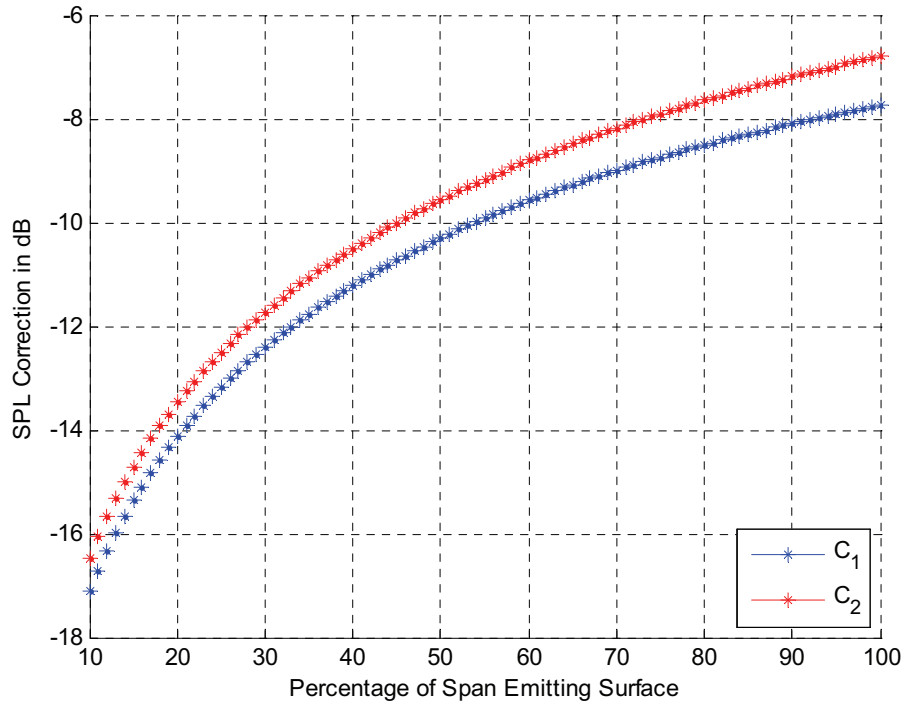


Figure 3.29: comparison between acoustic corrections C_1 (3.53) and C_2 (3.54)

3.4.3 NACA 0012 Experimental Test-Case and Numerical

Approach

Two experimental data sets were taken into account as reference for the aerodynamic and aeroacoustic simulation performed. They are respectively published in reference [93] and [94], both on NACA 0012 aerofoil geometry, for comparable aerodynamic conditions.

According to reference [93] the NACA 0012 aerofoil with sharp trailing edge was tested in the low-turbulence potential core of a free jet located in an anechoic chamber. This jet was provided by a vertically mounted nozzle with a 30.48 x 45.72 cm rectangular exit. The span of the model was 45.72 cm while the chord was 22.86 cm. The trailing edge thickness was very sharp, and it was designed to be less than 0.05 mm.

At a geometric tunnel angle of 0 deg the model was located 61 cm above the nozzle exit, supported by 2 cylindrical hubs on its sides. It was tested at a free-stream velocity equal to 39.6 and 71.3 m/sec for an equivalent angle of attack of 0, 5.4 and 7.3 degrees, with a Reynolds number based on the chord length ranging from 0.62 and 1.1 millions.

The equivalent angle of attack is defined as the angle of attack able to give the pressure coefficient distribution and forces typical for the tested airfoil for a certain angle condition. This condition is normally achieved with a geometrical angle of attack quite different, as the aerodynamic flow field is affected by the interference of the experimental devices.

Aerofoil model was tested both with untripped and tripped leading edge. For the untripped case the surface was smooth and cleaned with a natural development of turbulence over the boundary layer. On the other hand for tripped model boundary layer transition was achieved by a random distribution of grit in strips from the leading edge to 20% of chord. The grit particles had a mean diameter of 0.29 mm with a mean distribution of 380 particles/cm² and this was considered enough to establish a well developed turbulent boundary layer.

Acoustic tests were performed with 7 ½ inch diameter microphones located in the plane of model midspan. One additional microphone was located outside this plane. Microphones were identified by a ID number, as M1 and M2 were perpendicular to the chord line at the trailing edge for geometrical angle of attack equal to 0 degree, at a distance of 122 cm (5.5 chords lengths). Moreover the pairs of microphones M4-M7 and M5-M8 were located at the same distance from the trailing edge respectively 30 degrees forward and backward the pair M1-M2.

A sketch of experimental device mid-plane, with microphones locations is provided in Figure 3.30.

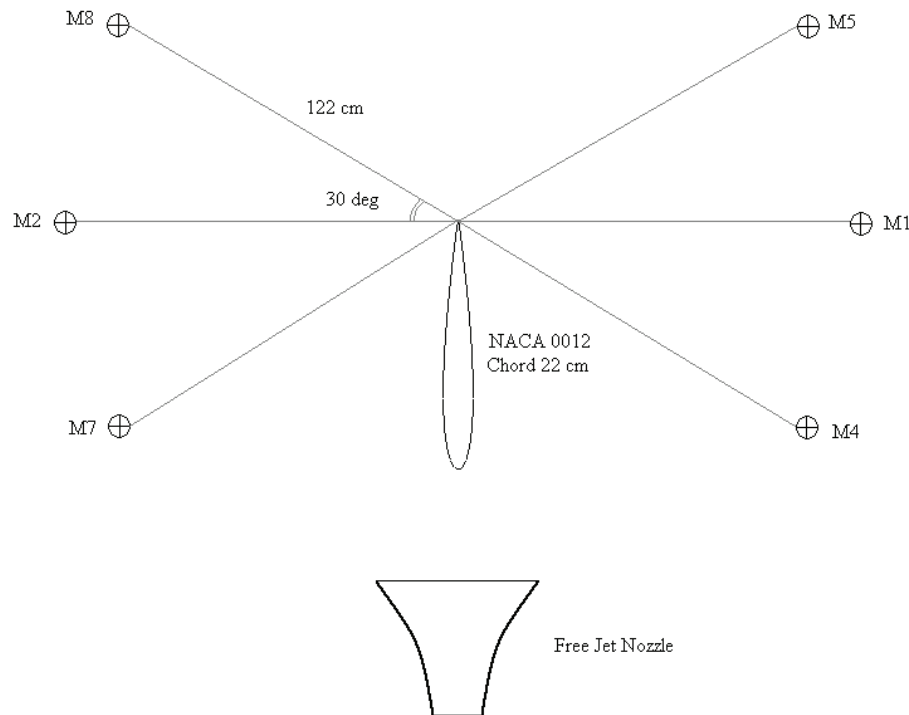


Figure 3.30: sketch of experimental device mid-plane and microphones locations [93].

Microphone signals were recorded during the tests with a 14 channels FM analog tape recorder, operated to provide flat response up to 40 KHz. Amplifiers were used to magnify the signal-to-noise ratio for each microphone channel and a pure tone and white-noise were used to calibrate the response. Sound Pressure Level (SPL) at microphones locations were provided in third-octave band from 0.2 to 10 KHz.

In reference [94] tests were carried out in NLR's Small Anechoic Wind Tunnel KAT. It is an open circuit wind tunnel, with its test section surrounded by a 5x5x3 m room that is completely covered with 0.5 m foam wedges, yielding more than 99% absorption above 500 Hz. Two horizontal endplates (0.90 x 0.70 m) were mounted to the upper and lower sides of the rectangular 0.38 x 0.51-m nozzle, providing a semi-open test section for airfoil self-noise measurements. To suppress reflections, the endplates were acoustically lined with a 5.5 cm layer of sound-absorbing foam covered by a 5% open-perforated plate. In case of inflow turbulence measurements, a turbulence grid was installed in the nozzle.

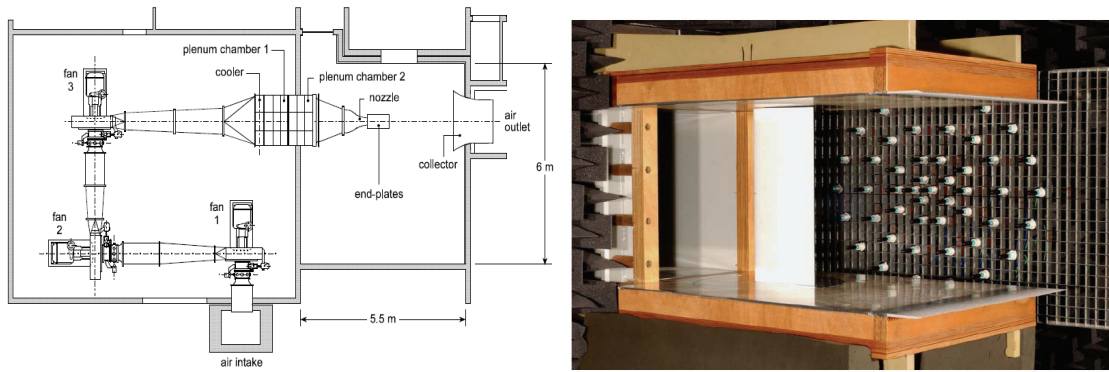


Figure 3.31: sketch of KAT Wind Tunnel plant (left) – KAT Wind Tunnel test-chamber and microphones array (right) [94].

The turbulence grid consisted of diagonally oriented, cylindrical, 12-mm bars with a mesh width of 60 mm. A sketch of the KAT wind tunnel plant is provided in Figure 3-left, while a picture of test-chamber is provided on the right side.

NASA 0012 aerofoil with sharp trailing edge was operated into KAT wind tunnel for the same Reynolds number range and the same equivalent angles of attack mentioned above.

The microphone array consisted of 48 $\frac{1}{2}$ inch diameter microphones mounted in an open 0.8 x 0.6 m grid designed for maximum side-lobe suppression at frequencies between 1 and 20 kHz. It was placed outside the tunnel flow at a distance of 0.6 m from the tunnel axis, on either the suction or the pressure side of the model. The relatively short distance between the array and the model was chosen to obtain maximum signal-to-noise ratio. The center of the array was placed at the same height as the tunnel axis.

Data were acquired with a sample frequency of 51.2 KHz with a frequency resolution of 25 Hz, for a total time of 30 seconds and microphones averaged noise spectra are provided from 0.8 to 10 KHz in one-third octave bands.

Two computational grid were generated in order to perform the RANS and the ELES calculations. A first 2D computational grid for RANS was made by 112 K quad cells, divided into an outer and inner computational domain (Figure 3.32) by a grid interface. This solution was chosen to save cells in the outside region and provide an optimal wall condition ($y^+ < 1$) on the airfoil surface for all velocities simulated, as well a sufficient number of cells inside physical boundary layer in order to be correctly resolved.

In Figure 3.33 the details of the leading edge, trailing edge and outer/inner domain interface are provided. Moreover an additional 3D grid was made in order to perform the

ELES calculations. The 2D grid was extended to 5 parallel layers (4 cells) in the RANS outer and inner domain and an additional box was built around the trailing edge in order to refine the grid for the LES calculation. Then each cell in the span direction was divided into 8 cells, achieving the final number of 32 cells in the span direction for the LES region. Pictures of the computational domain with the ELES refinement box and of the RANS-LES grid transition are provided in Figure 3.34 and 3.35.

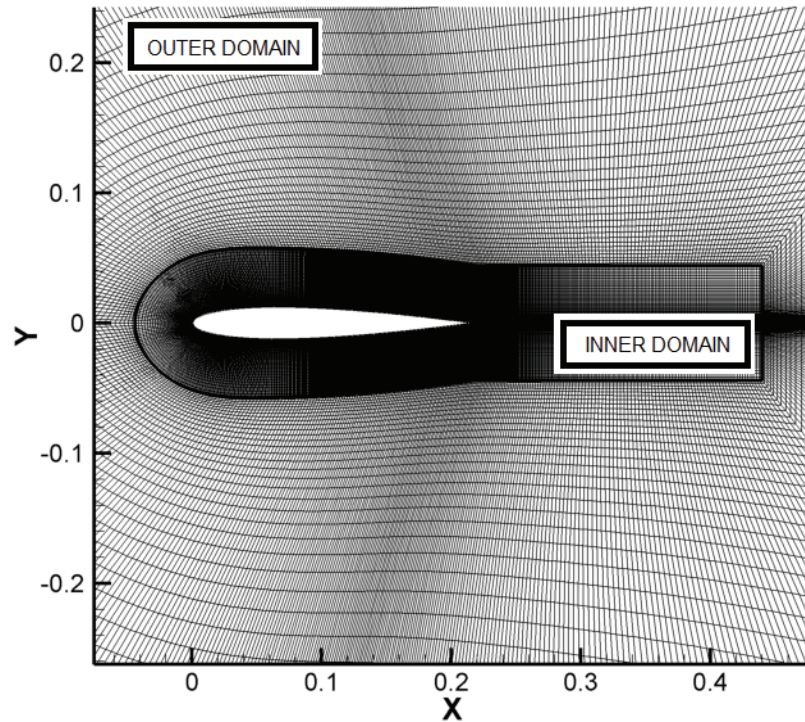


Figure 3.32: 2D URANS computational grid.

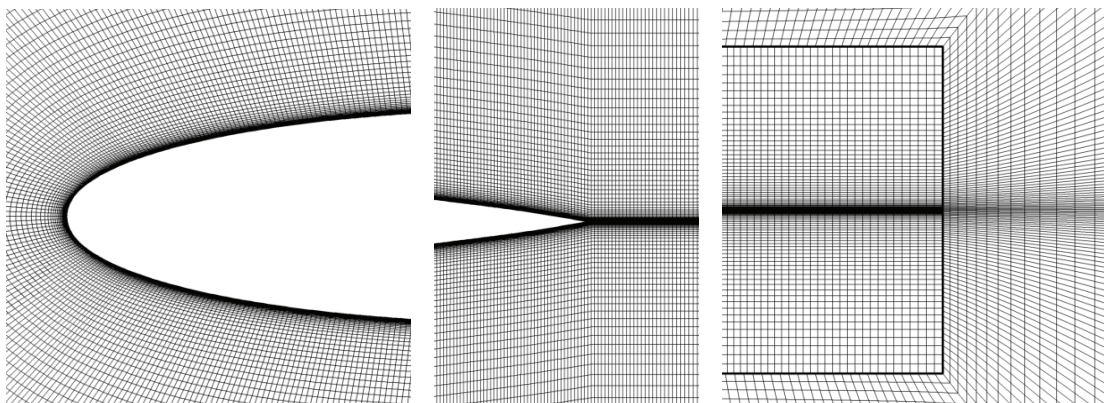


Figure 3.33: 2D URANS computational grid.

Leading edge detail (left) – Trailing edge detail (center) – Inner/outer interface (right)

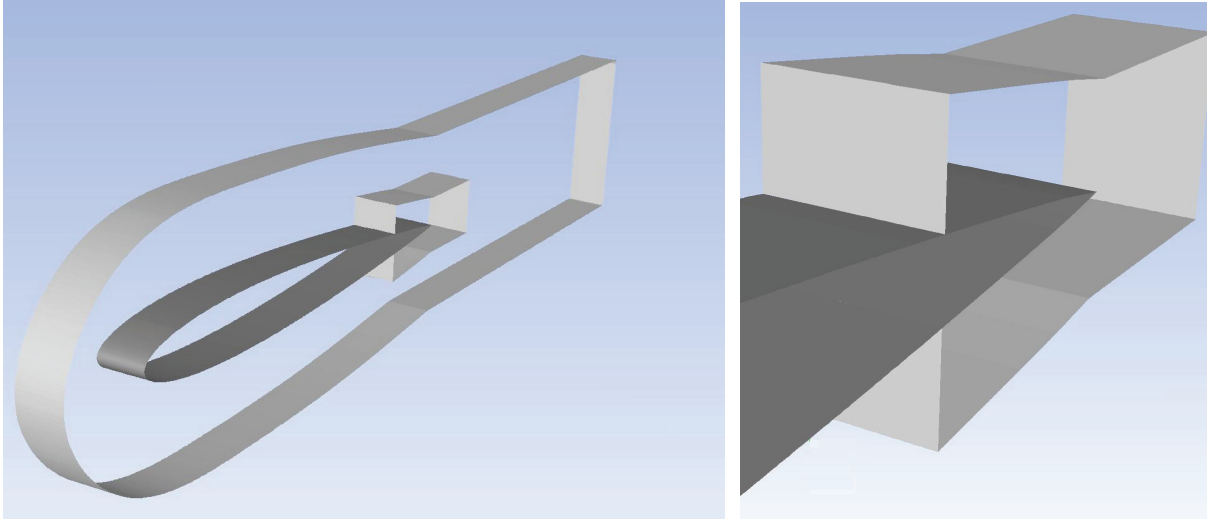


Figure 3.34: 3D ELES computational domain: outer/inner domain and ELES refinement box

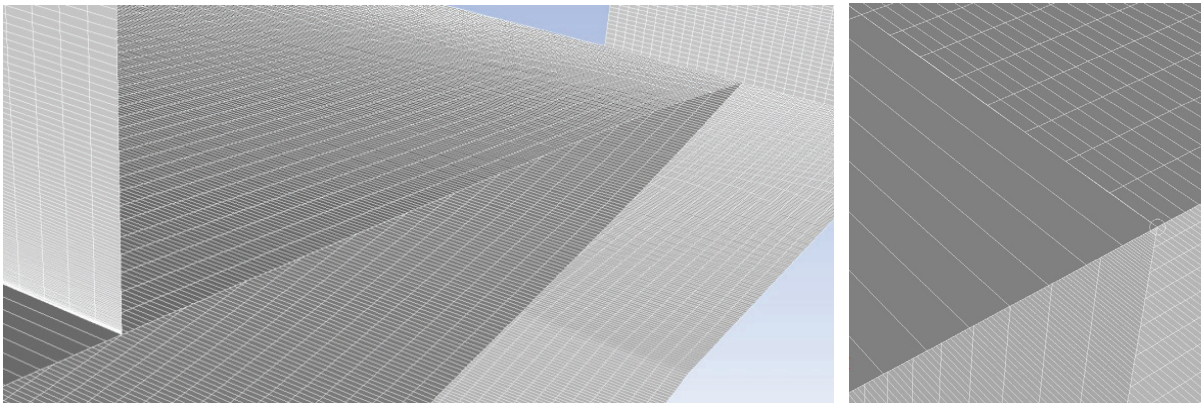


Figure 3.35: 3D ELES computational grid: ELES refinement box details

RANS simulations were performed with the SIMPLE pressure-based transient solver, $k-\omega$ SST transitional (4 equations) turbulence model and the $k-k_1-\omega$ (3 equations) turbulence model, 2nd order time discretization scheme, standard transport scheme for pressure and QUICK transport scheme for all other variables [23]. The airfoil chord length was chosen equal to 0.22 m according to the experimental references while the time-step size equal to 10^{-5} seconds. The acoustic sampling was performed every 5 time steps, with a frequency equal to 20KHz, in order to provide acceptable acoustic results up to 10KHz of the noise spectra. Noise pressure time histories were calculated with the Ffowcs Williams-Hawkings acoustic

analogy implemented into the CFD solver ANSYS-FLUENT[®] [23], [24]. A summary of simulation settings is provided in Table 3.7.

P-V Coupling	SIMPLE
Turbulence Model	$k-\omega$ SST Transitional – $k-kl-\omega$ – Embedded LES
Pressure Transport Scheme	Standard
Momentum/ $k/\omega/\gamma/Re_{\theta t}$	QUICK
Asymptotic Velocity	Variable (from 40 to 70 m/sec)
Angle of Attack	Variable (from 0 to 7 deg)

Table 3.7: NACA 0012 airfoil self-generated noise simulation settings.

3.4.4 NACA 0012 Self-Generated Noise: Results

In this paragraph the results for the NACA 0012 airfoil self-generated noise are provided, according to the experimental data sets [93] and [94], respectively referenced as NASA and NREL in the figures of next pages. The test matrix chosen for numerical simulations is given in Table 3.8, for 2 different asymptotic velocities and 4 different AoAs. These conditions were able to take into account all different noise generation mechanisms mentioned in the paragraph 3.4.1, and for a correct noise simulation different numerical methods were needed for the different aerodynamic conditions tested. Table 3.8 also contains the different numerical approaches used for each case. In particular the noise of the airfoil with 0 deg AoA is a TBL-TE noise, and its prediction is failed by URANS models as they are not able to take into account the formation of turbulent eddies. For this reason the ELES approach was used being able to improve considerably the simulation accuracy, as shown in Figure 3.36. ELES was tested only for the 70 m/sec case, as it is very demanding from a computational point of view, and a span correction is applied to the provided results in order to take into account the span correlation length.

	0deg	4 deg	5 deg	7deg
40 m/sec	$k-\omega$ trans. $k-k_1-\omega$	$k-\omega$ trans. $k-k_1-\omega$ laminar	$k-\omega$ trans. $k-k_1-\omega$	$k-\omega$ trans. $k-k_1-\omega$
70 m/sec	$k-\omega$ trans. $k-k_1-\omega$ ELES	$k-\omega$ trans. $k-k_1-\omega$	$k-\omega$ trans. $k-k_1-\omega$	$k-\omega$ trans. $k-k_1-\omega$

Table 3.8: airfoil self-generated noise test matrix

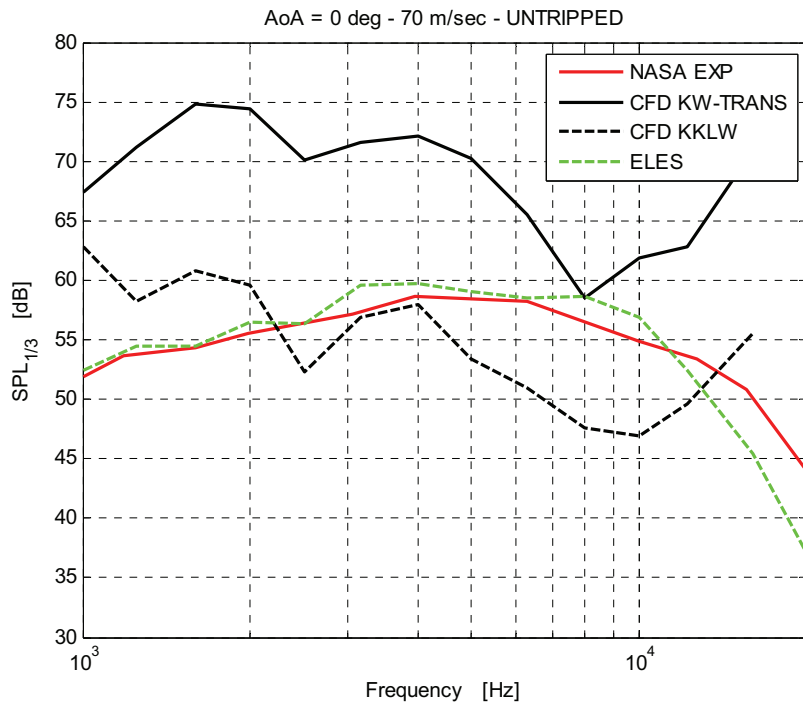
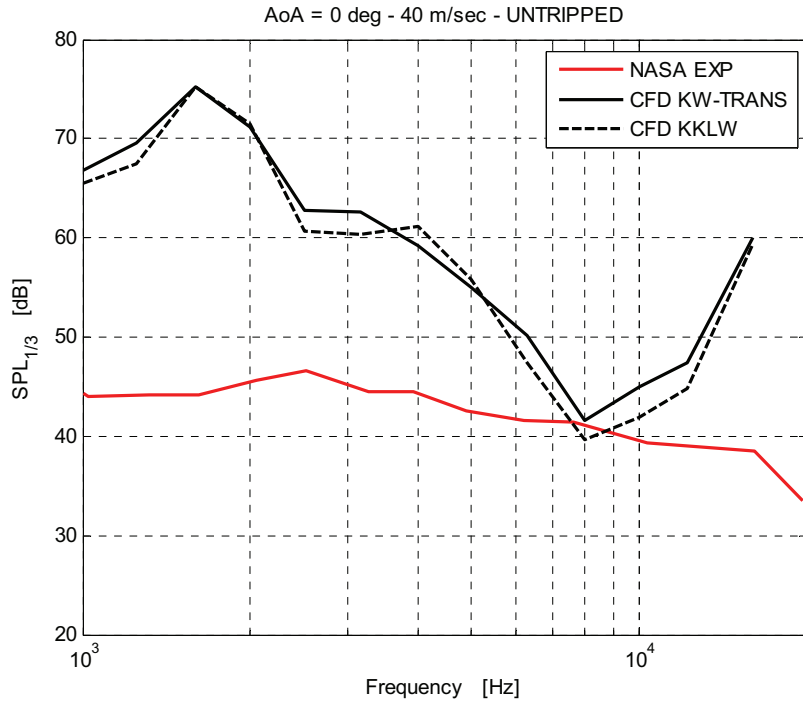


Figure 3.36: airfoil self-noise numerical results, 40/70 m/sec, 0 deg.

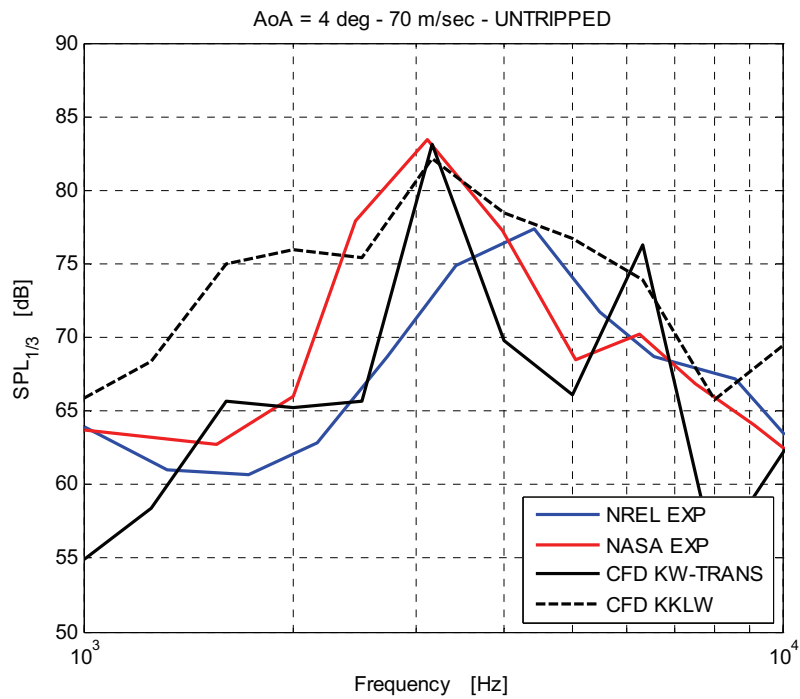
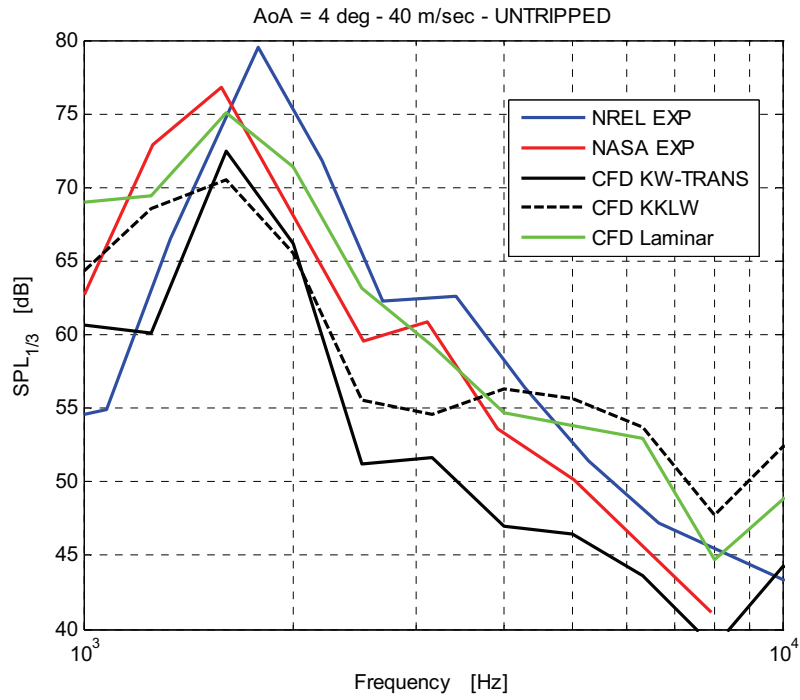


Figure 3.37: airfoil self-noise numerical results, 40/70 m/sec, 4 deg.

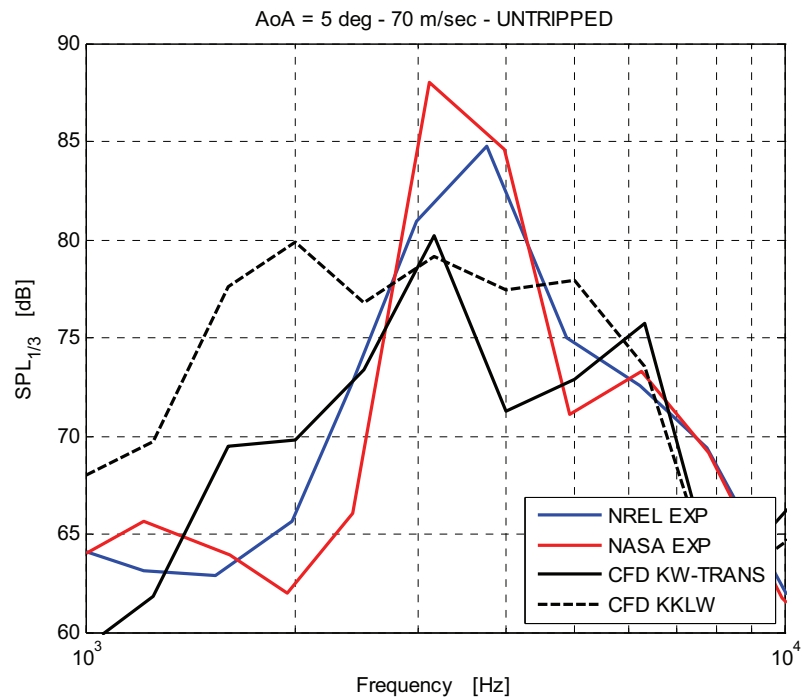
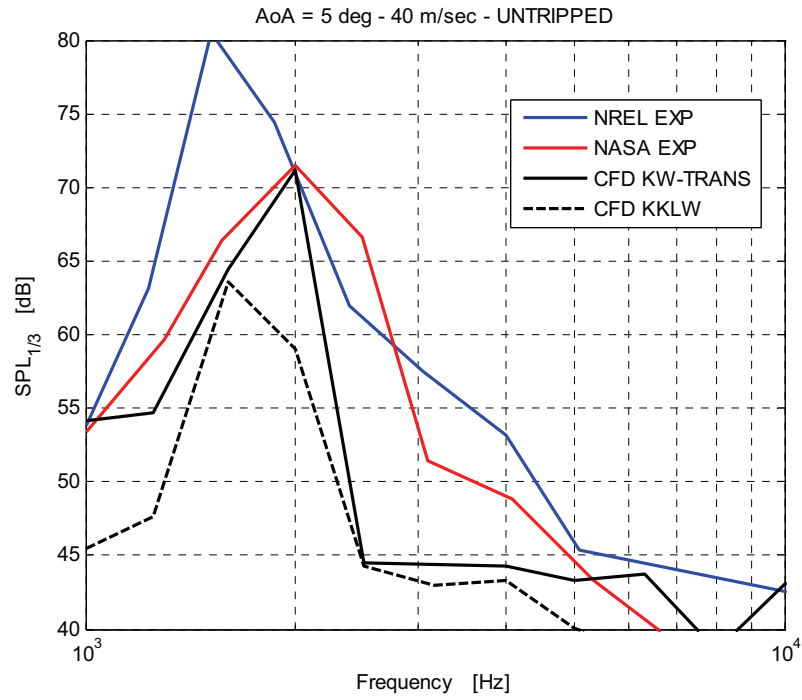


Figure 3.38: airfoil self-noise numerical results, 40/70 m/sec, 5 deg.

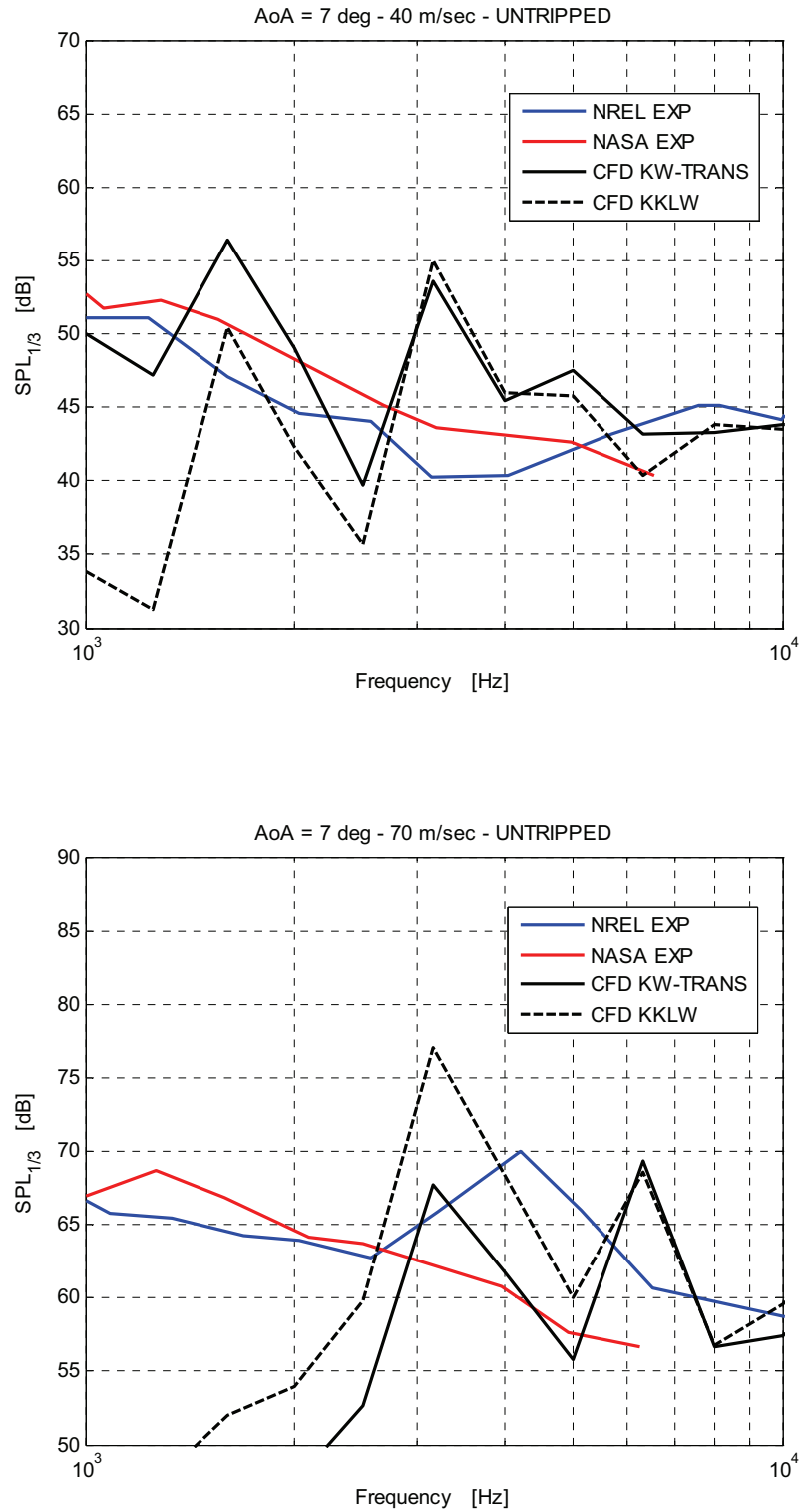


Figure 3.39: airfoil self-noise numerical results, 40/70 m/sec, 7 deg.

ELES approach is expected to be able to provide good results also for the 40 m/sec velocity and further simulations will be performed in future. Visualization of the velocity magnitude contours on Q-Criterion iso-surfaces into the LES refinement box are provided in Figure 3.40 and 3.41, showing the details of the turbulent eddies formation due to the local LES modelling.

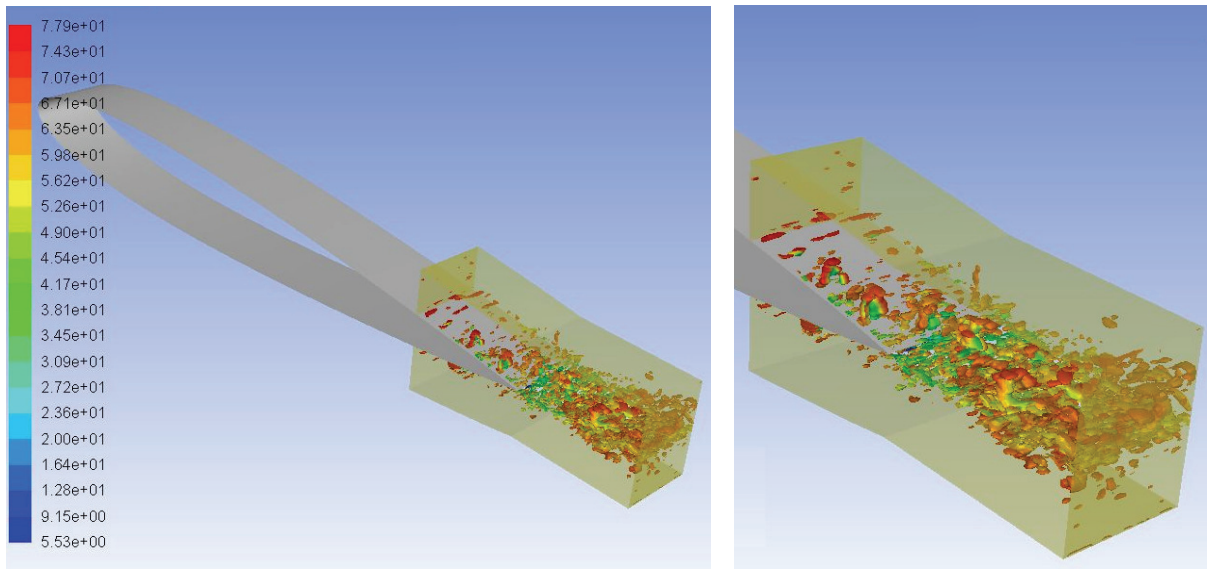


Figure 3.40: ELES velocity magnitude contours on Q-Criterion iso-surfaces in the LES box. Turbulent eddies visualizations, NACA 0012, 0 deg, 70 m/sec.

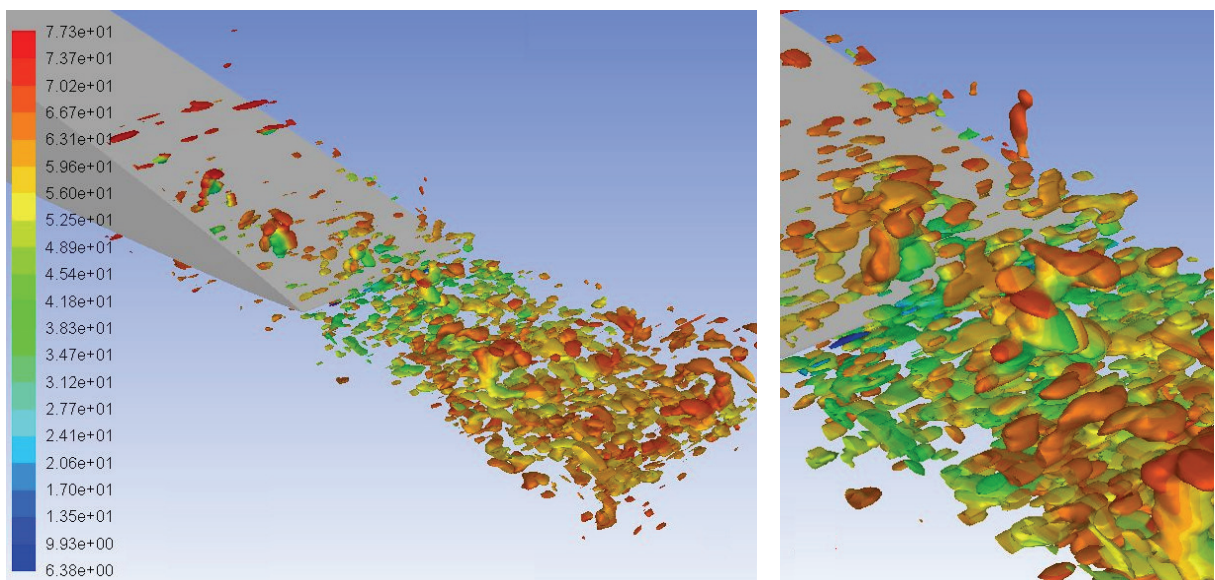


Figure 3.41: ELES velocity magnitude contours on Q-Criterion iso-surfaces in the LES box. Turbulent eddies visualizations (details), NACA 0012, 0 deg, 70 m/sec.

For the 4 and 5 deg cases the noise generation mechanism is dominated by the LBL-VS, as the noise spectra appear mastered by a typical tonal component. In this case the laminar instabilities that develop over the airfoil surface determine a very late transition together with a oscillatory motion responsible of the tonal noise generation. Comparison between the experimental data and the computational data are provided in Figure 3.37 and 3.38, showing how both the $k-\omega$ transitional and the $k-k_1-\omega$ turbulence models are able to capture this oscillatory phenomenon. In particular for all cases a good prediction of frequency location and SPL noise level was reached with both models, but the $k-k_1-\omega$ seems to spread a little bit more the noise spectrum than the $k-\omega$ and it is more numerical instable, meaning that it requires lower under relaxation factors to converge. In order to show the laminarity of this phenomenon also a laminar run was performed for the 40 m/sec and 4 deg case, with a noise results that is slightly higher than the turbulent one, as the instability region is larger in this case.

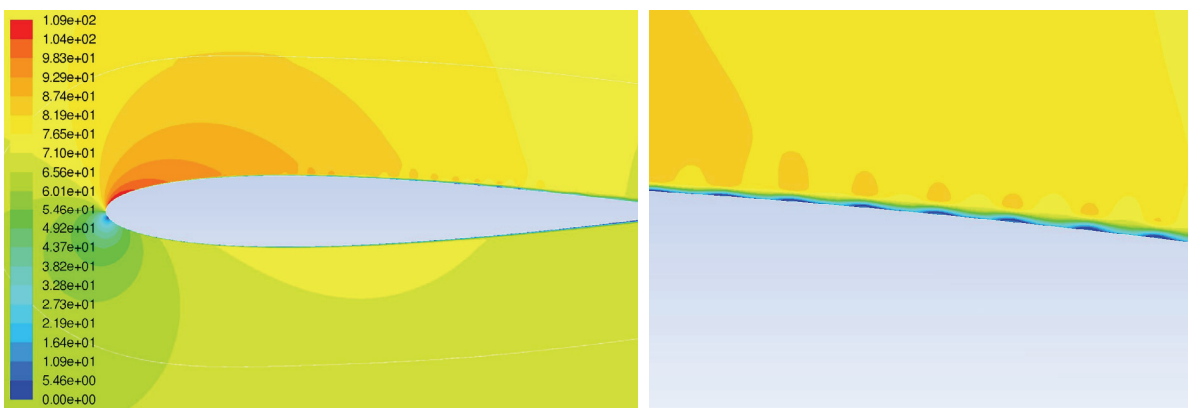


Figure 3.42: Velocity magnitude contours, NACA 0012, 4 deg, 70 m/sec.
Velocity oscillations on the airfoil suction side.

In Figure 3.42 and 3.43 velocity and vorticity magnitude contours are respectively provided for the case at 4 deg and 70 m/sec in order to visualize the laminar instabilities that affect the airfoil suction side from the 30% to the 80% and the pressure side from the 90% to the 100% approximately. These instabilities are responsible of the noise production, and they are only captured with the transitional turbulence models, as they are totally damped with other turbulence models.

Moreover these oscillations characterize also the instantaneous pressure coefficient diagram, where they are clearly visible for both airfoil sides, Figure 3.44.

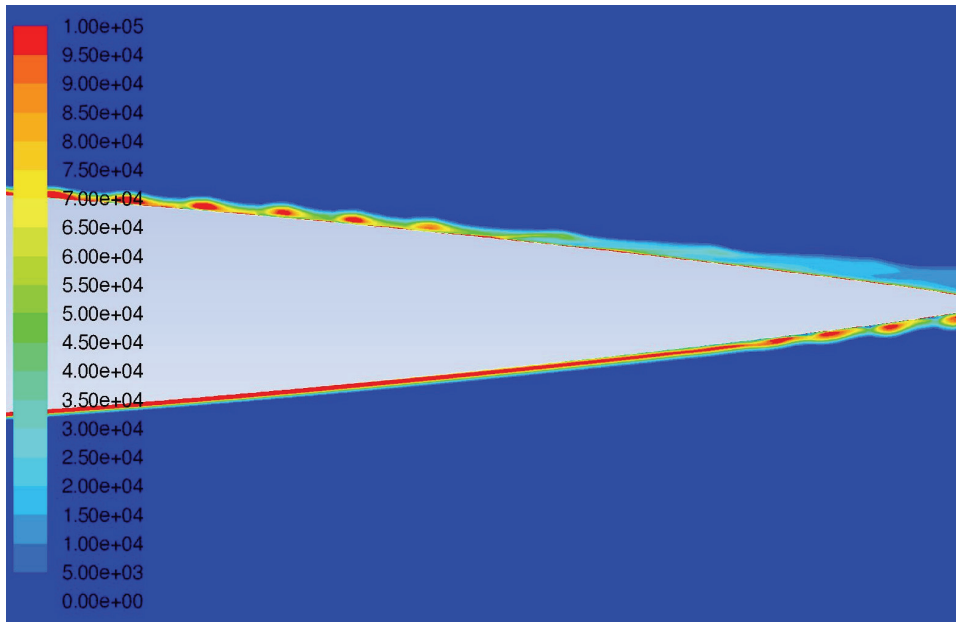


Figure 3.43: Vorticity magnitude contours, NACA 0012, 4 deg, 70 m/sec.
Vorticity oscillations of airfoil suction and pressure sides.

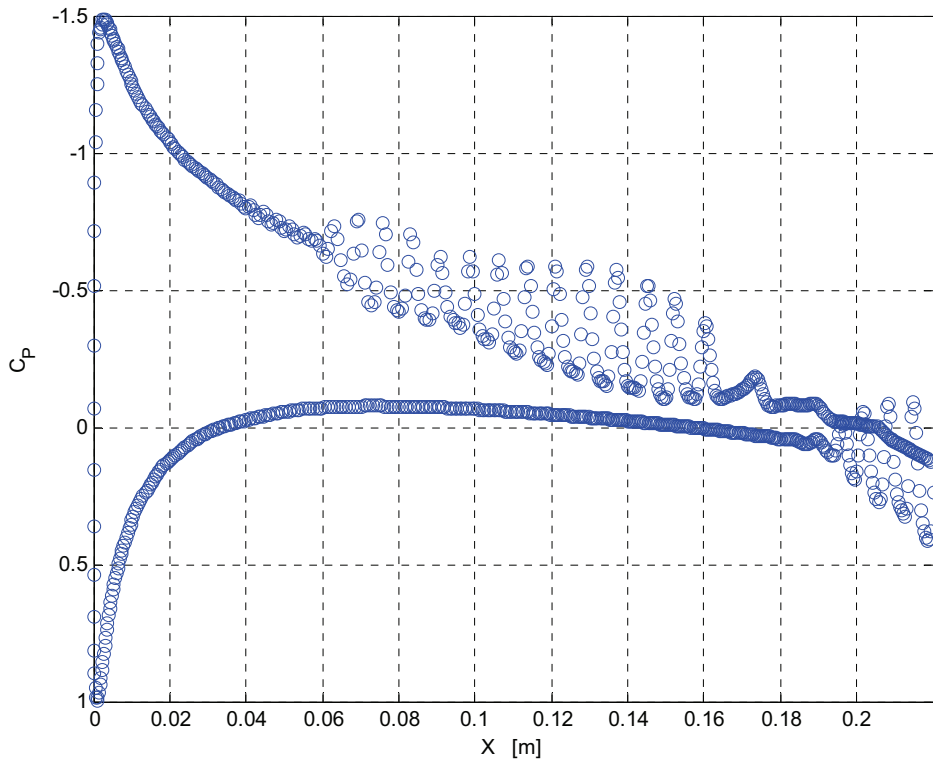


Figure 3.44: Pressure coefficient, NACA 0012, 4 deg, 70 m/sec.
Laminar instabilities affect the pressure coefficient on suction and pressure airfoil side.

The last simulations about the airfoil self-generated noise were performed for the 7 deg case, for both velocities. Here the dominating noise generation mechanism is the separation-stall noise, which includes both large vortex shedding phenomena that can be captured by a URANS approach, as well as turbulent eddies which need of the LES approach. Simulations were performed with the URANS transitional models, showing that the noise level was well captured for these cases. Anyhow an ELES, with an extended box respect to that one considered for the 0 deg case in order to follow the movement of transition to turbulence point towards the leading edge, is expected to be able to provide a better noise spectra prediction, and it will be object of investigation for future developments.

Chapter 4

Aerodynamic and Aeroacoustic Modelling of High Speed Propellers

This chapter is focused on the problem of CFD modelling of propellers, and in particular on the aeroacoustic simulation of high speed propellers. The problem of the propeller simulation is introduced by the Blade Element Theory (BET), a classical theory widely used for propeller simulation and design. This theory, able to provide reliable predictions for low speed propeller design purposes was used for approaching the problem of propeller simulation.

Therefore CFD was used for the simulation of three propeller geometries: the subsonic vintage NACA 4-(3)(08)-03 propeller and the two transonic NASA SR2 and SR3 propellers.

Aerodynamic and aeroacoustics simulations were performed with a RANS based approach integrated with the Ffowcs Williams-Hawkings (FWH) acoustic analogy for different data sets, different number of blades, rotational speed, free-stream Mach numbers and atmospheric conditions. Results show how this approach is able to predict forces and noise levels for high Mach number transonic cruise conditions. Moreover optimized CFD simulation strategies able to perform complete aerodynamics and aeroacoustic calculations with highly competitive computational cost and noise corrections criteria have been also investigated.

4.1 Fundamentals of Aerodynamics of Propellers

The propeller is a fluid machine based on the aerodynamic lift properties of the blades. It is a swept wing affected by a translational and rotational motion designed to provide optimal aerodynamic conditions over all its span extension, in order to produce as much lift as possible (thrust) with the minimum drag (torque).

From a classical point of view the propeller can be investigated with the Blade Element Theory which is able to provide the elemental thrust and power coefficients for each blade section based on classical aerodynamic consideration for the 2D airfoils. Therefore the entire blade performances are estimated by integration of the elemental results. The BET is based on the computation of induced velocity components on the blade (upwash, downwash and blades interference effect) in order to estimate the aerodynamic velocity and the AoA conditions of each airfoil. Moreover this theory is very easy to be implemented and able to provide reliable results for propeller testing conditions close to the design condition.

A literature research about the available methodologies to implement the BET has been carried out and 3 approaches are provided and implemented. Then they have been applied for a subsonic (take-off) condition for NASA SR2 in order to validate BET and CFD results. Furthermore BET was also applied as benchmark on higher Mach number conditions of paragraph 4.3, where attention is mostly focused on aeroacoustic results for the NASA SR2 and SR3 propellers.

4.1.1 Blade Element Theory

In the frame of classical approaches, propeller aerodynamic characteristics can be determined with the Blade Element Theory (BET), based on the estimation of lift and drag characteristics of the blade airfoils

For a fixed advance ratio condition (e.g. fixed asymptotic and rotational speed) each airfoil of a propeller blade experiences a velocity and an AoA condition according to the triangular composition represented in Figure 4.1 (right). If we consider V the asymptotic speed and ωr the angular velocity of the airfoil, this composition provides a velocity equal to V_R and an angle equal to Φ . Unfortunately they are not representative of the real aerodynamic conditions

experienced by the airfoil because they have to be corrected with the axial and tangential induced components which change both velocity magnitude and AoA.

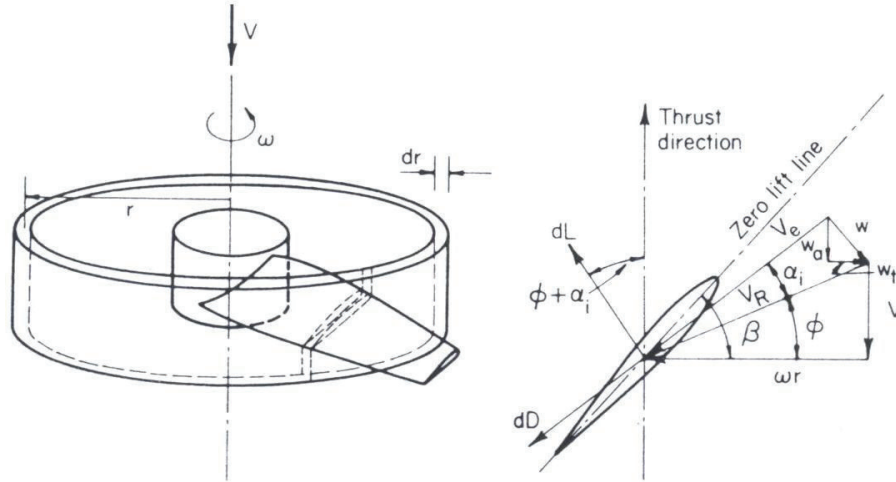


Figure 4.1: air speed and AoA conditions for the generic propeller blade airfoil

From a physical point of view the induced components are related to the upwash and downwash effects of the single blade combined with the aerodynamic interference effect with the other blades.

BET consists of a methodology for the estimation of these induced velocity components in order to be able to compute the exact aerodynamic conditions experienced by each airfoil of the blade. Therefore airfoil aerodynamic coefficients can be estimated and the thrust and power coefficients of each section can be calculated with the (4.1) and (4.2).

$$dC_T = \frac{\pi}{8} \left[J^2 + (\pi r)^2 \right] \sigma \left[C_l \cos(\phi + \alpha_i) - C_d \sin(\phi + \alpha_i) \right] dr \quad (4.1)$$

$$dC_p = \frac{\pi^2 r}{8} \left[J^2 + (\pi r)^2 \right] \sigma \left[C_l \cos(\phi + \alpha_i) + C_d \sin(\phi + \alpha_i) \right] dr \quad (4.2)$$

where J is the advance ratio and σ the propeller solidity.

Moreover the coefficients of the entire blade can be calculated by integrations of these equations in the blade spanwise direction. A further correction for the induced AoA can be applied as suggested by McCormick [102] to take into account the radial effects (4.3).

$$\Delta\alpha_i = \frac{2w_a(v_\infty + w_t)}{(v_\infty + w_t)^2 + [\omega Rr(\omega Rr - 2w_a)]} \quad (4.3)$$

Induced velocity components can be calculated according 3 methodologies herein provided. The first two methodologies (methodology A and B) are based on the explicit computation of induced AoA α_i , while the third one (methodology C) is based on the implicit estimation of tangential induced velocity w_t .

Assuming the hypothesis of small α_i the elementary thrust of a generic blade airfoil is given by (4.4).

$$dT = \rho(2\pi r dr)(V + \alpha_i V_R \cos \phi) 2\alpha_i V_R \cos \phi \quad (4.4)$$

Moreover for the N-blade propeller the elementary thrust is also given by the (4.5).

$$dT = \frac{N}{2} \rho V_R^2 c C_{l\alpha} (\beta - \phi - \alpha_i) \cos \phi dr \quad (4.5)$$

The composition of equations (4.4) and (4.5) provides a second order linear equation for the unknown α_i (4.6), whose explicit solution is provided in (4.7).

$$\alpha_i^2 + \alpha_i \left(\frac{\lambda}{r} + \frac{\sigma C_{l\alpha}}{8r^2} \frac{V_R}{V_T} \right) - \frac{\sigma C_{l\alpha}}{8r^2} \frac{V_R}{V_T} (\beta - \phi) = 0 \quad (4.6)$$

$$\alpha_i = -\frac{1}{2} \left[-\left(\frac{\lambda}{r} + \frac{\sigma C_{l\alpha}}{8r^2} \frac{V_R}{V_T} \right) + \sqrt{\left(\frac{\lambda}{r} + \frac{\sigma C_{l\alpha}}{8r^2} \frac{V_R}{V_T} \right)^2 + \frac{\sigma C_{l\alpha}}{2r^2} \frac{V_R}{V_T} (\beta - \phi)} \right] \quad (4.7)$$

where $\lambda = V/\Omega R$, $V_T = \Omega r$ and $V_R = V_T(\lambda^2 + r^2)^{1/2}$. Choosing the positive root of the (4.7) the induced axial and tangential velocity components can be calculated according the (4.8) and (4.9), according to the methodology A.

$$w_a = v_R \alpha_i \cos(\phi + \alpha_i) \quad (4.8)$$

$$w_t = v_R \alpha_i \sin(\phi + \alpha_i) \quad (4.9)$$

The second methodology is based on the Lancaster-Prandtl vortex theory [102], [103], with the hypothesis that the flow on the blade is a composition of the asymptotic flow and of blade-induced vortex components. Under these hypotheses the rotational induced velocity is given by the (4.10)

$$w_i(r) = \frac{\sigma C_{l\alpha}}{8rF} v_e (\beta - \phi - \alpha_i) \quad (4.10)$$

as function of v_e and α_i . By the assumption of $\alpha_i \ll 1$ it follows that $v_e \approx v_R$ and (4.9) and (4.10) yield to (4.11).

$$\frac{\sigma C_{l\alpha}}{8rF} (\beta - \phi - \alpha_i) = \alpha_i \sin(\phi + \alpha_i) \quad (4.11)$$

that linearized becomes

$$\alpha_i^2 + \alpha_i \left(\frac{\sigma C_{l\alpha}}{8rF \cos \phi} + \tan \phi \right) - \frac{\sigma C_{l\alpha}}{8rF \cos \phi} (\beta - \phi) = 0 \quad (4.12)$$

where F is the Prandtl's correction factor (4.13).

$$F = \frac{2}{\pi} \cos^{-1} \left[e^{\frac{(r-1)N}{2 \sin \phi}} \right] \quad (4.13)$$

By the solution of equation (4.12) the induced AoA can be explicitly calculated. The solution according to the methodology B is provided in (4.14).

$$\alpha_i = -\frac{1}{2} \left[-\left(\frac{\lambda}{r} + \frac{\sigma C_{l\alpha}}{8rF \cos \phi} \right) + \sqrt{\left(\frac{\lambda}{r} + \frac{\sigma C_{l\alpha}}{8rF \cos \phi} \right)^2 + \frac{\sigma C_{l\alpha}}{2rF \cos \phi} (\beta - \phi)} \right] \quad (4.14)$$

The last methodology here discussed is based on the same approach mentioned above, but without the hypothesis of small α_i . Thus in the equation (4.10) $v_e \neq v_R$ and α_i has to be calculated by the implicit resolution of the (4.15).

$$w_t(r) = \frac{\sigma C_{l\alpha}}{8rF} v_e (\beta - \phi - \alpha_i) = \frac{\sigma C_{l\alpha}}{8rF} v_e \left[\beta - \tan^{-1} \left(\frac{w_t}{w_a} \right) \right] \quad (4.15)$$

Therefore the axial induced velocity is given by the (4.16) by geometric considerations on the velocity composition of Figure 4.2.

$$w_a = \frac{1}{2} \left[\sqrt{v_\infty^2 + 4w_t(\Omega R r - w_t)} - v_\infty \right] \quad (4.16)$$

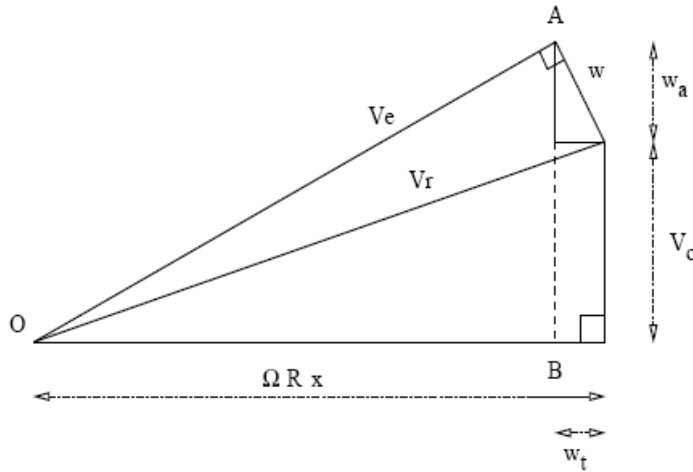


Figure 4.2: induced axial and tangential components for the generic blade section

Thus the effective velocity is given by (4.17)

$$v_e^2 = (\Omega R r - w_t)^2 + (w_a + v_\infty)^2 = (\Omega R r - w_t)^2 + \left[v_\infty + \frac{1}{2} \sqrt{v_\infty^2 + 4w_t(\Omega R r - w_t)} - \frac{1}{2} v_\infty \right]^2 \quad (4.17)$$

which substituted into the (4.15) yields to the implicit equation (4.18)

$$w_t = \frac{\Omega \sigma C_{l\alpha}}{8rF} v_e \left[\beta - \tan^{-1} \left(\frac{w_t}{w_a} \right) \right] \sqrt{\left(r - \frac{w_t}{\Omega R} \right) + \frac{1}{4} \left[\sqrt{\lambda^2 + 4 \frac{w_t}{\Omega R} \left(r - \frac{w_t}{\Omega R} \right)} + \lambda \right]^2} \quad (4.18)$$

that has to be solved numerically. By the knowledge of the axial and tangential induced velocities it is easy to estimate the induced AoA by (4.19).

$$\alpha_i = \tan^{-1} \left(\frac{w_t}{w_a} \right) - \phi \quad (4.19)$$

These 3 methodologies have been implemented in order to provide benchmark results for the propeller CFD simulation of the next paragraphs. The lift and drag coefficients database used were the same mentioned in the paragraph 3.2.1 for the VAWT even if, especially for design conditions, the lift and drag coefficients are quite standard for all airfoils and propeller thrust and torque mainly depends by blade chord distribution and blade swept design law..

An example of BET application is provided for the NASA SR2 propeller tested in low Mach number condition. The NASA SR2 blade geometry details, CFD computational grid and solver settings are provided in the paragraph 4.3.1 and 4.3.2. The results presented here are part of some preliminary tests made on this propeller before performing the final aerodynamic simulations in transonic conditions. The SR2 blade was tested for an asymptotic Mach number equal to 0.34, and an advance ratio ranging from 0.43 to 0.63, according to the experimental data provided in [109]. The experimental propeller design angle is equal to 59 deg while CFD simulations were performed with a blade design angle equal to 62 deg in order to achieve the aerodynamic calibration.

Thrust and torque coefficients are provided in Figure 4.3 and experimental data, BET and CFD results are compared for the tested conditions showing a good prediction of propeller forces, especially in proximity of an advance ratio equal to 0.55, corresponding to the design condition.

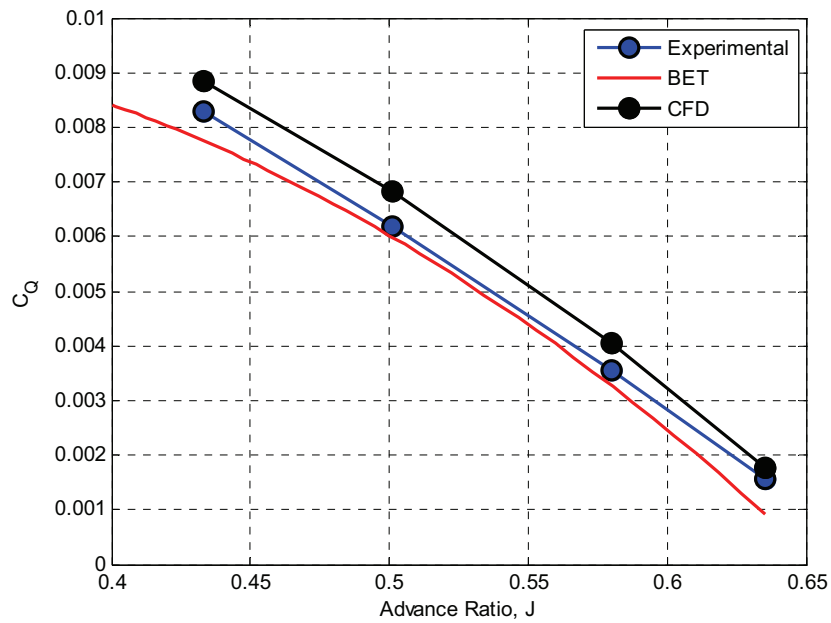
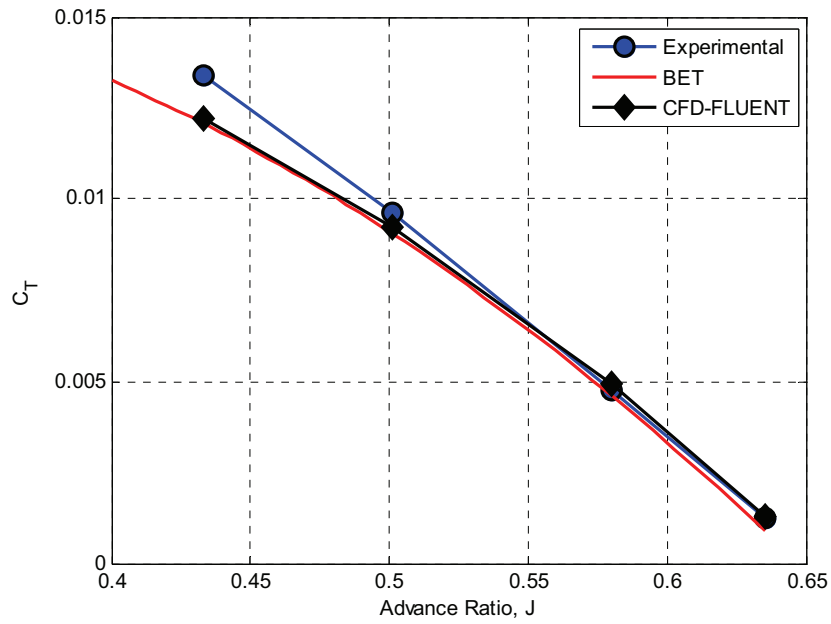


Figure 4.3: thrust and torque coefficients for NASA SR2, $M=0.34$, J from 0.43 to 0.63. Comparison between experimental data, BET and CFD results.

4.2 Subsonic Propeller Test-Case: NACA 4-(3)(08)-03

In this paragraph the results of the aerodynamic and aeroacoustics simulations of the NACA 4-(3)(08)-03 propeller are provided. This test-case is based on the experimental data of references [100] and [101], provided by NACA for different subsonic blade geometries and it was chosen for the wide amount of experimental data available in literature at different rotational velocities as well as different blade numbers. The target of the performed simulations is the numerical prediction of force (thrust) on the blade together with the noise level measured in the far-field microphone locations.

The numerical analysis methodology is based on a RANS aerodynamic approach for the simulation of the steady-state blade loading and acoustic sources combined with the Ffowcs Williams-Hawkings (FW-H) acoustic analogy based on the Farassat & Brentner formulation of moving surfaces for the noise levels prediction [104], [105].

Aerodynamic simulations were performed with both the Multiple Reference Frame (MRF) and Sliding Mesh (SLM) approach, with the Pressure-Based Coupled Solver and $k-\omega$ SST turbulence model [24]. Moreover particular attention was given to mesh generation, in order to build a mesh able to provide optimal y^+ , an adequate number of points in the boundary layer and quality for all experimental conditions simulated.

Optimized numerical settings and strategy, including periodic rotational boundary conditions, and Full MultiGrid initialization (FMG) have also been object of investigations to perform accurate aerodynamic and aeroacoustic calculations with CPU time requirements compatible to the industrial design process. Results of the simulations are compared with experiments showing the ability of this approach to predict noise with a discrepancy that lies in a range between 1 to 3 dB for higher rotational speeds. Investigations at lower rpm were carried out by performing unsteady simulations as the flow field is characterized by separated flow on the blade, with a significant increase of computational time.

The results provided below have been published in [115].

4.2.1 Geometry and Experimental Data

Experimental acoustic data published in [100], [101] have been used as reference for CFD aerodynamic and aeroacoustic simulations. The propeller blade geometry is the NACA 4-

(3)(08)-03, a straight blade propeller constructed from the NACA 16 2D airfoil section for its entire length, with a diameter of 4 feet. Geometrical details are given in Figure 4.4 where, blade-width ratio, blade-thickness ratio, ideal lift coefficient and design angle are given as function of the non-dimensional span position, r/R . Geometrical data are provided from 27% to 100% of span and the blade root is assumed to be mounted on a cylindrical shaped body while the blade tip is assumed to be smooth. The blade angle is given by the reference design angle (measured at $3/4$ of span) added or subtracted to the β curve of Figure 4.4.

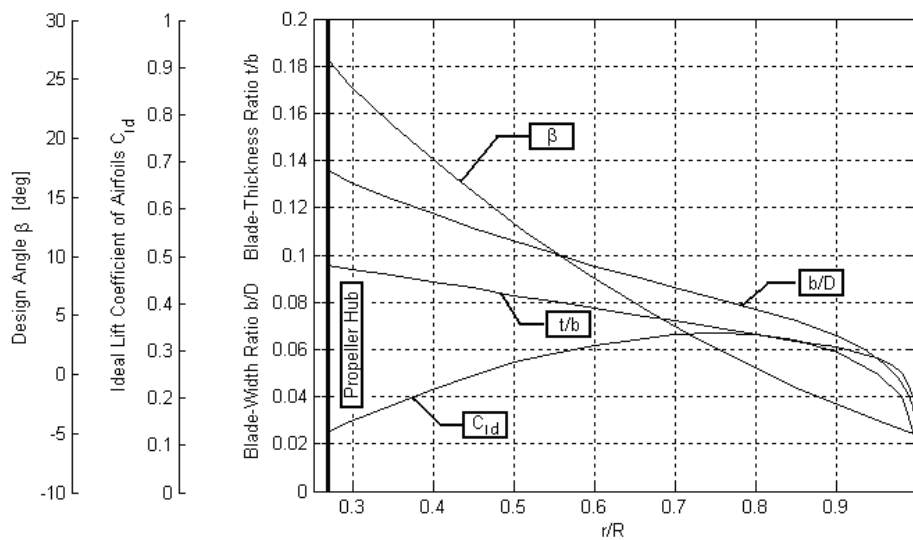


Figure 4.4: geometry of the NACA 4-(3)(08)-03 blade.

A 200 HP variable speed electric engine is used to change the rotational speed of propeller and the experiments were done with the propeller mounted on an adjustable hub which allowed the blade design angle to be changed manually. Experiments were carried out in a free-stream environment with zero wind speed. A survey rake was used to measure total pressure at a position 4 inches behind the engine, and the estimation of thrust was obtained as integration of pressure field, with an accuracy of $\pm 25\%$. Sound pressure and frequencies were measured with a Western Electric moving-coil pressure-type microphone and a Hewlett Packard Wave Analyzer. The nearest obstruction was located at 65 feet from the test stand and any discrepancy related to reflections of acoustic pressure is believed to be within the ordinary range of error of measurement for these tests. The ground is approximately located at a distance of 1 diameter from propeller axis of rotation.

A microphone was placed at ground level located 30 feet from the propeller hub and at a 15° angle behind the plane of rotation to achieve a visual angle $\theta = 105^\circ$ (where θ is the angle from propeller axis of rotation taken from the horizontal axis in front of the propeller). This particular angular position was chosen because it is near the value of θ for the maximum sound pressure at the range of sound harmonics measured.

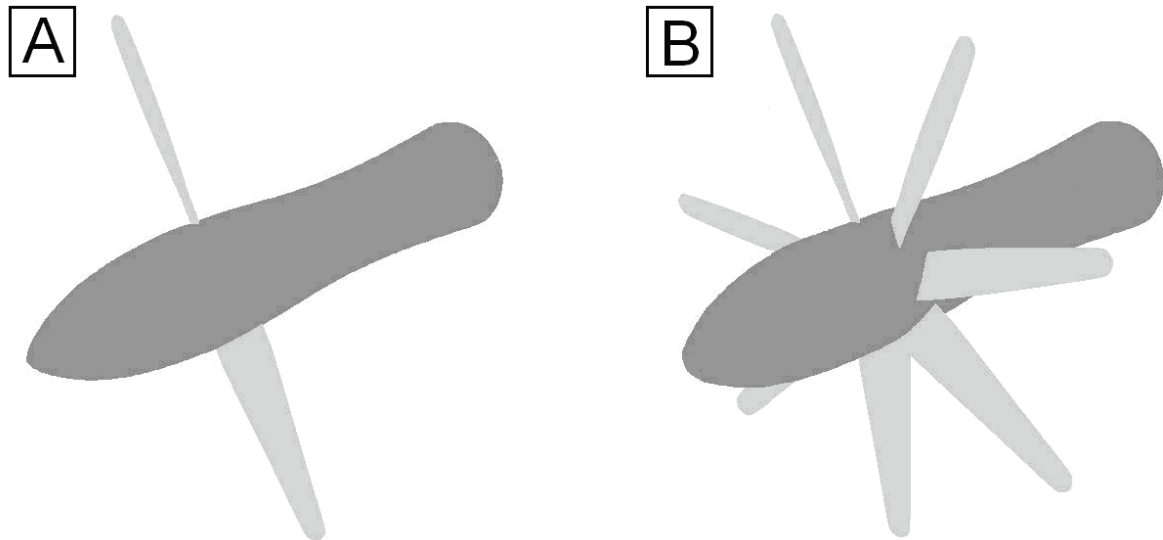


Figure 4.5: NACA 4-(3)(08)-03 propeller, 2-bladed and 7-bladed configurations

Sound pressures were measured for the first five harmonics of the fundamental rotational frequency for each test condition. Data were obtained for different rotational velocities and design angles of the propeller, and for different numbers of blades.

Experimental results show that the propeller thrust growth is different for the two and seven bladed propellers when the rotational speed is increased. It is interesting to note that for comparable thrust, the seven bladed propeller is always quieter than two bladed configuration.

The propeller geometry was constructed from 18 airfoil sections of the NACA 16 series family. Airfoil sections were located from 30% to 90% of span with a constant spacing of 5% of span, while tip airfoil sections at 92.5%, 95%, 96.5%, 98% and 99% of span were located to follow tip chord gradient. Moreover a smooth tip was generated to cover the gap between 99% and 100% of span.

Airfoil section points were imported into ANSYS-GAMBIT[®], where NURBS lines and surfaces were generated, and the propeller was mounted on a shaped cylindrical body used as

spinner. The propeller tip was modelled with a smoothed rounded surface, while the propeller root was intersected with spinner, Figure 4.6.

In ANSYS-GAMBIT[®] a triangular surface mesh was generated, unstructured on the blade and spinner body and tri-mapped around the leading edge. A hybrid volume mesh was then generated in ANSYS-TGRID[®] with prism layer extrusion and tetrahedral mesh giving a suitable value of y^+ on the blade surface for all rotational speeds considered (in general less than 1). Periodic sliced domains containing only one blade were generated to simulate the isolated propeller. This reduced the total number of cells as just half and one seventh of the domain had to be modelled respectively for 2 and 7 blade configurations.

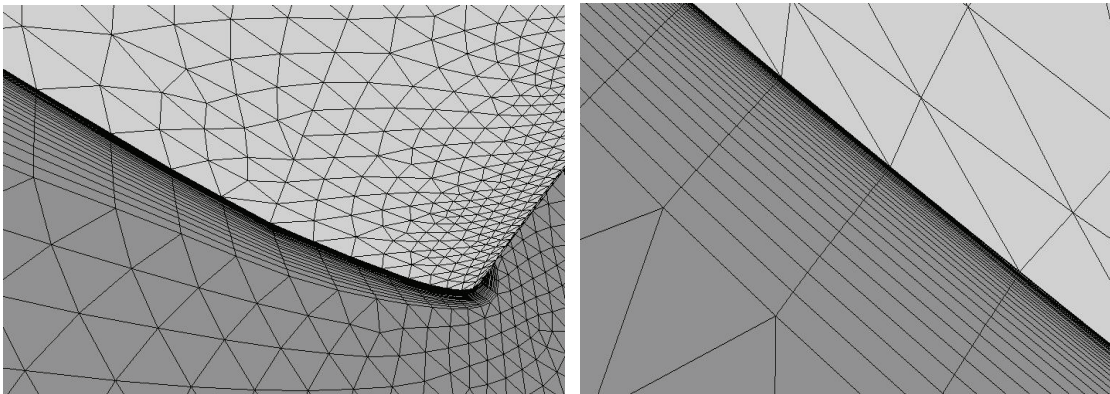


Figure 4.6: grid details, leading edge (left) – Blade suction side (right).

Prism layers were designed in order to have at least 20 layers within the physical boundary layer. This was achieved monitoring the contours of Turbulent Viscosity Ratio at different stations in the spanwise direction. By looking at those contours it is possible to estimate the boundary layer thickness by doubling the distance from the wall of the position of the maximum Turbulent Viscosity Ratio. This gave us the possibility to monitor the boundary layer thickness on the blade for both configurations and for all rpm conditions, generating a final mesh with the desired specifications.

The final grid had 40 prism layers extruded from the blade surface mesh, with tetrahedral cells filling the rest of the fluid domain, giving a total cell count of approximately 10M, per sliced periodic domain, Table 4.1. Pictures of this final grid around leading edge and on the suction side are given in Figure 4.6.

Wall optimal y^+ value for all test conditions was also a required specification. In Figure 4.7 a contour of the y^+ value on the blade is given for a higher rotational speed (2-Blades, 4850rpm) in order to show that for all tested cases this value is below 1 on the whole blade surface except for a small region close to tip leading edge.

All available experimental rpm conditions are given in Table 4.2 for configurations A and B. Lower rpm values are available for both configurations while for higher rpm they are different.

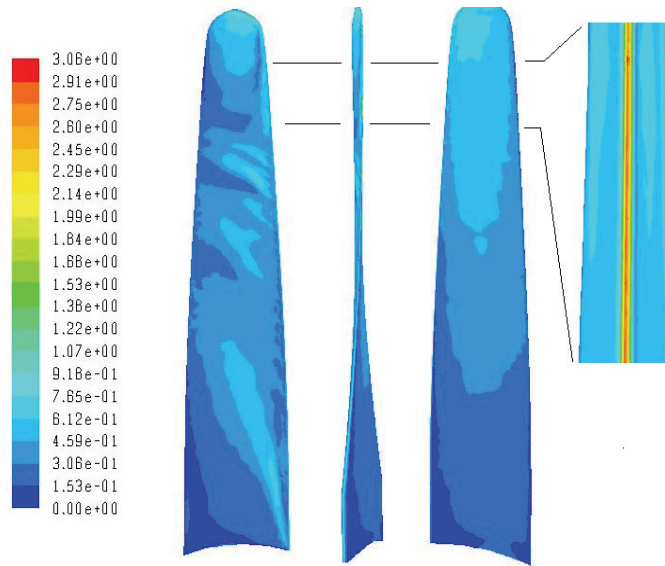


Figure 4.7: y^+ contours on blade – 2-blades 4850RPM
From left to right: suction side, front view, pressure side and tip leading edge detail

Aerodynamic simulations were performed with RANS Pressure Based Coupled Solver with Periodic Rotational Conditions, Multiple Reference Frame and $k-\omega$ SST turbulence model (Table 4.3).

Conf. ID	Description	Cells
A	2 Blades – Periodic 40 Prisms Layers	10M
B	7 Blades – Periodic 40 Prisms Layers	10M

Table 4.1: simulated configurations for NACA 4-(3)(08)-(03) propeller.

All simulations were performed at the blade angle $\beta_{3/4}$ of 16.5 deg based on experimental references.

Conf. ID	Rotational Speed [rpm]				
	1600	2680	3450	3770	4850
A	✓	✓	—	✓	✓
B	✓	✓	✓	—	—

Table 4.2: rotational speed conditions for NACA 4-(3)(08)-(03) propeller.

P-V Coupling	COUPLED
Turbulence Model	$k-\omega$ SST
Pressure Transport Scheme	Standard
Density/Momentum/k- ϵ /Energy	2 nd order
Asymptotic Mach Number	0
Rotational Speed	Variable

Table 4.3: ANSYS-FLUENT[®] settings.

Acoustic Sound Pressure Level (SPL) at microphone locations was estimated applying FW-H Acoustic Analogy based on Lighthill's equations (2.65) extended for boundary conditions on surfaces in arbitrary motion [104], [23], [24]. The surfaces were introduced into Lighthill's equation by the Heaviside function $H(f)$ leading to the equation (2.90). In this relation the first source term T_{ij} is the Lighthill's stress tensor, related to volume sources while F_i and Q_i are the FW-H source terms related to surface noise emission [23], [24]. Its solution is provided in equation (2.102), where monopole, dipole and quadrupole sources terms, respectively related to body thickness, flow interaction with moving bodies and unsteady stresses, are given. It is important to notice that monopole and dipole are related to surface integrals while quadrupoles are volume sources. This contribution, often smaller than the other two, becomes zero for subsonic flows, and it is dropped off in the performed calculations [23], [24].

One of the main advantages of the FW-H model is the possibility to be coupled with a steady RANS simulation for the calculation of noise sources, avoiding the need for a direct computational aeroacoustic calculation.

This is of particular interest for propeller applications, where for most of operating conditions, a steady load can be assumed on the blade.

Flow field initialization was done with zero wind speed, a very low rotational speed (50 rpm), and 1st order transport schemes for all variables. Then a gradual increasing of rotational velocity was applied (50→100→500→ Final rpm). At the final rpm condition, the turbulence model was switched on and after 50 iterations the transport schemes were switched to 2nd order. The convergence of each case was checked according to thrust force and torque oscillation around the mean value (< 1%), obtaining a fully converged case in approximately 500/600 iterations.

A speed up of convergence can be achieved by initializing the flow field using a Full MultiGrid technique (FMG) [24]. This consists of building up a certain number of grid levels using the Full-Approximation (FAS) Multigrid procedure [106], [107]. The FMG algorithm performs an inviscid Euler solution on the coarser grid level until a given order of residual reduction or a maximum number of cycles are reached. Then it interpolates the solution on the next finer level and solves, and so on up to the first grid level. This approach allowed a saving of up to 50% of computational cost achieving a fully converged solution in approximately 300 iterations.

4.2.2 Simulations and Results

Good agreement between experimental and predicted values of thrust for all simulated cases was achieved. In Figure 4.8 and Figure 4.9 comparisons between experimental and simulated data are available for the 2-bladed and 7-bladed configurations respectively.

For almost all rotational speeds simulated, CFD results are close to the upper boundary (+25%) of experimental data. No significant difference in thrust prediction between MRF and SLM simulations is obtained.

Very good agreement between experimental and simulated values of Sound Pressure Level was also achieved from 2680 to 4850 rpm for configuration A and from 2680 to 3450 for configuration B. The difference between experimental results and these cases lies in a range between 1 to 3 dB, while the under-prediction at the lowest rotational speed of 1600 rpm is quite evident. Before discussing these discrepancies it is useful to highlight the difference between the two methods used to measure the propeller noise: classic microphone-voltmeter and wave-analyzer processed data.

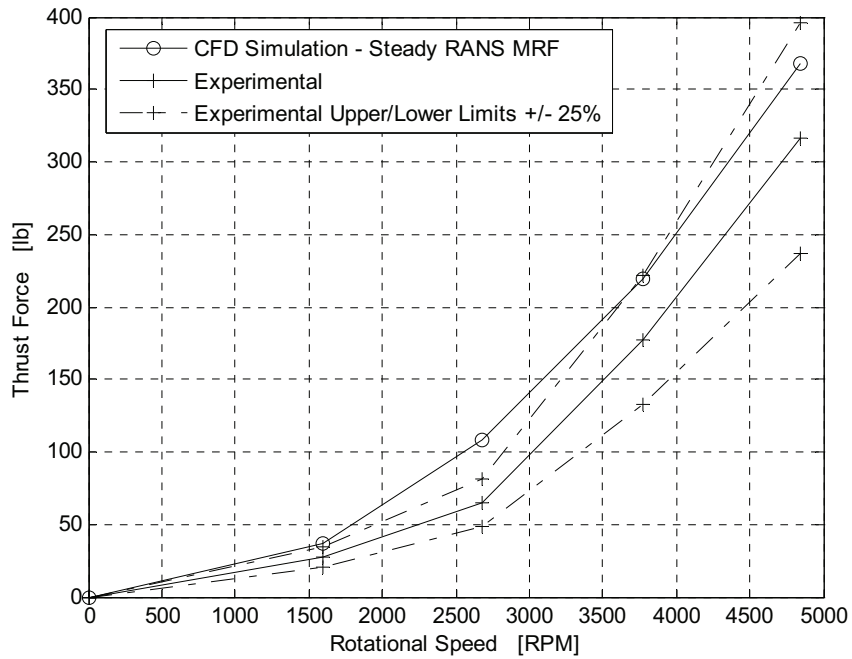


Figure 4.8: propeller thrust [lb]
NACA 4(3)-(08)(03) – 2-bladed configuration.

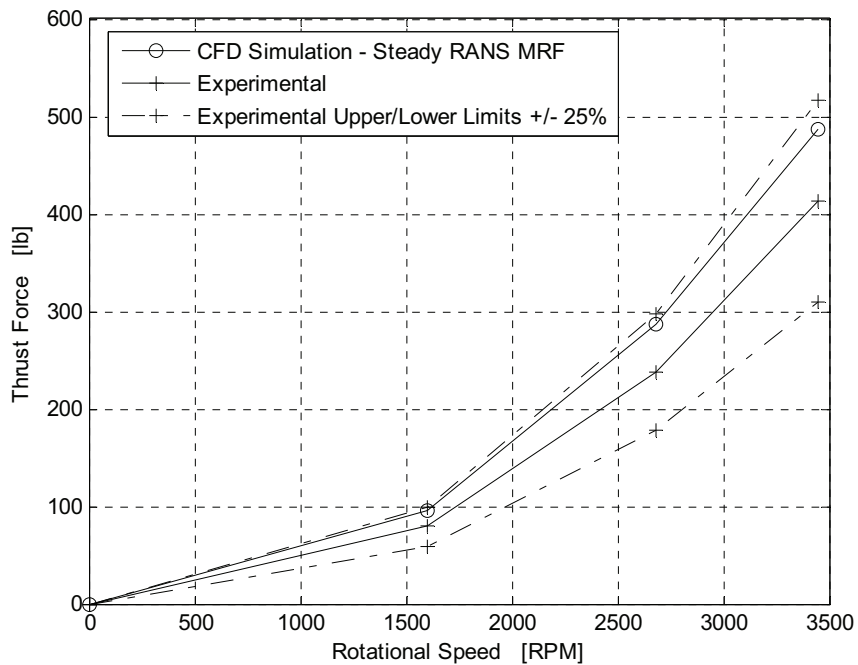


Figure 4.9: propeller thrust [lb]
NACA 4(3)-(08)(03) – 7-Bladed configuration.

In the first case, the measured total microphone voltage is converted directly to decibels. This procedure gives the summation of the entire band of frequencies emitted. When measurements are filtered by the wave-analyzer only the sound pressure corresponding to the rotational noise-frequency peaks are summed (the first 5 harmonics).

Therefore, if the vortex noise is strong compared with the rotational noise, as is usually the case at lower rotational speeds, values determined by microphone voltmeter will be larger than values determined from wave-analyzer measurements.

Based on this and looking at the increasing discrepancies between the experimental data obtained with the two different measurement methodologies, it is evident that the noise at the 1600 rpm condition has a stronger vortex broadband noise component compared to higher rpm conditions due to the presence of separated and unsteady flow on the blade.

Moreover, this separation is also clearly visible by post-processing of the CFD results, where a wide cross flow is visible on the blade for this rotational speed.

This is also responsible for the noise discrepancy between the RANS-FWH prediction and experimental data, while it disappears for higher rotational velocities, where most of the flow is attached on the blade and the prediction is very accurate.

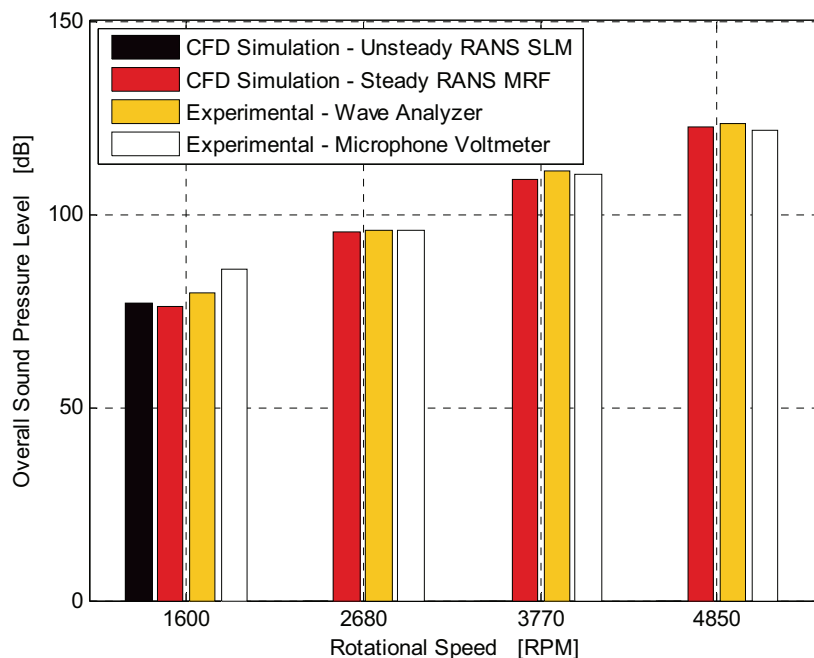


Figure 4.10: propeller overall SPL [dB]
NACA 4(3)-(08)(03) – 2-Bladed configuration.

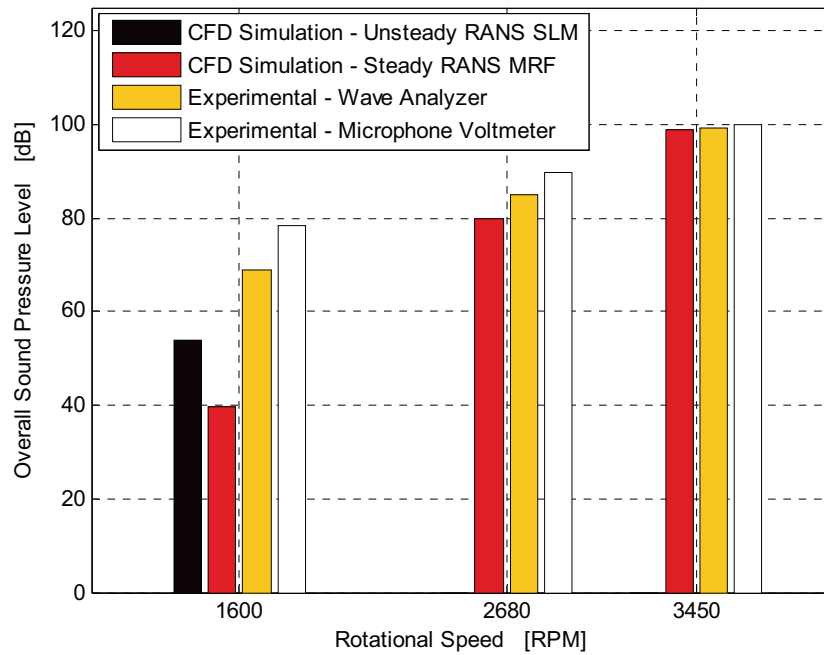


Figure 4.11: propeller overall SPL [dB]
NACA 4(3)-(08)(03) – 7-Bladed configuration.

To better investigate this phenomenon an Unsteady RANS Sliding Mesh simulation was performed at 1600 rpm, with a time step of 0.00045 sec (1000 time steps per revolution at 1600 rpm). For each time step 15 iterations were needed to achieve a stabilizations of forces on blade, and 1 sec of simulation was performed (2000 time steps, 30000 iterations approximately).

The computational cost of this simulation was very high, due to the unsteady approach of solver, and this is the reason why only the lower rotational speed, where higher discrepancies were found, was investigated.

As we can see in Figure 4.10 and Figure 4.11 (black tab) a small correction of a few dB is given by this approach for the 2-blades configuration, while a big correction, from 42.5 dB to 54 dB, is achieved for the 7-blades configuration, but wave-analyzer is still in poor agreement at approximately 68 dB.

This result suggests that to obtain better prediction at very low rotational speed such as 1600 rpm, more accurate simulations are needed to be able to catch all the transient features and broadband noise (DES, LES or SAS turbulence model, smaller timestep, finer hexahedral grid), with a much higher computational cost.

The possibility of reducing the computational cost of RANS-FWH was investigated by performing some simulations on a coarser grid.

A new grid with only 5 prism layers and a 2.2M total cell count per sliced periodic domain was therefore generated. Simulations were performed with the MRF steady state approach, with RANS modelling and a wall function, and the Full MultiGrid Initialization technique (FMG) as used for the 10M cells grid. With this coarser grid a fully converged solution was obtained in approximately the same number of iterations (about 300) but with a very competitive computational time for an industrial simulation, about 3 hours on a dedicated LINUX QUAD-CORE Machine, with a 2.8GHz CPU Clock, 85% lower than finer 10M computational grid.

Simulations were performed at the higher rotational speed for both blade configurations, achieving an SPL prediction within 0.5 dB of that of the 10M cell grid.

The reason for the small difference in the noise prediction between the fine and coarse grid can be explained by the following considerations:

- According to equation (2.102) the FW-H model takes into account the effects of monopole and dipole sources related to surface integral of pressure loads on emitting surfaces.
- Pressure loads are mostly related to blade lift and for attached flow this is mainly an inviscid problem.
- At higher rotational speeds in our case the flow is attached.

We can conclude that, only in the case of attached flow, a coarser grid can be used to perform an indicative analysis of propeller noise at a cruise condition. Moreover this can be important in order to save time for early design stage simulations, where computational cost and time play a fundamental role, but for off-design conditions, where flow is characterized by zones of separation, it is recommended that a more refined grid is used.

4.3 Transonic Cruise Propellers: NASA SR2 and SR3

In the last 20 years, the flight services market has significantly increased its business volume led by the increase of demand for fast and cheap connections among European countries. The proliferation of regional jet aircraft (e.g. A319/320/321, or B737) is a product of this trend; they are designed and optimized according to market requirements, with a passenger capacity approximately between 150 and 210 seats, and ranges between 800 and 1500 km, able to cover the most of the flight market in Europe.

Looking at the last 10 years in particular, this demand moved also towards shorter routes affected by geographical barriers (i.e. sea or mountain chains) where other solutions (i.e. trains, ferries) are not able to provide the quick and cheap service demanded.

Design trends are motivated also by the general interest from all aerospace manufacturer companies in the reduction of fuel-related costs and the environmental footprint of aircraft. These two phenomena underlie a recent re-emergence of interest in the regional turboprop aircraft, smaller than the regional jet and able to be competitive for shorter ranges, less fuel-demanding and more environmentally respectful.

As already discussed in the first chapter, a key point in the modern turboprop industry is the comfort perceived by the passenger (especially in terms of vibrations and noise), together with the increase of cruise speed of aircraft. Looking at the recent success of the Bombardier Dash Q400, a new concept turboprop aircraft which is currently used by a number of companies in Europe, it is clear that it covers a key market window, providing a cruise speed of 670 km/h, high level of comfort experienced by passenger, together with a reduction of about 30% in fuel demand and CO₂ emissions relative to an equivalent small size turbofan aircraft. Therefore we can anticipate a growing interest among all aircraft manufacturer towards the advanced turboprop concept in the coming decades, in order to increase the cruise speed up to actual turbofan standard, and improve comfort issues.

In the next paragraphs the attention will be focused on the aerodynamic and aeroacoustic simulation of the two high speed propeller geometries NASA SR2 and NASA SR3. The approach used is quite similar to the approach applied for the NACA 4-(3)(08)-03 propeller in paragraph 4.2, based on a RANS aerodynamic approach for the simulation of the steady state load on the blades and acoustic sources and on the FW-H acoustic analogy for the prediction of SPL at microphone locations.

Moreover the test conditions chosen in this case are transonic, based on the Flight Test (FT) and Wind Tunnel (WTL) conditions provided in [110], [98], [111] and [112].

These two transonic cruise propellers were tested from a far-field Mach number ranging from 0.6 to 0.9 and for rotational velocities between 6000 and 9000 RPM, experiencing transonic flow conditions and fully developed shock waves on the blades.

The results of the simulations are compared with experiments, showing the ability of the RANS-FWH approach to predict noise levels for such kind of problems with discrepancies which lie in a few decibels. Moreover an optimized CFD simulation strategy has been deeply investigated to perform the complete aerodynamic and aeroacoustic calculations with highly competitive computational cost.

The results achieved in these paragraphs are published in [116], [117] and [118].

4.3.1 Geometry and Experimental Data

Two transonic propeller geometries have been used as test cases for these simulations: the NASA SR2 and SR3. They are both 8-bladed propellers, constructed from the NACA 65 2D airfoil section from root to 37% of its span extension, and from the NACA 16 2D airfoil section from 44% to the tip. The mid region, from 37% to 44% of span, is made by a transition zone where airfoils do not lie in any standard family. Furthermore the NASA SR2 is a straight blade propeller, while the NASA SR3 is a swept blade propeller [108], [109].

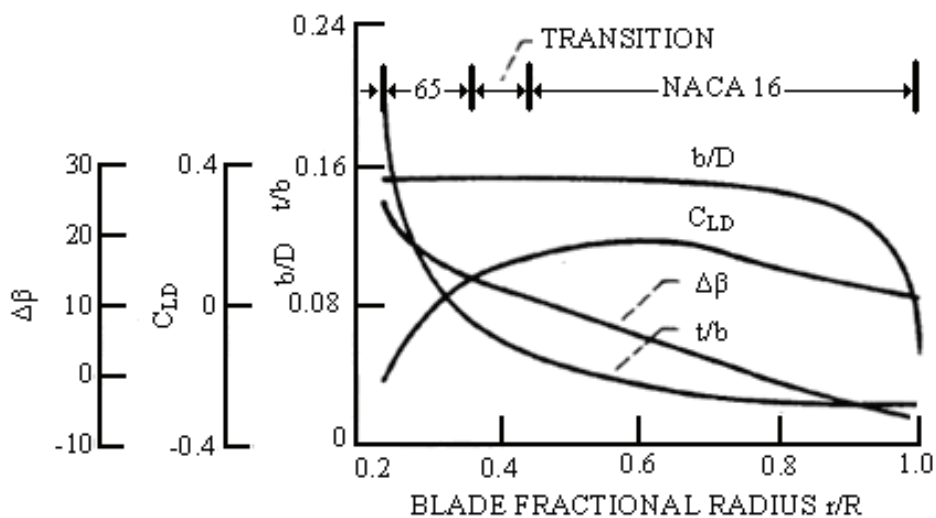


Figure 4.12: geometry of NASA SR2 propeller

In both cases propeller diameter is 0.622 m (24.5 inches) and geometrical details are given in form of blade-width ratio (b/D), ideal lift coefficient (C_{LD}), design angle ($\Delta\beta$) and blade-thickness ratio (t/b) as function of blade fractional radius (r/R). Moreover also the swept angle as function of span extension is provided for the NASA SR3 only.

Geometrical data are provided from 24% to 100% of span and the blade root is assumed to be mounted on a cylindrical shaped body while the blade tip is assumed to be smooth. The blade angle is given by the reference design angle (measured at $3/4$ of span) added or subtracted to the $\Delta\beta$ curve. In Figure 4.12 and 4.13 the geometrical data are provided for the NASA SR2 and SR3 respectively.

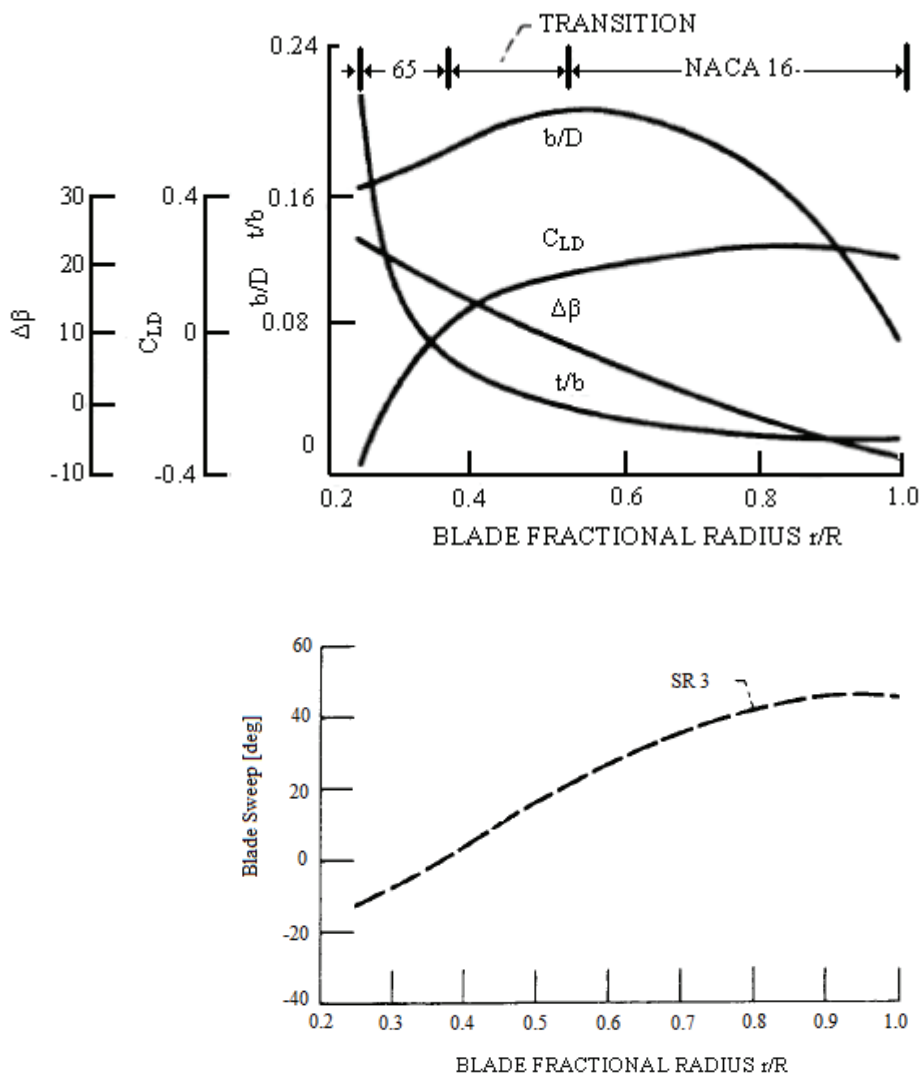


Figure 4.13: geometry of NASA SR3 propeller

Experimental data taken as reference for the performed calculation are based on data published by NASA in [110], [98] and [112].

These data contain both Wind Tunnel (WTL) and Flight Test (FT) experiments. WTL data were achieved in the NASA Lewis 8-by-6 foot wind tunnel with different $\beta_{3/4}$ and the blade mounted on a adjustable-pitch axisymmetric body used as spinner mounted to tunnel ceiling with a rear support, as shown in Figure 4.14.

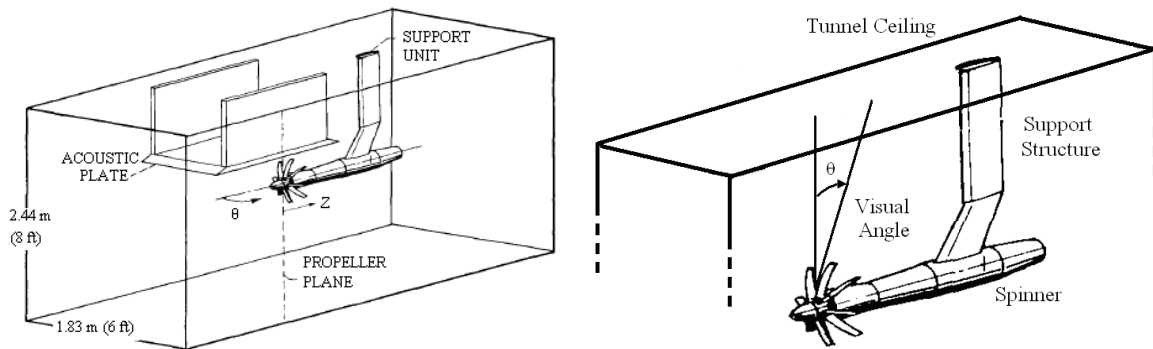


Figure 4.14: sketch of NASA propeller mounted in NASA Langley 8-by-6 foot wind tunnel with and without acoustic plate device

Microphones were located on tunnel ceiling in the propeller plane at a distance equal to 0.8 diameters from propeller tip [98] as shown in Figure 4.14 (right) or on a acoustic plate aligned along a direction out of the propeller plane [110] as shown in Figure 4.14 (left).

This acoustic plate, located 0.3 diameters far from the propeller tip, allows microphone positions at the same distance of tunnel ceiling (0.8 diameters) in order to achieve a set of comparable data being able to control the acoustic interference effect given by this experimental device.

Microphone location is provided as function of propeller longitudinal coordinate Z and microphone azimuthal angle θ for acoustic plate data set (Figure 4.14-left) and as function of the only microphone longitudinal angle θ (also called visual angle) for tunnel ceiling data set (Figure 4.14-right). In both cases the microphones located approximately 20 degrees behind the propeller plane are assumed to be the most accurate as well as the less affected by repeatability error according to the NASA references [98] and [112].

On the other hand experiments were performed also in FT, mounting the propeller on a support located on the NASA Jetstar Aircraft and the microphones on the aircraft fuselage or on an upper dedicated support (boom), as shown in Figure 4.15.



Figure 4.15: flight test instrumented NASA Jetstar aircraft

In both cases microphones are located in the propeller plane at a distance equal to 0.8 diameters to the propeller tip. This positioning was designed in order to achieve comparable FT and WTL data.

The experimental data have been divided in 5 different data sets according to the following list, and for all of these sets computational results will be provided in next paragraphs.

- **DATA SET 1:** SR2-WTL, 2 microphones mounted on tunnel ceiling, Mach = 0.85, Rot. Speed = 9070 RPM.
- **DATA SET 2:** SR2-FT, 6 microphones mounted on aircraft fuselage, Mach = 0.787, Rot. Speed = 7127 RPM.
- **DATA SET 3:** SR2-WTL, 12 microphones mounted on acoustic plate, Mach from 0.6 to 0.8, Rot. Speed from 6478 to 8650 RPM.
- **DATA SET 4:** SR3-FT, 6 microphones mounted on aircraft fuselage, Mach = 0.787, Rot. Speed = 7461 RPM.
- **DATA SET 5:** SR3-FT/WTL, 2 microphones mounted on aircraft fuselage and tunnel ceiling, Mach from 0.6 to 0.85, Helical Tip mach Number from 0.86 to 1.21.

In these different experimental data sets the propellers were operated changing the nominal advance ratio J defined according the relation (4.20)

$$J = \frac{V}{nD} \quad (4.20)$$

where V is the asymptotic velocity in m/sec, n the rotational speed in rps and D the diameter in m. Aerodynamic performances were measured by the power coefficient C_P (4.21)

$$C_P = \frac{P}{\rho_o n^3 D^5} \quad (4.21)$$

where P is the power in W, ρ_o the density in Kg/m³, n the rotational speed in RPS and D the propeller diameter in m.

At this stage it is important to point out that the acoustic experimental data are affected by several spurious effects (e.g. experimental devices interference, pressure loss in the wind tunnel, etc.) and they need to be corrected to be properly compared to computational data. An extensive literature research was done in order to quantify these corrections and this aspect will be discussed in the next paragraph.

4.3.2 NASA SR2 and SR3 Aerodynamic and Aeroacoustic Modelling

The NASA SR2 and SR3 blade geometries were constructed from 6 airfoil sections of the NACA 65 series family for the lower part and 14 of the NACA 16 series family for the upper part. Airfoil sections were located with a constant spacing up to 90% of span, while a decreasing spacing was adopted up to 99% of span to follow tip chord gradient. Moreover a smooth tip was generated to cover the gap between 99% and 100% of span.

In Figure 4.16 and 4.17 a picture of CAD model for NASA SR2 and SR3 are respectively provided. CAD model and computational grid were constructed according to the same quality criteria adopted for NACA 4-(3)(08)-03 propeller (paragraph 4.2.1). Moreover as in these cases the Mach and the Reynolds numbers are much higher than in the previous case and consequently the computational grid requirements are much more demanding.

Airfoil section points were imported into ANSYS-GAMBIT[®], where NURBS lines and surfaces were generated, and the propeller was mounted on a shaped cylindrical body used as spinner. A triangular surface mesh was generated in ANSYS-GAMBIT[®] on the blade and spinner while a hybrid volume mesh was then built in ANSYS-TGRID[®] consisting of 40 prism layers and tetrahedral cells in the remaining computational domain.

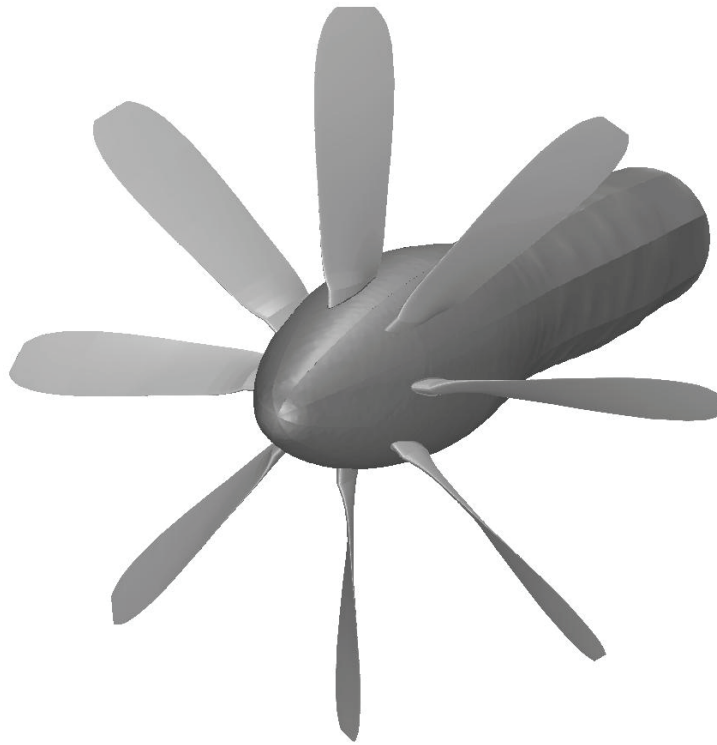


Figure 4.16: NASA SR2 propeller, CAD model

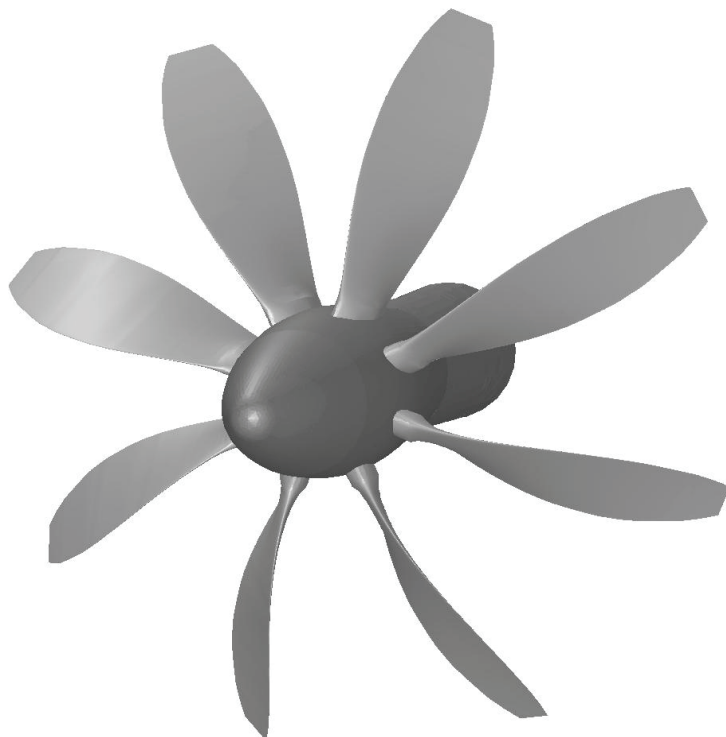


Figure 4.17: NASA SR3 propeller, CAD model

This approach gave a suitable value of y^+ on the blade surface for all rotational speeds considered, in general less than 1, and the thickness of the first prism layer on the blade was approximately $1\ \mu\text{m}$.

To reduce the total number of cells, periodic sliced domains containing only one blade were generated to simulate the isolated propeller. Prism layers were designed in order to have not less than 20 layers within the physical boundary layer, whose size was estimated by looking at the maximum reached by the Turbulent Viscosity Ratio (TVR) at different stations in the span wise direction.

In fact the maximum is approximately located in the middle of the physical boundary layer, and doubling its distance from wall gives a measure of boundary layer thickness. These criteria were adopted for all the grids generated for NASA SR2 and SR3 in different design angle configurations.

The final grid configuration had 40 prism layers extruded from the blade surface mesh, with tetrahedral cells filling the rest of the fluid domain giving a total cell count of approximately 10.5M per sliced periodic domain.

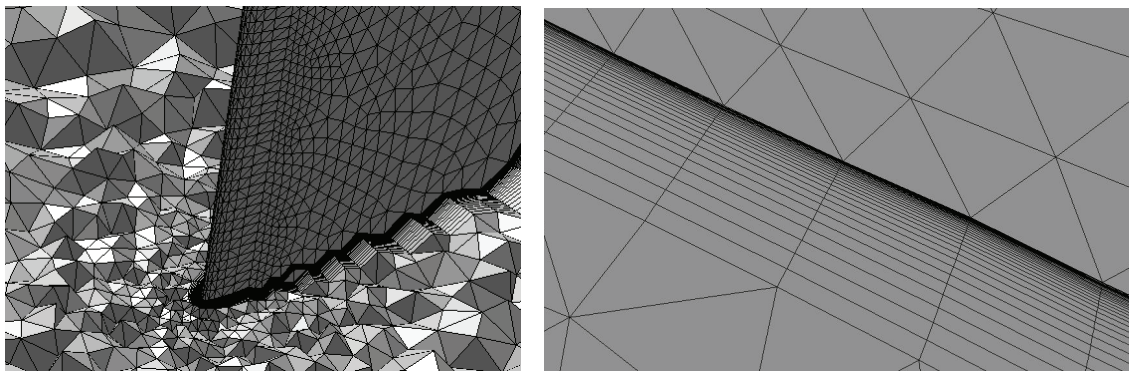


Figure 4.18: computational grid details

Pictures of this final grid around leading edge and on the suction side are given in Figure 4.18 for the NASA SR2, and an example of the TVR contour used to detect boundary layer thickness is given in Figure 4.19 (left).

Moreover also a picture of the optimal y^+ reached on the blade surface for a cruise Mach number condition equal to 0.8 is provided in Figure 4.19 (right) in order to show that this value is below 1 on the whole blade surface except for a small region close to tip leading edge.

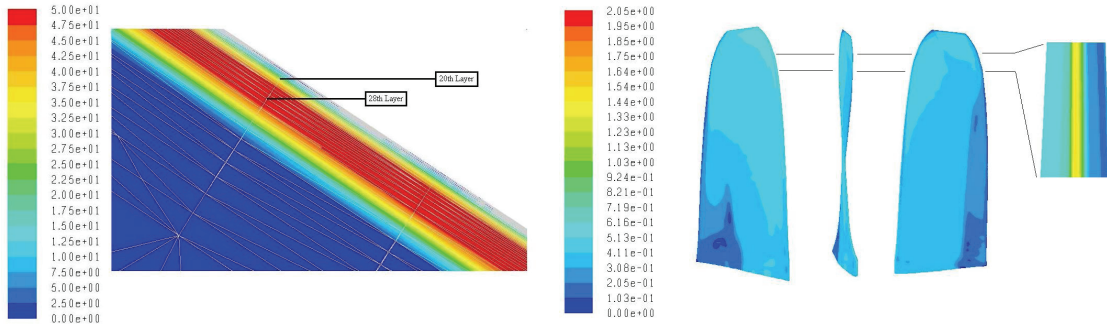


Figure 4.19: turbulent viscosity ratio contours at 90% of span, pressure side (left) and y^+ contours on blade (right), NASA SR2, $M=0.8$ – 8650 RPM

Aerodynamic simulations were performed with RANS Pressure Based Coupled Solver with Periodic Rotational Conditions, Multiple Reference Frame [24] and $k-\omega$ SST turbulence model, Table 4.4.

Fluid Model	ideal-gas
Turbulence Model	$k-\omega$ SST
P-V Coupling	COUPLED
Pressure Transport Scheme	PRESTO
Density/Momentum/ $k-\omega$ /Energy	2 nd order
Asymptotic Mach Number	variable
Rotational Speed	variable

Table 4.4: ANSYS FLUENT settings

Acoustic SPL at microphone locations was estimated applying the Farassat & Brentner formulation of the FW-H Acoustic Analogy, as already discussed in the paragraph 4.2.1. The time-signal transformed via FFT gave us a complete noise spectrum up to a frequency of 25 KHz, but to compare simulated results and experimental data only the maximum of SPL that coincides with the first Blade Passing Frequency (BPF) was taken into account. This approach is of particular interest for propeller applications, for the majority of operating conditions, where a steady load can be assumed on the blade.

The convergence of each case was checked according to thrust force and torque oscillation around the mean value ($< 1\%$), obtaining a fully converged case in approximately 800/1000 iterations.

The simulation strategy adopted consists of a gradual increase of the rotational speed, Mach number, and other settings achieve a stable and fast convergence. For example the following was found to give a smooth convergence solution:

1st Step: Segregated solver. Initialize with asymptotic flow field. Gradual increase of rpm (50→200→500→2000)

2nd Step: Gradual increase of Mach and rpm (0.1→0.4, 2000→4000, 0.4 →0.6, 4000→6000), activation of compressibility and turbulence model

3rd Step: Switch to final Mach and rpm, switch to COUPLED solver and activation of energy equation

A further speed up of convergence was achieved by initializing the flow field using a Full Multigrid technique (FMG) [24]. This consists of building up a certain number of grid levels using the Full-Approximation (FAS) Multigrid procedure [106], [107]. The FMG algorithm performs an Inviscid Euler solution on the coarser grid level until a given order of residual reduction or a maximum number of cycles are reached. Then it interpolates the solution on the next finer level and solves, and so on up to the first grid level. This approach allows to significantly reduce the time for convergence when compared to the mentioned steps procedure, allowing us to skip the 1st and 2nd steps saving up to 50% of computational cost.

Moreover the same approach was performed on a coarser grid of approximately 2M cells, constructed with only 5 prism layers in the boundary layer and a y^+ suitable to apply the turbulence model with the wall functions.

Results show very small discrepancies respect to the results achieved on the finer grid, with a much faster calculation time, being able to perform a complete aerodynamic and aeroacoustic simulation in less than 5 hours on a dedicated LINUX Quad-Core machine, 2.8 GHz Core Clock.

As previously anticipated all the data set taken as reference for our calculations are affected by effects cannot be taken into account into the performed numerical simulations. Moreover these effects are not the same for all experimental configurations, but depend by the devices used in each experiment and by the WTL and FT conditions experienced during the tests.

For this reason there was the clear necessity to have a set of correction to apply to different data sets in order to compare computational and experimental data.

From a general point of view these effects and the involved corrections can be classified as following:

- Experimental device interference (acoustic plate for WTL and fuselage for FT)
- Pressure loss in wind tunnel
- Near-Field/Far-Field SPL scaling and Pseudo-Noise
- Wind Tunnel effects
- Non-linear effects

For example experimental interference and wind tunnel effects can be simulated with CAA modelling the noise sources and the noise propagation up to the receivers, so losing the advantages of FW-H analogy and the domain periodicity. This implies a huge increase of the computational cost of the simulations both for the increase in domain cells number as for the increase of computational effort required by the direct CAA, making this approach unfeasible for the industrial application.

Furthermore these effects can be taken into account by fixed contribution added or subtracted to the computational value as indicated into the experimental reports. In particular plate device interference effect is determined to be equal to 8 dB to be subtracted to the experimental noise values [110], the fuselage interference effect is determined to be equal to 6 dB [98], while the wind tunnel effect is estimated in 5.5 dB for $M=0.6$ and 2.5dB for $M=0.8$ according to [112]. These corrections are applied to all microphones independently by their angular positions respect to the rotor plane. This means that no directivity dependence is considered, and this is not true. However as stated already above the corrections are designed to match the most accurate microphones located approximately 20 degree behind the propeller plane [110], [98] indicated also as the locations less affected by repeatability errors in different test-campaigns [98], [112].

Another important correction was applied in order to extend the FW-H acoustic analogy predictions to the near-field microphones, as it is valid for far-field locations only. In this context “near field” implies the region affected by pseudo-noise.

In our case the microphones are located quite closer to the propeller, and this gives an underestimation of the computed SPL values. So the microphones were located at 16

diameters far from propeller and the SPL results were scaled to 0.8 diameters with equation (4.22) for correction of distance D, according to [98].

$$SPL_{NEAR} = SPL_{FAR} + 20\log_{10}(D_{FAR}/D_{NEAR}) \quad (4.22)$$

This correction obviously depends by how far microphones are located, and in the case of 16 diameters, 26 dB are needed to scale the 0.8 diameter position. Then 1dB was added to take into account of the pseudo-noise for M=0.6 and 1.5 dB for M=0.8, considering the estimates reported by NASA [98], [111].

Moreover NASA Lewis 8-by-6 foot transonic wind tunnel is affected by pressure loss depending on the test Mach number [112]. In particular, the static pressure in the test chamber is 90KPa for M=0.6 and 76KPa for M=0.8. This effect can be taken into account with the altitude correction (4.23) for pressure P, as provided in [98].

$$SPL_{P1} = SPL_{P2} + 20\log_{10}(P_1/P_2) \quad (4.23)$$

This correction is 1dB for M=0.6 and 2.5dB for M=0.8 for all microphones, according to simulations that were all performed with an asymptotic static pressure of 101KPa.

Finally the last correction applied is related to non-linear effects for the presence of large shock waves in the flow field. One way of dealing with this is via the quadrupole source term in the acoustic analogy. The first valid analysis of the importance of the quadrupole source for high-speed rotors was made based on a two-dimensional aerodynamic calculation [113], showing how important such source effects are for the generation of additional noise in the blade section in the speed range between the critical Mach number (when flow over the aerofoil exceeds the speed of sound) and a Mach number of 1. The magnitude of this correction is in the order of a few dB as reported in reference [113] and it was estimated to be about 1dB for M=0.6 and 3dB for M=0.8 test conditions.

4.3.3 NASA SR2 Results: Data Sets 1-2-3

In this paragraph the computational results achieved for the NASA SR2 propeller are provided, from data set 1 to data set 3.

The data set 1 consists of the WTL test of NASA SR2 according to the reference [98]. Propeller is tested at a Mach number equal to 0.85 with a rotational number equal to 9070 RPM, in order to achieve an advance ration equal to 3.06, comparable with the nominal cruise condition for this propeller [110]. Test conditions and microphone locations are summarized in Table 4.5. Aerodynamic solution was correlated to experimental data in order to match the experimental C_P by changing the $\beta_{3/4}$ design angle. The optimal correlation was achieved for computational design angle 2 degrees higher than the experimental one equal to 60 deg.

Wind Tunnel – 2 Microphones mounted on tunnel ceiling 0.8 D far from propeller tip NASA SR2 – M=0.85, 9070 RPM, J=3.06							
Microphone ID	M1-WTL				M2-WTL		
Visual Angle θ [deg]	110				130		
	Mach numb.	J	RPM	$C_{P,EXP}$	$C_{P,CFD}$	$\beta_{3/4,EXP}$ [deg]	$\beta_{3/4,CFD}$ [deg]
Wind Tunnel Test	0.85	3.06	9070	1.89	1.88	60	62

Table 4.5: Data Set 1, overview and aerodynamic correlation

The comparison between acoustic computational and experimental results is provided for the two microphones considered in Figure 4.20. Here the SPL level measured and computed for the Blade Passing Frequency (BPF) are compared, showing how the RANS-FWH is able to provide a very accurate prediction. Furthermore the prediction seems to be better for the first microphone located at a visual angle equal to 110 deg which means 20 degrees behind the propeller plane, according to NASA experimental references.

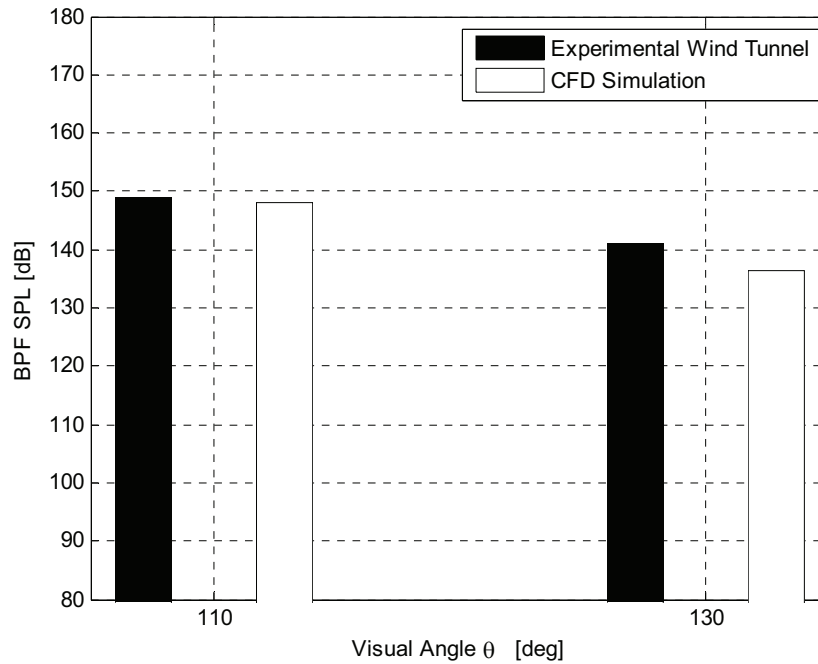


Figure 4.20: Data Set 1, results

Experimental data set 2 is focused on FT performed for NASA SR2 propeller. Here the NASA SR2 blade is mounted on the NASA Jetstar aircraft and tested with a flight Mach number equal to 0.787 and a rotational speed equal to 7127 RPM. These conditions allow advance ratio equal to 3.18. All data are reported in Table 4.6.

Flight Test – 6 Microphones mounted on fuselage 0.8 D far from propeller tip NASA SR2 – M=0.787, 7127 RPM, J=3.18							
Microphone ID	M1-FT	M2-FT	M3-FT	M4-FT	M5-FT	M6-FT	
Visual Angle θ [deg]	69.4	78.8	90.5	98.8	107.3	117.8	
	Mach numb.	J	RPM	$C_{P,EXP}$	$C_{P,CFD}$	$\beta_{3/4,EXP}$ [deg]	$\beta_{3/4,CFD}$ [deg]
Wind Tunnel Test	0.787	3.186	7127	2.09	2.10	58	62

Table 4.6: Data set 2, Overview and aerodynamic correlation

As discussed above computational and experimental results were correlated by matching the power coefficient, and optimal correlation was found for a design angle equal to 62 deg.

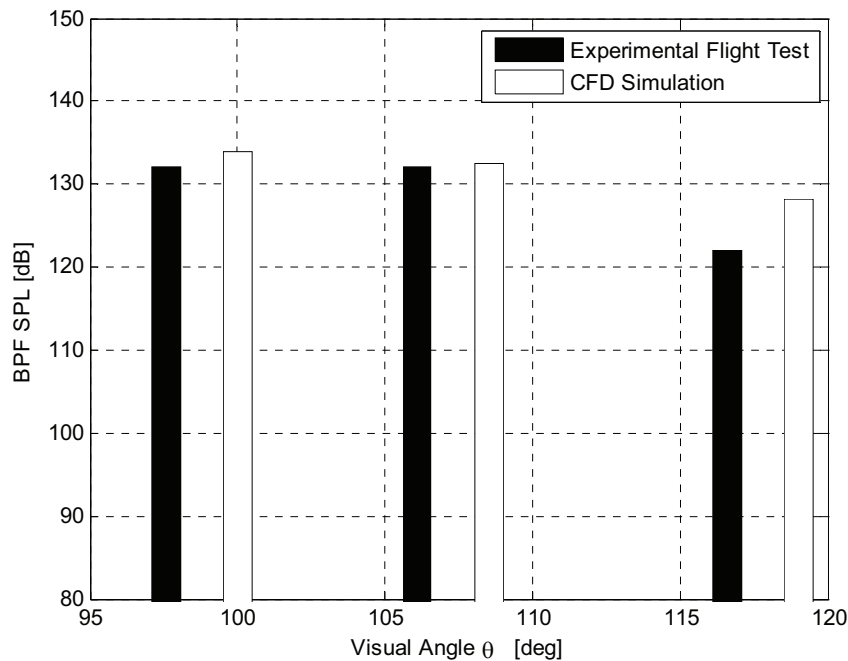


Figure 4.21: Data Set 2, results

Results are provided in Figure 4.21, where only the microphones located behind the propeller plane (M4-FT, M5-FT and M6-FT, Table 4.6) are shown as they are the most accurate. In particular we can see that again the microphone located approximately 20 degrees behind the propeller (M5-FT) is the most accurate as happened in the data set 1 for M1-WTL.

The last data set that is going to be presented for the NASA SR2 propeller is the data set 3, focused on WTL tests performed with the acoustic plate device. In this case a plate was firmly attached to the tunnel ceiling at a distance of 0.3 diameters from the propeller tip, and 12 microphones were located on this plate along the longitudinal direction from an azimuthal angle θ ranging from 46.8 deg to 130.4 deg, where θ is the angle from propeller axis of rotation taken from the horizontal axis in front of the propeller. A sketch of the propeller and acoustic plate device is given in Figure 4.14 (left), while the microphone locations are given in Table 4.7 as function of Z coordinate in cm and θ in deg.

Signals from the microphones were recorded on a magnetic tape, and narrowband spectra were obtained for each point with a range from 0 to 10 KHz and a bandwidth of 32 Hz.

With reference to the data given in Table 4.7, the microphones are located on a straight line whose linear distance from propeller tip is 0.8 diameters. The locations were chosen to make these data comparable with the other sets previously described.

Microphone ID											
1	2	3	4	5	6	7	8	9	10	11	12
Transducer Distance from Propeller Plane, Z [cm]											
-46.7	-41.7	-30.5	-16.0	-8.9	0.8	8.9	12.4	18.0	25.0	28.7	42.4
Visual Angle θ , from upstream (0 in front) [deg]											
46.8	50.0	58.5	72.2	80	90.9	100	104	110	116.8	120	130.4

Table 4.7: microphone locations on acoustic plate device

Mach Number	Advance Ratio J	Rot. Speed [rpm]	$C_{P,EXP}$	$C_{P,CFD}$
0.6	3.06	6487	1.32	1.34
0.8	3.06	8650	1.51	1.57

Table 4.8: comparison between experimental and CFD results

For this data set 2 Mach number conditions were tested and calibration was achieved for both conditions with a design angle 60 deg in place of an experimental design angle of 59 deg. Aerodynamic results are provided in Table 4.8. Moreover an analysis of sensitivity to initial conditions and grid resolution was performed for Mach equal to 0.8 only, in order to find out the dependency of the computed results on the simulation parameters. In particular the asymptotic Turbulent Viscosity Ratio and Turbulent Intensity were decreased by one order of magnitude, and mesh adaption [24] was applied between $M=0.9$ and $M=1.1$ in order to refine the cells in the shock wave region. In this sensitivity analysis, the propeller thrust and torque showed a maximum deviation with respect to the basic case of 2% of absolute values with a percentage increase in cell number of 100% (from 10.5M to 20.1M cells).

To visualize the aerodynamic flow solution, two sections, A and B respectively, have been chosen at 30% and 90% of span extension in Figure 4.22. This choice was made to show the differences in flow field between the two test conditions, $M=0.6$ and $M=0.8$ respectively.

Because of the composition of the asymptotic and rotational velocity components, the propeller relative Mach number increases along the span direction. This implies that different Mach number regimes may be met by the propeller depending on the asymptotic and rotational conditions.

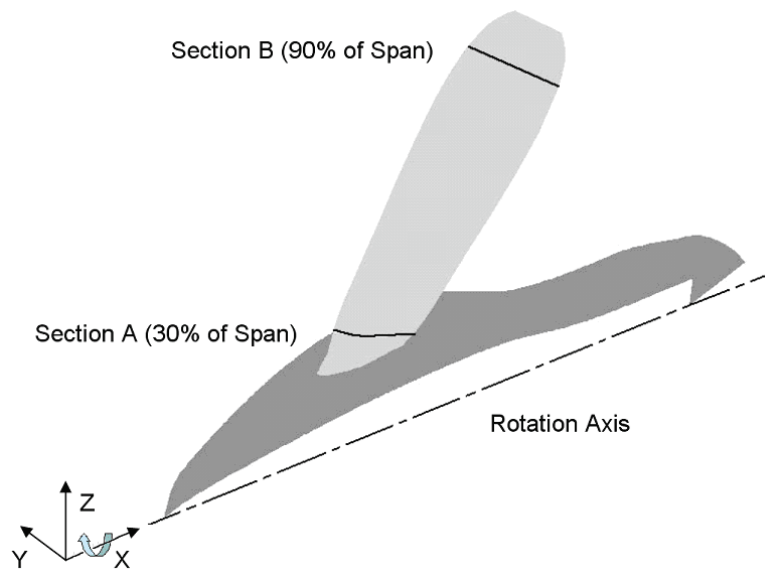


Figure 4.22: sections positioning, section A (30% of Span) – section B (90% of Span). The circle arrow indicates the sense of rotation.

For the first test condition, $M=0.6$ and 6487 rpm, the flow field becomes locally supersonic only around the upper part of the propeller (section B) with the formation of an attached shock wave on the blade suction side (figure 4.23-B). For the second test condition, $M=0.8$ and 8650 rpm, in the lower part of the propeller (section A) the flow field becomes locally supersonic on both pressure and suction sides, with the formation of two attached shock waves (figure 4.24-A). On the other hand, in the upper part of the propeller (section B) the asymptotic relative Mach number is supersonic and a detached shock wave is formed in front of the leading edge. This switch of physics around the blade happens at approximately at 60% of span extension.

Moreover also the plot of the iso-surface for the relative Mach equal to 1 is provided in Figure 4.25. In this picture the borderline of the shock wave is highlighted with a blue line, showing the difference between the two Mach numbers tested. In particular in the lower picture it is clear the switch of physics mentioned above, with an attached shock wave on the lower half and a detached shock wave in the upper half of the blade.

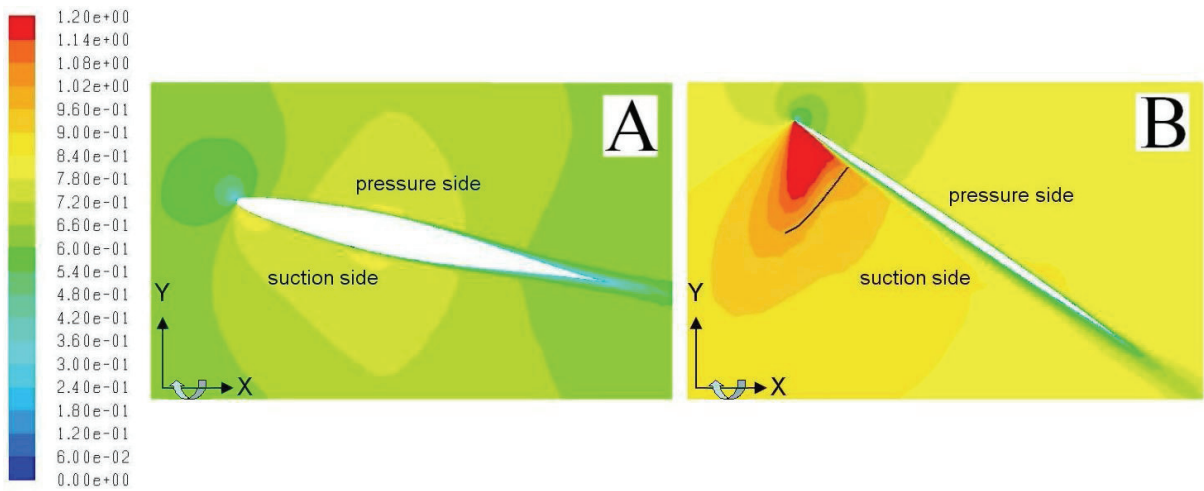


Figure 4.23: relative Mach contours, $M=0.6$ - 6487 RPM
 Section A (left) – Section B (right)

Black line indicates the shock wave position, circle arrow indicates the sense of rotation.

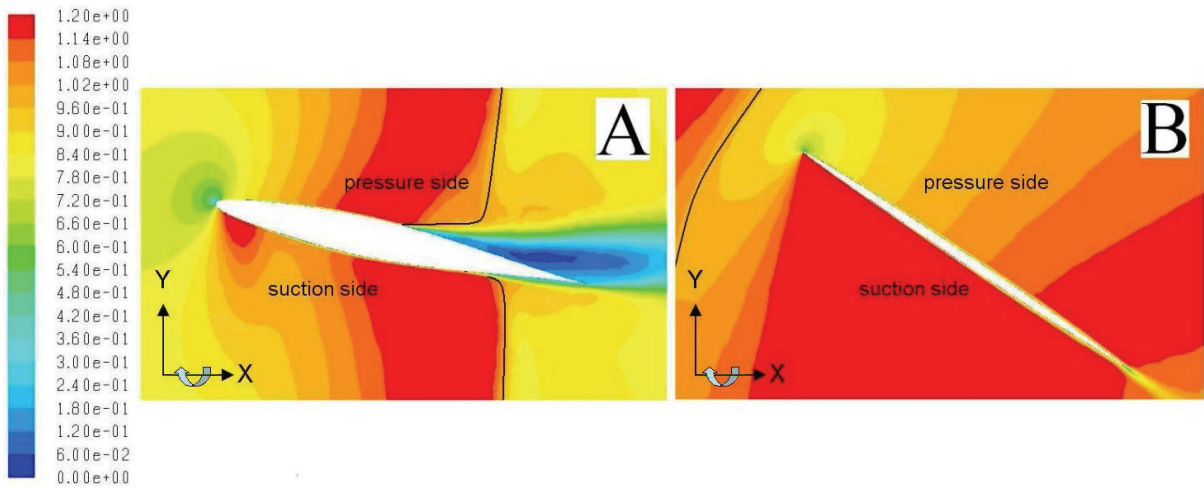


Figure 4.24: relative Mach contours, $M=0.8$ - 8650 RPM
 Section A (left) - Section B (right)

Black lines indicate the shock wave positions, circle arrow indicates the sense of rotation.

BPF SPL computed and corrected results are given in Figure 4.26 and Figure 4.27 for $M=0.6$ and 0.8 respectively for the most accurate microphones located behind the propeller plane (from microphone ID 7 to 11, Table 4.7). The results have been corrected taking into account the Near-Field/Far-Field correction, the WTL pressure correction, the WTL and acoustic plate interference effects, the pseudo-noise and the quadruple effects. It is shown a good agreement between experimental and computational data, both for absolute noise levels and acoustic trends. Furthermore another computational grid with only 5 prism layers and a 1.7M total cell count per sliced periodic domain was therefore generated. Simulations were performed with the MRF steady state approach, with RANS modelling and a wall function, and the Full MultiGrid Initialization technique (FMG) as used for the 10.5M cells grid. With this coarser grid a fully converged solution was obtained in approximately the same number of iterations (about 600) but with a very competitive computational time for an industrial simulation, about 5 hours on a dedicated LINUX QUAD-CORE Machine, with a 2.8GHz CPU Clock, 85% less than for the 10.5M computational grid.

Simulations were performed for both Mach numbers conditions, achieving an SPL prediction within 0.5 dB of that of the 10.5M cell grid.

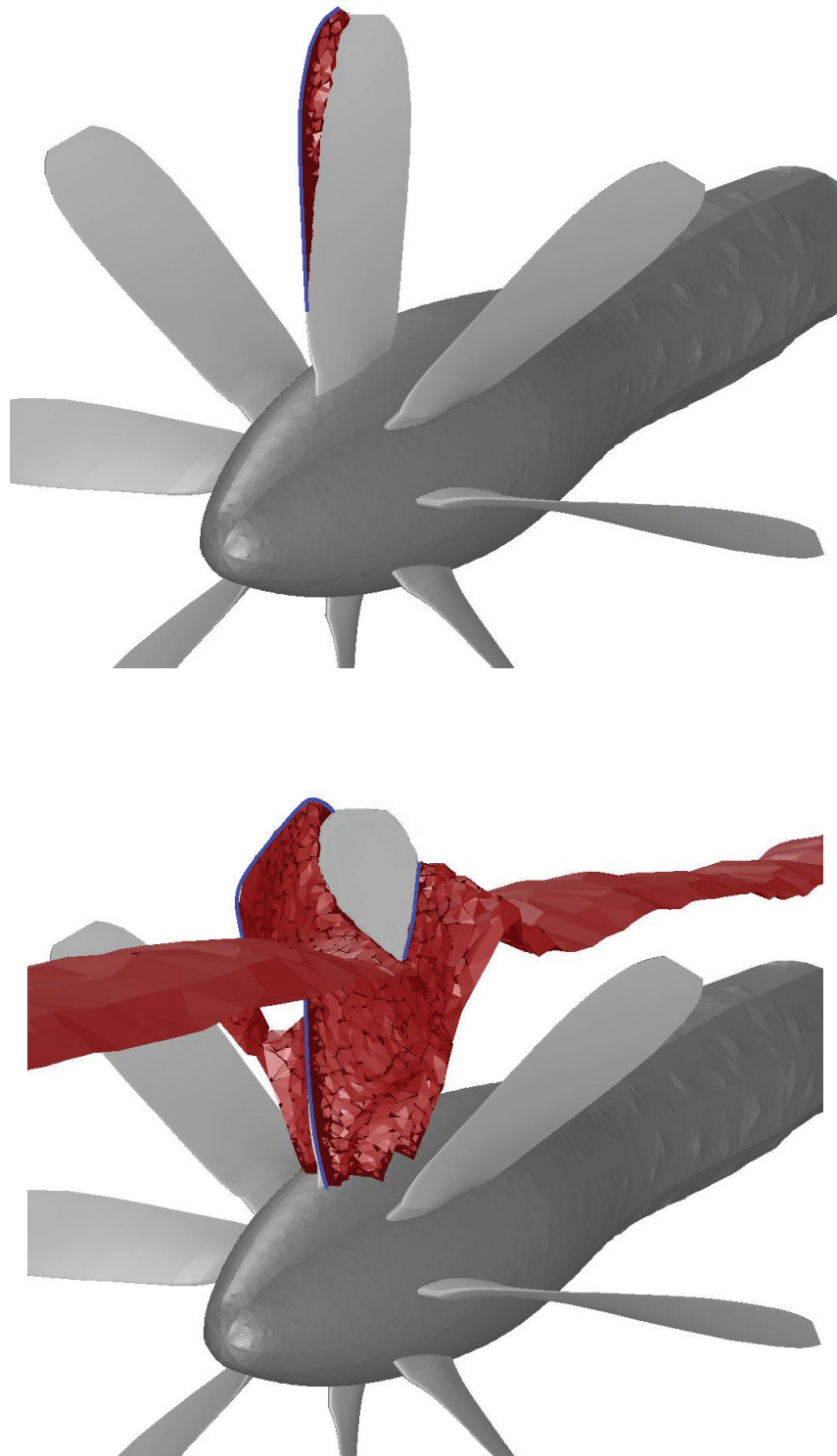


Figure 4.25: shock wave visualization
Iso-surface for relative Mach number = 1
Asymptotic Mach number and rotational speed respectively equal to
0.6 and 6487 RPM (upper) and to 0.8 and 8650 RPM (lower)
Blue lines indicate the border of the shock wave

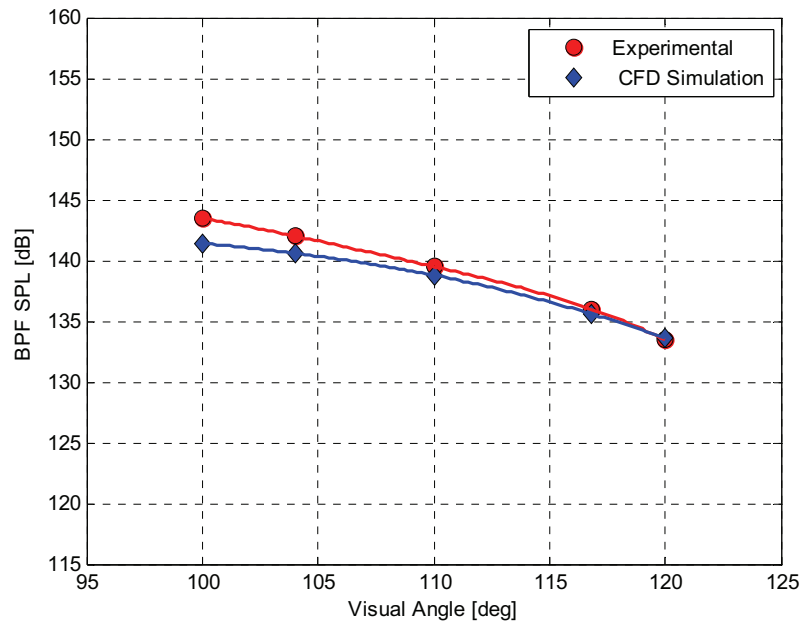


Figure 4.26: Data Set 3 Results
SPL Level of First Harmonic (BPF), NASA SR2 (M=0.6, Rot. Speed=6487 rpm)

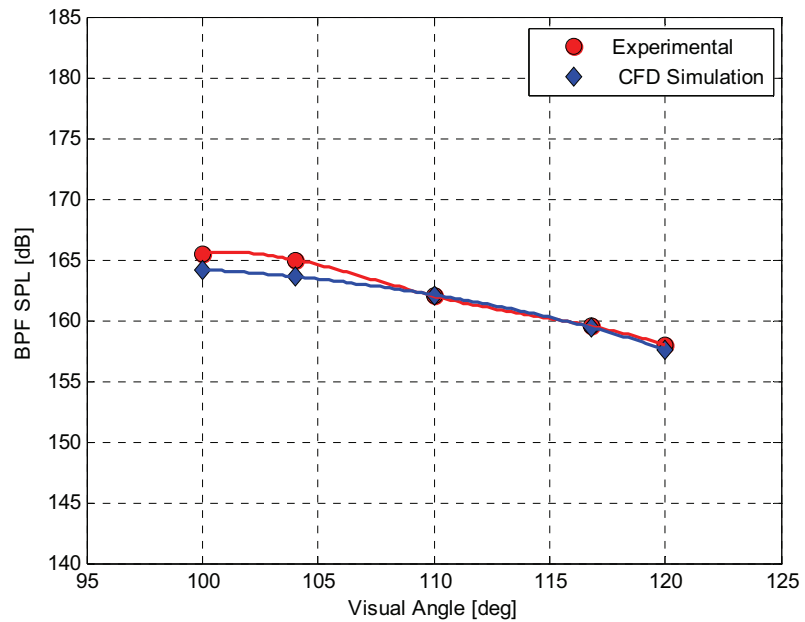


Figure 4.27: Data Set 3 Results
SPL Level of First Harmonic (BPF), NASA SR2 (M=0.8 Rot. Speed=8650 rpm)

4.3.4 NASA SR3 Results: Data Sets 4-5

The first experimental data set analyzed for the NASA SR3 propeller is the data set 4, based on FT data provided in [110]. The propeller was mounted on the instrumented NASA Jetstar aircraft and operated at a Mach number equal to 0.787 and a rotational speed equal to 7461 RPM. Noise was measured with 6 microphones located on the aircraft fuselage from a visual angle of 69 deg to 117 deg, at a distance of 0.8 diameters to propeller tip. The test is designed to be comparable with the test performed in the data set 2 for the NASA SR2.

Aerodynamic correlation with the experimental data was achieved for a design angle of the CFD model equal to 61 deg and an overview of all results is provided in Table 4.9.

	Flight Test – 6 Microphones mounted on fuselage 0.8 D far from propeller tip NASA SR3 – M=0.787, 7461 RPM, J=3.06						
Microphone ID	M1-FT	M2-FT	M3-FT	M4-FT	M5-FT	M6-FT	
Visual Angle θ [deg]	69.4	78.8	90.5	98.8	107.3	117.8	
	Mach numb.	J	RPM	$C_{P,EXP}$	$C_{P,CFD}$	$\beta_{3/4,EXP}$ [deg]	$\beta_{3/4,CFD}$ [deg]
Wind Tunnel Test	0.787	3.06	7461	1.99	2.10	58.9	61

Table 4.9: Data set 4, overview and aerodynamic correlation

Aeroacoustic simulations were performed for the last 4 microphones (from M3-FT to M6-FT) and corrected acoustic BPF-SPL predictions are plotted in Figure 4.28. As usual the best agreement between experiments and computations was achieved for the microphone located approximately 20 deg behind the propeller plane, like M5 and M6.

This data set was also designed to provide a valid comparison between NASA SR2 and SR3 in FT, at the same altitude and approximately at the same advance ratio. A visualization of the 3D shock wave was performed with an iso-surface of Mach number equal to 1 for both propellers in Figure 4.29, showing the differences in the shape for the two geometries simulated.

In particular it is remarkable to observe the difference in the shape of shock front in the upper part of the propeller that seems to be smoother for the SR3 blade.

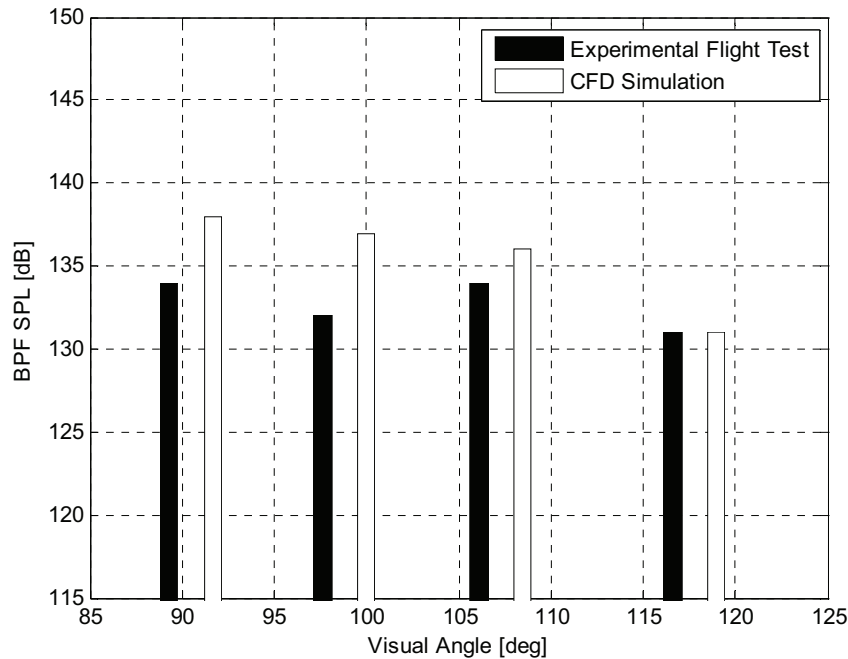


Figure 4.28: Data Set 4 results

SPL Level of First Harmonic (BPF), NASA SR3 ($M=0.787$, Rot. Speed=7461 rpm)

The last experimental set of results provided is the data set 5, based on the test performed on NASA SR3 published in [112]. Here both WTL and FT results are provided and for two microphones locations behind the propeller plane at a different distance from propeller tip. All experimental data were scaled for a flight condition (altitude 30.000 ft) and microphones located $0.8D$ far from the propeller tip.

Test conditions and correlated aerodynamic data are summarized in table 4.10, from Mach number 0.6 to 0.85 and from the rotational speed from 6573 to 8933 RPM.

Acoustic SPL BPF results are provided in Figure 4.30 and 4.31 for the microphones M1 and M2 respectively (Table 4.10).

These results show how the noise increasing trend is well captured for both microphones, providing the good prediction accuracy achieved for the previous data sets.

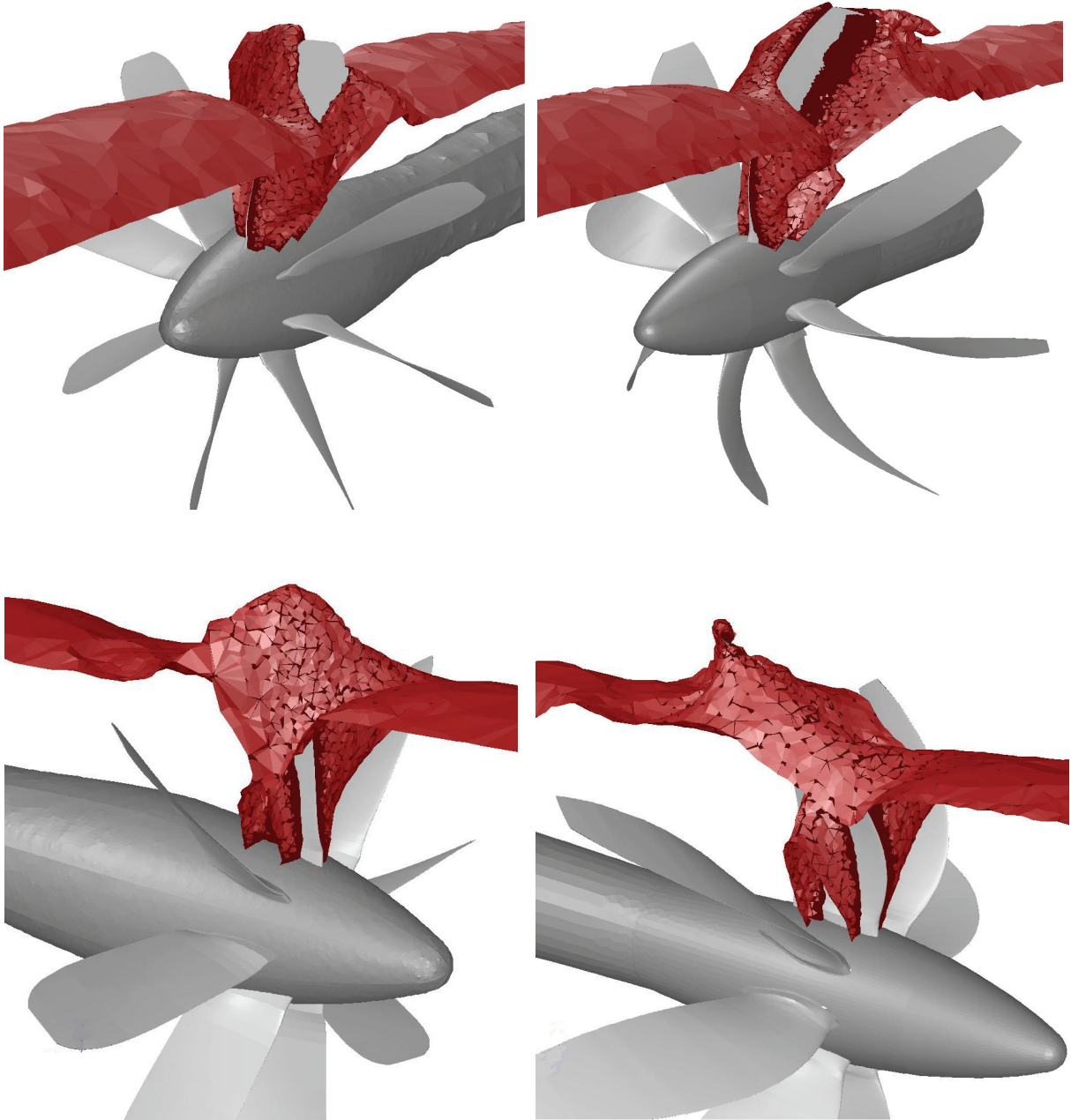


Figure 4.29: shock wave visualization on NASA SR2 (left) and NASA SR3 (right)
NASA SR2: FT, $M=0.787$, 7127 RPM, $J=3.18$ (Data Set 2)
NASA SR3: FT, $M=0.787$, 7461 RPM, $J=3.06$ (Data Set 4)

FT and WTL							
data scaled to a FT conditions and microphones located 0.8D far from propeller tip							
NASA SR3 – Mach number from 0.6 to 0.85, Rot. Speed from 6573 to 8933 RPM, J=3.06							
Microphone ID		M1			M2		
Visual Angle [deg]		101			110		
Mach numb.	J	RPM	Mach Tip	$C_{P,EXP}$	$C_{P,CFD}$	$\beta_{3/4,EXP}$ [deg]	$\beta_{3/4,CFD}$ [deg]
0.6	3.06	6573	0.86	1.91	1.83	61.3	61
0.7	3.06	7550	1	1.89	1.79	61.3	61
0.75	3.06	8093	1.08	1.79	1.76	61.3	61
0.8	3.06	8495	1.14	1.71	1.71	61.3	61
0.85	3.06	8933	1.21	1.53	1.53	61.3	61

Table 4.10: Data set 5, overview and aerodynamic correlation

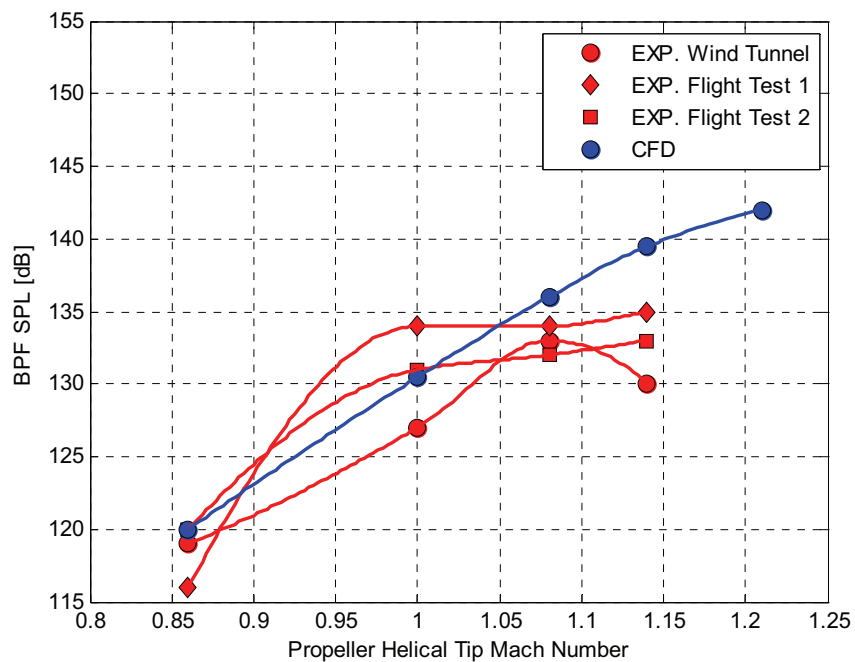


Figure 4.30: Data Set 5 results, Microphone M1

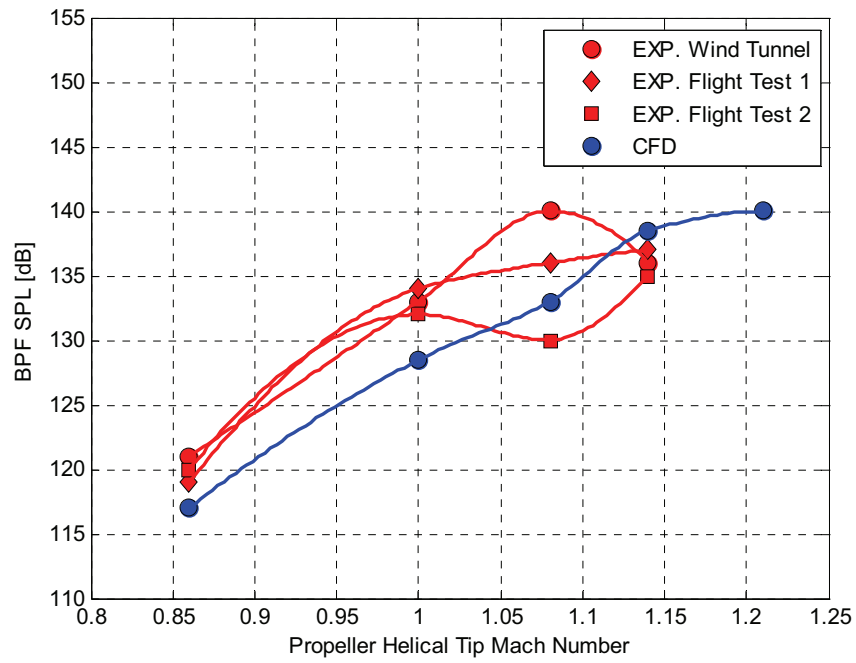


Figure 4.31: Data Set 5 Results, Microphone M2

Chapter 5

Conclusions

The work carried out in this Ph.D. Thesis is focused on the CFD and CAA turbomachinery simulation, with specific application on two problems: the VAWT and the high speed transonic cruise propellers.

Both of these research topics are key-points for the engineering of next years in the frame of energy industry and transportation industry.

The renewable energies and in particular the field of small wind power generation is growing a lot in the recent period, pushed by the competitive clean energies policies adopted by the most of industrialized countries. Moreover small scale wind turbines, able to satisfy the necessities of a limited number of families are affordable with small investments and can be implemented directly into the urban environment, providing a localized and renewable energy source.

In the first part of this thesis the attention is focused on the aerodynamic modelling of VAWT, developing a numerical aerodynamic model based on the coupling of a classical theory for VAWT, the Paraschivoiu Double Streamtube theory, and an advanced theory for the unsteady aerodynamic modelling of airfoils, the Beddoes-Leishman theory. The DS theory is based on a double streamtube global approach and provides the mathematical

relations able to estimate the aerodynamic conditions experienced by an airfoil with imposed rotation (e.g. velocity and AoA). Moreover to compute the forces on the blade the aerodynamic coefficients are needed but they are affected by the hysteretic behavior as they are subject to oscillating far-field conditions due to the rotational dynamics. The estimation of the coefficients hysteresis is performed with the BL method, which consists in a reformulation of the Theodorsen theory for unsteady aerodynamic modelling in a form of a system of 4 ordinary differential equations in 4 state-space variables. The Beddoes separation theory implemented and the Leishman correction to the unsteady lift formulation make this theory able to overcome the two main limitations of Theodorsen classical theory: the thin airfoil and the attached flow hypotheses. The BL theory was implemented into the DS model and built into a wind turbine simulator package. This new approach was tested and compared to CFD results achieved for a VAWT experimental data set.

Results showed that wind turbine aerodynamic behavior is well captured by DS-BL approach as well as by the CFD calculations. Moreover the DS-BL approach is able to provide useful information about the aerodynamic behavior of wind turbines, showing the real conditions experienced on the blade during the rotation. This information can be used in the wind turbine design phase to lead to new solutions and to perform fast predictions of the turbine overall performances.

On the other hand CFD brute-force approach can be used for more complex scenarios as pitching control law design and optimization. Few investigations in this direction were performed, showing the possibility to use the dynamic mesh approach for blade pitching optimization. Preliminary results are provided, nevertheless further investigations are needed in order to achieve more affordable and reliable results.

The problem of wind turbine aeroacoustic modelling was approached on a general basis focusing on the airfoil self-generated noise modelling. The bibliographic research carried out showed that many and different noise generation mechanisms can occur for aerodynamic surfaces, depending on Reynolds and Mach numbers as well as on the AoA conditions experienced. On a general basis, they can be classified in three different typologies:

- Turbulent Boundary Layer – Trailing Edge noise (TBL-TE)
- Laminar Boundary Layer – Vortex Shedding noise (LBL-VS)
- Separation stall noise

The TBL-TE noise occurs at high Reynolds numbers and low angle of attack, when the turbulent boundary layer passes over the trailing edge. It is produced by the turbulent vortex structures of airfoil pressure and suction sides and it is mainly a broadband noise. On the other hand, the LBL-VS noise occurs at lower Reynolds numbers and low angle of attack, where a large laminar boundary layer develops over the airfoil surface, generating laminar instabilities waves before the transition point. These instabilities produce an unsteady pressure load on the airfoil surface, which generates a typical narrowband tonal noise.

For higher angle of attacks, the separation point moves towards the leading edge, and the wake region is characterized by a separated zone. In this case, a large vortex shedding together with a well-stabilized turbulence level characterizes the wake, generating the broadband separation stall noise.

Furthermore other noise generation mechanisms can occur for an airfoil like blunt trailing edge noise, high-lift devices noise or non-stationary far-field conditions noise, but in general these other noise sources are less prominent than the sources mentioned above.

The airfoil self-generated noise modelling was approached by CFD simulation for 2 velocities conditions and 4 AoAs for the NACA 0012 airfoil, according to the NASA experimental reference adopted. The angular positions chosen range from 0 to 7 deg while the Reynolds number ranges from 600K to 1.1M, over relevant values for wind turbine applications. The tested conditions allowed experiencing all the noise generation mechanisms mentioned and different numerical approaches were used in order to model the different acoustic sources. In particular URANS model coupled with innovative turbulence models ($k-\omega$ transitional and $k-k_1-\omega$) were used for LBL-VS and the separation-stall noise, while the Embedded LES approach was adopted for the TBL-TE noise. Acoustic pressure computation was performed with the FW-H acoustic analogy, while acoustic signal processing, spectrum and SPL computations were performed with an external self-generated tool.

Results showed that the proper aerodynamic models are able to perform reliable simulations of the noise spectra for the airfoil self-generated noise, reaching results considerably improved respect the computational data published in literature.

Furthermore additional investigations, especially on the ELES approach which is very computational demanding, will be performed in future in order to assess the results achieved.

The second part of this thesis is focused on the numerical modelling of high speed propellers for transonic cruise turboprop applications. Despite of the global crisis, the

transportation industry and in particular the flight services market is growing a lot, under the push of low cost companies and development policies. The market demand mainly focuses on two topics: increase the safety of the service and reduce the costs. Today the fuel consumption reduction is an issue for all aircraft manufacturer industries, as the fuel is even more expensive, and its price will certainly increase over the next decades. For this reason research is focusing on the fuel demand reduction investigating on turbofan engine optimization as well on alternative solutions like the high speed turboprop.

The turboprop engine is a solution already adopted for short-range aircrafts since a long time but it is affected by a strong limitation on the cruise speed related to the formation of shock waves on the blade tip. Moreover noise and vibrations problems are also fundamental, and the research of the turboprop aircraft manufacturer industries focuses mainly on their reduction. The work carried out deals with the aerodynamic and aeroacoustic modelling of propeller noise focusing on 3 blade geometries: the NACA 4-(3)(08)-03 and the NASA SR2 and SR3.

The NACA 4-(3)(08)-03 is a subsonic blade geometry that was used as driving problem in order to define the numerical approaches for the simulations. It was tested in 2-bladed and 7-bladed configurations and aerodynamic and aeroacoustic results were compared with NACA experimental data available in literature.

High speed propeller test campaign was designed in order to reproduce the results of the huge Jetstar research program carried out by NASA from the early 1970s to the 1990s, providing an enormous amount of computational and experimental data on several high speed blade geometries. The NASA SR2, a 8-bladed straight propeller and the NASA SR3 a 8-bladed swept propeller were simulated over a simulation pool consisting of 5 different experimental data sets in Wind Tunnel and Flight Test conditions. The Mach number tested ranges from 0.6 to 0.9 while the rotational speed ranges from 6000 to 9000 rpm approximately.

A deep exploration of the computational methods available for simulating rotors was carried out using Multiple Reference Frame, Periodic modeling approach and FMG initialization, providing a detailed description of mesh building guidelines, solver numerical settings and optimized simulation strategies. A computational grid of 10.5M cells was generated for each blade geometry with 40 prism layers on the blade to achieve optimal resolution of the boundary. Simulations were performed with a URANS-MRF approach for

the aerodynamic part while the FW-H acoustic analogy was used for the acoustic pressure computation.

Most of the work was focused on the definition of optimized numerical simulation strategy, reaching a complete converged result for a transonic case in only 600 iterations, with highly competitive computational cost compatible to the industrial demands.

Computational results are compared with experiments, showing the ability of this approach to predict noise with a discrepancy within a few dB for the different simulated conditions and microphones locations. Particular attention is given to the set of corrections to be applied to acoustic experimental data in order to be consistently compared with free field CFD results.

References

- [1] http://en.wikipedia.org/wiki/Lockheed_JetStar.
- [2] The United Nations Framework Convention on Climate Change, http://unfccc.int/essential_background/convention/background/items/1353.php. Retrieved 15 November 2005. "Such a level should be achieved within a time-frame sufficient to allow ecosystems to adapt naturally to climate change, to ensure that food production is not threatened and to enable economic development to proceed in a sustainable manner".
- [3] Kyoto Protocol: Status of Ratification, United Nations Framework Convention on Climate Change. 2009-01-14.
http://unfccc.int/files/kyoto_protocol/status_of_ratification/application/pdf/kp_ratification.pdf. Retrieved 2009-05-06.
- [4] World Wind Energy Association, World Wind Energy report, 2009.
- [5] Bombardier Q400 website, <http://www.q400.com>.

-
- [6] M. Smirti, M. Hansen, The potential of Turboprops to Reduce Aviation Fuel Consumption, University of California, Transportation Center, Research paper No. 883, 2009.
- [7] Alfred Voß, LCA and External Costs in Comparative Assessment of Electricity Chains, Decision Support for Sustainable Electricity Provision, University of Stuttgart, IEA Conference, 2001.
- [8] Ad de Graaff, Estimating the demand for Personal Air Transport, CIRA, February 2009.
- [9] <http://www.easyjet.com/>.
- [10] <http://www.flybaboo.com/>
- [11] O. Reynolds, Phil. Trans. R. Soc. Lond. 174 935-982, 1883.
- [12] L.D. Landau, Akad. Nauk. Doklady 44-339 1944, in Russian. English translation: C.R. Acad. Sc. URSS 44-311, 1944.
- [13] D. Ruelle and F. Takens, Commun. math. Phys. 20-167 1970 and 23-343 1971. Articles reproduced in: Hao Bai-Lin, Ed., Chaos II, World Scientific, Singapore, pp. 115-119 and pp. 120-147 1990.
- [14] E. Ott, Chaos in dynamical systems, Cambridge University Press, Cambridge, UK, 1993.
- [15] H. Schlichting, Boundary Layer Theory, McGraw-Hill Series in Mechanical Engineering, 7th Ed., 1979.
- [16] Smith, A. M. O. Transition, Pressure Gradient and Stability Theory. Proc. 9th Int. Con. of Appl. Mech., vol.4, 234-244, 1956.
- [17] Smith, A. M. O. and Gamberoni, N., Transition, Pressure Gradient and Stability Theory, Technical Report ES-26388, Douglas Aircraft Company, 1956.
- [18] Drela, M., XFOIL: An Analysis and Design System for Low Reynolds Number Airfoils, Conference on Low Reynolds Number Airfoil Aerodynamics, University of Notre Dame, June 1989.
- [19] J.L. van Ingen, The e^N method for transition prediction. Historical review of the work at TU Delft, 38th Fluid Dynamics Conference and Exhibition, AIAA 2008-3880, 2008.
- [20] F.R. Menter, Two-Equation Eddy-Viscosity Turbulence models for Engineering Applications, AIAA Journal 32(8), pp. 1598-1605, 1994.

-
- [21] F.R. Menter, R.B. Langstry, S.R. Likki, Y.B. Suzen, P.G. Huang and S. Volker, A correlation based transition model using local variables, Part-1, Model Formulation, ASME-GT2004-53452, 2004.
- [22] D. Keith Walters and Davor Cokljat, A three-equation eddy-viscosity model for Reynolds-averaged Navier-Stokes simulation of transitional flows, *Journal of Fluids Engineering*, 130, 2008.
- [23] ANSYS FLUENT 12.0 Theory Guide, ANSYS-Fluent Inc., 2010.
- [24] ANSYS FLUENT 12.0 User-Guide, ANSYS-Fluent Inc., 2009.
- [25] S. Marburg, B. Nolte Editors, *Computational Acoustics of Noise Propagation in Fluids, Finite and Boundary Element Methods*, Springer, 2007.
- [26] Kolmogorov, A.N. 1941a. Local structure of turbulence in an incompressible fluid for very large Reynolds numbers, *Comptes rendus (Doklady) de l'Academie des Sciences de l'U.R.S.S.*, 31: 301–305 Reprinted in: S.K. Friedlander & L. Topper (editors). 1961.
- [27] Kolmogorov, A.N. 1941b. On degeneration of isotropic turbulence in an incompressible viscous liquid. *Comptes, Rendus (Doklady) de l'Academie des Sciences de l'U.R.S.S.*, 31: 538–540.
- [28] Kolmogorov, A.N. 1962. A refinement of previous hypotheses concerning the local structure of turbulence in a viscous incompressible fluid at high Reynolds number. *Journal of Fluid Mechanics*, 13: 82–85.
- [29] F.R. Menter, M. Kuntz, R.B. Langtry, Ten years of Experience with the SST Turbulence Model, *Turbulence Heat and Mass Transfer*, 625-632, Begell House Inc. 2003.
- [30] M. Schur, P.R. Spalart, M. Strelets and A. Travin, Detached-Eddy Simulation of an Airfoil at High Angle of Attack, 4th International Symposium on Engineering Turbulence Modelling and Experiments, Corsica, France 1999.
- [31] P. R. Spalart, S. Deck, M.L. Schur, K.D. Squires, M.K. Stretlets and A. Travin, A new version od detached-eddy simulation, resistant to ambiguous grid densities, *Theoretical and Computational Fluid Dynamics*, 20:181-195, 2006.
- [32] Mathey F., Cokljat D., Bertoglio J.P. and Sergent E. (2006), Specification of LES Inlet Boundary Condition Using Vortex Method, *Progress in Computational Fluid Dynamics*, Vol. 6, No 1-3, pp. 58--67.

-
- [33] D. Cokljat, D. Caridi, G. Link, R. Lechner, F.R. Menter, Embedded LES Methodology for General Purpose CFD Solvers, 2009.
- [34] F.R. Menter, and Y. Egorov, Re-visiting the turbulent scale equation, Proc. IUTAM Symposium; One hundred years of boundary layer research, Göttingen, 2004.
- [35] F.R. Menter, and Y. Egorov, A scale-adaptive simulations model using two equations models, AIAA Paper 2005-1095, Reno 2005.
- [36] F. Menter, Y. Egorov, Scale Adaptive Simulation in the DESIDER Project, Proceedings of ECCOMAS CFD Conference, 2006.
- [37] Bies, D. A., and Hansen, C. H., Engineering noise control: theory and practice, 2nd edn. London: E. & F.N. Spon., 1996.
- [38] Hirschberg, A., and Rienstra, S. W., An Introduction to Aeroacoustics, Lecture Notes, Eindhoven University of Technology, Jul 2004
- [39] Lighthill, M. J., On Sound Generated Aerodynamically, I. General Theory, Proceedings of the Royal Society of London, Vol. A211, No 1107, pp. 564-587, 1952.
- [40] Lighthill, M. J., On Sound Generated Aerodynamically, II. Turbulence as a source of sound, Proceedings of the Royal Society of London, Vol. A222, No 11048, pp. 1-32, 1954.
- [41] Curle, N., The Influence of Solid Boundaries upon Aerodynamic Sound, Proceedings of the Royal Society of London, Vol. A231, pp. 505-514, 1955.
- [42] Crighton, D.G., Basic principles of aerodynamic noise generation, Prog. Aerospace Sci., 16:31-96, 1975.
- [43] Howe, M.S., Theory of Vortex Sound, Cambridge University Press, 2003.
- [44] J.E. Ffowcs Williams, D.L. Hawkins, Sound generated by turbulence and surfaces in arbitrary motion, Philosophical Transaction of the Royal Society, A 264, No 1151, pp. 321-342, 1969.
- [45] C. Schram, Sound generation and propagation in Low Mach number confined flows, Von Karman Institute for Fluid Dynamics, KTH Summer School for Aeroacoustics in Low Mach Number Confined Flows, Stockholm, June, 2010.
- [46] C.A. Wagner, T. Huttl, P. Sagaut, Large Eddy Simulation for Acoustics, Cambridge University Press, 2007.

-
- [47] S. Marburg, B. Nolte, Computational Acoustics of Noise Propagation in Fluids – Finite and Boundary Element Methods, Springer, 2007.
- [48] P.K. Banarjee, The Boundary Elements Methods in Engineering, 2nd edition, McGraw-Hill, New York, 1994.
- [49] C.A. Brebbia, J. Dominguez, Boundary Elements – An Introductory Course, McGraw-Hill, New York, 1989.
- [50] J.H. Kane, Boundary Element Analysis in Engineering Continuum Mechanics, Prentice Hall, Englewood Cliffs, NJ, 1994.
- [51] T.W. Wu, Boundary Element Acoustics: Fundamentals and Computer Codes, Wit Press, Southampton, 2000.
- [52] A.J. Burton, G.F. Miller, The application of integral equation methods to the numerical solution of some exterior boundary-value problems, Proc. R. Soc. Lond A, 323, No. 201-210, 1971.
- [53] Y.J. Liu, S.H. Shen, A new form of hypersingular boundary integral equation for 3-D acoustics and its implementation with C^0 boundary elements, Computer Methods in Applied Mechanics and Engineering, 173, No. 3-4, 375-386, 1999.
- [54] Y.J. Liu, Fast Multipole Boundary Element Method – Theory and Applications in Engineering, Cambridge University Press, 2009.
- [55] <http://www.lmsintl.com/SYSNOISE>.
- [56] <http://www.fastbem.com/>
- [57] D. Caridi, Industrial CFD Simulation of Aerodynamic Noise, Ph.D. Thesis in Industrial Engineering, University of Naples Federico II, 2008.
- [58] Paraschivoiu I., Wind Turbine Design with Emphasis on Darrieus Concept, Polytechnic Press, Ecole Polytechnique de Montreal, 2002.
- [59] Paraschivoiu, I., Double-Multiple Streamtube model for Darrieus Wind Turbines, Second DOE/NASA Wind Turbines Dynamic Workshop, NASA CP-2185, Cleveland, Ohio, February 1981, pp. 19-25.
- [60] Paraschivoiu I., Aerodynamic Loads and Performance of the Darrieus Rotor, AIAA Journal of Energy, Vol.6, November-December 1982, pp. 406-412.

-
- [61] Berg D., VAYWT Aerodynamic Modelling Codes at SNL-Development and Capabilities, 2nd vertical Axis Wind Turbine Aerodynamic Seminar, Sandia National Laboratories, Albuquerque, N.M., January 19-20, 1982.
- [62] Paraschivoiu I., Double-Multiple Streamtube model for studying Vertical-Axis Wind Turbines, AIAA Journal of Propulsion and Power, Vol. 4, 1988, pp. 370-378.
- [63] Lapin E.E., Theoretical Performance of Vertical Axis Wind Machines, ASME Conference, 75-WA/ENER-1, 1975.
- [64] Theodorsen, T., General Theory of Aerodynamic Instability and The Mechanism of Flutter, NACA Report 496, 1935, pp.413-433.
- [65] Tran, C. T. and Petot, D., Semi-Empirical Model for Dynamic Stall of Airfoils in View of the Application to the Calculation of Responses of a Helicopter Blade in Forward Flight, 6th European Rotorcraft and Powered Light Aircraft Forum, Papers and Programme, 1980.
- [66] Dat, R. and Tran, C. T., Investigation of the Stall Flutter of an Airfoil with a Semi-Empirical Model on 2-D Flow, Vertica, Vol. 7, No. 2, 1983, pp. 73-86.
- [67] Beddoes, T. S., A Synthesis of Unsteady Aerodynamic Effect Including Stall Hysteresis, Vertica, Vol.1, 1976, pp. 113-123.
- [68] Beddoes, T. S., Representation of Airfoil Behaviour, Vertica, Vol.7, No.2, 1983, pp. 183-197.
- [69] Beddoes, T.S., Practical Computation of Unsteady Lift, Vertica, Vol.8, No.1, 1984, pp. 55-71.
- [70] Leishman, J.G. and Beddoes, T.S., A Generalized Model for Airfoil Unsteady Aerodynamics Behavior and Dynamic Stall using Indicial Method, Proceedings of the 42nd Annual Forum of the American Helicopter Society, Washington D.C., June 1986.
- [71] Leishman, J.G. and Beddoes, T.S., A Semi-Empirical Model for Dynamic Stall, Journal of the American Helicopter Society, Vol.34, No. 3, 1989, pp. 3-17.
- [72] Hansen, M. H., Gaunaa, M., Madsen, H. A., A Beddoes-Leishman type dynamic stall model in state-space formulations, Riso National Laboratory, Roskilde, Denmark, June 2004.

-
- [73] Van der Wall, B. G. and Leishman, J. G., On the Influence of Time-Varying Flow Velocity on Unsteady Aerodynamics, *Journal of the American Helicopter Society*, Vol. 39, No.4 October 1994, pp. 25-36.
- [74] Leishman, J.G. and Crouse, G.L., A State-Space Model for the Aerodynamics in a Compressible Flow for Flutter Analysis, *AIAA Paper 89-0022*, 1989, pp. 1-11.
- [75] Leishman, J. G., *Principles of Helicopter Aerodynamics*, Cambridge University Press, 2000.
- [76] Experimental Database of Sheldahl, R. E. and Klimas, P. C., 1981, Sandia National Laboratories, Albuquerque, New Mexico, www.cyberiad.net.
- [77] Losito., V., *Teoria e Metodi di Aerodinamica Applicata*, Department of Aerospace Engineering, University of Naples, Italy, 1972.
- [78] Quarteroni, A. *Modellistica Numerica per Problemi Differenziali*, Springer Italy, Milan, 2000.
- [79] Quarteroni, A., Saleri, F., *Introduzione al Calcolo Scientifico*, Springer Italy, Milan, 2002.
- [80] Mathews, J. H. and Fink, K K., *Numerical Methods Using Matlab*, 4th Edition, 2004, Prentice-Hall Inc. Upper Saddle River, New Jersey, USA.
- [81] Ford J.A., Improved Algorithms of Illinois-type for the Numerical Solution of Nonlinear Equations, Technical Report CSM-257, University of Essex, 1995.
- [82] Richard L. Burden, J. Douglas Faires, *Numerical Analysis (7th Ed)*, Brooks/Cole, 2000.
- [83] Abbott, I. A. and Van Doenhoff, A. E., "Theory of Wing Section" Dover Publications 1949.
- [84] Strickland, J.H., Smith T., Sun K., A vortex model of the Darrieus Wind Turbine: An Analytical and Experimental Study, Sandia National Laboratories, Albuquerque, N.M., SAND81-7017, June 1981.
- [85] A.V. Oppenheim, R.W. Schaffer with J. R. Buck, *Discrete Time Digital Signal Processing*, Prentice Hall.
- [86] M. Luise, G.M. Vitetta, *Teoria dei segnali*, McGraw-Hill, 1999.
- [87] FFTW (<http://www.fftw.org>)

-
- [88] Frigo, M. and S. G. Johnson, FFTW: An Adaptive Software Architecture for the FFT, Proceedings of the International Conference on Acoustics, Speech, and Signal Processing, Vol. 3, 1998, pp. 1381-1384.
- [89] J.W. Cooley, J.W. Tukey, An Algorithm for the Machine Computation of the Complex Fourier Series, Mathematics of Computation, Vol. 19, April 1965.
- [90] Rader, C. M., Discrete Fourier Transforms when the Number of Data Samples Is Prime, Proceedings of the IEEE, Vol. 56, June 1968, pp. 1107-1108.
- [91] Duhamel, P. and M. Vetterli, Fast Fourier Transforms: A Tutorial Review and a State of the Art, Signal Processing, Vol. 19, April 1990, pp. 259-299.
- [92] Brooks, T.F., Pope, D. and Marcolini, M.A., Airfoil Self-Noise and Prediction, NASA Reference Publication 1218, 1989.
- [93] S. Oerlemans, Wind Tunnel Aeroacoustic Tests of Six Airfoils for Use on Small Wind Turbines, Nationaal Lucht-en Ruimtevaart laboratorium National Aerospace Laboratory NLR Emmeloord, The Netherlands, NREL/SR-500-35339, 2004.
- [94] Herr, M., Design Criteria for Low Noise Trailing Edges, AIAA Paper 2007-3470, 2007.
- [95] Oerlemans, S., and Migliore, P., Aeroacoustic Wind Tunnel Tests of Wind Turbine Airfoils, AIAA Paper 2004-3042, 2004.
- [96] NASA/CP-2004-212954, Fourth Computational Aeroacoustics Workshop on benchmark Problems, <http://gltrs.grc.nasa.gov/reports/2004/CP-2004-212954.pdf> September 2004.
- [97] Bies D.A., Hansen C. H., Engineering Noise Control 4th Edition, Taylor & Francis Spon Press, 2009.
- [98] C.E. Whitfield, P.R. Gliebe, R. Mani, P. Mungur, High Speed Turboprop Aeroacoustic Study (Single Rotation) NASA CR-182257, Vol. 1 1989.
- [99] Graham, G. M., Measurement of Instantaneous Pressure Distributions and Blade Forces on an Airfoil Undergoing Cycloidal Motion, Texas Tech University, 1982.
- [100] NACA Technical Note 1354, Comparison of Sound Emission from Two-Blade, Four-Blade, and Seven-Blade Propeller, July 1947.

-
- [101] NACA Research Memorandum, L50D28, Effect of Compressibility and Camber as determined from an Investigation of the NACA 4-(3)(08)-03 and 4-(5)(08)-03 Two-Blade Propellers up to forward Mach Numbers of 0.925, June 1950.
- [102] Aerodynamics Aeronautics and Flight Mechanics, McCormick, 1967.
- [103] R. Tognaccini, Aerodynamics of the Rotating Wing, Department of Aerospace Engineering, University of Naples Federico II, 2005.
- [104] K. S. Brentner and F. Farassat, An Analytical Comparison of the Acoustic Analogy and Kirchoff Formulations for Moving Surfaces, AIAA Journal, 36(8), 1998.
- [105] J. E. Ffowcs-Williams and D. L. Hawkings, Sound Generation by Turbulence and Surfaces in Arbitrary Motion, Proc. Roy. Soc. London, A264:321-342, 1969.
- [106] A. Brandt, Multi-level Adaptive Computations in Fluid Dynamics, Technical Report AIAA-79-1455, AIAA, Williamsburg, VA, 1979.
- [107] A. Jameson, Solution of the Euler Equations for Two Dimensional Transonic Flow by a Multigrid Method, MAE Report 1613, Princeton University, June 1983.
- [108] R.J. Jaracki, D.C. Mikkelson, B.J. Blaha, Wind Tunnel Performance of Four Energy Efficient Propellers, Designed for Mach 0.8 Cruise, NASA TM-79124 (1979).
- [109] G.L. Stefko, R.J. Jaracki, Wind Tunnel Results of Advanced High Speed Propellers in the Takeoff, Climb and Landing operating Regimes, NASA TM-87054 (1985).
- [110] J.H. Dittmar, Cruise Noise of the SR2 Propeller Model in a Wind Tunnel, NASA TM-101480 (1989).
- [111] Sulc, J., Hofr, J., and Benda, L, Exterior Noise on the Fuselage of Light Propeller Driven Aircraft in Flight, J. Sound Vib., Vol. 84, No. 1,198, pp 105-120.
- [112] J.H. Dittmar, P.L. Lasagna, H.L. Dryden, A Preliminary Comparison Between the SR-3 Propeller Noise in Flight and in a Wind Tunnel, NASA TM-82805 (1982).
- [113] Aeroacoustics of Flight Vehicles: Theory and Practice, NASA Reference Publication, No. 1258, Vol. 1 WRDC Technical Report 90-3052, 1991.
- [114] D.C. Mikkelson, B.J. Blaha, Design and Performance of Energy Efficient Propellers for Mach 0.8 Cruise, NASA TMX-73612, (1977).

- [115] D. Caridi, M. De Gennaro, C. de Nicola, Ffowcs Williams-Hawkings Acoustic Analogy for Simulation of NACA 4-(3)(08)-03 Propeller Noise in Take-Off Conditions, ASME-ATI-UIT 2010 Conference on Thermal and Environmental Issues in Energy Systems, pp. 1183-1188, 2010.
- [116] M. De Gennaro, D. Caridi, M. Pourkashanian, Ffowcs Williams-Hawkings Acoustic Analogy for Simulation of NASA SR2 Propeller Noise in Transonic Condition, ECCOMAS CFD 2010 Conference Proceedings, ID 1364 pp.1-16, 2010.
- [117] M. De Gennaro, D. Caridi, C. de Nicola, Noise Prediction of NASA SR2 in Transonic Conditions, ICNAAM 2010 Conference and American Institute of Physics Proceedings, 2010.
- [118] M. De Gennaro, H. Kuehnelt, Computational Aeroacoustic for Coupled and Uncoupled Problems, 10th ERCOFTAC ADA PC Meeting, Wien, Austria, 2009.